

**IDENTIFIED PARTICLE PRODUCTION AND
FREEZE-OUT DYNAMICS IN STAR AT RHIC BEAM
ENERGY SCAN PROGRAM**

By

SABITA DAS

(Enrolment No.: PHYS07200904003)

Institute of Physics,

Bhubaneswar - 751005, India

A thesis submitted to the

Board of Studies in Physical Sciences

In partial fulfillment of requirements

for the Degree of

DOCTOR OF PHILOSOPHY

of

HOMI BHABHA NATIONAL INSTITUTE

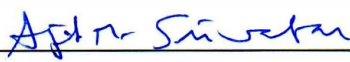



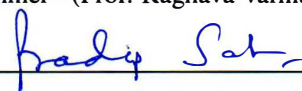


October, 2015

Homi Bhabha National Institute

Recommendations of the Viva Voce Board

As members of the Viva Voce Board, we certify that we have read the dissertation prepared by **Sabita Das** entitled **"Identified Particle Production and Freeze-out Dynamics in STAR at RHIC Beam Energy Scan Program"** and recommend that it may be accepted as fulfilling the thesis requirement for the award of Degree of Doctor of Philosophy.

	26-10-15
Chairman - (Prof. Ajit Mohan Srivastava)	Date: 26/10/15
	
Guide/Convener - (Prof. Sudhakar Panda)	Date: 26/10/15
	
Co-Guide - (Prof. Bedangadas Mohanty)	Date: 26/10/2015
	26/10/2015
Examiner - (Prof. Raghava Varma)	Date:
	26/10/2015
Member - (Prof. Pradip Kumar Sahu)	Date:

Final approval and acceptance of this dissertation is contingent upon the candidate's submission of the final copies of the dissertation to HBNI.

I hereby certify that I have read this dissertation prepared under my direction and recommend that it may be accepted as fulfilling the dissertation requirement.

Date: 26/10/2015

Place: IOP, Bhubaneswar


Prof. Bedangadas Mohanty

(Co-guide)


Prof. Sudhakar Panda

(Guide)

STATEMENT BY AUTHOR

This dissertation has been submitted in partial fulfillment of requirements for an advanced degree at Homi Bhabha National Institute (HBNI) and is deposited in the Library to be made available to borrowers under rules of the HBNI.

Brief quotations from this dissertation are allowable without special permission, provided that accurate acknowledgement of source is made. Requests for permission for extended quotation from or reproduction of this manuscript in whole or in part may be granted by the Competent Authority of HBNI when in his or her judgement the proposed use of the material is in the interests of scholarship. In all other instances, however, permission must be obtained from the author.

Sabita Das
Sabita Das

CERTIFICATE

This is to certify that the thesis entitled “**Identified Particle Production and Freeze-out Dynamics in STAR at RHIC Beam Energy Scan Program**” which is being submitted by **Sabita Das**, in partial fulfillment of the degree of **Doctor of Philosophy in Physics** of **Homi Bhabha National Institute** is a record of her own research work carried by her. She has carried out her investigations for the last five years on the subject matter of the thesis under my supervision at **Institute of Physics, Bhubaneswar**. To the best of our knowledge, the matter embodied in this thesis has not been submitted for the award of any other degree.

Date: 26.10.2015


Place: IOP, Bhubaneswar


Prof. Bedangadas Mohanty

(Co-guide)


Prof. Sudhakar Panda

(Guide)


Sabita Das

DECLARATION

I, Sabita Das, hereby declare that the investigation presented in the thesis has been carried out by me. The work is original and has not been submitted earlier as a whole or in part for a degree/diploma at this or any other Institution/University.

Sabita Das
Sabita Das

*Dedicated
to
My Family and Teachers*

Acknowledgements

Here I would like to thank all those people who contributed in many ways to the success of my doctoral study.

First, I owe my deepest gratitude to Prof. D. P. Mahapatra, who has given me a chance to work with him as a graduate student at Institute of Physics, India. His continuous encouragement, support both academically and personally meant a lot to me. I am also thankful to Mrs. Mahapatra for supporting me during my stays at BNL and till then.

My sincere thanks to Prof. S. Panda, Director of IOP, for agreeing to be my supervisor after the retirement of Prof. D. P. Mahapatra. He has always been approachable for any discussions and help.

I am extremely indebted to my co-supervisor Prof. B. Mohanty for his support, guidance, and encouragement throughout my research period. Under his guidance, I was able to overcome many difficulties and learned a lot specially about his sincerity, patience, hard work and giving equally importance to each part of work. His constructive suggestions always encouraged me to complete my work. I am very much thankful to him for giving me a very interesting thesis topic and also allowing me to carry out a part of my thesis work at BNL.

I would like to thank Prof. A. M. Srivastava, Prof. P. K. Sahu for being in my doctoral committee and for their help, encouragement, and interesting suggestions on my thesis work. I take this opportunity to sincerely thank Prof. S. M. Bhattacharjee, Prof. P. Agrawal, and Prof. B. R. Sekhar for being a part of my doctoral committee members at different stages of my Ph.D..

I gratefully acknowledge the help and encouragement of Dr. L. Kumar for my analysis work. He has helped me always, whenever I approached him.

My sincere thanks to Dr. Z. Xu, the STAR spokesperson and Dr. J. Dunlop, ex-group leader of the STAR group at BNL, for giving me an opportunity to carry out a part of my thesis work at BNL for a year. I am also thankful to them for providing me financial support to present my analysis work at SQM 2013 conference held at Birmingham, UK. Special thanks to Dr. Z. Xu for his guidance and support for my thesis work. I have greatly benefited from many useful discussions with him.

I am very much thankful to Dr. R. Majka, Dr. G. V. Buren, Dr. A. Ogawa, Dr. J. Landgraf, Dr. G. Visser, Dr. N. Smirnov, Dr. T. Ljubicic, Mr. S. Yang, and Mr. C. Yang for helping me much on GMT work. I have really enjoyed the discussions with them and it was a nice experience working with all of them.

Special thanks to Dr. N. Xu for his help and guidance during my thesis work. I would like to thank Dr. F. Geurts, Dr. X. Zhu, Dr. B. Huang, Dr. L. Ruan, Dr. F. Zhao, Dr. X. Li, Dr. Y. Pandit, Dr. H. Huang, Dr. Q. Xu, Dr. H. Masui, Dr. V. Fine, Dr. Y. Fisyak, Dr. J. Laurete, Prof. B. Ilope, Dr. X. Dong, Dr. A. Schmah, Mr. P. Shanmuganathan and Dr. L. C. De Silva for their help in many ways. I am very much thankful to Ms. L. Mogavero for helping me in all official work during my visit to BNL and after that.

Most of the results on statistical-thermal models described in this thesis would not have been obtained without the help of Prof. S. Wheaton, Prof. J. Cleymans, Prof. J. Takahashi, Dr. R. D. de Souza, Dr. D. Worku, and Dr. S. Chatterjee. I owe a great appreciation and gratitude to all of them.

My sincere thanks to Dr. Y. P. Viyogi, the ex-leader of the PMD project for his encouragement. I would like to express my sincere thanks to Dr. T. K. Nayak and Dr. S. Chattopadhyay for their help and support during my visit to VECC for collaboration meetings, conferences, and/or analysis works.

I am deeply thankful to all the faculties of physics department at Utkal University who encouraged me to pursue research in physics. I am so grateful to my school and college teachers. I am also thankful to all the faculty members of IOP for their help and encouragement in all aspect.

I would like to thank the convenors of STAR physics working group members for their valuable comments and suggestions. My sincere thanks to all the PMD collaborators and STAR collaborators for all their help and support.

I greatly appreciate all the administrative, library, laboratory, hostel mess, guest house, and computer centre staff members of IOP who have been kind enough to advise and help.

I wish to thank the RHIC Operations Group and RACF at BNL, the NERSC Center at LBNL, and Grid Computing Facilities at VECC, and IOP for providing resources and support. I acknowledge the financial support provided from HBNI, IOP, and BNL to present my work at many national, international conferences and meetings.

Special thanks to Dr. M. M. Mondal for his selfless support and giving me his precious time during my stay at BNL. He has helped me a lot in many difficult times both academically and non-academically. Specially, I will never forget his help during the time when I got injured just before leaving BNL. I would also like to thank Sanjit bhai and his family, Atikur bhai and his family, Matibur bhai and his family, for helping me many times at BNL. I really enjoyed my stay at BNL with all of them and these days will stay in memory forever.

It is also my pleasure to thank all my seniors, juniors and other friends for creating a pleasant atmosphere at IOP. My special thanks to Ananta bhai, Ajay bhai, Ranjita di, Rupali di, Sankha bhai, Ashutosh bhai, Jatis bhai, Ambresh bhai, Jaya di, Rama bhai, Partha, Shubhashis, Tanmoy, Anjan, Subrata, and Sudipta for all their help, care, support, and sharing memorable time with me. I have also spent some unforgettable moments with Dronika,

Bhanu, Nihar bhai, Nirbhaya, Amal, Sunita di, Neha di, Deepali di, Priyanka, Mukesh, and Shikshit. My warm and sincere thanks to all my seniors, juniors, and friends of Utkal University, all of my school and college friends, who have been always with me to help and support. I would like to thank all our group members of IOP and NISER, Dr. Ranbir Singh, Dr. Md. Nasim, Dr. Subhash Singha, Md. Rihan Haque, Mr. Shreekant Tripathy, Mr. Nihar Ranjan Panda, Mrs. Sarita Sahoo, Mr. Vipul Bairathi, Mr. Kishora Nayak, Miss Debadeepti Mishra, and Dr. Saikat Biswas for many useful discussions.

I would like to express high regards to my parents, brothers, sisters, my in-laws for their encouragement, support, and inspiration throughout my research work and lifting me this phase of life. I owe everything to them.

Besides this, thanks to all those who have knowingly and unknowingly helped me in the successful completion of this project.

Finally, I would like to express my heartfelt thanks to my beloved husband Dr. Chitrasen Jena for his continued emotional support, inspiration, and help in every possible way for my research work and for the completion of this thesis.

SYNOPSIS

One of the early goals of heavy-ion collision experiments was to establish the existence of a new state of matter, the quark-gluon plasma (QGP), which is believed to have existed in the early universe during few microseconds after the Big Bang. Quantum chromodynamics (QCD), the theory of strong interactions, predicts a phase transition at sufficiently high temperature (T) and/or high energy density from normal hadronic matter to a QGP state. Finite temperature lattice QCD calculations predict a crossover from hadronic to QGP phase at vanishing baryon chemical potential (μ_B) and large T , while several QCD-based calculations show that at lower T and higher μ_B , a first-order phase transition may take place. The point in the QCD phase diagram, where the first-order phase transition ends would be the QCD critical point. The QGP phase is confirmed at $\mu_B = 0$ through experiments at both Relativistic Heavy Ion Collider (RHIC) and Large Hadron Collider (LHC) facilities. The existence of a critical point and first-order phase transition needs to be confirmed experimentally at high μ_B . Therefore, nowadays, the major objective of the RHIC experiment is to create necessary conditions to investigate the phase diagram of hadronic matter, especially the expected first-order phase transition to QGP state and search for the QCD critical point. With this purpose, the Solenoidal Tracker At RHIC (STAR) which is one of the experiments at RHIC, has collected data at various collision energies $\sqrt{s_{NN}} = 7.7, 11.5, 19.6, 27, \text{ and } 39 \text{ GeV}$ as a part of its first phase of the Beam Energy Scan (BES-I) program in the year 2010 and 2011. The QCD phase diagram is characterised by T and μ_B . Within the framework of the statistical thermal models, these two thermodynamic quantities together with other freeze-out parameters, can be extracted using the integrated particle yields (dN/dy) at chemical freeze-out.

This thesis work is based on the identified particle production in Au+Au collisions at $\sqrt{s_{NN}} = 27 \text{ GeV}$ and a detailed study of the freeze-out dynamics at the above mentioned RHIC BES-I energies. In addition, the data from Alternating Gradient Synchrotron (AGS),

Super Proton Synchrotron (SPS), RHIC, and LHC energies have been analysed for most central collisions to understand the energy dependence of the freeze-out properties. A description of the STAR detector and its different subsystems is presented in the thesis. Out of many sub systems of STAR, the Time Projection Chamber (TPC) and the Time-of-Flight (TOF) detectors have been used to identify the hadrons such as pion (π^\pm), kaon (K^\pm), proton (p), and antiproton (\bar{p}). In this thesis, we also report a study on the performance of triple Gas Electron Multiplier (GEM) chambers to monitor the TPC tracking with the cosmic ray. This is essential for future upgradation of the STAR TPC in the second phase of BES program (BES-II).

We have studied the identified particle production in Au+Au collisions at $\sqrt{s_{NN}} = 27$ GeV, which was collected by the STAR experiment in the year 2011 as a part of BES-I program. The transverse momentum (p_T) spectra and the integrated yields of identified particles are essential observables to study the kinetic and chemical freeze-out dynamics of the system formed in heavy-ion collisions. The p_T -spectra have been obtained for π^\pm , K^\pm , p, and \bar{p} up to $p_T = 2$ GeV/c for nine collision centralities at mid-rapidity ($|y| < 0.1$). The results show that there is a variation of inverse slope of the spectra with particle mass and the effect is observed to be more pronounced at low p_T . In order to study the change in the measured spectral shapes quantitatively, the average transverse momentum ($\langle p_T \rangle$) and the average transverse mass ($\langle m_T \rangle$) have been investigated as a function of collision energy and centrality. It is observed that with increasing centrality, the values of $\langle m_T \rangle$ increase, indicating the development of stronger collective motion in more central collisions. The variation of $\langle m_T \rangle - m$ versus collision energy can be very useful regarding understanding the order of the phase transition. However, a more systematic study is needed to firmly establish this conclusion. The measured particle density provides information about the longitudinal dynamics of collisions. The energy and centrality dependence of dN/dy and particle ratios have been studied. All the results have been compared with results from other BES-I ener-

gies and also with AGS, SPS, top RHIC, and LHC energies.

This thesis also discuss the centrality and energy dependence of chemical freeze-out parameters at $\sqrt{s_{NN}} = 7.7, 11.5, 19.6, 27, 39, 62.4$, and 200 GeV. At chemical freeze-out, the inelastic collisions stops and the particle yields get fixed. In order to study the QCD phase structure experimentally as a function of T and μ_B , it is important to extract the thermodynamic quantities through a detailed chemical freeze-out study at RHIC BES-I energies at $\sqrt{s_{NN}} = 7.7, 11.5, 19.6, 27$, and 39 GeV along with top RHIC energies $\sqrt{s_{NN}} = 62.4$ and 200 GeV. We have used THERMUS model (statistical model on thermodynamic equilibrium) to study the particle production at RHIC energies. Experimental particle yields and the obtained particle ratios from those yields have been used as input separately to THERMUS model in both grand canonical ensemble (GCE) and strangeness canonical ensemble (SCE) approach. From the best fit to the particle yields from THERMUS and experimental data, the energy and centrality dependence of the extracted chemical freeze-out parameters such as chemical freeze-out temperature (T_{ch}), baryon chemical potential (μ_B), strangeness chemical potential (μ_S) and strangeness saturation factor (γ_S) in Au+Au collisions at above BES-I energies have been obtained. From present analysis, we observe that the BES-I energies from $\sqrt{s_{NN}} = 7.7$ to 39 GeV, along with the top RHIC energies, cover a wide range of μ_B from 20 to 420 MeV in the QCD phase diagram. The results of the search for the critical point and the first-order phase boundary have narrowed the region of interest to the collision energies below $\sqrt{s_{NN}} = 20$ GeV.

We also present a systematic study of chemical freeze-out (CFO) conditions from lower AGS energies up to higher LHC energies ($\sqrt{s_{NN}} = 2.7 - 2760$ GeV). In such a study, we have also investigated the dependence of freeze-out parameters on (a) the choice of the thermodynamic ensemble, (b) choice of the free parameters, (c) choice of particles whose yields are used as inputs to extract the values of the thermal parameters, and (d) choice of the CFO scheme. We have compared the particle ratios as obtained in single (chemi-

cal) freeze-out (1CFO), where all particles are assumed to freeze-out together, and double (chemical) freeze-out (2CFO), where strange and non-strange particles freeze-out at different times, to that obtained from the experimental data. We see that particle ratios of unlike flavor like K/π and Λ/p discriminate between different CFO schemes while those of same flavor like p/π^+ and Λ/K^- appear similar in both the schemes. The 2CFO scheme seems to describe all the ratios better compared to 1CFO.

In the end, we have presented a study of the Gas Electron Multiplier (GEM) chambers with cosmic rays. This has been carried out with a goal of implementing some corrections for space charge induced distortions in the TPC. Earlier a model of the accumulated charge in the TPC was used to correct distortions, which was valid at radii smaller than the inner radius of the TPC. However, no precision points outside the TPC were available to check the corrected tracks. With this purpose, eight GEM chambers to Monitor the TPC Tracking (GMT) have been installed at eight locations at the same radius as the TOF in STAR in the year 2013. This thesis explains the fabrication and test of the detectors using cosmic ray, before installation in STAR. Each of the GMT test modules has been evaluated with a ^{55}Fe source to study gain uniformity. Efficiency in excess of 95% has been achieved for all the chambers. On the test stand, with cosmic rays, an upper limit for the resolution of $\sim 150\text{ }\mu\text{m}$ has been achieved. This is significantly better than the TPC pointing resolution of $\sim 1\text{ mm}$. All the chambers have been installed and tested in STAR during Run-13 data taking and found to be working perfectly.

Publications

List of Publications as a primary author:

- * 1. Identified particle production and freeze-out properties in heavy-ion collisions in RHIC BES program.
Sabita Das (for the STAR Collaboration),
EPJ Web of Conf. 90 (2015) 08007.

- * 2. Freeze-out parameters in heavy-ion collisions at AGS, SPS, RHIC, and LHC energies.
Sandeep Chatterjee, Sabita Das, and Bedangadas Mohanty *et al.*,
Adv. in High Eng. Phys., Vol. 2015, Review Article ID: 349013.

- * 3. Cosmic ray test of Mini-drift Thick Gas Electron Multiplier for Transition Radiation Detector.
Shuai Yang, Sabita Das, and Zhangbu Xu *et al.*,
Nucl. Instr. Meth. A 785 (2015) 33–39.

- * 4. Chemical freeze-out parameters in Beam Energy Scan program of STAR at RHIC.
Sabita Das (for the STAR Collaboration),
EPJ Web of Conf. 90 (2015) 10003.

- * 5. Study of freeze-out dynamics in STAR at RHIC Beam Energy Scan program.
Sabita Das (for the STAR Collaboration),
J. Phys. Conf. Ser. 509 (2014) 012066.

- * 6. Centrality dependence of freeze-out parameters from the beam energy scan at STAR.
Sabita Das (for the STAR Collaboration),
Nucl. Phys. A 904 (2013) 891c.

Papers under review in STAR collaboration (as a primary author):

- *1. Energy and centrality dependence of freeze-out parameters in search of the QCD critical point from the Beam Energy Scan program at RHIC.
L. Adamczyk, ..., S. Das *et al.* (STAR Collaboration),
Target Journal: **Phys. Rev. Lett.** (under PWG review).
- *2. Bulk properties from the Beam Energy Scan program at RHIC.
L. Adamczyk, ..., S. Das *et al.* (STAR Collaboration),
Target Journal: **Phys. Rev. C** (under GPC review).

List of DAE Proceedings in India:

- *1. Chemical freeze-out condition for central heavy-ion collisions at AGS, SPS, RHIC, and LHC Energies.
Sandeep Chatterjee, Sabita Das, Bedangadas Mohanty *et al.*,
Proceedings of the DAE Symposium on Nuclear Physics, Vol. 59 (2014).
- *2. Study of the charged pions, kaons and protons production in Au+Au collisions at $\sqrt{s_{NN}} = 27$ GeV in STAR at RHIC.
Sabita Das (for the STAR Collaboration),
Proceedings of the DAE Symposium on Nuclear Physics, Vol. 58 (2013).
- *3. Chemical freeze-out parameters from Au+Au collisions at $\sqrt{s_{NN}} = 7.7, 11.5$, and 39 GeV.
Sabita Das (for the STAR Collaboration),
Proceedings of the DAE Symposium on Nuclear Physics, Vol. 56 (2011).

Internal Note of STAR Collaboration:

- *1. Studying the phase diagram of QCD matter at RHIC,
<https://drupal.star.bnl.gov/STAR/starnotes/public/sn0598>.

Selected List of Publications/Preprints as a part of STAR Collaboration:

1. Centrality dependence of identified particles in relativistic heavy-ion collisions at $\sqrt{s_{NN}} = 7.7\text{-}62.4$ GeV,
L. Adamczyk *et al.* (STAR Collaboration), arXiv:1509.08397.
2. Centrality and transverse momentum dependence of elliptic flow of multi-strange hadrons and ϕ meson in Au+Au collisions at $\sqrt{s_{NN}} = 200$ GeV,
L. Adamczyk *et al.* (STAR Collaboration), arXiv:1507.05247.
3. Probing Parton Dynamics of QCD Matter with Ω and ϕ Production,
L. Adamczyk *et al.* (STAR Collaboration), arXiv:1506.07605.
4. Azimuthal anisotropy in U+U and Au+Au collisions at RHIC,
L. Adamczyk *et al.* (STAR Collaboration), arXiv:1506.07605.
5. Energy Dependence of K/π , p/π , and K/p Fluctuations in Au+Au Collisions from $\sqrt{s_{NN}} = 7.7$ to 200 GeV,
N. M. Abdelwahab *et al.* (STAR Collaboration), Phys. Rev. C 92 (2015) 021901.
6. Di-Hadron Correlations with Identified Leading Hadrons in 200 GeV Au+Au and d+Au Collisions at STAR,
N. M. Abdelwahab *et al.* (STAR Collaboration), arXiv:1410.3524.
7. Isolation of Flow and Nonflow Correlations by Two- and Four-Particle Cumulant Measurements of Azimuthal Harmonics in $\sqrt{s_{NN}} = 200$ GeV Au+Au Collisions,
N. M. Abdelwahab *et al.* (STAR Collaboration), arXiv:1409.2043.
8. Charged-to-neutral correlation at forward rapidity in Au+Au collisions at $\sqrt{s_{NN}} = 200$ GeV,

- N. M. Abdelwahab *et al.* (STAR Collaboration), Phys. Rev. C 91 (2015) 034905.
9. Elliptic flow of non-photonic electrons in Au+Au collisions at $\sqrt{s_{NN}} = 200, 62.4$ and 39 GeV,
L. Adamczyk *et al.* (STAR Collaboration), arXiv:1405.6348.
 10. Precision Measurement of the Longitudinal Double-spin Asymmetry for Inclusive Jet Production in Polarized Proton Collisions at $\sqrt{s_{NN}} = 200$ GeV,
L. Adamczyk *et al.* (STAR Collaboration), Phys. Rev. Lett. 115 (2015) 092002.
 11. Measurement of longitudinal spin asymmetries for weak boson production in polarized proton-proton collisions at RHIC,
L. Adamczyk *et al.* (STAR Collaboration), Phys. Rev. Lett. 113 (2014) 072301.
 12. Observation of D^0 meson nuclear modifications in Au+Au collisions at $\sqrt{s_{NN}} = 200$ GeV,
L. Adamczyk *et al.* (STAR Collaboration), Phys. Rev. Lett. 113 (2014) 142301.
 13. Beam-energy dependence of charge separation along the magnetic field in Au+Au collisions at RHIC,
L. Adamczyk *et al.* (STAR Collaboration), Phys. Rev. Lett. 113 (2014) 052302.
 14. Beam energy dependent two-pion interferometry and the freeze-out eccentricity of pions in heavy-ion collisions at STAR,
L. Adamczyk *et al.* (STAR Collaboration), Phys. Rev. C 92 (2015) 014904.
 15. Dielectron Azimuthal Anisotropy at mid-rapidity in Au+Au collisions at $\sqrt{s_{NN}} = 200$ GeV,
L. Adamczyk *et al.* (STAR Collaboration), arXiv:1402.1791.

16. Beam energy dependence of moments of the net-charge multiplicity distributions in Au+Au collisions at RHIC,
L. Adamczyk *et al.* (STAR Collaboration), arXiv:1402.1558.
17. Beam-Energy Dependence of Directed Flow of Protons, Antiprotons and Pions in Au+Au Collisions,
L. Adamczyk *et al.* (STAR Collaboration), Phys. Rev. Lett. 112 (2014) 162301.
18. Dielectron Mass Spectra from Au+Au Collisions at $\sqrt{s_{NN}} = 200$ GeV,
L. Adamczyk *et al.* (STAR Collaboration), Phys. Rev. Lett. 113 (2014) 022301.
19. Suppression of Upsilon Production in d+Au and Au+Au Collisions at $\sqrt{s_{NN}} = 200$ GeV,
L. Adamczyk *et al.* (STAR Collaboration), Phys. Lett. B 735 (2014) 127.
20. J/ψ polarization in $p + p$ collisions at $\sqrt{s} = 200$ GeV in STAR ,
L. Adamczyk *et al.* (STAR Collaboration), arXiv:1311.1621.
21. J/ψ production at low p_T in Au+Au and Cu+Cu collisions at $\sqrt{s_{NN}} = 200$ GeV at STAR,
L. Adamczyk *et al.* (STAR Collaboration), Phys. Rev. C 90 (2014) 024906.
22. Energy dependence of moments of net-proton multiplicity distributions at RHIC,
L. Adamczyk *et al.* (STAR Collaboration), Phys. Rev. Lett. 112 (2014) 32302.
23. Neutral pion cross section and spin asymmetries at intermediate pseudorapidity in polarized proton collisions at $\sqrt{s} = 200$ GeV,
L. Adamczyk *et al.* (STAR Collaboration), Phys. Rev. D 89 (2014) 12001.
24. Measurement of Charge Multiplicity Asymmetry Correlations in High Energy Nucleus-Nucleus Collisions at 200 GeV,

- L. Adamczyk *et al.* (STAR Collaboration), Phys. Rev. C 89 (2014) 044908.
25. Jet-Hadron Correlations in $\sqrt{s_{NN}} = 200$ GeV Au+Au and p+p Collisions,
L. Adamczyk *et al.* (STAR Collaboration), Phys. Rev. Lett. 112 (2014) 122301.
 26. Fluctuations of charge separation perpendicular to the event plane and local parity violation in $\sqrt{s_{NN}} = 200$ GeV Au+Au collisions at RHIC,
L. Adamczyk *et al.* (STAR Collaboration), Phys. Rev. C 88 (2013) 64911.
 27. Freeze-out Dynamics via Charged Kaon Femtoscopy in $\sqrt{s_{NN}} = 200$ GeV Central Au+Au Collisions,
L. Adamczyk *et al.* (STAR Collaboration), Phys. Rev. C 88 (2013) 34906.
 28. System Size Dependence of Transverse Momentum Correlations at RHIC,
L. Adamczyk *et al.* (STAR Collaboration), Phys. Rev. C 87 (2013) 64902.
 29. Elliptic flow of identified hadrons in Au+Au collisions at $\sqrt{s_{NN}} = 7.7\text{--}62.4$ GeV,
L. Adamczyk *et al.* (STAR Collaboration), Phys. Rev. C 88 (2013) 14902.
 30. Third Harmonic Flow of Charged Particles in Au+Au Collisions at $\sqrt{s_{NN}} = 200$ GeV,
L. Adamczyk *et al.* (STAR Collaboration), Phys. Rev. C 88 (2013) 14904.
 31. Observation of an energy-dependent difference in elliptic flow between particles and antiparticles in relativistic heavy-ion collisions,
L. Adamczyk *et al.* (STAR Collaboration), Phys. Rev. Lett. 110 (2013) 142301.
 32. Measurement of J/psi Azimuthal Anisotropy in Au+Au Collisions at $\sqrt{s_{NN}} = 200$ GeV,
L. Adamczyk *et al.* (STAR Collaboration), Phys. Rev. Lett. 111 (2013) 52301.

33. Studies of di-jets in Au+Au collisions using angular correlations with respect to back-to-back leading hadrons,
L. Adamczyk *et al.* (STAR Collaboration), Phys. Rev. C 87 (2013) 44903.
34. J/ψ production at high transverse momenta in p+p and Au+Au collisions at $\sqrt{s_{NN}} = 200$ GeV,
L. Adamczyk *et al.* (STAR Collaboration), Phys. Lett. B 722 (2013) 55.
35. Single Spin Asymmetry A_N in Polarized Proton-Proton Elastic Scattering at $\sqrt{s} = 200$ GeV,
L. Adamczyk *et al.* (STAR Collaboration), Phys. Lett. B 719 (2013) 62.
36. Inclusive charged hadron elliptic flow in Au + Au collisions at $\sqrt{s_{NN}} = 7.7 - 39$ GeV,
L. Adamczyk *et al.* (STAR Collaboration), Phys. Rev. C 86 (2012) 54908.

(*) indicates papers on which this thesis is based.

Contents

1	Introduction	1
1.1	Standard Model	1
1.2	Quantum Chromodynamics	3
1.2.1	Confinement and Asymptotic Freedom	4
1.2.2	QCD Phase Transition and Quark-Gluon Plasma	6
1.3	Relativistic Heavy Ion Collisions	8
1.3.1	Space-Time Evolution of Heavy Ion Collisions	9
1.3.2	QCD Phase Diagram	12
1.4	RHIC Beam Energy Scan Program	15
1.5	Signatures of Quark-Gluon Plasma	17
1.5.1	Strangeness Enhancement	18
1.5.2	Azimuthal Anisotropy or Flow	20
1.5.3	High p_T Probes	25
1.5.4	Quarkonia Suppression	28
1.5.5	Photons and Dileptons	30
1.6	Identified Particle Production	32
1.6.1	Transverse Momentum Spectra	33
1.6.2	Particle Yields and Ratios	34
1.6.3	Average Transverse Momentum	35

1.6.4	Average Transverse Mass	36
1.7	Freeze-out Dynamics	37
1.8	Outline of the Thesis	42
2	The Experimental Details	48
2.1	Introduction	48
2.2	Relativistic Heavy Ion Collider	50
2.3	The STAR Detector	56
2.3.1	Time Projection Chamber	59
2.3.1.1	Technical Design	60
2.3.1.2	Track Reconstruction	62
2.3.1.3	Particle Identification	63
2.3.2	Space Charge Distortion in the TPC and GEM Monitor	65
2.3.3	Time-of-Flight and pseudo Vertex Position Detector	67
2.3.4	Trigger Detectors	69
2.3.4.1	Zero Degree Calorimeter	70
2.3.4.2	Beam-Beam Counter	71
2.3.4.3	Electromagnetic Calorimeters	71
3	Identified Particle Production in Au+Au Collisions at $\sqrt{s_{NN}} = 27$ GeV	77
3.1	Introduction	77
3.2	Procedure for Data Analysis	79
3.3	Data Set, Trigger, and Analysis Cuts	79
3.3.1	Event Selection	80
3.3.2	Track Selection	81
3.3.3	Centrality Selection	83
3.4	Particle Identification Using TPC and TOF	85

3.5	Raw Yields Extraction	88
3.5.1	Using TPC	88
3.5.2	Using TOF	90
3.6	Raw Spectra and Corrections	92
3.6.1	Energy loss Correction	94
3.6.2	TPC–TOF Matching Efficiency Correction	96
3.6.3	Track Reconstruction Efficiency and Acceptance Correction	97
3.6.4	Pion Feed–down Correction	99
3.6.5	Proton Background Correction	101
3.7	Results and Discussions	104
3.7.1	Transverse Momentum Spectra	104
3.7.2	Average Transverse Momentum ($\langle p_T \rangle$)	108
3.7.3	Average Transverse Mass ($\langle m_T \rangle$)	110
3.7.4	Particle Yields	112
3.7.4.1	Centrality Dependence of dN/dy	115
3.7.4.2	Energy dependence of dN/dy	116
3.7.5	Particle Ratios	118
3.7.5.1	p_T Dependence of Particle Ratios	118
3.7.5.2	Centrality Dependence of Particle Ratios	119
3.7.5.3	Energy Dependence of Particle Ratios	122
3.8	Summary	125
4	Study of Freeze-out Dynamics in STAR at RHIC BES Program	131
4.1	Introduction	131
4.2	QCD Phase Diagram and BES-I program	133
4.3	Chemical Freeze-out	133

4.4	The Statistical-Thermodynamic Model	134
4.5	The THERMUS Package	135
4.5.1	The Grand-Canonical Ensemble	136
4.5.2	The Canonical Ensemble	138
4.5.3	The Strangeness-Canonical Ensemble	139
4.6	Additional Considerations	140
4.6.1	Feed-down	140
4.6.2	Deviations from Chemical Equilibrium in Strangeness Sector	141
4.7	Analysis Details	142
4.7.1	Data Set	142
4.7.2	Choice of Particle Yields and Ratios	143
4.7.3	Choice of Ensemble	144
4.7.4	Choice of Freeze-out Parameters	144
4.7.5	Feed-down Correction	145
4.8	Results and Discussions	146
4.8.1	Particle Yields	146
4.8.1.1	Grand-Canonical Ensemble (GCE)	146
4.8.1.2	Strangeness-Canonical Ensemble (SCE)	151
4.8.2	Particle Ratios	153
4.8.3	Chemical Freeze-out Curve: T_{ch} vs. μ_B	155
4.9	Kinetic Freeze-out	160
4.10	Summary	163
	Appendix A	171
5	Systematic Study of Freeze-out Parameters in Central Heavy-ion Collisions at AGS, SPS, RHIC, and LHC Energies	178

5.1	Introduction	178
5.2	Chemical Freeze-out	181
5.3	Model	183
5.4	Results and Discussions	185
5.5	Summary	195
	Appendix B	205
6	Performance of the GEM Chambers to Monitor the TPC Tracking Calibrations in STAR	210
6.1	Introduction	210
6.2	The GEM Technology	213
6.3	Read-out Electronics	214
6.4	Cosmic Ray Test System Setup	216
6.5	Performance of the GEM Chambers	218
6.5.1	Efficiency	220
6.5.2	Gain	221
6.5.3	Spatial Resolution	222
6.6	Installation of GMT in STAR TOF trays	224
6.7	Commissioning in STAR	224
6.8	Thick GEM for Transition Radiation Detector	226
6.9	Summary	227
7	Conclusions	230

List of Figures

1.1	Overview of fundamental particles of the standard model and the force mediating gauge bosons.	3
1.2	Summary of measurements of $\alpha_s(Q)$ as a function of energy scale Q . The curves show the QCD predictions [9].	5
1.3	Lattice QCD calculations for energy density (left) and pressure (right) as a function of temperature for 2, 2+1, and 3 flavor QCD [12]. The dependence on the number of quark flavors are shown in different colored lines. The arrows indicate the Stefan-Boltzmann limit in both the figures.	6
1.4	Schematic diagram of before and after collision of two nuclei with non zero impact parameter. The participants and the spectator nucleons are also shown.	9
1.5	Schematic view of the space-time diagram and various stages of a relativistic heavy-ion collisions.	11
1.6	Proposed QCD phase diagram for nuclear matter [18].	14
1.7	The schematic picture of the QCD Phase Diagram with marked coverage of the RHIC BES-I program. Yellow trajectories represent the different energies of the BES-I program. The red circle symbolises the critical point. Note that the yellow lines and the red circle are for illustrative purpose only [18].	16

1.8	Upper panel: The ratio of the yields of K^- , ϕ , $\bar{\Lambda}$, and $\Xi + \bar{\Xi}$ normalised to $\langle N_{\text{part}} \rangle$ in Au+Au and Cu+Cu collisions to corresponding yields in inelastic p+p collisions as a function of $\langle N_{\text{part}} \rangle$ at $\sqrt{s_{\text{NN}}} = 200$ GeV. Lower panel: Same as above but for only ϕ mesons in Au+Au and Cu+Cu collisions at $\sqrt{s_{\text{NN}}} = 62.4$ and 200 GeV [29]. The error bars shown here represent the statistical and systematic errors added in quadrature.	19
1.9	Schematic diagram showing the transformation of initial coordinate space anisotropy into a momentum space anisotropy in a non-central heavy-ion collision.	20
1.10	The centrality dependence of p_T integrated v_2 as measured by the NA49 experiment at SPS [37] and STAR experiment at RHIC [38, 39].	21
1.11	The p_T dependence of the elliptic flow parameter, v_2 , in Au+Au collisions at $\sqrt{s_{\text{NN}}} = 200$ GeV as measured by the STAR experiment. The hydrodynamic calculations are shown as dot-dashed lines. This figure is taken from Ref. [39].	22
1.12	v_2 as a function of p_T for different hadrons in minimum bias Au+Au collisions at $\sqrt{s_{\text{NN}}} = 200$ GeV [39]. Hydrodynamical calculations are shown by solid and dotted curves [40].	23
1.13	Upper panel: v_2/n vs. p_T/n for identified particles measured by the STAR experiment. n is the number of constituent quarks. The dashed-dotted line is the polynomial fit to the data. Lower panel: The data from the upper panel is divided by the polynomial fit as a function of p_T/n [39].	24

1.14	Upper panel: In p+p collisions, the partons (quarks depicted in green, red, and blue balls) can hit each other where some of these partons (pink balls) can fly away and hadronise forming dijets of energetic hadrons (white balls). Lower panel: The jets produced in early stages of heavy-ion collisions travelling in opposite directions, propagating through QGP, and one of two jets is quenched. This figure is taken from Ref. [44].	25
1.15	The measurement of dihadron azimuthal correlations at high p_T for p+p at $\sqrt{s} = 200$ GeV, and for central d+Au and Au+Au collisions at $\sqrt{s_{NN}} = 200$ GeV in STAR experiment [46].	26
1.16	$R_{AA}(p_T)$ for charged hadrons for different centralities as measured in the STAR experiment [49].	28
1.17	Upper panel: $J/\psi R_{AA}$ vs. N_{part} for Au+Au collisions at $\sqrt{s_{NN}} = 200$ GeV. The mid (forward) rapidity data are shown with open (solid) circles. Lower panel: Ratio of forward and mid-rapidity $J/\psi R_{AA}$ as a function of N_{part} [58].	29
1.18	Invariant cross section and invariant yield of direct photons as a function of p_T in p+p at $\sqrt{s} = 200$ GeV and in Au+Au collisions at $\sqrt{s_{NN}} = 200$ GeV, respectively [62]. The three curves on the p+p data represent NLO pQCD calculations [63], and the dashed curves show a modified power-law fit to the p+p data, scaled by T_{AA} . The black solid curves are exponential plus the T_{AA} scaled p+p fit. The red dotted curve near the 0–20% centrality data is a theory calculation [64].	30
1.19	Theoretical calculations of thermal photon emission are compared with the direct photon data in central 0–20% Au+Au collisions from PHENIX experiment [65].	31

1.20	Ratio of mid-rapidity net-protons to half the number of participants vs. the number of participants in p+p collisions at $\sqrt{s} = 200$ GeV and in Au+Au collisions at $\sqrt{s_{NN}} = 62.4, 130, \text{ and } 200$ GeV. Errors shown are the quadratic sum of statistical and systematic uncertainties [17].	34
1.21	K/ π ratio as a function of collision energies. The curves going through the heavy-ion data are the phenomenological fits [17].	35
1.22	Average transverse momenta as a function of dN_{ch}/dy for Au+Au at $\sqrt{s_{NN}} = 62.4, 130, \text{ and } 200$ GeV. The results from p+p and d+Au collision systems are also shown [17].	36
1.23	The variation of $\langle m_T \rangle - m$ as a function of $\sqrt{s_{NN}}$ for Au+Au and Pb+Pb collisions in AGS, SPS, and RHIC energies [66].	37
1.24	The mid-rapidity particle ratios (red symbol) obtained from p_T integrated yields for different hadron species in Au+Au collisions at $\sqrt{s_{NN}} = 200$ GeV. The blue lines represent the statistical model fits to the particle ratios. The fit parameters are $T_{ch} = 163 \pm 4$ MeV, $\mu_B = 24 \pm 4$ MeV, $\gamma_S = 0.99 \pm 0.07$ [68]. The inset shows the variation of γ_S with centrality. The figure is taken from Ref. [46].	38
1.25	The variation of T_{ch} and μ_B as a function of center-of-mass energy. The solid curve represents the theoretical curve [69].	39
1.26	Left: The T_{ch} vs. μ_B at different center-of-mass energies from AGS-LHC [69]. The curves corresponds to various models [71]. Right: The hadronic freeze-out line in the $\rho_B - \varepsilon$ phase obtained from the values of T_{ch} and μ_B [70]. . .	40
1.27	The χ^2 contours for T_{fo} and $\langle \beta_T \rangle$ extracted from thermal and radial flow fits for different hadrons produced in Au+Au collisions at $\sqrt{s_{NN}} = 200$ GeV. The figure is taken from Ref. [46].	41

2.1	Schematic diagram showing the various stages of acceleration of ions at the RHIC.	51
2.2	The nucleon-pair luminosity is defined as $L_{NN} = A_1 A_2 L$, where L is the luminosity and A_1, A_2 are the number of nucleons of the ions in the two beam, respectively.	53
2.3	Overview of the RHIC accelerator complex at Brookhaven National Laboratory, Upton, New York.	54
2.4	Three dimensional view of STAR detector system [19].	57
2.5	A cut-away side view of the STAR detector.	58
2.6	Beam's eye view of a central event in the STAR TPC [28].	59
2.7	The three dimensional schematic diagram of the STAR TPC [21].	60
2.8	One sector of the TPC anode plane with the inner and outer subsectors and their respective padrows [21].	61
2.9	The energy loss distribution for charged particles in the STAR TPC as a function of momentum [21].	64
2.10	Simulated shape of the potential due to space charge in the TPC (left) and the azimuthal distortions of electron clusters (right) caused by drifting through that potential as a function of radius R and drift Z . The cathode is at $Z = 0$, and electron clusters drift to the endcaps at high Z [33].	65
2.11	The schematic diagram of GMT positions (red box) in TOF trays placed outside TPC [34].	66
2.12	Geometry of TOF trays, modules, and pads.	68
2.13	The schematic diagram of TOF system with one TOF tray and pVPD. The TPC is cut away, while the STAR magnet and other subsystems are not drawn [23].	68

2.14	TOF $1/\beta$ as a function of momentum from p+p collisions at $\sqrt{s} = 200$ GeV [35].	69
2.15	The schematic diagram of all the trigger detectors fit together in the STAR system [37]. Now Central Trigger Barrel (CTB) is replaced by the barrel TOF system and Forward Pion Detector (FPD) is preceded by Forward Meson Spectrometer (FMS) at STAR.	70
3.1	The vertex position distributions in Au+Au collisions at $\sqrt{s_{NN}} = 27$ GeV. .	81
3.2	$\langle dE/dx \rangle$ of e^\pm , π^\pm , K^\pm , p, and \bar{p} as a function of rigidity in Au+Au collisions at $\sqrt{s_{NN}} = 27$ GeV.	87
3.3	$\frac{1}{\beta}$ as a function of rigidity in Au+Au collisions at $\sqrt{s_{NN}} = 27$ GeV.	88
3.4	Distributions of z_π for π^+ , z_K for K^+ , and z_p for p in TPC for different p_T bins in mid-rapidity, $ y < 0.1$ for 0–5% centrality in Au+Au collisions at $\sqrt{s_{NN}} = 27$ GeV. Errors are statistical only. The curves are Gaussian fits representing contributions from pions (dotted-red), electrons (dotted-green), kaons (dotted-blue), and protons (dotted-magenta).	89
3.5	The m^2 distributions for positively charged particles in TOF for different p_T bins in mid-rapidity, $ y < 0.1$, for 0–5% centrality in Au+Au collisions at $\sqrt{s_{NN}} = 27$ GeV. Errors are statistical only. The curves are predicted m^2 fits representing contributions from pions (solid-red), kaons (solid-green), protons (solid-blue), and the total fit (dot-dashed-red).	91
3.6	Comparison of the distributions of DCA and number of fit points (nHitsFit) for pions from embedding and from real data at mid-rapidity in Au+Au collisions at $\sqrt{s_{NN}} = 27$ GeV.	93

3.7	The energy loss correction for different particles as a function of p_T . Here p_T^{REC} is the reconstructed p_T before the energy loss correction, and p_T^{MC} is the input p_T of embedded track in Au+Au collisions at $\sqrt{s_{\text{NN}}} = 27$ GeV for 0–5% centrality. Errors are statistical only.	95
3.8	Matching efficiency of π^+ , K^+ , and p as a function of p_T and $ y < 0.1$ for 0–5% centrality in Au+Au collisions at $\sqrt{s_{\text{NN}}} = 27$ GeV. Errors are statistical only. Lines represent parametrisations to the data and are used for corrections.	97
3.9	Tracking efficiency including detector acceptance for reconstructed π^+ , K^+ , and p in the TPC as a function of input MC p_T and $ y < 0.1$ for 0–5% centrality in Au+Au collisions at $\sqrt{s_{\text{NN}}} = 27$ GeV. Errors are statistical only. Lines represent parametrisations to the data.	98
3.10	Percentage of pion background as a function of p_T in $ y < 0.1$ in Au+Au collisions at $\sqrt{s_{\text{NN}}} = 27$ GeV.	100
3.11	DCA distributions of p and \bar{p} for $0.4 < p_T < 0.45$ GeV/c and $0.6 < p_T < 0.65$ GeV/c for 0–5% centrality in Au+Au collisions at $\sqrt{s_{\text{NN}}} = 27$ GeV. Errors are statistical only. The solid red line represent the fitted p distribution, the dotted blue line represent the \bar{p} distribution scaled up by the \bar{p}/p ratio obtained from the fit, the dashed black line is the proton background obtained from the fit.	102
3.12	Centrality dependence of identified particle spectra measured in mid-rapidity ($ y < 0.1$) in Au+Au collisions at $\sqrt{s_{\text{NN}}} = 27$ GeV. Spectra are plotted at nine centrality bins and are scaled for different collision centrality for clarity. Curves represent Bose-Einstein function for pions, m_T exponential for kaons, and double exponential for protons/antiprotons. Errors are statistical and systematic errors added in quadrature.	106

3.13	The variation of $\langle p_T \rangle$ of π^+ , K^+ , and p as a function of $\langle N_{\text{part}} \rangle$ measured in $ y < 0.1$ in Au+Au collisions at $\sqrt{s_{\text{NN}}} = 27$ GeV and its comparison with other RHIC BES-I energies [35]. Errors are statistical and systematic errors added in quadrature. The 62.4 and 200 GeV results are from Ref. [32]. In the right bottom panel, the $\langle p_T \rangle$ as a function of mass is plotted for 0–5% centrality at RHIC energies.	109
3.14	The variation of $\langle m_T \rangle - m$ of π^\pm , K^\pm , and p (\bar{p}) as a function of $\sqrt{s_{\text{NN}}}$ measured in $ y < 0.1$ in Au+Au collisions at $\sqrt{s_{\text{NN}}} = 27$ GeV along with AGS [37], SPS [38], RHIC [32, 35], and LHC [33] energies. Errors are statistical and systematic errors added in quadrature.	111
3.15	dN/dy of π^+ , K^+ , p, and \bar{p} scaled by $\langle 0.5N_{\text{part}} \rangle$ as a function of $\langle N_{\text{part}} \rangle$ in Au+Au collisions at $\sqrt{s_{\text{NN}}} = 27$ GeV are shown along with other RHIC BES-I [35] and top RHIC [32] energies. Errors are the quadratic sum of statistical and systematic errors.	116
3.16	dN/dy of π^\pm , K^\pm , p, and \bar{p} scaled by $\langle 0.5N_{\text{part}} \rangle$ as a function of center-of-mass energy including Au+Au collisions at $\sqrt{s_{\text{NN}}} = 27$ GeV along with AGS [37], SPS [38], RHIC [32, 35], and LHC [33] energies. Errors are the quadratic sum of statistical and systematic errors.	117
3.17	π^-/π^+ , K^-/K^+ , and \bar{p}/p as a function of p_T for 0–5% centrality in Au+Au collisions at $\sqrt{s_{\text{NN}}} = 27$ GeV.	119
3.18	π^-/π^+ , K^-/K^+ , K^-/π^- , and K^+/π^+ as a function of $\langle N_{\text{part}} \rangle$ in Au+Au collisions at $\sqrt{s_{\text{NN}}} = 27$ GeV. The results are compared with other RHIC BES-I [35] and top RHIC [32] energies. Errors are the quadratic sum of statistical and systematic errors.	120

3.19	\bar{p}/p , p/π^+ , and \bar{p}/π^- in Au+Au collisions as a function of $\langle N_{\text{part}} \rangle$ at $\sqrt{s_{\text{NN}}} = 27$ GeV. The results are compared with other RHIC BES-I [35] and top RHIC [32] energies. Errors are the quadratic sum of statistical and systematic errors.	121
3.20	Particle ratios as a function of center-of-mass energy in Au+Au collisions at $\sqrt{s_{\text{NN}}} = 27$ GeV. The results are compared with AGS [37], SPS [38], RHIC [32, 35], and LHC [33] energies. Right bottom: the variation of K^-/K^+ as a function of \bar{p}/p for 0–5% centrality from SPS-LHC energies. Errors are the quadratic sum of statistical and systematic errors.	123
4.1	Comparison of statistical model prediction (lines) with experimental mid-rapidity particle yields using grand-canonical ensemble for 0–5% and 60–80% centrality in Au+Au at $\sqrt{s_{\text{NN}}} = 7.7$ GeV.	147
4.2	Chemical freeze-out parameters (T_{ch} , μ_B , μ_S , γ_S , and R) are shown as a function of $\langle N_{\text{part}} \rangle$ in Au+Au collisions at $\sqrt{s_{\text{NN}}} = 7.7, 11.5, 19.6, 27, 39, 62.4$, and 200 GeV obtained from THERMUS with GCE.	148
4.3	The variation of chemical freeze-out parameters as a function of $\langle N_{\text{part}} \rangle$ for different combinations of possible yields for Au+Au collisions at $\sqrt{s_{\text{NN}}} = 39$ GeV.	149
4.4	The variation of chemical freeze-out parameters as a function of $\langle N_{\text{part}} \rangle$ for different conditions on parameters (μ_Q and μ_S) for Au+Au collisions at $\sqrt{s_{\text{NN}}} = 7.7$ GeV.	150
4.5	Comparison of fit results to experimental mid-rapidity particle yields using strangeness-canonical ensemble for 0–5% and 60–80% centrality in Au+Au at $\sqrt{s_{\text{NN}}} = 7.7$ GeV.	151

4.6	Chemical freeze-out parameters (T_{ch} , μ_B , γ_S , and R) are shown as a function of $\langle N_{\text{part}} \rangle$ in Au+Au collisions at $\sqrt{s_{\text{NN}}} = 7.7, 11.5, 19.6, 27, 39, 62.4$, and 200 GeV in SCE.	152
4.7	The comparison of chemical freeze-out parameters as a function of $\langle N_{\text{part}} \rangle$ between GCE and SCE obtained from the yields in Au+Au collisions at $\sqrt{s_{\text{NN}}} = 7.7, 11.5, 19.6, 27, 39, 62.4$, and 200 GeV.	153
4.8	Comparison of fit results to experimental mid-rapidity particle ratios in GCE for 0–5% and 60–80% centrality in Au+Au at $\sqrt{s_{\text{NN}}} = 7.7$ GeV. . . .	154
4.9	Comparison of fit results to experimental mid-rapidity particle ratios in SCE for 0–5% and 60–80% centrality in Au+Au at $\sqrt{s_{\text{NN}}} = 7.7$ GeV. . . .	154
4.10	The comparison of chemical freeze-out parameters as a function of $\langle N_{\text{part}} \rangle$ between GCE and SCE obtained from the ratios in Au+Au collisions at $\sqrt{s_{\text{NN}}} = 7.7, 19.6$, and 39 GeV.	155
4.11	The comparison of chemical freeze-out parameters as a function of $\langle N_{\text{part}} \rangle$ obtained from the particle yields and ratios in Au+Au collisions at $\sqrt{s_{\text{NN}}} = 7.7, 19.6$, and 39 GeV in GCE.	156
4.12	The comparison of chemical freeze-out parameters as a function of $\langle N_{\text{part}} \rangle$ obtained from the particle yields and ratios in Au+Au collisions at $\sqrt{s_{\text{NN}}} = 7.7, 19.6$, and 39 GeV in SCE.	156
4.13	(a) Chemical freeze-out temperature (T_{ch}) vs. baryonic chemical potential (μ_B) obtained from a statistical model fit [10] to the yields of hadrons in 0–5% central Au+Au collisions at $\sqrt{s_{\text{NN}}} = 7.7, 11.5, 19.6, 27, 39, 62.4$, and 200 GeV in GCE. (b) The positions of the QCD critical point from two different lattice gauge theory calculations in the T_{ch} vs. μ_B plane are shown.	157

4.14	Chemical freeze-out temperature (T_{ch}) vs. baryonic chemical potential (μ_B) obtained from a statistical model fit [10] to the yields of hadrons and ratios in different centrality bins in Au+Au collisions at $\sqrt{s_{\text{NN}}} = 7.7, 11.5, 19.6, 27, 39, 62.4$ and 200 GeV in GCE.	158
4.15	Chemical freeze-out temperature (T_{ch}) vs. baryonic chemical potential (μ_B) obtained from a statistical model fit [10] to the yields of hadrons and ratios in different centrality bins in Au+Au collisions at $\sqrt{s_{\text{NN}}} = 7.7, 11.5, 19.6, 27, 39, 62.4$ and 200 GeV in SCE.	159
4.16	Invariant yields of π^\pm , K^\pm , p, and \bar{p} vs. p_T in 0–5% central Au+Au collisions at $\sqrt{s_{\text{NN}}} = 27$ GeV. Curves represent Blast-wave model fits [37]. . . .	161
4.17	Variation of T_{kin} with $\langle\beta\rangle$ for different energies and centralities. The data points other than BES-I energies are taken from Refs. [26, 42].	162
4.1	Comparison of data and model for particle yields in GCE and SCE shown along with standard deviations for Au+Au collisions at $\sqrt{s_{\text{NN}}} = 7.7$ GeV. .	171
4.2	Comparison of data and model for particle yields in GCE and SCE shown along with standard deviations for Au+Au collisions at $\sqrt{s_{\text{NN}}} = 11.5$ GeV. .	172
4.3	Comparison of data and model for particle yields in GCE and SCE shown along with standard deviations for Au+Au collisions at $\sqrt{s_{\text{NN}}} = 19.6$ GeV. .	173
4.4	Comparison of data and model for particle yields in GCE and SCE shown along with standard deviations for Au+Au collisions at $\sqrt{s_{\text{NN}}} = 27$ GeV. . .	174
4.5	Comparison of data and model for particle yields in GCE and SCE shown along with standard deviations for Au+Au collisions at $\sqrt{s_{\text{NN}}} = 39$ GeV. . .	175
4.6	Comparison of data and model for particle yields in GCE and SCE shown along with standard deviations for Au+Au collisions at $\sqrt{s_{\text{NN}}} = 62.4$ GeV. .	176
4.7	Comparison of data and model for particle yields in GCE and SCE shown along with standard deviations for Au+Au collisions at $\sqrt{s_{\text{NN}}} = 200$ GeV. .	177

5.1	Dependence on the choice of ensemble: Thermal parameters (a) T_{ch} , (b) μ (μ_B , μ_S , and μ_Q), (c) γ_s , and (d) radius, plotted as a function of collision energy, extracted within the GCE and SCE ensembles with 1CFO as the freeze-out scheme. The dotted curves in the figures represent parametrisations from Refs. [44, 45].	187
5.2	Dependence on the fitting procedure: Comparative study of the thermal parameters (a) T_{ch} , (b) μ (μ_B , μ_S , and μ_Q), (c) γ_s , and (d) radius, plotted as a function of collision energy, extracted within GCE with 1CFO as the freeze-out scheme in the three cases: both μ_S and γ_s free, $\gamma_s = 1$ and μ_S free, and in the third case $\gamma_s = 1$ and μ_S fixed from Eq. 5.5.	188
5.3	Dependence on the choice of particles whose yields are used as input to extract the thermal parameters: Comparative study of the thermal parameters (a) T_{ch} , (b) μ (μ_B , μ_S , and μ_Q), and (c) radius, plotted as a function of collision energy, extracted within GCE with 1CFO as the freeze-out scheme for the two cases: i) π^+ , π^- , K^+ , K^- , p , \bar{p} , Λ , $\bar{\Lambda}$, Ξ^- , and $\bar{\Xi}^+$ where available, and ii) all available particles at all energies as tabulated in Tables 5.1, 5.2, 5.3 and 5.4. Here $\gamma_s = 1$, μ_S fixed from Eq. 5.5, and μ_Q fixed from Eq. 5.4.	189
5.4	Dependence on the choice of CFO scheme: Comparative study of the thermal parameters (a) T_{ch} and (b) μ_B , plotted as a function of collision energy, extracted within SCE with 1CFO and 2CFO as the freeze-out schemes with $\gamma_s = 1$ and μ_Q obtained by solving Eq. 5.4.	191

5.5	Dependence on the choice of CFO scheme on several particle ratios: Comparative study of different particle ratios (a) K^\pm/π^\pm , (b) Λ/p ($\bar{\Lambda}/\bar{p}$), (c) Λ/K^- and p/π^+ , and (d) triple ratio $\left(\frac{\Lambda/\bar{\Lambda}}{(p/\bar{p})(K^-/K^+)})\right)$, plotted as a function of collision energy, within SCE with 1CFO and 2CFO as the freeze-out schemes with $\gamma_s = 1$. The solid curves in the figures (a), (b), and (c) represent 1CFO (black curve) and 2CFO (blue curve) schemes corresponding to ratios shown with solid symbols. The corresponding dotted curves for 1CFO (black) and 2CFO (blue) are for the ratios shown with open symbols.	192
5.6	The χ^2/NDF as a function of collision energy for the different cases in GCE and SCE along with 1CFO and 2CFO schemes are shown together for comparison.	193
5.7	(Color online) (a): Energy dependence of T_{ch} and T_{kin} . Curves represent different theory predictions [44, 45]. (b): T_{ch} and T_{kin} plotted as a function of μ_B .	194
5.1	Comparison of data and model (1CFO) for particle yields in GCE shown along with standard deviations for AGS and SPS energies ($\mu_Q = B/2Q$, $\mu_S = 0$, $\gamma_S = 1$).	205
5.2	Comparison of data and model (1CFO) for particle yields in GCE shown along with standard deviations for RHIC and LHC energies ($\mu_Q = B/2Q$, $\mu_S = 0$, $\gamma_S = 1$).	206
5.3	Comparison of data and model (1CFO) for particle yields in SCE shown along with standard deviations for AGS and SPS energies ($\mu_Q = B/2Q$, $\gamma_S = 1$).	207
5.4	Comparison of data and model (1CFO) for particle yields in SCE shown along with standard deviations for RHIC and LHC energies ($\mu_Q = B/2Q$, $\gamma_S = 1$).	208

5.5	Invariant yields of pion, kaon and (anti)proton vs. p_T in central collisions at different energies. The curves represent the blast wave fits.	209
6.1	Space charge distributions in TPC.	211
6.2	Left: the z -position of track at the TOF radius vs. DCA for pion tracks with uncorrected space charge distortions for luminosities of $10^{26} \text{ cm}^{-2}\text{sec}^{-1}$ (red) and $40 \times 10^{26} \text{ cm}^{-2}\text{sec}^{-1}$ (blue). Right: the z -position of track at the TOF radius vs. difference in actual track location and fitted TPC track projection at TOF radius for above mentioned luminosities [2].	212
6.3	Electron microscope picture of a GEM foil [10].	214
6.4	Two dimensional read-out board structure of GEM chamber with pitch width $800 \mu\text{m}$ in both x and y directions.	215
6.5	The cosmic ray test system setup with four regular GEM chambers.	216
6.6	Lower and upper portion of a assembled chamber.	217
6.7	The FEE board assembled with two APV chips.	217
6.8	The display of mean and sigma of pedestals in ADC as a function of channel number for two APV chips obtained from cosmic ray test system setup.	218
6.9	The event display of cosmic ray events for x and y co-ordinates. The red bar shows the linear track fit.	219
6.10	Schematic diagram of the GEM chamber high voltage divider.	220
6.11	The efficiency plateau of first and second chamber.	221
6.12	The absolute gain of different GEM chambers (G01, G02..etc.) as a function of voltage.	222
6.13	The exclusive and inclusive residual distributions in x -direction.	222
6.14	The exclusive and inclusive residual distributions in y -direction.	223

6.15	Schematic view of the GMT in STAR for space charge distortion correction to provide reference point outside TPC.	224
6.16	The schematic diagram of position of GMT chambers installed in STAR TOF trays.	225
6.17	The display of ADC as a function of channel number obtained from STAR cosmic data.	225
6.18	The residual distribution in x -direction, x_{project} is the x -position at the THGEM chamber projected from the two regular GEM chambers, x_{measure} is the x - position measured by the THGEM chamber.	226

List of Tables

2.1	Some of the typical designed parameters and performance information of the RHIC for top energy.	52
2.2	Summary of RHIC operating modes and total integrated luminosity delivered to all experiments [14].	55
3.1	Event and track selection criteria for the analysis presented in this chapter. .	82
3.2	Summary of centralities, average number of participating nucleons ($\langle N_{\text{part}} \rangle$), and average number of binary collisions ($\langle N_{\text{coll}} \rangle$) in Au+Au collisions at $\sqrt{s_{\text{NN}}} = 27$ GeV.	85
3.3	Summary of energy loss parametrisations for kaon and proton in Au+Au collisions at $\sqrt{s_{\text{NN}}} = 27$ GeV.	96
3.4	Parametrisations to π^+ , K^+ and p efficiencies for 0–5% centrality in Au+Au collisions at $\sqrt{s_{\text{NN}}} = 27$ GeV.	99
3.5	Fraction of proton background as a function of p_T for 0–5% centrality in Au+Au collisions at $\sqrt{s_{\text{NN}}} = 27$ GeV.	103
3.6	Event and track cuts variation to study the systematic uncertainties.	105
3.7	Main sources of systematic uncertainties on yields of identified hadrons. The event and track cut variation to study the systematic uncertainties is given in Table 3.6.	113
3.8	Yields and $\langle p_T \rangle$ of π^\pm in Au+Au collisions at $\sqrt{s_{\text{NN}}} = 27$ GeV.	113

3.9	Yields and $\langle p_T \rangle$ of K^\pm in Au+Au collisions at $\sqrt{s_{NN}} = 27$ GeV.	113
3.10	Yields and $\langle p_T \rangle$ of p and \bar{p} in Au+Au collisions at $\sqrt{s_{NN}} = 27$ GeV.	114
4.1	Overview of data taken in the RHIC BES-I program.	142
4.2	Fraction of feed-down contributions obtained from model and data in most central collisions.	145
4.3	Summary of average number of participating nucleons ($\langle N_{part} \rangle$) in Au+Au collisions at RHIC energies.	164
4.4	Freeze-out parameters obtained from yields in GCE and SCE ($\mu_Q = 0$).	165
4.5	Freeze-out parameters obtained from ratios in GCE and SCE ($\mu_Q = 0$).	166
5.1	Details of the AGS data sets used for fit with references.	196
5.2	Details of the SPS data sets used for fit with references.	197
5.3	Details of the RHIC data sets used for fit with references.	198
5.4	Details of the LHC data sets used for fit with references.	199

Chapter 1

Introduction

In this chapter, Quark-Gluon Plasma (QGP) and the observed QGP signatures in heavy-ion collisions will be discussed. The outline of thesis is described at the end of this chapter.

1.1 Standard Model

Elementary particle physics aims to understand the fundamental properties of nuclear matter, more specifically, to identify the basic constituents of matter and study their interactions. Earlier it was believed that the atoms are indivisible and are the fundamental building blocks of matter. Then, it was discovered that atoms are made up of nucleus and electrons. The electron can escape if it has enough energy (namely ionisation energy, 5–20 eV for most atoms) to overcome the electromagnetic force that binds it to the nucleus. However, it is much harder to break up the nucleus which is made up of protons and neutrons. The protons (p) and neutrons (n) are collectively called nucleons and the energy that binds them is of the order of MeV. Both p and n are found to be composed of even smaller constituents called quarks held together by the exchange of messenger particles called gluons [1]. The quarks and gluons are collectively called as “partons”. The existence of quarks was pro-

posed in the 1960s, independently by Murray Gell-Mann and George Zweig [2]. Quarks are not observed as free particles and are confined within hadrons by the inter quark potential. Particles made of quarks are called hadrons which are further divided into two subgroups - baryons and mesons. All baryons contain three quarks (qqq) and all mesons contain one quark and one antiquark ($q\bar{q}$).

The fundamental structure of matter as well as the fundamental interactions are governed by the Standard Model of particle physics and was proposed by Glashow, Salam, and Weinberg in 1970 [3]. It is a gauge theory concerning three of the four known fundamental interactions between the elementary particles such as the electromagnetic, weak, and strong interactions. The gravitational interaction has not yet been incorporated in this model. The elementary particles are categorised into 6 quarks, 6 leptons, and 5 gauge bosons with the recently discovered Higgs boson. The quarks are categorised into three generations each with two quarks, up (u), down (d) – charm (c), strange (s) – top (t), bottom (b) and their corresponding antiquarks. The leptons are categorised into electron (e^\pm), electron-neutrinos ($\nu_e, \bar{\nu}_e$) – muon (μ^\pm), muon-neutrinos ($\nu_\mu, \bar{\nu}_\mu$) – tau (τ^\pm), tau-neutrinos ($\nu_\tau, \bar{\nu}_\tau$).

An overview of elementary particles of the standard model along with the force mediating gauge bosons are shown in the Fig. 1.1. Here, gluons carry the strong force, photons carry the electromagnetic force, W^\pm and Z – bosons carry the weak force. The graviton (not yet discovered) is conjectured to be the corresponding carrier for gravitational force which is outside of standard model. The standard model also predicts the Higgs boson [4] which is recently confirmed through A Toroidal LHC Apparatus (ATLAS) [5] and Compact Muon Solenoid (CMS) [6] experiments at European Organization for Nuclear Research (CERN). The Higgs boson is responsible for the generation of mass of fundamental particles. The existing hadron spectrum can be described by conservation laws of the quantum numbers such as baryon number, isospin, strangeness number, hypercharge, electric charge, and spin.

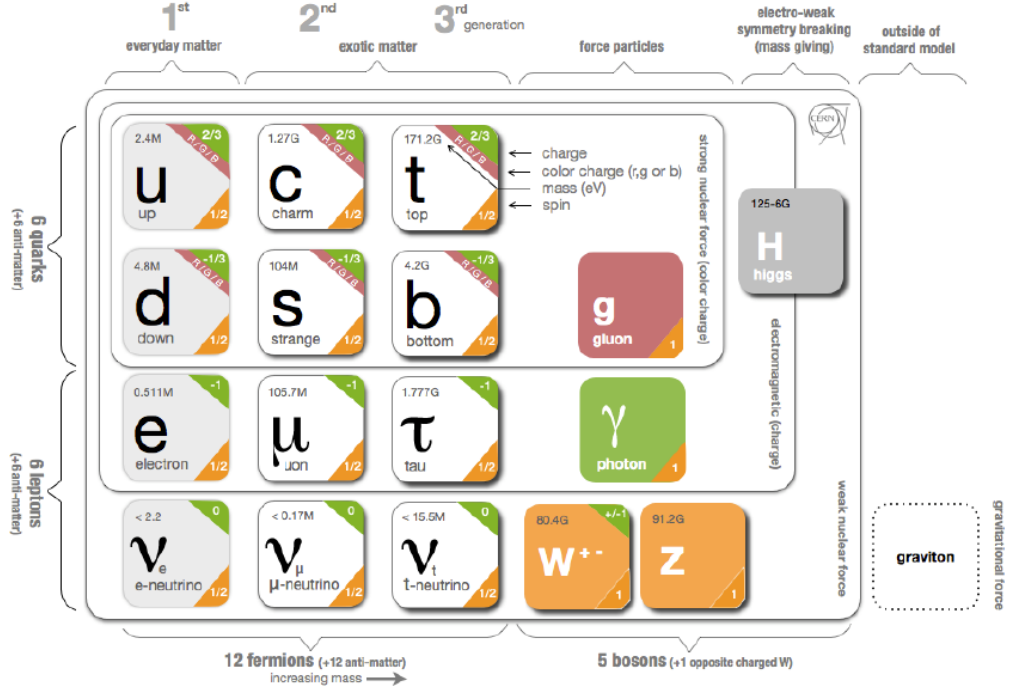


Figure 1.1: Overview of fundamental particles of the standard model and the force mediating gauge bosons.

1.2 Quantum Chromodynamics

The fundamental forces can be described by unitary groups of different dimensions: $U(1) \times SU(2) \times SU(3)$, where 1, 2, and 3 corresponds to the dimensions of unitary matrices, which represents the groups. $U(1)$ and $SU(2)$ combine to describe the electromagnetic and weak interactions. Number 3 in $SU(3)$ stands for the three colors and is the gauge group of the strong interactions known as quantum chromodynamics (QCD) [7]. It describes the interactions between quarks and gluons which bind together to form hadrons.

1.2.1 Confinement and Asymptotic Freedom

The discovery of $\Delta^{++}(\text{uuu})$, $\Delta^{-}(\text{ddd})$, and $\Omega^{-}(\text{sss})$ particles required a new quantum number in order to satisfy the Pauli Exclusion principle within the quark model [8]. Three color states are assigned to the quarks (called red, green, and blue), whereas the hadrons remain colorless. There are eight different types of gluons, each characterised by the color and anticolor. Gluons can change the color of a quark, but not its charge or flavor. The gluon exchange between quarks is analogous to the photon exchange between charged particles, governed by quantum electrodynamics (QED) theory. However, in QCD color plays the role of electric charge. The color charge is confined to the hadrons which can be described by the potential obtained from lattice QCD calculations,

$$V(r) \sim \frac{-\alpha_s}{r} + kr, \quad (1.1)$$

where α_s is the strong coupling constant, k is the color string tension, and r is the distance between the color charges. The non-Abelian gluon field leads to the self interaction between the gluons and the change in the effective coupling constant of the strong interaction. The values of α_s have been extracted from different experimental results and compared with perturbative QCD predictions [9]. Figure 1.2 shows the change in α_s as a function of momentum transfer. The effective coupling constant becomes small at large momentum transfer and the probed quarks appear to be free, as measured in deep inelastic scattering experiments. The experimental results in this region are well described by perturbative QCD. However, in the region where the momentum transfer is small, perturbative calculations are not applicable. The observed behaviour of the effective coupling constant can be described by the following expression:

$$\alpha_s(Q^2) \approx \frac{12\pi}{(33 - (2N_f) \ln(Q^2/\Lambda_{\text{QCD}}^2))}, \quad (1.2)$$

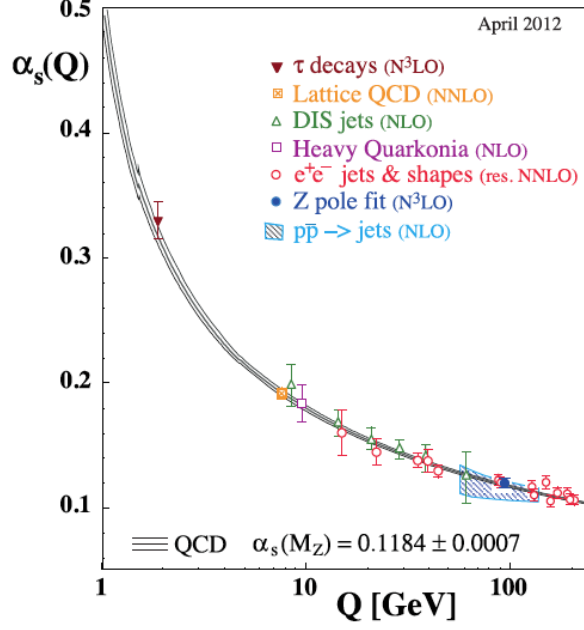


Figure 1.2: Summary of measurements of $\alpha_s(Q)$ as a function of energy scale Q . The curves show the QCD predictions [9].

where Q^2 is the momentum transfer, N_f is the number of quark flavors, and Λ_{QCD} is the scale parameter ~ 200 MeV, obtained from scattering experiments. At large distances or small momentum transfers, α_s is large and increases as the distance between two quarks increases. In this region, quarks remain bound together in groups of three in the form of baryons or as quark-antiquark pairs in the form of mesons. This property is called “Confinement”. Large momentum transfer corresponds to a small interaction distance. In this region, α_s tends to zero and quarks behave as free non-interacting particles. As a consequence, QCD medium at very high temperatures is predicted to be a gas of free quarks and gluons. The observed decrease of the effective coupling constant with increasing momentum transfer or decreasing distance is called “Asymptotic Freedom”.

1.2.2 QCD Phase Transition and Quark-Gluon Plasma

Following the discovery of asymptotic freedom in 1973 by David Gross, Frank Wilczek, and David Politzer; in the year 1975, J.C. Collins and M.J. Perry indicated that the dense nuclear matter at the center of neutron stars would consist de-confined quarks and gluons [10]. At sufficiently high temperatures, the hadrons are expected to melt, de-confining quarks and gluons from the hadrons. The transition of hadronic phase to a new phase of QCD matter, where color degrees of freedom become dominant, is known as the QCD phase transition. This predicted state of matter containing de-confined quarks and gluons interacting through color charge is called the Quark-Gluon Plasma (QGP) [11]. This form of matter is believed to have existed for a few microseconds (10^{-6} s) after the creation of the universe in the Big Bang.

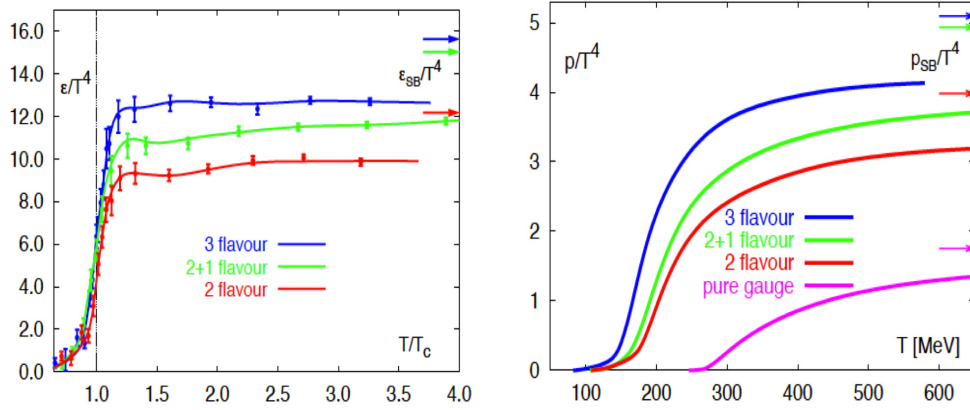


Figure 1.3: Lattice QCD calculations for energy density (left) and pressure (right) as a function of temperature for 2, 2+1, and 3 flavor QCD [12]. The dependence on the number of quark flavors are shown in different colored lines. The arrows indicate the Stefan-Boltzmann limit in both the figures.

Figure 1.3 shows the energy density ϵ , and pressure P , as functions of T which are lattice QCD calculations performed with varying the numbers of light quark flavors [12]. Each is expressed as a fraction of T^4 , enabling comparison with the Stefan-Boltzmann (SB) predictions. These lattice QCD calculations at non-zero temperatures and non-zero chemi-

cal potentials suggest the phase transition from the hadronic phase to the QGP phase occur, when sufficiently high energy density and temperature is reached. The ε/T^4 is proportional to the number of degrees of freedom. The arrow represents the SB limit;

$$\varepsilon = g \frac{\pi^2}{30} T^4, \quad (1.3)$$

where g is the number of degrees of freedom. For a non-interacting pion gas, Eq. 1.3 becomes,

$$\varepsilon = 3 \frac{\pi^2}{30} T^4, \quad (1.4)$$

where the number 3 is given by three pion states (π^\pm , π^0). In the QGP phase, the relative number of degrees of freedom are the quarks (fermion) and gluons (bosons). The energy density for QGP can be written as

$$\begin{aligned} \varepsilon_{\text{QGP}} &= 2_{\text{spin}} \times 8_{\text{colors}} \times \frac{\pi^2}{30} T^4 + 2_{\text{q}-\bar{\text{q}}} \times 2_{\text{spin}} \times 3_{\text{colors}} \times n_{\text{flavors}} \times \frac{7}{8} \frac{\pi^2}{30} T^4 \\ &= (16 + \frac{21}{2} \times n_{\text{flavors}}) \frac{\pi^2}{30} T^4 \end{aligned}$$

The factor 7/8 comes from the correct statistics consideration. The number of degrees of freedom is significantly increased in the QGP state with respect to that of the hadron gas phase. Figure. 1.3 shows the energy density rising very steeply at $T \simeq 170$ MeV, and rapidly reaching a plateau at roughly 80% of the SB value. This is a strong evidence for QGP at critical temperature $T_c \simeq 170$ MeV and energy density $\varepsilon_c \simeq 1$ GeV/ fm^3 [12]. Recent calculation on lattice suggest the T_c could be lower (~ 154 MeV) [13]. For $T \lesssim 3T_c$, the pressure falls appreciably below the SB value and the deviation suggests quarks and gluons interact among themselves in the QGP phase. Theoretical predictions on QGP motivated experimentalists to create such conditions for QGP formation in the laboratory through heavy-ion collisions.

1.3 Relativistic Heavy Ion Collisions

Relativistic heavy-ion experiments have been carried out to create the extreme conditions in the laboratory to understand similar condition that existed in the early universe. By accelerating two heavy nuclei to ultra-relativistic speeds and then colliding them, such extreme conditions can be created inside a laboratory to look for a formation of the QGP state. It can also be used as a tool to investigate the internal structure of the nuclei at both hadronic (baryons and mesons) and partonic (quarks and gluons) levels. Different experiments were carried out over the last thirty years to study the fundamental properties of nature. During 1986–1990, only light ions were used to produce nuclear matter at lower energy densities which were insufficient to produce a de-confined QGP state. Subsequently heavier targets (Pb, Au) with higher beam energy were used to achieve higher energy density and temperature.

The first experiments were performed with fixed target nuclei at the Alternating Gradient Synchrotron (AGS) in Brookhaven National Laboratory (BNL) and the Super Proton Synchrotron (SPS) at CERN, with centre of mass energies of $2A$ and $18A$ GeV, respectively (A is the number of nucleons in the nucleus). Nuclei such as Si, O, and Pb were used in these fixed target experiments. For the first time, the results from Pb+Pb collisions at center-of-mass energy of 17.3 GeV at CERN SPS signaled a possible phase transition and formation of QGP [14]. The Relativistic Heavy Ion Collider (RHIC) at BNL was the first machine in the world capable of colliding ions as heavy as Au and confirmed the formation of QGP. The Large Hadron Collider (LHC) at CERN is presently the worlds most energetic heavy-ion accelerator colliding two Pb nuclei at $\sqrt{s_{NN}} = 2.76$ TeV. It has significantly extended the temperature and kinematic ranges for the investigation of QGP.

1.3.1 Space-Time Evolution of Heavy Ion Collisions

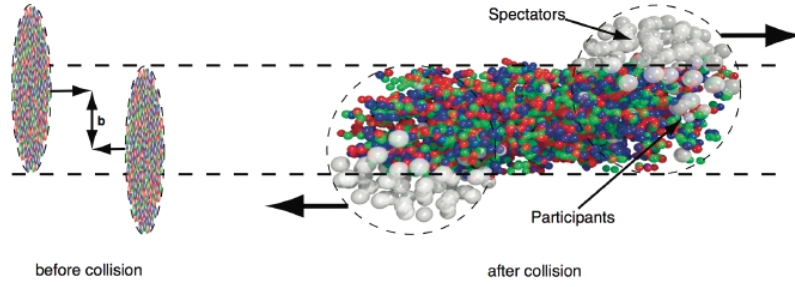


Figure 1.4: Schematic diagram of before and after collision of two nuclei with non zero impact parameter. The participants and the spectator nucleons are also shown.

In relativistic heavy-ion collisions, two incoming nuclei are accelerated to nearly the speed of light in opposite directions. Figure 1.4 represents the schematic diagram of before and after collision of two nuclei with non zero impact parameter. The nuclei traveling at relativistic velocities appear Lorentz contracted along the beam direction (z -axis) and take an elliptic shape as shown in Fig. 1.4. The overlap region between the incoming nuclei, is usually characterised by the impact parameter (b) of the collision which is the perpendicular distance between the centers of the two colliding nuclei. The events with small impact parameters are called as central collision events, while peripheral collisions have large impact parameters. The collisions in the intermediate range of impact parameters are termed as semi-central collisions. Nucleons in the overlap region that interact are called “participants” and non-interacting nucleons are called “spectators”. The number of interacting participant nucleons and non-interacting spectators depend on the overlap between the incident nuclei and hence on the impact parameter of the collision.

Consider a head-on collision of two heavy nuclei moving with relativistic energies in the center-of-mass (CM) frame. The various stages of such ultra-relativistic heavy-ion

collisions can be viewed in the space-time diagram with the longitudinal co-ordinate z and the time co-ordinate t as illustrated in Fig. 1.5. The colliding nuclei are spherical in their rest frame, but in the CM frame they are Lorentz contracted along their direction of motion due to their relativistic velocity $\beta = v/c$. The incoming projectile nucleus with velocity close to the speed of light comes from $z = -\infty$ and meets the incoming target nucleus coming from $z = +\infty$ with the same speed. When the nuclei meet at $z = 0$ and $t = 0$, a large amount of the energy is deposited in the interaction region to produce a “fireball” in the mid-rapidity region $y \simeq 0$ (where rapidity is defined as, $y = \frac{1}{2} \ln \frac{E+p_z}{E-p_z}$, E is the energy of the particle and p_z is the longitudinal momentum), which may lead to at least two possible scenarios. An important variable to assess these possibilities is due to Bjorken energy density [15], i.e. for a collision at origin $(z, t) = (0, 0)$, the energy density (ε) in the central region at proper time $\tau = \sqrt{t^2 - z^2}$ is given by,

$$\varepsilon(\tau) = \frac{1}{\tau A} \frac{dE_T}{dy}, \quad (1.5)$$

where A is the transverse area of the incident nuclei and dE_T/dy represents the transverse energy of the collision products (i.e. excluding kinetic energy due to motion parallel to z) per unit rapidity y , an experimentally measured quantity.

If the created energy density does not reach the critical value necessary for QGP formation, then the system consists of a gas of hadrons as shown on the right-hand side of Fig. 1.5. The other possibility is that, if the energy density produced in the mid-rapidity region is sufficient and the temperature of the created system exceeds the critical temperature T_c , a phase transition is expected to occur and a fireball of de-confined quarks and gluons is formed as shown on the left-hand side of Fig. 1.5. Initially, the fireball may not be in thermal equilibrium, but subsequent interactions among partons may bring it to local equilibrium at the proper time τ . This phase of matter can be identified as the QGP.

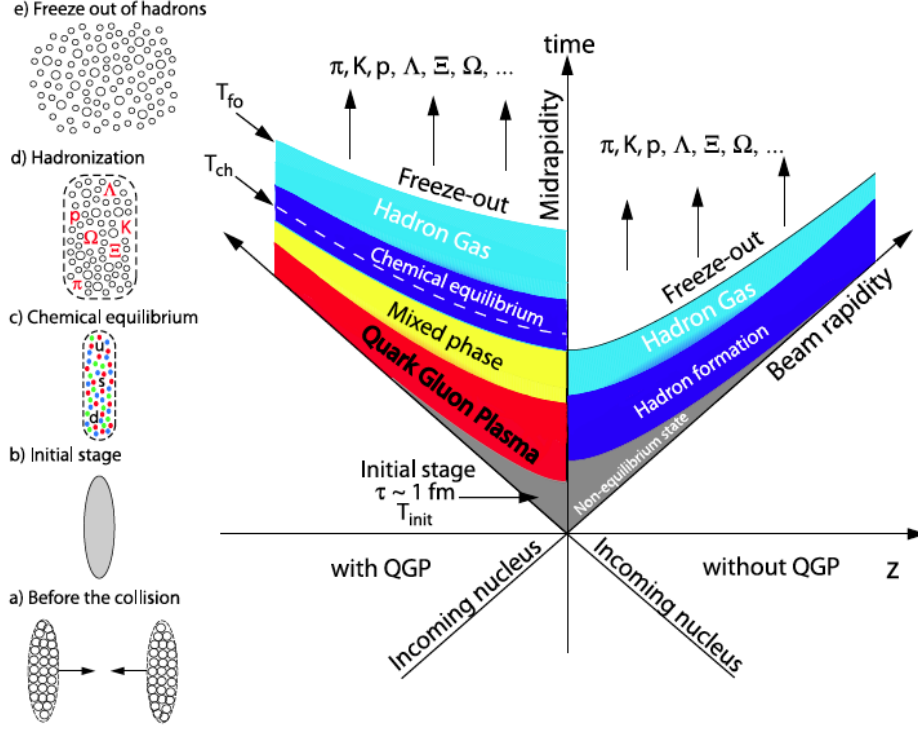


Figure 1.5: Schematic view of the space-time diagram and various stages of a relativistic heavy-ion collisions.

If QGP is formed, the system must quickly expand and cool due to its excess pressure with respect to the vacuum, this evolution can be described by relativistic hydrodynamics. At some point, therefore, T falls below T_c and hadrons are reformed and the quarks and gluons become confined. If there is a first-order phase transition from quarks and gluons to hadrons, then it will go through a mixed phase, in which quarks and gluons coexist with hadrons. The expansion is likely to be isothermal in this phase and latent heat is used to convert the quarks and gluons to hadrons. As the system of hadrons continues to expand, “chemical freeze-out” occurs at a temperature T_{ch} , where the inelastic interactions between the hadrons cease and the composition of different hadron species do not change any more. The resulting hadronic gas continues to cool until interaction rates become insufficient to

maintain thermal equilibrium in the expanding medium, i.e. up to a temperature T_{fo} , when the distance between the hadrons is larger than the mean free path and the elastic interactions between the hadrons cease. This is known as thermal or kinetic freeze-out, from this point the hadrons are free to stream away to be detected by the detectors. Information about conditions inside the fireball can be inferred from hadrons emitted from the surface of last scattering at thermal freeze-out.

Evidence of thermalisation can be known from the analysis of the distributions of transverse momentum, $p_T = \sqrt{p_x^2 + p_y^2}$, where p_x and p_y are the x and y components of total momentum (p) or transverse mass, $m_T = \sqrt{m^2 + p_T^2}$, where m is rest mass of produced particle. The energy density in Au+Au collisions at RHIC is $\simeq 5 \text{ GeV/fm}^3$ [16, 17], which is well above the critical energy density $\simeq 1 \text{ GeV/fm}^3$ expected from LQCD calculations for the transition to the QGP phase.

1.3.2 QCD Phase Diagram

A phase diagram usually is used to provide thermodynamical information, in which the different manifestations or phases of a substance occupy different regions of a plot, where the axes are calibrated in terms of the external conditions or control parameters. Phase transitions can be characterised by an order parameter, which is zero in one phase (usually called the disordered phase) and non-zero in the other phase (ordered phase). One of the most familiar example is H_2O , where the control parameters are temperature T and pressure P and the three regions correspond to the three phases of ice, water, and steam. The classification of different phase transitions are related to Gibbs free energy, $G(T, P)$. The first-order phase transition is characterised by discontinuous changes in entropy S and

volume V which are described through the first derivatives of Gibbs free energy;

$$S = -\left.\frac{\partial G}{\partial T}\right|_P ; \quad V = \left.\frac{\partial G}{\partial P}\right|_T.$$

At the critical point, the transition becomes second order, which means that singularities instead occur in specific heat C_P and isothermal compressibility κ_T . Those are related to second derivatives of the free energy;

$$C_P = -T \left.\frac{\partial^2 G}{\partial T^2}\right|_P ; \quad \kappa_T = \frac{1}{V} \left.\frac{\partial^2 G}{\partial P^2}\right|_T,$$

where each of the above mentioned quantities (C_P , κ_T) diverges at the critical point. Just beyond the critical point, thermodynamic observables still vary rapidly due to the large values of C_P and κ_T which is known as a crossover region.

A proposed QCD phase diagram is shown in Fig. 1.6 [18]. In QCD phase diagram, the control parameters are temperature T and baryon chemical potential μ_B , where μ_B is defined as the amount of energy needed to add or remove an additional baryon to the existing matter. Within QCD, baryon number B is defined as a conserved quantum number, $B = N_B - N_{\bar{B}}$, where N_B is the number of baryons and $N_{\bar{B}}$ is the number of antibaryons. For systems, in which baryon number is allowed to vary, the convenient thermodynamic potential to consider is the grand canonical potential $\Omega(T, V, \mu) = E - TS - \mu B$ and thermodynamic equilibrium is reached when Ω is minimised.

In the bottom left-hand corner of the phase diagram in Fig. 1.6, where T and μ_B are both small, the thermodynamic behaviour of QCD can be described in terms of a vapour of hadrons, which are the composite states of quarks and/or antiquarks. As T is raised, either a transition or a crossover occurs to a phase, where the dominant degrees of freedom are no longer hadrons but the quarks themselves, together with the gluons. Since quarks

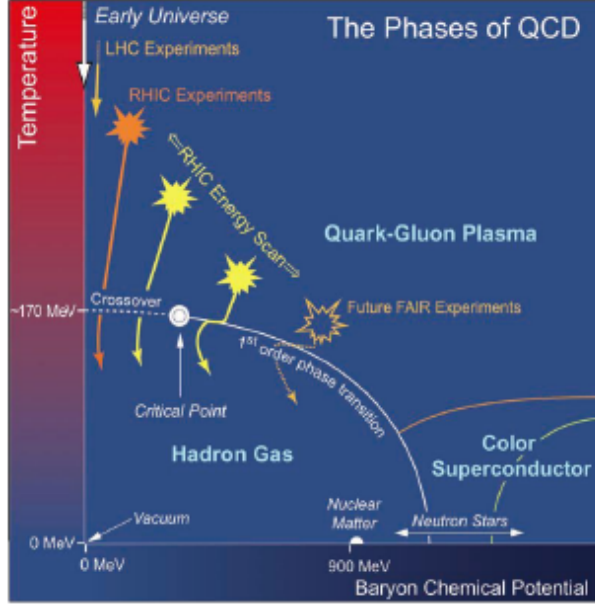


Figure 1.6: Proposed QCD phase diagram for nuclear matter [18].

and gluons play similar roles in QCD to the electrons and photons of QED, this phase is called the QGP. At a larger T and smaller μ_B , lattice QCD predicts a smooth crossover between phases [19], while at smaller T and larger μ_B theoretical calculations show a first-order phase transition between hadron gas and quark-gluon plasma [20]. The QCD Critical Point (CP) in the QCD phase diagram is the point where the first-order phase transition ends. The scenario of very high temperature and almost zero net baryon density is very similar to the early universe. The high net baryon density and very low temperature scenario has similarity to the inner core of the neutron star whereas color superconducting phase is predicted to exist at larger μ_B and relatively low T .

According to Lattice QCD calculations [21], at vanishing chemical potential, the fluctuations of the net-baryon number, net-charge, and net-strangeness are very sensitive to the critical fluctuation. The higher order moments of the conserved quantities (charge Q , Baryon number B , and strangeness S), which are variance (σ^2), skewness (S), and kur-

tosis (κ), are related to the corresponding higher order susceptibilities, which can be used as most sensitive probe to search the QCD critical point and may provide information about the phase boundary. Other QCD based calculations [22] show the relation of the various moments with the correlation length (ζ) of the system. At the critical point, the correlation length and susceptibilities are expected to diverge [23]. Experimentally, the critical point and QCD phase boundary can be accessed through colliding heavy-ions by varying beam energies. One of the primary goals of RHIC experiments at BNL is to search for the possible QCD critical point and to map the QCD phase diagram, for which it has started the Beam Energy Scan program in the year 2010.

1.4 RHIC Beam Energy Scan Program

The first few years of RHIC operation were dedicated to study the nuclear matter with partonic degrees of freedom (QGP) which was formed in the early stages of Au+Au collision at $\sqrt{s_{NN}} = 200$ GeV. The results from RHIC data revealed several unique properties of this matter but still there are some questions to be addressed. In particular, the process and mechanism of transformation from hadronic degrees of freedom to partonic ones, and back to the state of hadron gas, is still not known. The Au+Au collisions at lower energies, presently available at RHIC, allow a possible observation of a first-order phase transition ending with a critical point.

The datasets taken during BES-I with variable collision energies, provide different T and μ_B values which cover a large range of μ_B in the QCD phase diagram. This is complemented by the data collected earlier at higher energies $\sqrt{s_{NN}} = 62.4, 130, \text{ and } 200$ GeV. The BES-I data together with top energies cover the μ_B interval from 20 to 420 MeV, which is believed to contain the range associated with the first-order phase transition and CP. These dataset may also be used to provide the information about the energy at which

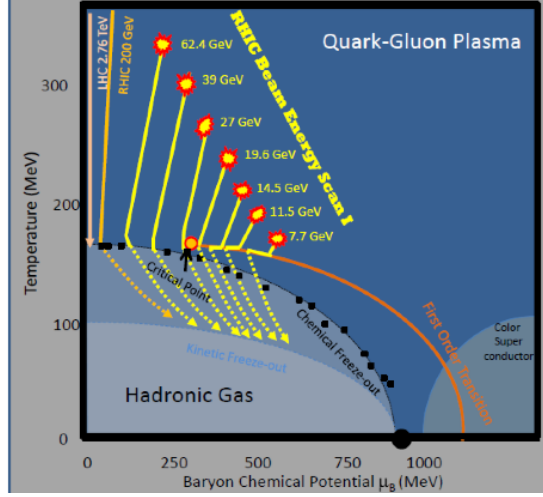


Figure 1.7: The schematic picture of the QCD Phase Diagram with marked coverage of the RHIC BES-I program. Yellow trajectories represent the different energies of the BES-I program. The red circle symbolises the critical point. Note that the yellow lines and the red circle are for illustrative purpose only [18].

we no longer observe any QGP signature. This would indicate that the system populated consists of hadrons. The modification or disappearance of several QGP signatures simultaneously would definitely provide a compelling case for such an observation. The particular observables identified at RHIC BES-I energies are the constituent quark number scaling, hadron suppression in central collisions characterised by R_{CP} , untriggered pair correlations in the space of pair separation in azimuth, pseudo-rapidity and local parity violation in strong interactions. The second goal is to find the critical fluctuations associated with a strong increase in the susceptibilities, which are expected in the vicinity of CP. The finite size effects in the experiment could be a problem to observe this critical behaviour. The search for evidence of the softening of equation of state as a system enters a mixed phase region implicitly associated with crossing first-order phase transition was proposed as a third goal of BES-I program. Essential observables in this search include elliptic and directed flow of charged particles and of identified protons and pions, azimuthally-sensitive

femtoscopy and fluctuations indicated by large jumps in baryon, charge, and strangeness susceptibilities, as a function of system temperature. The RHIC BES-I program in the $T - \mu_B$ plane is shown in Fig. 1.7. The yellow lines represent possible reaction trajectories at energies $\sqrt{s_{NN}} = 7.7, 11.5, 14.5, 19.6, 27,$ and 39 GeV. All energies, with the exception of 14.5 GeV (data taken in the year 2014 as a part of BES-I) are used to study the freeze-out dynamics which will be discussed in the later chapter of this thesis. This choice of energies provides almost uniform coverage of $T - \mu_B$ and may allow us to narrow down an area of interest for further study.

In addition to RHIC BES-I program, a second phase of BES program (BES-II) has also been proposed to achieve the above mentioned goals. The other future experiments such as SPS Heavy Ion and Neutrino Experiment at CERN (NA61/SHINE) [24], Nuclotron based Ion Collider fAcility (NICA) at Joint Institute for Nuclear Research (JINR) ($\sqrt{s_{NN}} = 3-9$ GeV) [25], and Facility for Antiproton and Ion Research (FAIR) at GSI ($\sqrt{s_{NN}} = 2.3-8.5$ GeV) [26] have been dedicated for the search of the QCD critical point.

1.5 Signatures of Quark-Gluon Plasma

Heavy-ion collisions at sufficiently high energies lead to the formation of QGP state, which undergoes several stages during its evolution, like a pre-equilibrium process and its formation through thermalisation, a mixed phase (containing partons mixed with hadrons), a hadron gas phase and a phase of free hadrons. Each stage is associated with certain characteristic properties related to the type of particles produced, their life time and production mechanism. The hot and dense medium created in the heavy-ion collisions is extremely short-lived ($\sim 5-10$ fm/c) and the final state particles are only measured in the detectors of the experiments. Several experimental observables can be used to characterise the prop-

erties of the system created in such collisions. The experimental probes can be basically categorised into soft and hard probes. The bulk matter signatures such as particle multiplicities, particle ratios, transverse momentum spectra, flow, and particle correlations are considered as soft probes and provide a picture of thermalisation and spatial evolution of the system found in heavy-ion collisions. The hard probes are used to probe the system before thermalisation through hard scattering processes and provide information on the partonic energy loss in the medium formed. We briefly discuss some of the QGP signatures in the following subsections.

1.5.1 Strangeness Enhancement

Nuclear matter contains only up and down quarks at normal pressure and temperature. If strangeness is present in the final particle yields, it has to be produced from the collisions. The enhanced production of strange particles in nucleus-nucleus (AA) collisions, relative to nucleon-nucleon (NN) collisions, has been proposed as a signature of QGP formation [27]. The initial strangeness content of the colliding nuclei is very small and there is no net strangeness which implies that all strange hadrons must be formed in the matter produced. The two main production channels for $s\bar{s}$ pairs are $q\bar{q} \rightarrow s\bar{s}$ and $gg \rightarrow s\bar{s}$. When the QGP is formed, a large increase of strange hadrons is expected because gluons can self-interact, create $s\bar{s}$ pairs, and the threshold of such process is relatively low (~ 300 MeV) because of dominant QCD processes of $s\bar{s}$ production, i.e. $gg \rightarrow s\bar{s}$. Later on, those strange quarks combine with other quarks to form strange hadrons. In a hadronic system, e.g., in p+p, the higher threshold for strangeness production was argued to make the strangeness yield considerably smaller and the equilibration time much longer than in QGP [28]. In experiments, the measured strangeness enhancement is defined as the ratio of the yield of a strange particle per participating nucleon in the large AA system (e.g., Au+Au at RHIC) to the yield of the same strange particle in the small reference system (e.g., p+p at RHIC).

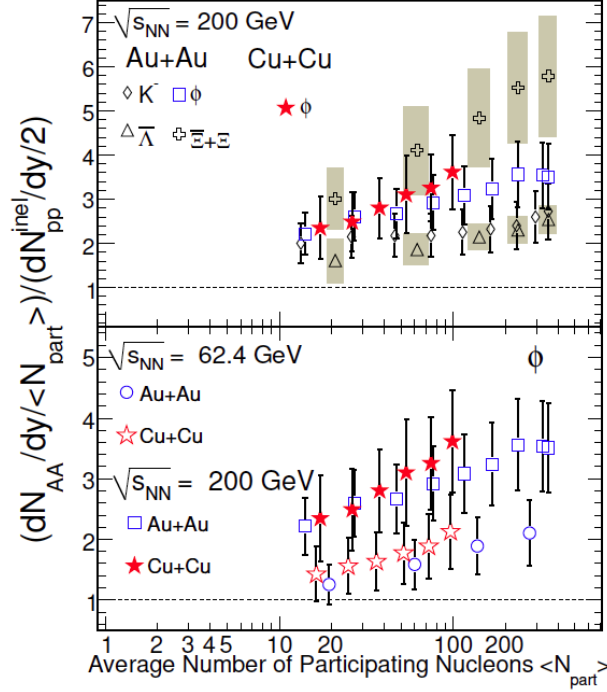


Figure 1.8: Upper panel: The ratio of the yields of K^- , ϕ , $\bar{\Lambda}$, and $\Xi + \bar{\Xi}$ normalised to $\langle N_{\text{part}} \rangle$ in Au+Au and Cu+Cu collisions to corresponding yields in inelastic p+p collisions as a function of $\langle N_{\text{part}} \rangle$ at $\sqrt{s_{\text{NN}}} = 200$ GeV. Lower panel: Same as above but for only ϕ mesons in Au+Au and Cu+Cu collisions at $\sqrt{s_{\text{NN}}} = 62.4$ and 200 GeV [29]. The error bars shown here represent the statistical and systematic errors added in quadrature.

In Fig. 1.8, the strangeness enhancement as a function of average number of participating nucleons ($\langle N_{\text{part}} \rangle$) for K^- , ϕ , $\bar{\Lambda}$, and $\Xi + \bar{\Xi}$ for Au+Au and Cu+Cu collisions relative to p+p collisions at $\sqrt{s_{\text{NN}}} = 62.4$ and 200 GeV in the STAR experiment [29] is shown. These experimental data indicate the formation of a dense partonic medium in heavy-ion collisions where strange quark production is enhanced.

In Au+Au collisions, the strangeness yields are found to increase with centrality as well as with energy, whereas the kaon yields relative to pions are enhanced over those from p+p and p+p collisions at similar energies [30, 31]. These results are consistent with the

numerical study as reported in [32].

1.5.2 Azimuthal Anisotropy or Flow

If thermalisation occurs in nuclear collisions, collective effects such as flow should determine how the system develops in later stages. Not only it indicates whether the system is thermalised or not, it also provides information about the initial state, the equation of state and freeze-out condition of the system [33]. In non-central heavy-ion collisions, the

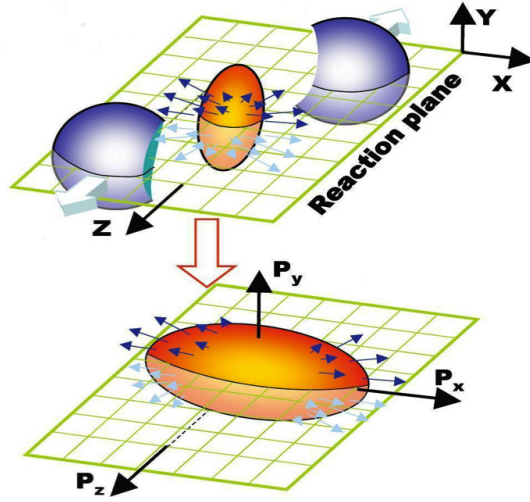


Figure 1.9: Schematic diagram showing the transformation of initial coordinate space anisotropy into a momentum space anisotropy in a non-central heavy-ion collision.

overlap region of two colliding nuclei is spatially asymmetric with the system having an almond-like shape as shown in the Fig. 1.9. This particular spatial anisotropy is largest right after the collision. A pressure gradient, i.e. force generated due to the interactions among constituents of the system, is larger along the short axis than along the long axis of the almond-shaped collision region. The interaction between the constituent nucleons in the overlap region transforms the initial spatial anisotropy into a momentum anisotropy. Consequently, the azimuthal distribution of produced particles in momentum space in a

non-central collision provides a signature of transverse collectivity at the early stages of the heavy-ion collisions [34].

The measurement of the azimuthal anisotropy distribution can be quantified by studying the Fourier expansion of azimuthal angle distribution of produced particles with respect to the reaction plane, which is the plane spanned by the beam direction and impact parameter vector [35]:

$$E \frac{d^3N}{d^3p} = \frac{1}{2\pi} \frac{d^2N}{p_T dp_T dy} \left(1 + \sum_{n=1}^{\infty} 2v_n \cos [n (\phi - \Psi_r)] \right), \quad (1.6)$$

where ϕ is the azimuthal angle of the particle, Ψ_r is the reaction plane angle and v_n is the n^{th} harmonic coefficient. The first term (1) provides information about the “isotropic flow”, the first harmonic coefficient, v_1 , is called the “directed flow” and the second harmonic coefficient, v_2 , is called the “elliptic flow”. In a non-central collision, the largest component is the second anisotropy coefficient, v_2 . Directed flow, v_1 , describes the side-splash of particles away from the mid-rapidity and it probes the early dynamics of the system in relativistic heavy-ion collisions. The variation of the directed flow as function of rapidity

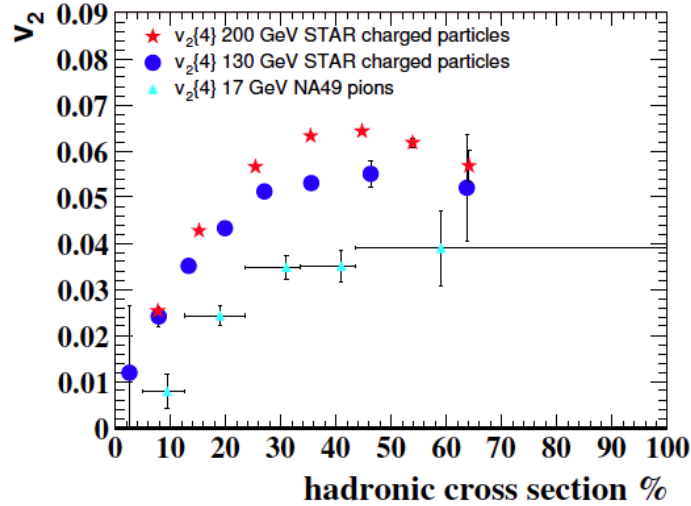


Figure 1.10: The centrality dependence of p_T integrated v_2 as measured by the NA49 experiment at SPS [37] and STAR experiment at RHIC [38, 39].

for identified particles is sensitive to the equation of state and may carry a phase transition signal [36].

The elliptic flow can be calculated from transverse momentum and azimuthal angle of the produced particles as,

$$v_2(p_T) = \langle \cos(2(\phi - \Psi_2)) \rangle_{p_T}, \quad (1.7)$$

where for the other components, $v_n = \langle \cos(n(\phi - \Psi_n)) \rangle$. v_2 has been measured for a wide range of particles, including Ξ , Ω , π^0 , photons, and electrons to study mass and baryon-meson effects of the collective flow.

The p_T integrated mid-rapidity elliptic flow coefficient, v_2 , as a function of collision centrality for SPS [37] and RHIC [38, 39] energies is shown in Fig. 1.10. The characteristic centrality dependence reflects the increase of the initial spatial eccentricity of the collision overlap geometry with increasing impact parameter. The differential elliptic flow, $v_2(p_T)$,

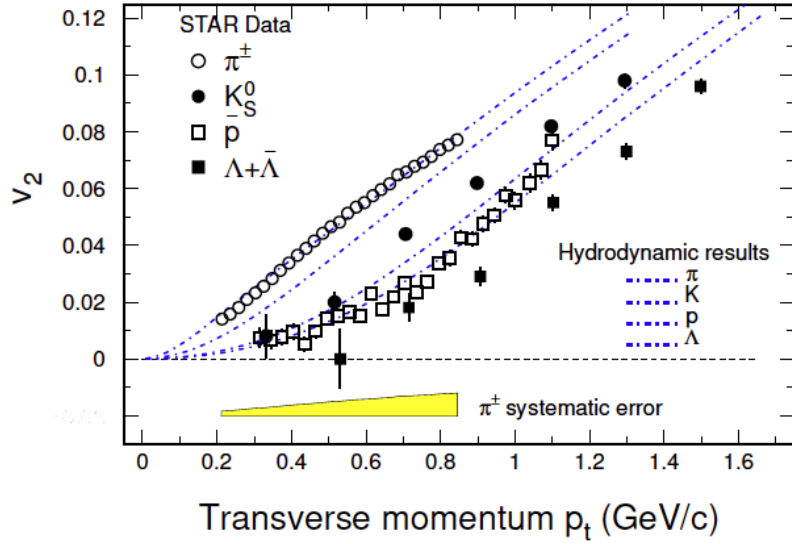


Figure 1.11: The p_T dependence of the elliptic flow parameter, v_2 , in Au+Au collisions at $\sqrt{s_{NN}} = 200$ GeV as measured by the STAR experiment. The hydrodynamic calculations are shown as dot-dashed lines. This figure is taken from Ref. [39].

for different identified particles at low p_T (~ 2 GeV/c) is shown in Fig. 1.11 for Au+Au collisions at $\sqrt{s_{NN}} = 200$ GeV [39]. The hadron mass ordering of v_2 is seen in the low p_T region, whereas at a given p_T , the higher hadron mass corresponds to the lower value of v_2 . Hydrodynamic calculations [40] reproduce this mass dependence as well as the absolute magnitude of v_2 . The agreement with the hydrodynamic calculations, which assume early thermalisation and ideal relativistic fluid expansion, is one of the centrepieces of the discovery of QGP, as claimed at RHIC. The v_2 measurements for identified hadrons in

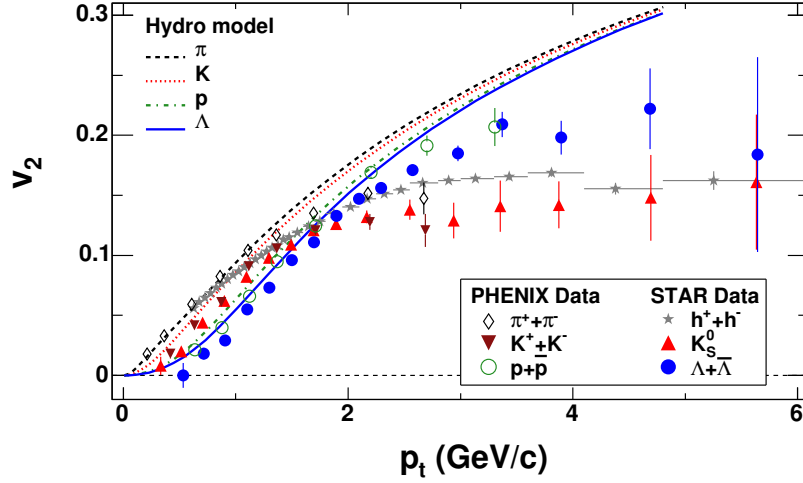


Figure 1.12: v_2 as a function of p_T for different hadrons in minimum bias Au+Au collisions at $\sqrt{s_{NN}} = 200$ GeV [39]. Hydrodynamical calculations are shown by solid and dotted curves [40].

minimum bias Au+Au collisions at $\sqrt{s_{NN}} = 200$ GeV [39] and that from hydro calculations are shown in Fig. 1.12. For $p_T > 2$ GeV/c, the observed values of v_2 saturate and the saturation level differs substantially for mesons and baryons. This provides some important information regarding the origin of baryon-meson difference found in this p_T range and here the hydrodynamic calculations over predict the data. If the v_2 values are divided with the number of constituent quarks, n (i.e. $n = 2$ for mesons and $n = 3$ for baryons), then a scaling for $p_T/n > 1$ GeV/c is observed, which is called the Number of Constituent

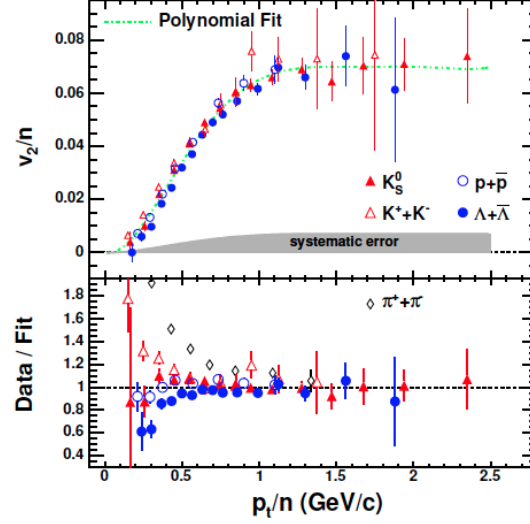


Figure 1.13: Upper panel: v_2/n vs. p_T/n for identified particles measured by the STAR experiment. n is the number of constituent quarks. The dashed-dotted line is the polynomial fit to the data. Lower panel: The data from the upper panel is divided by the polynomial fit as a function of p_T/n [39].

Quark (NCQ) scaling. The upper panel in Fig. 1.13 shows the STAR results on v_2/n as a function of p_T/n for identified hadrons in minimum bias Au+Au collisions at $\sqrt{s_{NN}} = 200$ GeV. A polynomial fit to the data is shown with the dashed-dotted line. The data from the top panel are scaled by the fitted polynomial function and plotted in the bottom panel of Fig. 1.13 to investigate the quality of agreement between particle species. This shows that in the intermediate p_T range ($0.6 < p_T/n < 2$ GeV/c), the v_2 of the identified hadrons (except pion) scale with the number of constituent quarks. The large resonance decay contribution to pion production has been suggested as a possible explanation for the apparent deviation from this scaling [41]. The observed NCQ scaling indicates that the system is in a de-confined stage, i.e. the high energy nuclear collisions provide an opportunity to prove that hadron production indeed happens via coalescence of the constituent quarks [42]. The constituent quarks carry their own substantial azimuthal anisotropy which is later summed up to give the flow of the hadrons.

1.5.3 High p_T Probes

The low and high p_T regions of particle spectra are dominated by different processes. High p_T particles are expected to come from the parton-parton hard scattering process and measurement of those particles provide a unique tool to understand the dense nuclear medium effects. The high momentum partons traversing the plasmas are expected to lose a significant amount of energy due to the high gluon density inside the QGP [43]. After a hard

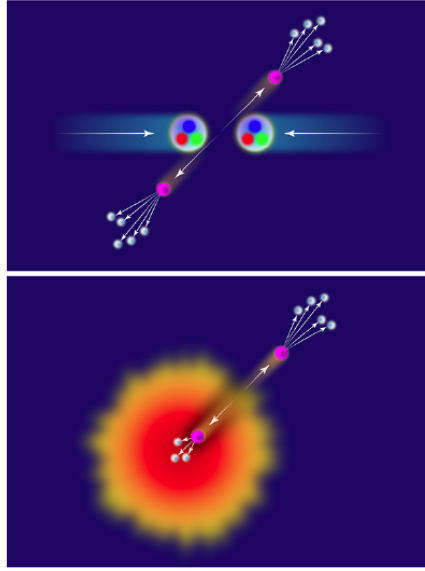


Figure 1.14: Upper panel: In p+p collisions, the partons (quarks depicted in green, red, and blue balls) can hit each other where some of these partons (pink balls) can fly away and hadronise forming dijets of energetic hadrons (white balls). Lower panel: The jets produced in early stages of heavy-ion collisions travelling in opposite directions, propagating through QGP, and one of two jets is quenched. This figure is taken from Ref. [44].

scattering, the parton fragments to create a high energy clusters of particles, moving in approximately the same direction. In other words, a collection of fast hadrons emerging from an event, associated within a small solid angle, is called a “jet”. For p+p collisions, two jet structures with back to back momenta, namely dijets are observed. In heavy-ion collisions because of momentum conservation, two jets are generated, traveling in opposite

directions and one of two jets traverses the medium is extinguished or “quenched” in the dense medium and the other is emitted away from the fireball escaping the medium without interaction and fragments in vacuum. The schematic picture of such phenomena for p+p and heavy-ion collisions is shown in Fig. 1.14. The significant softening and broadening of jets in the dense partonic medium is known as “jet-quenching” and has been considered as a signature of QGP at RHIC [45]. In high energy collisions, this phenomena can be observed through dihadron azimuthal correlations.

The measurements of azimuthal distribution of hadrons with $p_T > 2$ GeV/c relative to

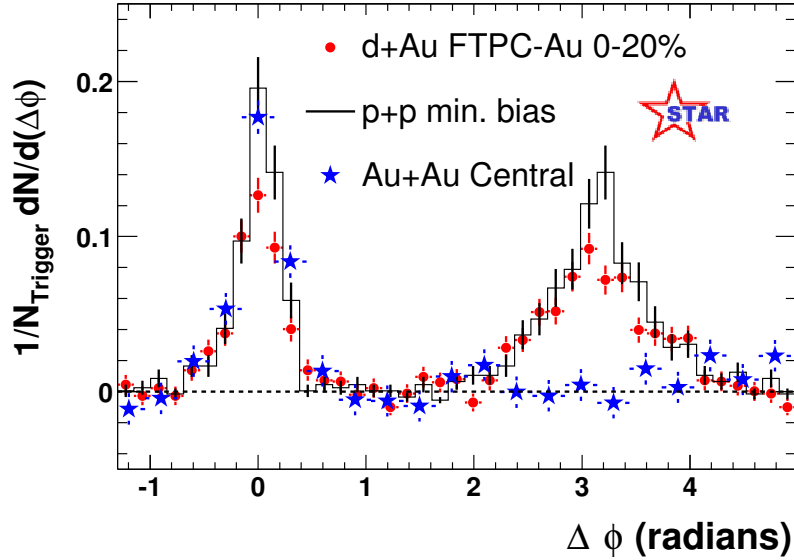


Figure 1.15: The measurement of dihadron azimuthal correlations at high p_T for p+p at $\sqrt{s} = 200$ GeV, and for central d+Au and Au+Au collisions at $\sqrt{s_{NN}} = 200$ GeV in STAR experiment [46].

a trigger hadron with $p_T^{\text{trig}} > 4$ GeV/c in STAR for p+p, d+Au, and Au+Au collisions is shown in Fig. 1.15 [46]. It is observed that for p+p, d+Au, and Au+Au collisions, a hadron pair drawn from a single jet generate an enhanced correlation at $\Delta\phi \approx 0$ (near-side). In contrast, a hadron pair drawn from back-to-back dijets generate an enhanced correlation at $\Delta\phi \approx \pi$ (away-side), which is observed for p+p and d+Au collisions with a broader width

than the near-side correlation peak. For central Au+Au collisions, the back-to-back di-hadron correlation is absent. The strong suppression of away-side correlations for dijet events in central Au+Au collisions could be due to final state interaction of hard partons or their fragmentation products in the dense medium generated in such collisions [47, 48].

The effects of the medium on particle production can be further understood through a experimental observable called Nuclear Modification Factor (R_{AA}) which measures the particle yield from ion-ion (AA) collisions (dense QCD medium) relative to that from nucleon-nucleon (NN) collisions (QCD vacuum). It is defined as

$$R_{AA} = \frac{d^2 N^{AA}/dp_T d\eta}{T_{AA} d^2 \sigma^{NN}/dp_T d\eta}, \quad (1.8)$$

where AA and NN in case of RHIC, are the Au+Au and p+p collision, respectively. $T_{AA} = \langle N_{bin} \rangle / \sigma_{inel}^{NN}$ is the nuclear thickness function, where N_{bin} is the average number of binary NN inelastic collisions calculated from the Glauber model and σ^{NN} is the inelastic cross-section of a nucleon-nucleon collision. If there are no nuclear modification effects, an AA collision could be viewed simply as a superposition of individual NN collisions, where the R_{AA} factor should be equal to unity at high p_T where hard scattering dominates. $R_{AA} < 1$ indicates the effect of strongly interacting matter produced in heavy-ion collisions.

The $R_{AA}(p_T)$ measured in STAR experiment for unidentified charged hadrons in different centralities in Au+Au collisions at $\sqrt{s_{NN}} = 200$ GeV relative to the measured p+p spectrum is shown in Fig. 1.16 [49]. For high p_T ($6 < p_T < 10$ GeV/c), $R_{AA}(p_T)$ is suppressed for each collision centrality except for the most peripheral collisions. It is much more suppressed in central Au+Au relative to p+p collisions. It can be seen from the results that the Cronin enhancement and shadowing alone cannot explain the suppression, which is reproduced only if parton energy loss in dense matter is included. The suppression is

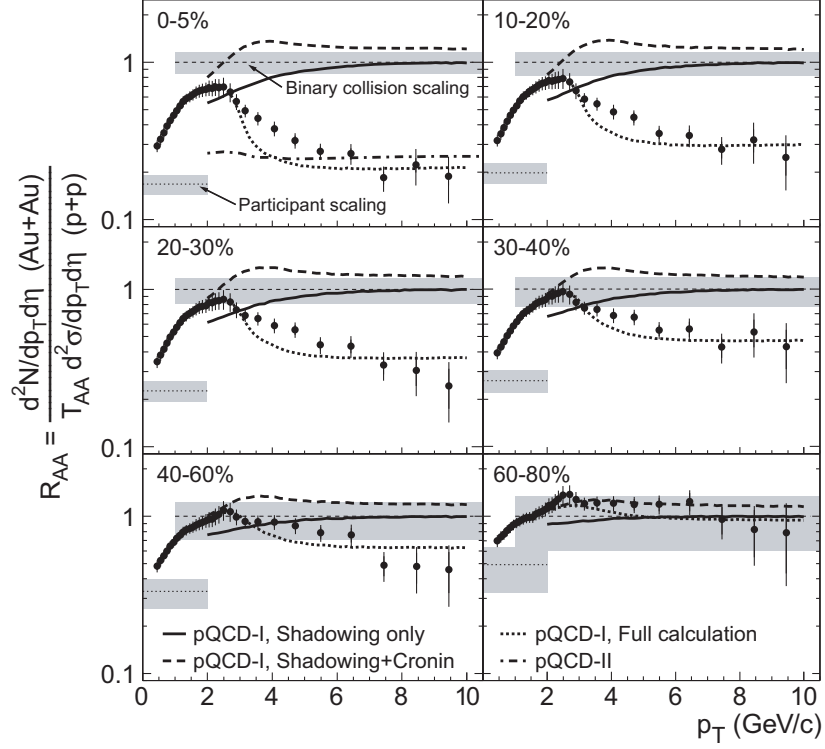


Figure 1.16: $R_{AA}(p_T)$ for charged hadrons for different centralities as measured in the STAR experiment [49].

found to be larger at LHC energy than RHIC energies [50]. The peripheral $R_{AA}(p_T)$ is in agreement with p+p measurement indicating that strong medium effects are only taking place in central collisions. The suppression of $R_{AA}(p_T)$ at high p_T was predicted to be one of the signature of QGP formation [51, 52].

1.5.4 Quarkonia Suppression

The heavy flavor quarks like charm (c , \bar{c}) and bottom (b , \bar{b}) are expected to be formed at an early stage via the gluon fusion or quark-antiquark annihilation channels. Quarkonia particles like J/ψ , Υ , Υ' , Υ'' are made up of from $c\bar{c}$ and $b\bar{b}$. The suppression of quarkonia production in ultra-relativistic heavy-ion collisions predicted by Matsui and Satz is counted

as one of the dominant signature for the formation of QGP [53]. In the de-confined state, the color charge of a quark is subject to screening due to the presence of quarks and gluons in the plasma, which weakens the interaction between heavy quark and antiquark pairs and broken up into open charm or bottom particles by other smaller quarks inside the de-confined medium. This is called Debye color screening [54] which leads to the suppression of heavy quarkonia yield in high energy heavy-ion collisions. The magnitude of the suppression depends on the binding energies of the quarkonia and the temperature of the system. The J/ψ (a bound state of $c\bar{c}$) production has been studied in detail at the CERN SPS in Pb+Pb and In+In collisions [55, 56] and at RHIC experiments in Au+Au collisions [57, 58]. The suppression of this J/ψ particle production can reveal the thermodynamic properties of the medium.

The p_T integrated J/ψ yields for Au+Au and p+p collisions defined by R_{AA} as a function

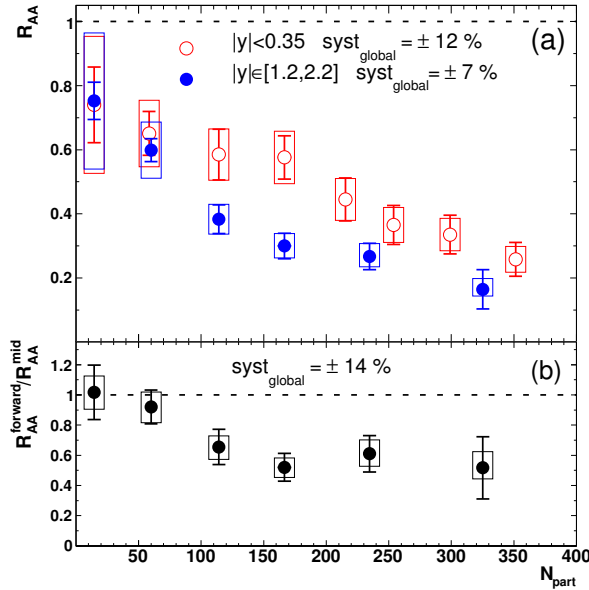


Figure 1.17: Upper panel: J/ψ R_{AA} vs. N_{part} for Au+Au collisions at $\sqrt{s_{NN}} = 200$ GeV. The mid (forward) rapidity data are shown with open (solid) circles. Lower panel: Ratio of forward and mid-rapidity J/ψ R_{AA} as a function of N_{part} [58].

of N_{part} at mid and forward rapidity at $\sqrt{s_{\text{NN}}} = 200$ GeV is shown in Fig. 1.17. In central Au+Au collisions, a significant J/ψ suppression relative to the binary scaling of p+p collisions has been observed. The suppression is significantly larger at forward rapidity and is similar to that observed at the SPS in mid-rapidity [59]. Models of quarkonia suppression studied the probability for recombination into heavy quark-antiquark pairs, called quarkonia regeneration [60]. The R_{AA} of J/ψ production can also be described through the regeneration approach [61].

1.5.5 Photons and Dileptons

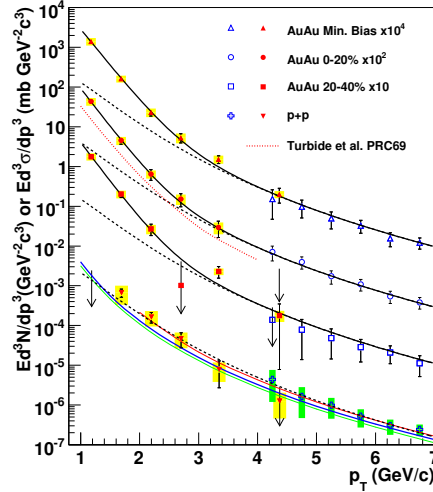


Figure 1.18: Invariant cross section and invariant yield of direct photons as a function of p_T in p+p at $\sqrt{s} = 200$ GeV and in Au+Au collisions at $\sqrt{s_{\text{NN}}} = 200$ GeV, respectively [62]. The three curves on the p+p data represent NLO pQCD calculations [63], and the dashed curves show a modified power-law fit to the p+p data, scaled by T_{AA} . The black solid curves are exponential plus the T_{AA} scaled p+p fit. The red dotted curve near the 0–20% centrality data is a theory calculation [64].

Photons and dileptons interact with medium or other particles only electromagnetically and do not participate in strong interaction due to their large mean free path. They can traverse the dense medium while losing much less energy than hadrons. Therefore, photon

and di-lepton signals can provide a probe of the early state of the system. In QGP, direct photons are produced through annihilation of $q\bar{q} \rightarrow \gamma\gamma$ channel and via Compton scattering of $qg \rightarrow q\gamma$ and $\bar{q}g \rightarrow \bar{q}\gamma$. In addition, these are too produced through fragmentation of hard partons, which are called bremsstrahlung photons. The dilepton production is mainly from

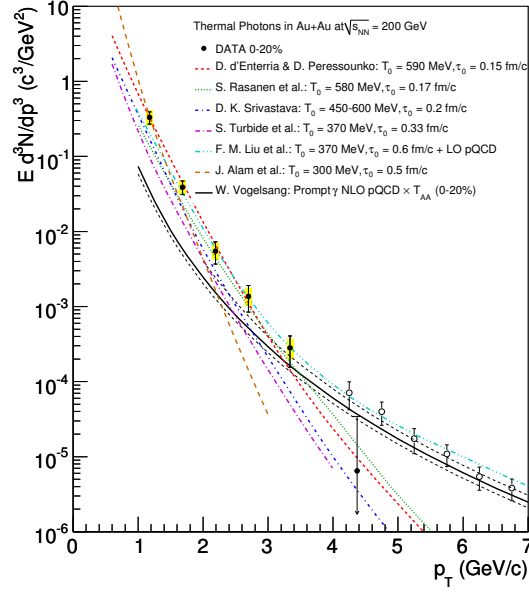


Figure 1.19: Theoretical calculations of thermal photon emission are compared with the direct photon data in central 0–20% Au+Au collisions from PHENIX experiment [65].

annihilation of $q\bar{q} \rightarrow \gamma^* \rightarrow l^-l^+$, i.e. a quark can interact with an antiquark to form a virtual photon (γ^*) and the virtual photon subsequently decays into a lepton l^- and an antilepton l^+ . The detection of direct photons is very challenging due to the small production rate and the large background from hadronic decays.

Figure 1.18 represents the comparison of direct photon spectra obtained by the PHENIX experiment at RHIC [62] and the Next to Leading Order pQCD (NLO pQCD) calculations [63]. The pQCD calculation is consistent with the p+p data within the theoretical uncertainties for $p_T > 2$ GeV/c. The Au+Au data are above the p+p fit curve scaled by

T_{AA} (dashed curves) for $p_T < 2.5$ GeV/ c , indicating that in the low p_T range the direct photon yield increases faster than the binary NN collision scaled by p+p cross section. The red dotted curve in Fig. 1.18 shows a thermal photon spectrum in central Au+Au collisions calculated with initial temperature $T_{\text{init}} = 370$ MeV [64]. Figure 1.19 shows a comparison between the direct photon data in central 0–20% Au+Au collisions and the results of several theoretical calculations of thermal photon emission [65]. The hydrodynamical models which assume the formation of a hot QGP system with initial temperature ranging from $T_{\text{init}} = 300$ MeV at thermalisation time $\tau_0 = 0.6$ fm/ c to $T_{\text{init}} = 600$ MeV at $\tau_0 = 0.15$ fm/ c , provide results in qualitative agreement with the data.

1.6 Identified Particle Production

In relativistic heavy-ion collisions, particle production is a basic tool for both understanding the collision dynamics and search for the QGP state. The QGP signals in the bulk can serve as a strong evidence for the QGP formation. These bulk properties include strangeness and baryon production rates and collective radial flow. Experimentally, the bulk observables can be studied via transverse momentum (p_T) spectra of identified particles in the heavy-ion collisions. The p_T spectra of identified hadrons and the measured yields are the most basic physical observables which can be used to test the predictions for non-perturbative QCD processes like hadronisation and soft-parton interactions. These observables are used for the study of the collective and thermal properties of the produced matter. At top RHIC energies, it has been observed that the bulk matter created in high-energy nuclear reactions can be quantitatively described in terms of hydrodynamic models and bulk chemical freeze-out properties are extracted using thermal equilibrium model.

In this thesis, we present identified charged hadron spectra p_T spectra ($\pi/K/p$ and their antiparticles), particle yields, particle ratios, average transverse momentum, chemical and kinetic freeze-out properties at different collision energies.

1.6.1 Transverse Momentum Spectra

The p_T spectra of identified particles is an important tool for studying the state and evolution of the nuclear matter at high energy density and is very useful in extracting the chemical and kinetic freeze-out properties. It is basically divided into two parts in p_T region which are soft and hard particle productions. Soft part ($p_T \lesssim 2 \text{ GeV}/c$) means particle emission from a thermal source with collective flow and hard part ($p_T \gtrsim 2 \text{ GeV}/c$) means hard scattering followed by jet fragmentation. In this thesis, we have focused on low p_T region and is studied by calculating the invariant yield which is given by;

$$E \frac{d^3N}{dp^3} = \frac{1}{2\pi p_T} \frac{d^2N}{dp_T dy}, \quad (1.9)$$

where E is the particle energy and $d^2N/dp_T dy$ represents an event-wise yield density. The p_T spectra can be characterised by extracting yield (dN/dy), inverse slope parameter (T), and average transverse momentum ($\langle p_T \rangle$). It contains the information about the system when both inelastic and elastic collisions stop. Majority of the particles are produced at low transverse momentum ($p_T \lesssim 2 \text{ GeV}/c$), where the analysis of particle spectra allow one to extract the bulk properties such as the degrees of thermalisation and collectivity of the system. The quantities such as yields (dN/dy), average transverse momentum ($\langle p_T \rangle$), and average transverse mass ($\langle m_T \rangle$) are used to characterise the p_T spectra, discussed below in the following subsections.

1.6.2 Particle Yields and Ratios

The observed identified particle abundances are very useful in understanding the dynamics of collisions at chemical freeze-out. Experimentally, the yields are calculated from the p_T spectra for the measured region and are extrapolated to the unmeasured region. At low energy collision region, the incoming nuclei undergoes a significant stopping in the collision zone which results in higher yield of nucleons (e.g., protons) at mid-rapidity. The

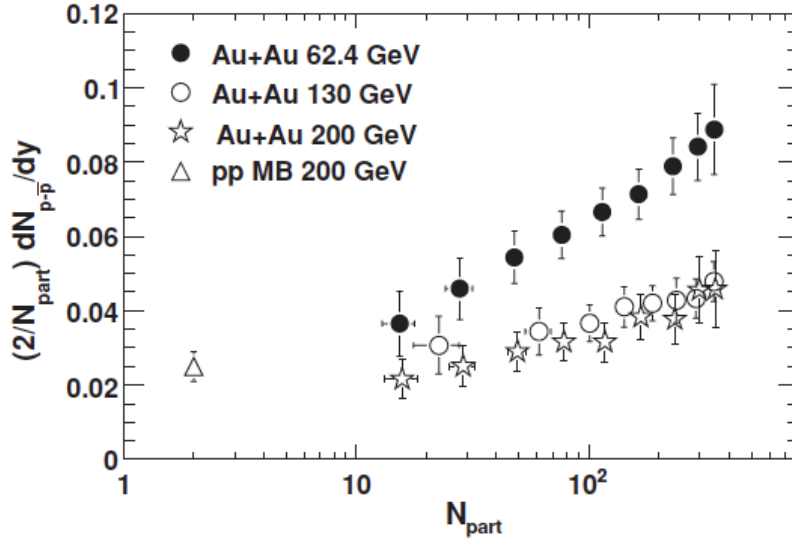


Figure 1.20: Ratio of mid-rapidity net-protons to half the number of participants vs. the number of participants in p+p collisions at $\sqrt{s} = 200$ GeV and in Au+Au collisions at $\sqrt{s_{\text{NN}}} = 62.4, 130$, and 200 GeV. Errors shown are the quadratic sum of statistical and systematic uncertainties [17].

ratio of number of net-protons ($p-\bar{p}$) to $\langle N_{\text{part}} \rangle / 2$, which reflects the approximate probability of each incoming nucleon to be transported to mid-rapidity, as a function of $\langle N_{\text{part}} \rangle$ is shown in Fig. 1.20. This probability is larger in central heavy-ion collisions in comparison with p+p at the same energy. At $\sqrt{s_{\text{NN}}} = 62.4$ GeV, the probability of baryon transport to mid-rapidity is larger. So, for higher energies, the nuclei become more transparent and contribution due to stopping is less.

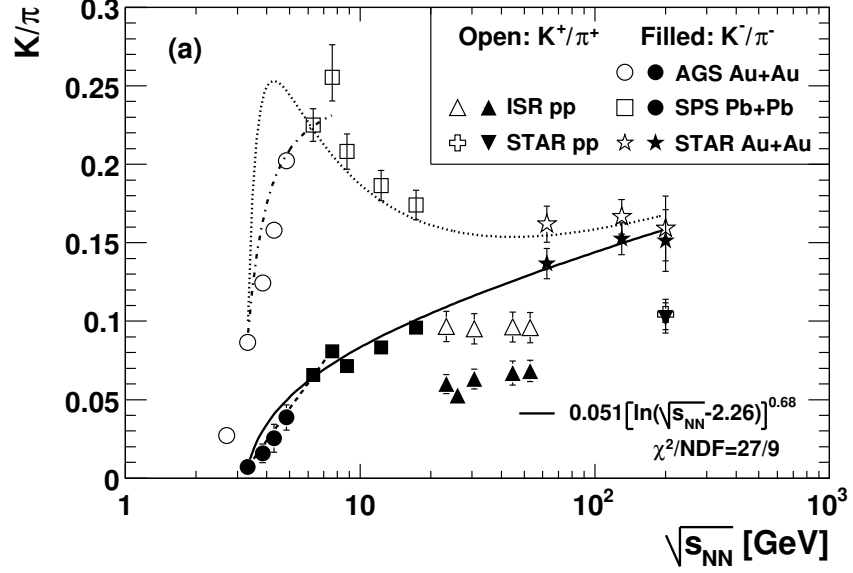


Figure 1.21: K/π ratio as a function of collision energies. The curves going through the heavy-ion data are the phenomenological fits [17].

Different particle ratios are calculated from the measured yields and can also be used to understand the collision dynamics. In heavy-ion collisions, particle ratios have been studied in different experiments like AGS, SPS, RHIC, and LHC. Figure 1.21 shows the variation of K/π as a function of $\sqrt{s_{NN}}$ for central heavy-ion collisions and the curves through the ratios are the phenomenological fits [17]. The K^+/π^+ ratio increases sharply at lower energies which is due to the associated production of K^+ , whereas at higher energies, pair production dominates. It has a peak, namely as “horn” at energy around $\sqrt{s_{NN}} = 8$ GeV.

1.6.3 Average Transverse Momentum

Average transverse momentum ($\langle p_T \rangle$) is used to quantify the shape of p_T spectra. The evolution of $\langle p_T \rangle$ as a function of dN_{ch}/dy (N_{ch} is charged particle multiplicity) for different

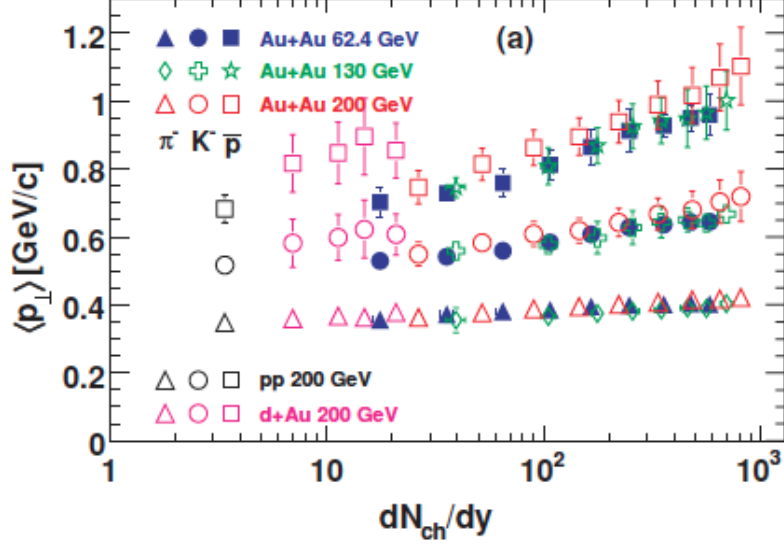


Figure 1.22: Average transverse momenta as a function of dN_{ch}/dy for Au+Au at $\sqrt{s_{NN}} = 62.4, 130, \text{ and } 200 \text{ GeV}$. The results from p+p and d+Au collision systems are also shown [17].

collision systems such as p+p, d+Au, and Au+Au is shown in Fig. 1.22. It is observed that for pions, $\langle p_T \rangle$ increases slightly with centrality whereas for kaons and (anti)protons, it increases significantly with centrality. Also, the $\langle p_T \rangle$ in central Au+Au collisions is larger than that in peripheral collisions which could be due to the effects including multiple scatterings, transverse radial flow, caused by thermodynamic pressure, and the remaining contributions from (semi)hard scatterings [17]. The trend of $\langle p_T \rangle$ with dN_{ch}/dy are similar for Au+Au collisions at $\sqrt{s_{NN}} = 62.4, 130, \text{ and } 200 \text{ GeV}$.

1.6.4 Average Transverse Mass

In stead of p_T , one can also use $m_T = \sqrt{p_T^2 + m^2}$, where m is rest mass of the particle species $\pi, K, p (\bar{p})$, to understand the p_T spectra. The variation of $\langle m_T \rangle - m$ with $\sqrt{s_{NN}}$ obtained from AGS, SPS, and RHIC is shown in Fig. 1.23. The $\langle m_T \rangle - m$ increases from

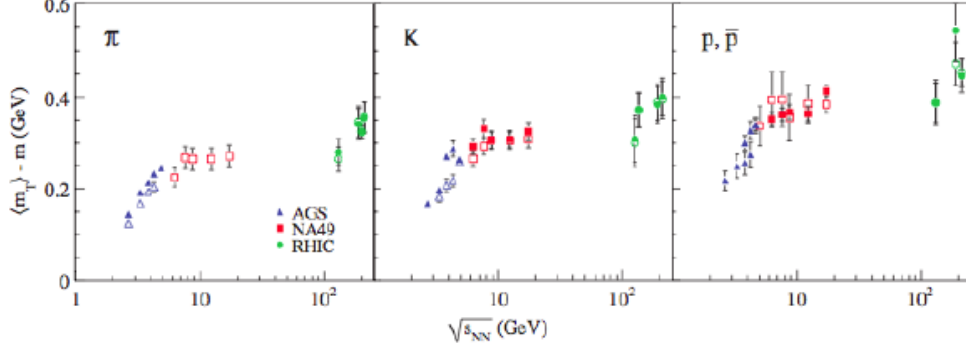


Figure 1.23: The variation of $\langle m_T \rangle - m$ as a function of $\sqrt{s_{NN}}$ for Au+Au and Pb+Pb collisions in AGS, SPS, and RHIC energies [66].

lower AGS energies to lowest SPS energies. Then it remains constant for other higher SPS energies following the increasing trend towards the RHIC energies. If $\langle m_T \rangle - m$ is regarded as temperature and $\log(\sqrt{s_{NN}})$ is related to dN/dy which represents entropy of the system then the plateau region can be considered as mixed phase. This type of variation of $\langle m_T \rangle - m$ with $\sqrt{s_{NN}}$ provide information about the transition from hadronic phase to QGP phase [66].

We will discuss details about p_T spectra, $\langle p_T \rangle$, and $\langle m_T \rangle - m$ in chapter 3 of this thesis.

1.7 Freeze-out Dynamics

The fireball produced in high energy heavy-ion collisions expands with time due to the pressure gradient. During this process, the produced particles interact with each other elastically and inelastically. The large number of produced particles as well as the large system size compared to the interaction length, allows one to treat the system created in heavy-ion collisions macroscopically. Investigation of relative hadron abundances provides an indirect way to study the degree of thermalisation and can be described by thermal models assuming the system to be in thermal and chemical equilibrium. In this case, the system

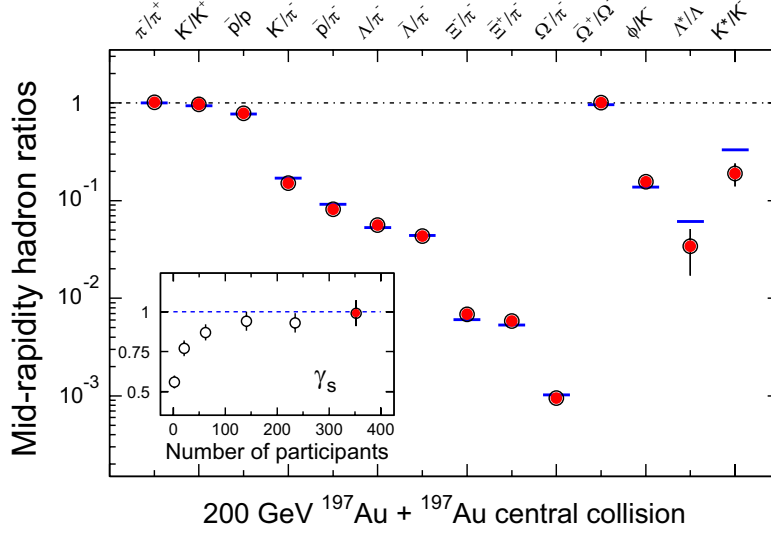


Figure 1.24: The mid-rapidity particle ratios (red symbol) obtained from p_T integrated yields for different hadron species in Au+Au collisions at $\sqrt{s_{NN}} = 200$ GeV. The blue lines represent the statistical model fits to the particle ratios. The fit parameters are $T_{ch} = 163 \pm 4$ MeV, $\mu_B = 24 \pm 4$ MeV, $\gamma_S = 0.99 \pm 0.07$ [68]. The inset shows the variation of γ_S with centrality. The figure is taken from Ref. [46].

is governed mainly by two parameters, the chemical freeze-out temperature (T_{ch}) and the baryon chemical potential (μ_B), where the latter describes the net-baryon content of the system. Identified particle yields measured by identified particle spectra are used as the inputs for the thermal analysis. Measured particle yields in heavy-ion collisions at RHIC, as well as SIS, AGS, SPS, and LHC are consistent with a statistical chemical equilibrium populations, allowing the extraction of model parameters from fits to the measured particle yields and also particle ratios. It has been argued that interactions modifying the relative abundances of particle species are negligible in the hadronic phase and T_{ch} can be linked to the phase transition temperature.

In heavy-ion collisions, the measured particle yields can provide information about the system at chemical freeze-out, when inelastic collisions cease and the chemical composition of the final state will not change any further. It is characterised by the chemical freeze-out

temperature T_{ch} and the baryon and strangeness chemical potentials μ_B and μ_S , respectively. An additional strangeness suppression factor γ_S was introduced by some models to account for the non-fully equilibrated system. Statistical Models use the particle ratios or particle yields to constrain the system temperature and the baryonic chemical potential at chemical freeze-out, under the assumption that the system is in thermal and chemical equilibrium at that stage [67]. A comparison of the mid-rapidity experimental p_T integrated yield ratios which includes identified hadrons, strange and multi strange hadrons measured by STAR for Au+Au collisions at $\sqrt{s_{\text{NN}}} = 200$ GeV and that obtained from grand-canonical formalism of statistical model fits [46] is shown in Fig. 1.24 [68]. The excellent agreement between data and model indicates that the light flavors have reached chemical equilibrium at a temperature, $T_{\text{ch}} = 163 \pm 4$ MeV. This temperature is essentially close to the critical value for a transition of QGP to hadron gas predicted by lattice QCD. The inset in Fig. 1.24

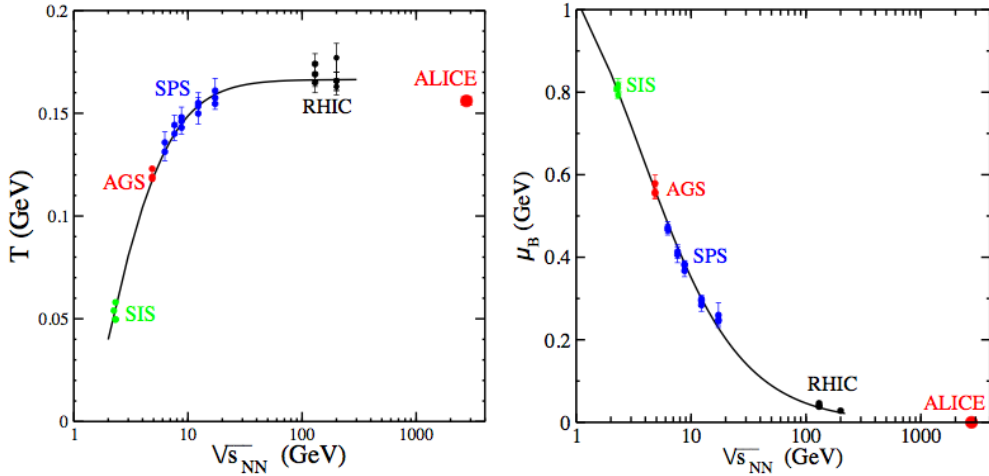


Figure 1.25: The variation of T_{ch} and μ_B as a function of center-of-mass energy. The solid curve represents the theoretical curve [69].

shows the variation of γ_S with centrality (number of participants), which reaches unity for most central collisions. This indicates that the system created in central collisions at RHIC is in chemical equilibrium.

The T_{ch} and μ_B values extracted from the thermal fits are reported in Fig. 1.25 as a function of $\sqrt{s_{\text{NN}}}$ obtained from SIS, AGS, SPS, top RHIC, and LHC energies [69]. T_{ch} is observed to be flat as a function of $\sqrt{s_{\text{NN}}}$ beyond 10 GeV (SPS energy). The saturation of T_{ch} above top SPS energy may be due to the fact that the freeze-out temperature lies close to the phase transition line. This suggests above a certain energy (top SPS energy), the chemical freeze-out happens right after the hadronisation. Below this energy, the T_{ch} may deviate from phase transition temperature which could be due to a longer equilibrium phase after hadronisation or to the fact that the energy density in such collisions is not high enough to create the QGP. The μ_B values decreases with increasing $\sqrt{s_{\text{NN}}}$ which is due to the smaller baryon number transport at mid-rapidity with increasing energy, due to larger transparency. This results in a vanishing μ_B at LHC energy as shown in Fig. 1.25. The measurements can

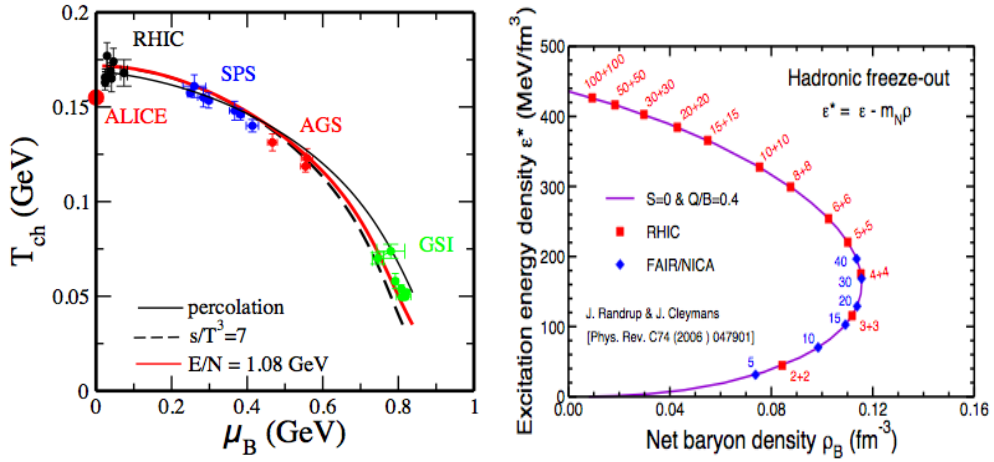


Figure 1.26: Left: The T_{ch} vs. μ_B at different center-of-mass energies from AGS-LHC [69]. The curves corresponds to various models [71]. Right: The hadronic freeze-out line in the $\rho_B - \epsilon$ phase obtained from the values of T_{ch} and μ_B [70].

be presented in the $T_{\text{ch}} - \mu_B$ plane, called phase diagram. So the measurement of freeze-out parameters includes T_{ch} and μ_B as the key measurement in this picture. A large gap in the μ_B , from SPS to RHIC energies in the phase diagram as shown in left-panel of Fig. 1.26, has been covered through RHIC BES-I program. This forms one of the main study of this

thesis, which will be discussed in the later chapters. The resulting $T_{\text{ch}} - \mu_B$ freeze-out curve can also be drawn in the excitation energy density vs. net baryon density plane as shown in the right-panel of Fig. 1.26 [70]. The calculation has been done employing the $\langle \mu_S \rangle$ and $\langle \mu_Q \rangle$ values that ensure $\langle S \rangle = 0$ and $\langle Q \rangle = 0.4B$ for each value of μ_B . The results suggest that the highest net baryon density will be reached in the beam energy covered by the RHIC BES/FAIR/NICA experiments. In heavy-ion collisions, after chemical freeze-out, further expansion leads to a stage where the elastic collisions eventually cease, and the kinetic properties of the system are frozen and it is called kinetic freeze-out. It is explored by

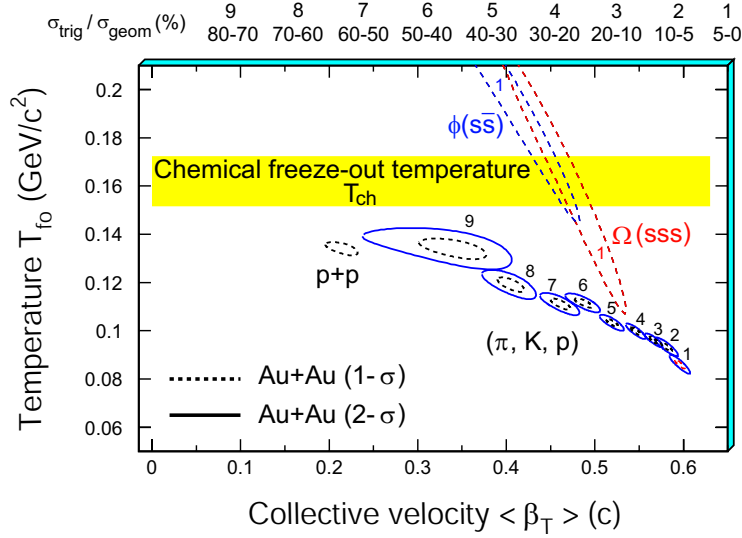


Figure 1.27: The χ^2 contours for T_{f0} and $\langle \beta_T \rangle$ extracted from thermal and radial flow fits for different hadrons produced in Au+Au collisions at $\sqrt{s_{NN}} = 200$ GeV. The figure is taken from Ref. [46].

analysing the spectra of various hadron species and characterised by the kinetic freeze-out temperature (T_{f0}) and the average transverse flow velocity $\langle \beta_T \rangle$. Hereafter, the particles free stream towards the detector. T_{f0} and $\langle \beta \rangle$ are extracted by using the p_T spectra which are fitted by hydrodynamics motivated Blast-wave models [72, 40]. Kinetic equilibration is thought to prevail over the transverse degrees of freedom, therefore, p_T or m_T distributions are used to extract T_{f0} . Figure 1.27 shows the values of T_{f0} and $\langle \beta_T \rangle$ extracted from ther-

mal and radial flow fits for different centrality bins and hadron species obtained in Au+Au collisions at $\sqrt{s_{NN}} = 200$ GeV [46]. It is observed that bulk of the system consisting of pions, kaons, and protons freeze-out at T_{fo} which is lower than T_{ch} and develop a stronger collective flow. It indicates that there is a rapid expansion after chemical freeze-out which is observed to increase with centrality. The results obtained for ϕ and Ω indicate reduced hadronic interactions after chemical freeze-out for multi-strange hadrons.

In heavy-ion physics, thermalisation plays an important role. Since all the experimental measurements take place after the phase transition in the hadronic stage, it is not possible to observe the evidence of thermalisation in QGP phase directly. But, the agreement between measured data and statistical model in the thermal equilibrium can serve as a strong signature of thermalisation.

1.8 Outline of the Thesis

In chapter 2, the details of the RHIC, STAR detector and subsystems used for the analysis, are discussed. Chapter 3 presents the identified particle production (π^\pm , K^\pm , p (\bar{p})) at $\sqrt{s_{NN}} = 27$ GeV and studies of the bulk matter properties in Au+Au collisions at $\sqrt{s_{NN}} = 7.7, 11.5, 19.6, 27$, and 39 GeV. The results on p_T spectra, centrality and energy dependence of particle yields, ratios, $\langle p_T \rangle$, and $\langle m_T \rangle$ are discussed. In chapter 4, we discuss the QCD phase diagram through the centrality and energy dependence of chemical freeze-out parameters at RHIC BES-I energies $\sqrt{s_{NN}} = 7.7, 11.5, 19.6, 27$, and 39 GeV along with top RHIC energies $\sqrt{s_{NN}} = 62.4$ and 200 GeV. The extracted freeze-out parameters are T_{ch} , μ_B , μ_S , γ_S , and R . In chapter 5, the systematic measurements of freeze-out properties at AGS, SPS, RHIC, and LHC energies in Au+Au and Pb+Pb collisions for top most centrality are presented. Chapter 6 discusses the fabrication and cosmic ray test results of GEM chambers and its installation in STAR for the TPC tracking calibrations. Finally, conclusions of the work carried out in this thesis are given in chapter 7.

Bibliography

- [1] S. F. Novaes, Standard Model: An Introduction, arXiv:0001283.
- [2] G. Zweig, (1981), Developments In The Quark Theory Of Hadrons, vol. 1, 22-101 and CERN Geneva - TH. 401.
- [3] S. L. Glashow, Nucl. Phys. 22, 579 (1961); A. Salam and J. C. Ward, Phys. Lett. 13, 168 (1964); S. Weinberg, Phys. Rev. Lett. 19, 1264 (1967).
- [4] P. W. Higgs, Phys. Lett. 12, 132 (1964); Phys. Rev. Lett. 13, 508 (1964); F. Englert and R. Brout, Phys. Rev. Lett. 13, 321 (1964).
- [5] G. Aad *et al.* (ATLAS Collaboration), Phys. Lett. B 716, 1 (2012).
- [6] W. Adam *et al.* (CMS Collaboration), Phys. Lett. B 716, 30 (2012).
- [7] H. Kastrup *et al.*, QCD 20 yrs later World Scientific, Singapore (1993).
- [8] M. Gell-Mann, Phys. Rev. 125, 1067 (1962).
- [9] S. Bethke, MPP-2012-132, arXiv:1210.0325.
- [10] J. C. Collins and M. J. Perry, Phys. Rev. Lett. 34, 1353 (1975).
- [11] J. Adams *et al.*, Nucl. Phys. A 757, 102 (2005); K. Adcox *et al.*, Nucl. Phys. A 757, 184 (2005).

- [12] F. Karsch, Nucl. Phys. A 698, 199 (2002).
- [13] A. Bazavov *et al.*, Phys. Rev. D 85, 054503 (2012).
- [14] T. Csorgo, Nucl. Phys. Proc. Suppl. 92, 62 (2001); M. Gazdzicki, The Europ. Phys. Journal -Special Topics. 155, 37 (2008).
- [15] J. D. Bjorken, Phys. Rev. D 27, 140 (1983).
- [16] K. Adcox *et al.* (PHENIX Collaboration), Phys. Rev. Lett. 87, 52301 (2001);
- [17] B. I. Abelev *et al.* (STAR Collaboration), Phys. Rev. C 79, 034909 (2009).
- [18] M. M. Aggarwal *et al.* (STAR Collaboration), arXiv:1007.2613 (2010).
- [19] F. R. Brown *et al.*, Phys. Rev. Lett. 65, 2491 (1990).
- [20] Y. Hatta and T. Ikeda, Phys. Rev. D 67, 014028 (2003) and references therein.
- [21] M. Cheng *et al.*, Phys. Rev. D 79, 074505 (2009); R.V. Gavai and S. Gupta, Phys. Rev. D 71 (2005) 114014; R. V. Gavai and S. Gupta, Phys. Rev. D 78, 114503 (2008).
- [22] M. A. Stephanov, Phys. Rev. Lett. 102, 032301 (2009).
- [23] M. A. Stephanov *et al.*, Phys. Rev. D 60, 114028 (1999); M. Asakawa *et al.*, Phys. Rev. Lett. 103, 262301 (2009); M. A. Stephanov, Phys. Rev. Lett. 107, 052301 (2011).
- [24] N Abgrall *et al.*, JINST 9 P06005 (2014).
- [25] http://nica.jinr.ru/files/NICA_CDR.pdf (2008).
- [26] J. M. Heuser (for CBM Collaboration), Nucl. Phys. A 830, 563c (2009).
- [27] J. Rafelski and B. Muller, Phys. Rev. Lett. 48, 1066 (1982).

- [28] J. Cleymans, K. Redlich, and E. Suhonen, Z. Phys. C 51, 137 (1991); F. Becattini and G. Pettini, Phys. Rev. C 67, 015205 (2003).
- [29] B. I. Abelev *et al.* (STAR Collaboration), Phys. Lett. B 673, 183 (2009).
- [30] C. Adler *et al.* (STAR Collaboration) Phys. Lett. B 595, 143 (2004); J. Adams *et al.* (STAR Collaboration), Phys. Lett. B 567, 167 (2003).
- [31] J. Adams *et al.* (STAR Collaboration), Phys. Rev. Lett. 92, 182301 (2004); C. Adler *et al.* (STAR Collaboration), Phys. Rev. Lett. 89, 092301 (2002).
- [32] J. I. Kapusta and A. Mekjian, Phys. Rev. D 33, 1304 (1986).
- [33] P. Huovinen, arXiv:0305064.
- [34] J. Y. Ollitrault, Phys. Rev. D 46, 229 (1992); H. Sorge, Phys. Rev. Lett. 78, 2309 (1997); H. Sorge, Phys. Lett. B 402, 251 (1997).
- [35] S. Voloshin and Y. Zhang, Z. Phys. C 70, 665 (1996).
- [36] H. Stocker, Nucl. Phys. A 750, 121 (2005); H. Sorge, Phys. Rev. Lett. 78, 2309 (1997).
- [37] C. Alt *et al.* (NA49 Collaboration), Phys. Rev. C 68, 034903 (2003).
- [38] C. Adler *et al.* (STAR Collaboration), Phys. Rev. C 66, 034904 (2002).
- [39] J. Adams *et al.* (STAR Collaboration), Phys. Rev. C 72, 014904 (2005).
- [40] P. Huovinen *et al.*, Phys. Lett. B 503, 58 (2001); U. Heinz and P. Kolb, Nucl. Phys. A 702, 269 (2002); F. Retiere and M. A. Lisa, Phys. Rev. C 70, 044907 (2004).
- [41] X. Dong *et al.*, Phys. Lett. B 597, 328 (2004).

- [42] D. Molnar and S. A. Voloshin, Phys. Rev. Lett. 91, 092301 (2003); S. A. Voloshin, Nucl. Phys. A 715, 379 (2003).
- [43] X. N. Wang and M. Gyulassy, Phys. Rev. Lett. 68, 1480 (1992).
- [44] <http://physics.aps.org/articles/v7/97>.
- [45] M. Gyulassy and M. Plumer, Phys. Lett. B 243, 432 (1990).
- [46] J. Adams *et al.* (STAR Collaboration), Nucl. Phys. A 757, 102 (2005).
- [47] C. Adler *et al.* (STAR Collaboration), Phys. Rev. Lett. 90, 082302 (2003).
- [48] J. Adams *et al.* (STAR Collaboration), Phys. Rev. Lett. 91, 072304 (2003).
- [49] J. Adams *et al.*, Phys. Rev. Lett. 91, 172302 (2003).
- [50] K. Aamodt *et al.* (ALICE Collaboration), Phys. Lett. B 696, 30, (2011); B. Abelev, *et al.* (ALICE Collaboration), Phys. Rev. Lett. 110, 082302 (2013).
- [51] M. Gyulassy and M. Plumer, Phys. Lett. B 243, 432 (1990).
- [52] X. N. Wang, Nucl. Phys. A 715, 775 (2003).
- [53] T. Matsui and H. Satz, Phys. Lett. B 178, 416 (1986).
- [54] M. Gao, Phys. Rev. D 41, 626 (1990); H. Satz, Nucl. Phys. A 418, 447c (1984).
- [55] B. Alessandro *et al.* (NA50 Collaboration), Euro. Phys. J. C 39, 335 (2005); Eur. Phys. J. C 48, 329 (2006).
- [56] R. Arnaldi *et al.* (NA60 Collaboration), Phys. Rev. Lett. 99, 132302 (2007).
- [57] A. Adare *et al.* (PHENIX Collaboration), Phys. Rev. Lett. 98, 232002 (2007); Phys. Rev. Lett. 98, 232301 (2007).

- [58] A. Adare *et al.* (PHENIX Collaboration), Phys. Rev. Lett. 101, 122301 (2008); Phys. Rev. Lett. 96, 012304 (2006).
- [59] K. Tuchin, J. Phys. G 30, S1167 (2004).
- [60] A. Andronic *et al.*, Nucl. Phys. A 789, 334 (2007).
- [61] L. Yan, P. Zhuang, and N. Xu, Phys. Rev. Lett. 97, 232301 (2006).
- [62] A. Adare *et al.* (PHENIX Collaboration), Phys. Rev. Lett. 104, 132301 (2010).
- [63] L. E. Gordon and W. Vogelsang, Phys. Rev. D 48, 3136 (1993).
- [64] S. Turbide, R. Rapp, and C. Gale, Phys. Rev. C 69, 014903 (2004).
- [65] A. Adare *et al.* (PHENIX Collaboration), Phys. Rev. C 81, 034911 (2010).
- [66] C. Alt *et al.*, (NA49 Collaboration), Phys. Rev. C 77, 024903 (2008).
- [67] J. Cleymans and K. Redlich, Phys. Rev. C 60, 054908 (1999); P. Braun- Munzinger *et al.*, Phys. Lett. B 518, 41 (2001); N. Xu and M. Kaneta, Nucl. Phys. A 698, 306 (2002).
- [68] O. Barannikova (for the STAR Collaboration), arXiv:0403014.
- [69] J. Cleymans, arXiv:1412.7045.
- [70] J. Randrup and J. Cleymans, Phys. Rev. C 74, 047901, 2006.
- [71] J. Cleymans *et al.*, Phys. Rev. C 73, 034905 (2006).
- [72] E. Schnedermann, J. Sollfrank, and U. Heinz, Phys. Rev. C 48, 2462 (1993); D. Teaney, J. Lauret and E. V. Shuryak, Phys. Rev. Lett. 86, 4783 (2002); P. Kolb *et al.*, Nucl. Phys. A 696, 197 (2001).

Chapter 2

The Experimental Details

In this chapter, we describe briefly the accelerator and the detector systems used to record the data whose analysis and the corresponding physics results are presented in this thesis.

2.1 Introduction

The Bevatron-Bevalac at Lawrence Berkley National Laboratory (LBNL) was the first facility to exploit relativistic nucleus-nucleus collisions at fixed target energies. The primary purpose of this facility was to create dense nuclear matter in the laboratory. The first beams of carbon and oxygen nuclei were accelerated up to 2 GeV per projectile nucleon [1]. The promising theoretical work on QCD predicting hadron-parton de-confinement phase transition [2], generated interest in the community to obtain high energy density, necessary for the formation through relativistic heavy-ion collisions. This led to experiments with higher energy beams of heavier nuclei directed at fixed targets. The AGS at BNL provided oxygen, silicon, and gold ion beams at collision energies per nucleon pair, $\sqrt{s_{NN}} = 4.86$ GeV, and the SPS at CERN accelerated oxygen, sulphur, lead, and indium ion beams up to $\sqrt{s_{NN}} = 17.3$ GeV. At AGS energies, the phenomenon of nuclear stopping created a baryon

rich collision region [3]. At higher energies of SPS, the net baryon density decreases as the non-participating spectator nucleons pass through the interaction region. The strangeness enhancement measurements relative to elementary interactions indicated possibility of the thermal equilibrium of the system formed in the collisions at AGS and SPS energies [4]. The observation of J/ψ suppression in these collisions at SPS was a signature of formation of QGP [5].

In the year 2000, the RHIC at BNL became the first machine in the world, colliding heavy-ions at relativistic energies and the first facility which could clearly identify the QGP formation and study the characteristics of the plasma. It is a flexible accelerator and can accelerate different kinds of heavy nuclei such as gold, copper, uranium, and deuteron at center-of-mass energies from $\sqrt{s_{NN}} = 7.7$ up to 200 GeV, with about 10 times higher center-of-mass energies than what was achieved in previous fixed target experiments. In addition, It can also deliver polarised protons up to $\sqrt{s} = 500$ GeV which is required to study the spin structure of the nucleon [6, 7]. The LHC at CERN, started in 2010, collides lead ions at $\sqrt{s_{NN}} = 2.76$ TeV. The measurements at LHC have begun to produce interesting new results that are complementing the results at RHIC. In addition, since the energy density being much higher than RHIC, it has produced some new results not seen earlier at RHIC.

In the following sections, we describe the RHIC experimental facility and the STAR detector which are used for the work presented in this thesis.

2.2 Relativistic Heavy Ion Collider

The RHIC facility is situated at BNL, USA and its prime aim is to study the primordial form of matter of quarks and gluons that existed in the universe shortly after the Big Bang. With RHIC, nuclear physics entered into the high energy domain, where the QCD structure of matter directly manifested in terms of the dynamics of quarks and gluons [8]. The schematic diagram of the RHIC along with all other accelerators and experiments used to bring the heavy-ions up to the RHIC injection energy is shown in Fig. 2.1. The steps to produce Au+Au collisions at top RHIC energy of $\sqrt{s_{NN}} = 200$ GeV are described below.

1. Tandem Van de Graff: The Au ions, which are used in the collisions, are first generated as singly charged Au^{-1} from a pulsed Cesium ($_{55}\text{Cs}$) sputtering source. Negatively charged Au ions at the Tandem Van de Graaff [9] are accelerated through a 14 MV potential while passing through thin carbon stripping foil (areal density of $2 \mu\text{g}/\text{cm}^2$) that partially remove electrons off the ions. The resulting positive ions are then accelerated away from the positive terminal and go through a $15 \mu\text{g}/\text{cm}^2$ carbon electron stripper foil leaving them with a charge state of 32+ and kinetic energy of 1 MeV per nucleon as they exit the Tandem.

2. Tandem-to-Booster (TTB) line: The bunches of Au^{32+} ions from the Tandem pass through the 850 m long Tandem-to-Booster beam line, which carries them through a vacuum via a magnetic field to the booster synchrotron. The TTB consists of a series of bends arranged in pairs. The first pair selects the ions with desired momentum while the other two pairs are arranged in such a way that the ions of different momenta would emerge in same direction [10].

3. Linear Accelerator (Linac): For collision of proton beams at RHIC, the energetic protons are supplied by the 200 MeV Linac. Protons from the Linac are transferred to the

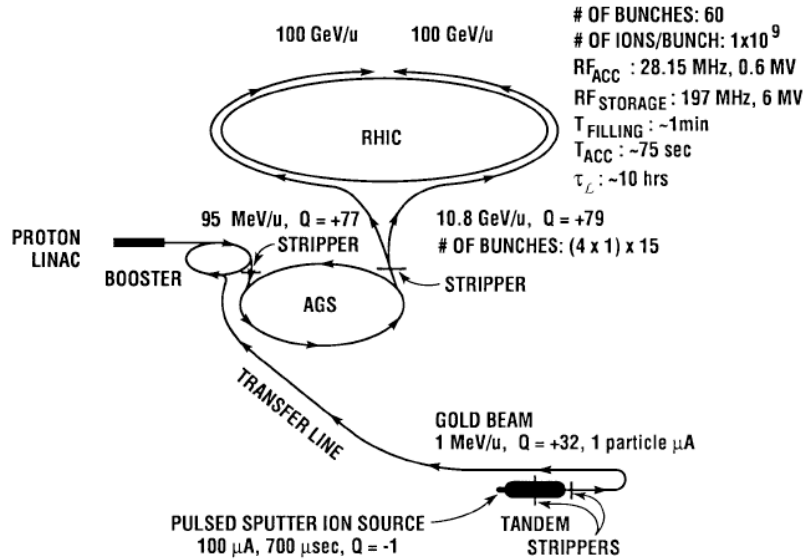


Figure 2.1: Schematic diagram showing the various stages of acceleration of ions at the RHIC.

booster synchrotron.

4. Booster Synchrotron: The booster synchrotron has circumference of 201.8 m. It is a powerful circular accelerator that provides the ions more energy by having them “surf ride” on the downhill slope of radio frequency electromagnetic waves. To confine the charged beam a series of bending magnets around the ring is used. Magnetic field is parallel to the path of the ions inside the synchrotron. An electric field is also used to accelerate particles. Inside the booster, the ions are put into six bunches, accelerated to about 37% of the speed of light and put through another electron stripper. So, for Au+Au collisions, the booster synchrotron accelerates the ions to 95 MeV per nucleon and the ions are stripped again to reach a charge state of Au^{77+} at the exit of the booster. The Au^{77+} ions from the booster are transferred by the Booster-to-AGS line into a larger synchrotron, with four-time the radius of the booster, called the Alternating Gradient Synchrotron (AGS).

5. Alternating Gradient Synchrotron: To fill one AGS cycle of 24 ion bunches, it takes

Table 2.1: Some of the typical designed parameters and performance information of the RHIC for top energy.

Parameter	Value
Luminosity (Au+Au)	$2 \times 10^{26} \text{ cm}^{-2}\text{s}^{-1}$
Luminosity (p+p)	$4 \times 10^{30} \text{ cm}^{-2}\text{s}^{-1}$
No. of bunches per ring	60
Revolution frequency	78 kHz
Ions (Au) per bunch	10^9
Ions (p) per bunch	10^{11}
Beam life time	10 hours
Ring circumference	3833.845 m

4 batches of ions from the booster. Inside the AGS, the Au^{77+} ions are de-bunched and re-bunched into four final bunches and further accelerated to 99.7% of the speed of light. The Au^{77+} ions are here accelerated to 10.8 GeV per nucleon. After passing through a final stripping foil, the ions are fully stripped off electrons and reach a charge state of 79+ at the exit of the AGS.

6. AGS-to-RHIC Line: Via AGS-to-RHIC transfer line, the Au^{79+} beam is injected into the RHIC collider. At the end of this line, there is a “fork in the road”, where a switching magnet sends the ion bunches down one of two beam lines. Bunches are directed either left to travel clockwise in the RHIC ring or right to travel anticlockwise in the second RHIC ring.

7. RHIC Rings: The RHIC is an intersecting storage ring particle accelerator. It consists of two quasi circular, underground counter-rotating rings of circumference 3.8 km, named “Blue Ring”, where the beam moves in a clockwise direction and “Yellow Ring”, where the beam moves in an anticlockwise direction. These independent rings have their sets of superconducting magnets which bend and focus the ions [11] as well as radio frequency acceleration cavities. This allows independent tuning of the magnetic fields in each ring

which is required to achieve equal rotation frequencies of the different particle/ion species in each ring. Both rings share a common horizontal plane inside the tunnel. The incoming ion beam splits into two beams, each traveling inside a beam pipe in the center of each ring. The ion beams are accelerated to the desired collision energy inside the RHIC rings and stored for data taking. When the luminosity drops below a certain level, the beams are removed from the rings (dumped). Then the cycle restarts inside the Tandem. Table 2.1 lists some of the designed parameters of the RHIC at top RHIC energy ($\sqrt{s_{NN}} = 200$ GeV). Its next major upgrades with eRHIC [12], with new and exciting physics possibilities are planned to start in the year 2020. Nowadays, RHIC provides beams of very high luminosi-

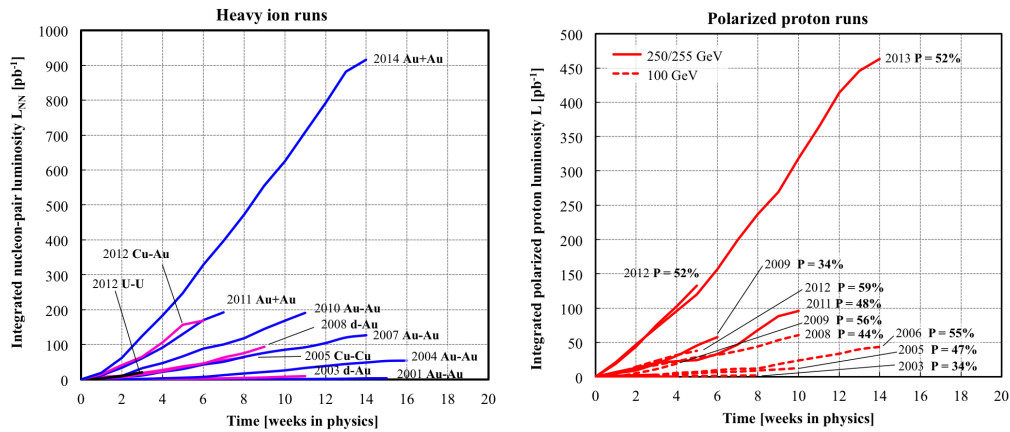


Figure 2.2: The nucleon-pair luminosity is defined as $L_{NN} = A_1 A_2 L$, where L is the luminosity and A_1, A_2 are the number of nucleons of the ions in the two beam, respectively.

ties as shown in Fig. 2.2, which makes possible to measure rare processes having small cross sections. The interaction rate (R) between two colliding beams depend on Luminosity (L) and cross section (σ), which is given by $R = L \times \sigma$. In experiment, luminosity can be controlled and optimised. If Blue beam has N_B particles per bunch, Yellow beam has N_Y particles per bunch, each beam with n bunches per revolution, circling in the machine

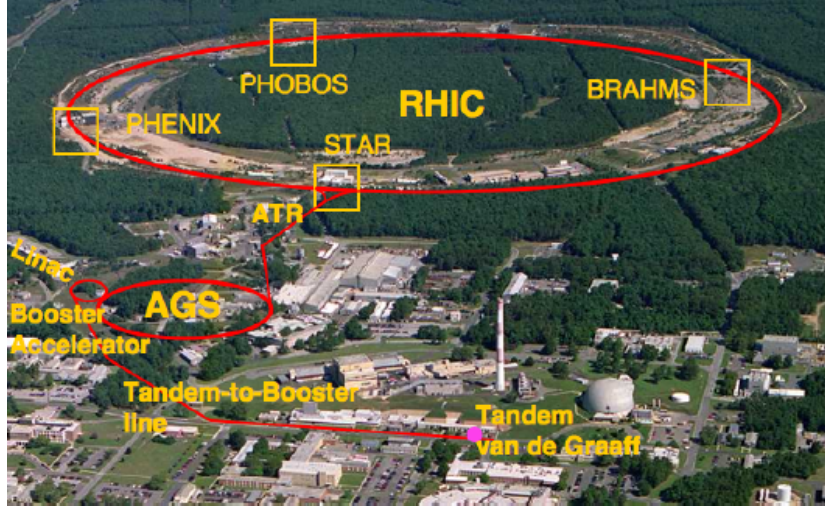


Figure 2.3: Overview of the RHIC accelerator complex at Brookhaven National Laboratory, Upton, New York.

at revolution frequency f , then the luminosity is given by [13],

$$L \simeq fn \frac{N_B N_Y}{A}, \quad (2.1)$$

where A is cross-sectional area of the overlap between the two colliding beams of particles. To date, different particle combinations explored at RHIC are p+p, d+Au, h+Au, Cu+Cu, Cu+Au, Au+Au, and U+U. During the start of RHIC, an average luminosity of $2 \times 10^{26} \text{ cm}^{-2}\text{s}^{-1}$ was targeted which has been increased and the current average Au+Au luminosity of the collider is $50 \times 10^{26} \text{ cm}^{-2}\text{s}^{-1}$ which is 25 times the designed value. The heavy-ion luminosity is substantially increased through stochastic cooling. An overview of RHIC runs and luminosities is given in Table 2.2.

Along the RHIC rings, there are six interaction points. If the RHIC is considered as a clock, the radio frequency system resides at one of the non-experimental crossing point (4 o'clock). Other crossing points are four heavy-ion experiments named Solenoidal Tracker

Table 2.2: Summary of RHIC operating modes and total integrated luminosity delivered to all experiments [14].

RHIC Run	Year	Species	$\sqrt{s_{NN}}$ (GeV)	Delivered Luminosity
Run-1	2000	Au+Au	56	$< 0.001 \mu\text{b}^{-1}$
		Au+Au	130	$20 \mu\text{b}^{-1}$
Run-2	2001-2002	Au+Au	200	$258 \mu\text{b}^{-1}$
		Au+Au	19.6	$0.4 \mu\text{b}^{-1}$
		p+p	200	1.4pb^{-1}
Run-3	2002-2003	d+Au	200	73nb^{-1}
		p+p	200	5.5pb^{-1}
Run-4	2003-2004	Au+Au	200	3.53nb^{-1}
		Au+Au	62.4	$67 \mu\text{b}^{-1}$
		p+p	200	7.1pb^{-1}
Run-5	2004-2005	Cu+Cu	200	42.1nb^{-1}
		Cu+Cu	62.4	1.5nb^{-1}
		Cu+Cu	22.4	0.02nb^{-1}
		p+p	200	29.5pb^{-1}
		p+p	409.8	0.1pb^{-1}
Run-6	2006	p+p	200	88.6pb^{-1}
		p+p	62.4	1.05pb^{-1}
Run-7	2006-2007	Au+Au	200	7.25nb^{-1}
		Au+Au	9.2	small
Run-8	2007-2008	d+Au	200	437nb^{-1}
		p+p	200	38.4pb^{-1}
		Au+Au	9.2	small
Run-9	2008-2009	p+p	500	110pb^{-1}
		p+p	200	114pb^{-1}
		pp2pp	200	0.6nb^{-1}
Run-10	2009-2010	Au+Au	200	10.3nb^{-1}
		Au+Au	62.4	$544 \mu\text{b}^{-1}$
		Au+Au	39	$206 \mu\text{b}^{-1}$
		Au+Au	7.7	$4.23 \mu\text{b}^{-1}$
		Au+Au	11.5	$7.8 \mu\text{b}^{-1}$
Run-11	2010-2011	p+p	500	166pb^{-1}
		Au+Au	19.6	$33.2 \mu\text{b}^{-1}$
		Au+Au	200	9.79nb^{-1}
		Au+Au	27	$63.1 \mu\text{b}^{-1}$
Run-12	2011-2012	p+p	200	74pb^{-1}
		p+p	500	277pb^{-1}
		U+U	193	$736 \mu\text{b}^{-1}$
		Cu+Au	200	27nb^{-1}
Run-13	2012-2013	p+p	500	1.04fb^{-1}
Run-14	2013-2014	Au+Au	14.5	$44.2 \mu\text{b}^{-1}$
		Au+Au	200	43.9nb^{-1}
		h+Au	200	134nb^{-1}

At RHIC (STAR) [15], Pioneering High Energy Nuclear Interaction experiment (PHENIX) [16], Broad RAnge Hadron Magnetic Spectrometers (BRAHMS) [17], and PHOBOS (not an acronym, but named after moon of Mars) [18] located at 2 o'clock, 6 o'clock, 8 o'clock, and 10 o'clock, respectively, as shown in Fig. 2.3. There is one empty hall at 12 o'clock position. The STAR and PHENIX experiments are still operational at RHIC, while the other two small experiments PHOBOS and BRAHMS have completed their operation in the year 2005 and 2006, respectively.

2.3 The STAR Detector

The Solenoidal Tracker at RHIC (STAR) [15] tracks thousand of particles produced by ion collisions at RHIC. It is one of the two large heavy-ion experiments (the other is PHENIX) at RHIC and has a wide acceptance and ability to detect high multiplicity events. STAR detector is used to measure many observables of nuclear collisions over a wide rapidity (y) and azimuthal (ϕ) range to understand the space-time evolution of the collision process in ultra-relativistic heavy-ion collisions. The initial parton distribution functions of the incident hadron/nuclei through p+p and p+A interactions is also studied using this detector. In addition to the heavy-ion physics program in STAR, there is also an ongoing spin physics program to study the spin structure of the nucleon from polarised p+p collisions.

The STAR detector consists of various detector subsystems for high precision tracking, momentum analysis, and particle identification at mid-rapidity. The schematic picture of STAR detector along with different subsystems are shown in Fig. 2.4. Figure 2.5 shows the cross-sectional view of the STAR detector [15, 19]. The whole detector is enclosed in a solenoidal magnet that provides a uniform magnetic field parallel to the beam direction. The magnetic field strength can be varied from 0 to a maximum value of 0.5 T. Data set used for this work were obtained at magnetic field of 0.5 T. The uniform magnetic field provides

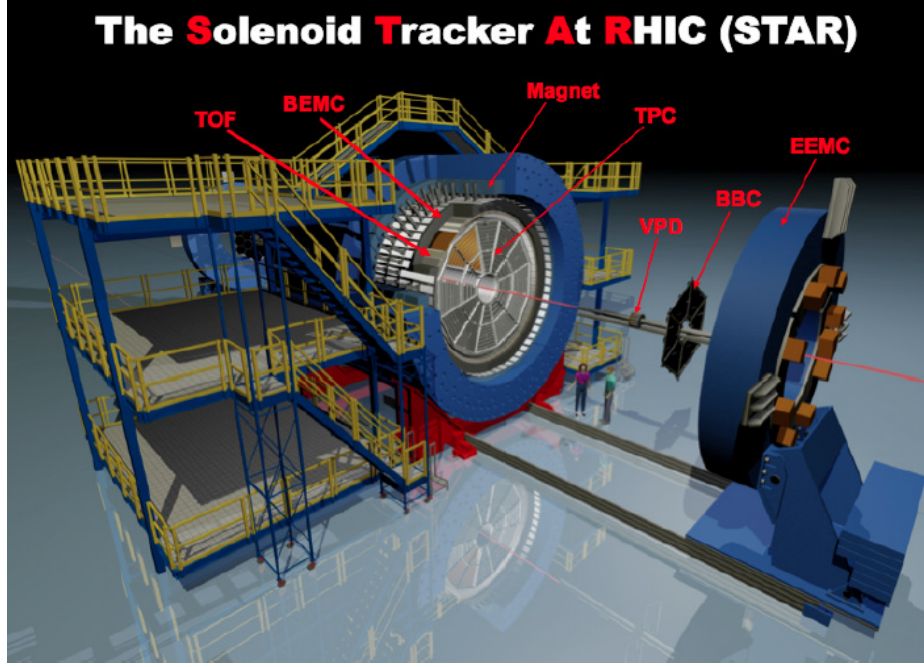


Figure 2.4: Three dimensional view of STAR detector system [19].

ability to perform momentum measurements of charged particles. The large acceptance of STAR detector makes it particularly well suited for the measurement of event-by-event correlations in heavy-ion collisions and for the detection of hadron jets. STAR local coordinate system [20] is defined with the right-handed Cartesian axes, where x points parallel to the ground and away from the center of RHIC, y points directly up from the ground and, therefore, z points west at STAR. The STAR experiment consists of different types of detectors, each specialising in detecting certain types of particles or characterising their motion. The Time Projection Chamber (TPC) [21] is the heart of the STAR detector, which is used for the charged particle tracking and particle identification. The TPC is 4.2 m long and covers a pseudo-rapidity range of $|\eta| \leq 1.8$ for tracking with complete azimuthal symmetry ($\Delta\phi = 2\pi$). Two Forward Time Projection Chambers (FTPC) [22] are installed on either side of the TPC in forward and backward rapidity, covering $2.5 < |\eta| < 4$ and with complete

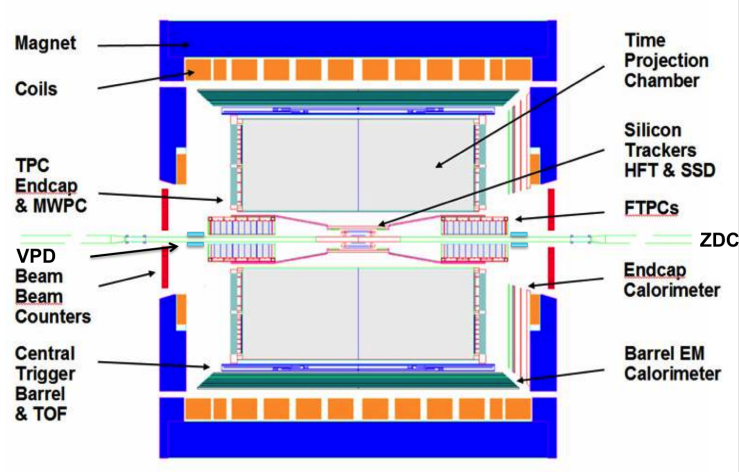


Figure 2.5: A cut-away side view of the STAR detector.

azimuthal coverage to extend the tracking to the forward region. In 2010, a barrel Time-of-Flight (TOF) detector [23] based on Multi-gap Resistive Plate Chamber (MRPC) [24] technique was fully installed in STAR. The TOF consists of a total of 120 trays spanning a pseudo-rapidity range $|\eta| \leq 0.9$ with full azimuthal coverage. Two upgraded Pseudo Vertex Position Detectors [23], each 5.7 m away from the TPC center along the beam line are used as the trigger system for the TOF detector and provides the start timing information for TOF. In STAR, the electromagnetic particles have been detected using a set of calorimeters, the full Barrel Electromagnetic Calorimeter (BEMC) [25] covers $|\eta| < 1$ and Endcap Electromagnetic Calorimeter (EEMC) [26] covers $1 < \eta \leq 2$. Both these detectors are azimuthally symmetric. These calorimeters include Shower Maximum Detector (SMD) to distinguish between energy deposited by single photons or from photon pairs arising from neutral pion (π^0) or η meson decays. The EEMC can also be employed to provide prompt charged particle signals essential to discriminate against pile-up tracks in TPC. In order to extend STAR's particle identification capabilities further into the heavy flavour domain, the Heavy Flavor Tracker (HFT) [27] was partially installed at the center of the STAR TPC in 2014. The Zero Degree Calorimeters (ZDCs), Beam Beam Counters (BBCs), and upgraded

Pseudo Vertex Position Detectors (VPDs) are used for event triggering.

The TPC and TOF are the main detectors, relevant to the analysis presented in this thesis.

In the next subsections, we describe those subsystems and the trigger system in detail.

2.3.1 Time Projection Chamber

TPC is a particle detector invented by an American physicist David R. Nygren, at LBNL, USA in the year 1970. The first major application of TPC was in the PEP-4 detector which studied 29 GeV electron-positron collisions at the PEP storage ring at SLAC. Since then

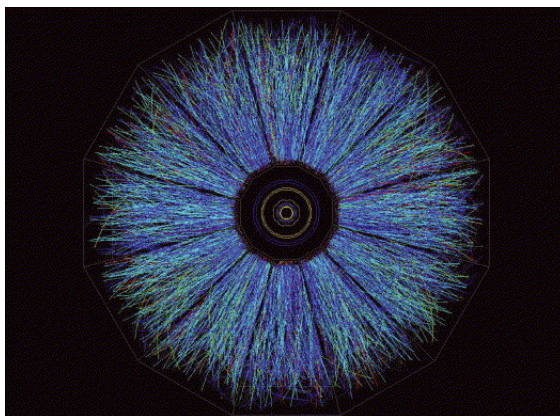


Figure 2.6: Beam's eye view of a central event in the STAR TPC [28].

TPCs have been used in a number of experiments starting from elementary collisions to heavy-ion collisions. It records the charged particles, provides 3-dimensional momentum information on points along a track and at the same time it provides energy loss information which can be used for particle identification. In STAR, TPC [21] is the primary tracking device. It covers a pseudo-rapidity region $|\eta| < 1.8$ with full azimuth ($0 < \phi < 2\pi$). Using TPC, the charged particle's momenta can be measured from 100 MeV/c to 30 GeV/c and identify them over a momentum range from 100 MeV/c to greater than 1 GeV/c. Figure 2.6 shows beam's eye view of a central event in the STAR TPC.

2.3.1.1 Technical Design

The TPC is a 4.2 m long cylinder having diameter of 4 m. The whole detector is enclosed in a solenoidal magnet that provides a uniform magnetic field of maximum value 0.5 T parallel to the beam direction and bends the tracks of the charged particles coming from a collision. The track curvature is used to determine the momenta and the charge sign of the outgoing charged particles. Figure 2.7 shows the three dimensional schematic diagram of

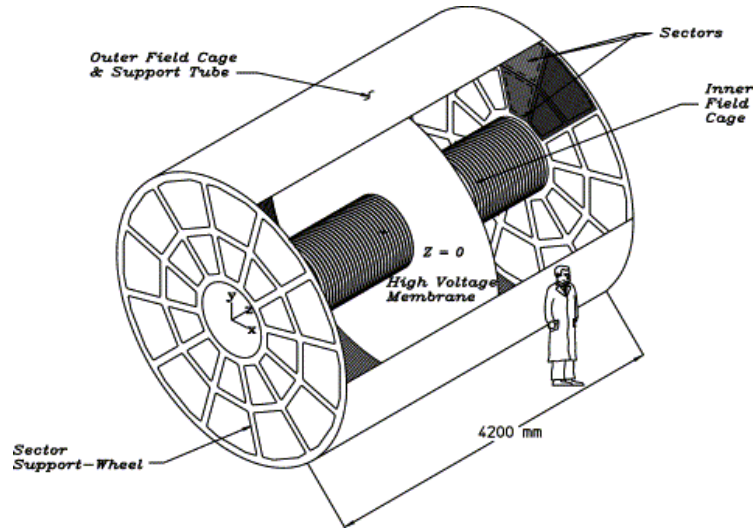


Figure 2.7: The three dimensional schematic diagram of the STAR TPC [21].

TPC in the STAR experiment. TPC consists of one outer field cage (OFC), one inner field cage (IFC) and two end caps. The OFC and IFC are used to provide a nearly perfect electric field in which the electrons drift to the anode plane. It avoids the distortions of the recorded tracks and also designed in such a way to contain the TPC gas and prevent it from being contaminated with outside air. The end caps providing the readout system are at ground potential act as anodes. A thin conductive central membrane (CM) made of 70 μm thick carbon coated kapton is located in the $x-y$ plane, which bisects the cylinder forming an east and west end of the TPC as shown in the Fig. 2.7. The CM is maintained at a voltage of

–28 kV with respect to the detection planes and acts as cathode. A uniform electric field of ~ 135 V/cm, pointing in $\pm z$ directions is maintained between the CM, concentric field-cage rings, and the readout end caps. A chain of 183 resistors and equipotential rings along the concentric field cage cylinders help to maintain this uniformity of the electric field which is critical for uniform electron drift [21]. An outer support hoop mounted on the outer field

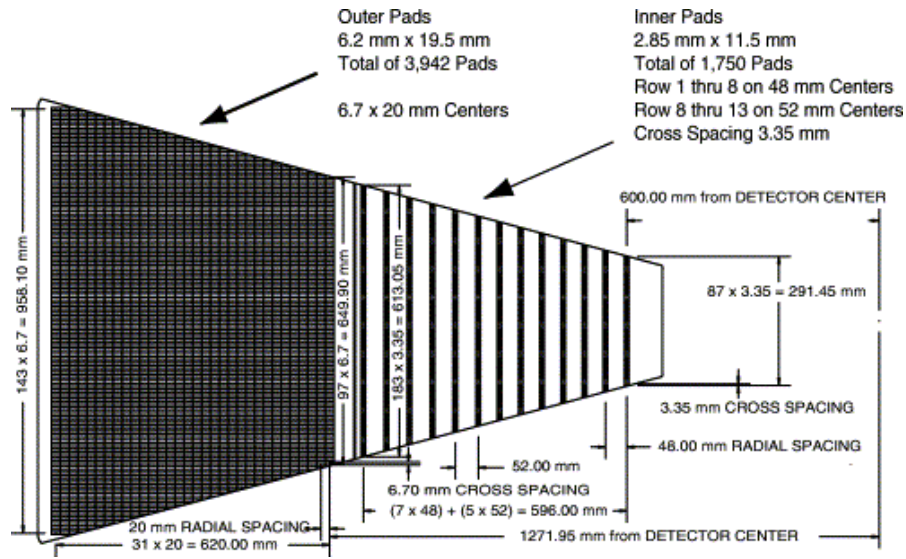


Figure 2.8: One sector of the TPC anode plane with the inner and outer subsectors and their respective padrows [21].

cage keeps the CM taut and secured under tension. There are 36 Al stripes which act as targets emitting electrons for the TPC Laser Calibration System and are attached on each side of the CM. TPC is filled with P10 gas, a mixture of Argon and Methane (90% Ar + 10% CH₄) and regulated at a pressure of 2 mbar above the atmospheric pressure. The P10 gas is chosen due to its fast drift velocity which peaks at a low electric field. Operating on the peak of the velocity curve makes the drift velocity stable and insensitive to small variations in temperature and pressure. The design of the detector becomes simpler because of lower field strengths which require lower voltages. The drift velocity of electron through

P10 gas is relatively fast, ~ 5.5 cm/ μ s at 130 V/cm drift field.

The TPC readout system is based on the Multi-Wire Proportional Chamber (MWPC). The MWPC, located at the readout endcaps, consists of the pad plane and three wire planes. The complete readout system is divided into 24 sectors, having 12 readout sectors for each endcap. Each sector is further divided into inner and outer subsectors characterised by a change in the readout pad-row geometry. Each inner sector contains a large number of small pads, distributed in 13 pad rows, to maximize the position and two-track resolution in a region with high particle density. The pads of the outer sectors are densely packed in 32 rows per sector to optimize the measurement of energy loss by ionisation in a region with lower particle densities [29]. Therefore, a track in the TPC can have a maximum of 45 hits if it crosses all 45 pad rows. Figure 2.8 represents one full sector of the anode pad plane.

2.3.1.2 Track Reconstruction

The TPC track can be reconstructed by identifying the three dimensional space coordinate points (x , y , z). When a charged particle traverses through the TPC volume, it ionizes the gas atoms and molecules along its path leaving behind a cluster of electrons. The signal in adjacent pads (along a single pad row) provides the information of $x - y$ position of each cluster. The z -position of the cluster is determined by dividing the drift time, measured from the point of origin of the cluster to the endcap, by the average drift velocity. After finding the positions of the clusters, a Time Projection Chamber Tracker (TPT) algorithm is used to reconstruct the tracks by a helical trajectory fit. Each track is a helix to first-order, but there can be deviations from the helical shape due to energy loss in the gas and multiple Coulomb scattering. To find a global track, the resulting track information collected from the TPC together with additional tracking information from other inner detectors are then refit by application of the Kalman Fit Method [30]. Extrapolating the trajectories of the

reconstructed global tracks back to the origin, the z-position of the primary collision vertex is determined. If a global track has a distance of closest approach (DCA) (with respect to the primary vertex) less than 3 cm, then the track is refitted to include the primary vertex as an additional space point and those tracks are called primary tracks. The reconstruction efficiency for primary tracks depends on the track quality cuts, particle type, and track multiplicity.

2.3.1.3 Particle Identification

Charged particles can be identified using TPC through their energy loss (dE/dx) due to interactions in the medium inside the TPC. If a particle travels through the entire volume of the TPC, it will provide 45 dE/dx points on the 45 pad rows. However, due to the large ionisation fluctuations and the short length over which the particle energy loss is measured, we use the most probable dE/dx instead of the average dE/dx . This is done by calculating the truncated mean of the 70% of the clusters and removing the remaining 30% of the largest ionisation clusters. The ionisation energy loss can be described by the Bichsel function [31], which is an extension of the Bethe-Bloch formula [32]. For a given track momentum and particle mass, it is given by,

$$-\frac{dE}{dx} = K z^2 \frac{Z}{A} \frac{1}{\beta^2} \left[\frac{1}{2} \ln \left(\frac{2m_e c^2 \beta^2 \gamma^2 T_{\max}}{I} \right) - \beta^2 - \frac{\delta^2}{2} \right], \quad (2.2)$$

where z is the integral charge of the particle, K is a constant, Z is the atomic number of the absorber, A is the atomic mass of the absorber, m_e is the electron mass, c is the speed of light in vacuum, I is the average ionisation energy of the material, T_{\max} is the maximum kinetic energy that can be given to a free electron in an interaction, δ is a correction based on the electron density, and $\beta\gamma = p/mc$, where p is the momentum and m is the mass of the charged particle. The equation shows that dE/dx is mass dependent and hence useful

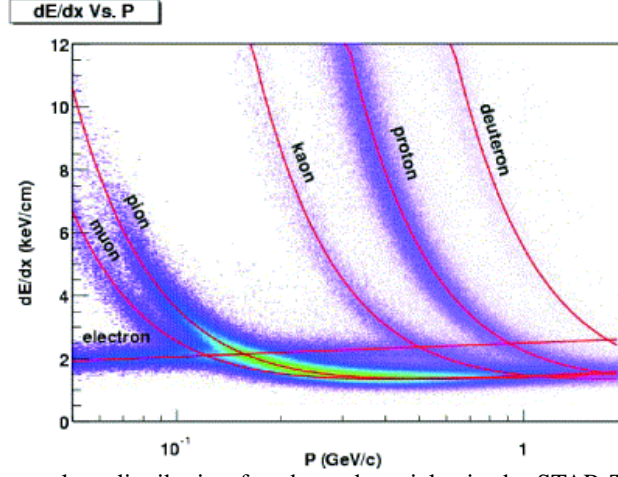


Figure 2.9: The energy loss distribution for charged particles in the STAR TPC as a function of momentum [21].

in particle identification. The energy loss for primary and secondary particles in the TPC as a function of particle momentum is shown in Fig. 2.9. The red lines are the theoretical predictions from Bichsel function for different particle species and the bands represent the measured values of dE/dx . The TPC dE/dx resolution of around 7–8% allows identification of charged pions and kaons up to a transverse momentum of about 0.75 GeV/c. Protons and antiprotons can be identified up to about 1.1 GeV/c.

Quantitatively, the particle identification can be described by the variable $n\sigma$, which corresponds to the standard deviation of a Gaussian between the measured track and its expected value. It is defined as,

$$n\sigma_i = \frac{1}{R} \log \frac{\langle dE/dx \rangle_{\text{measured}}}{\langle dE/dx \rangle_{i|\text{expected}}}, \quad (2.3)$$

where i is the particle type (e.g., e, π , K, p), $\langle dE/dx \rangle_{\text{measured}}$ is the measured energy loss of a charged particle track, $\langle dE/dx \rangle_{i|\text{expected}}$ is the expected mean energy loss of particle i at a given momentum, and R is the dE/dx resolution which is found to range between 6%

to 10%. Similarly, another variable z is also used to identify the particles and is defined as

$$z_i = \ln \left(\frac{\langle dE/dx \rangle_{\text{measured}}}{\langle dE/dx \rangle_{i|\text{expected}}} \right), \quad (2.4)$$

where $\langle dE/dx \rangle_{\text{measured}}$ is the measured mean energy loss of a charged particle track and $\langle dE/dx \rangle_{i|\text{expected}}$ is the expected mean energy loss calculated using a Bichsel function for the given particle type i (e.g., e, π , K, p). z variable is used in the analysis presented in this thesis.

2.3.2 Space Charge Distortion in the TPC and GEM Monitor

The TPC has different potential sources of field distortions like space charge, grid leak which must be considered and corrected for in the calibration procedures. The slow-drifting positively charged ions build up in the gas volume generated from standard operation of the TPC and it varies with the quantity of charged particles traversing through the TPC. Therefore, increase in the luminosity of the collider and/or the multiplicity of charged particles emitted in the collisions will increase the amount of the positive charge seen in the drift chamber [33]. The variations in this “space charge” can occur on time scales of ~ 0.5 s, the

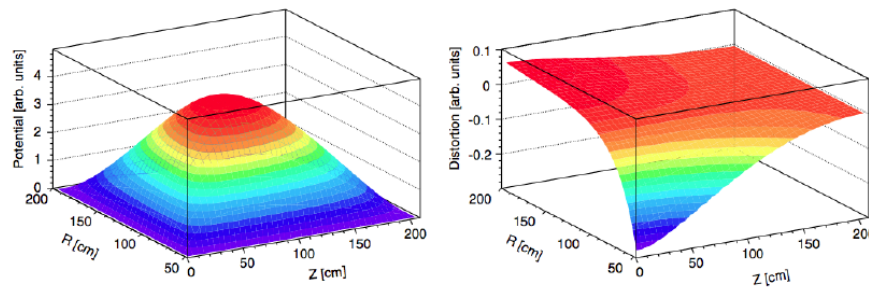


Figure 2.10: Simulated shape of the potential due to space charge in the TPC (left) and the azimuthal distortions of electron clusters (right) caused by drifting through that potential as a function of radius R and drift Z . The cathode is at $Z = 0$, and electron clusters drift to the endcaps at high Z [33].

time it takes for the positive ions to drift the length of the chamber which is relatively long compared to the drifting ionised electrons ($\sim 40 \mu\text{s}$) and therefore, affects multiple colliding events. These positive ions distort the electric field created by the TPC hardware and displaces the position of the reconstructed TPC tracks. The simulated potential created by this positive charge is shown in Fig. 2.10. The distortion is azimuthal and has the effect of rotating the tracks in the transverse plane midway along their path through the TPC. The build up of positive charge inside the TPC increases with increasing luminosity. However, this is not the only source of distortions, there are other sources which include grid leak. The STAR TPC was designed with a gated grid to prevent the ions created in the high gain region around the anode wires from leaking into the TPC main volume and drifting across to the cathode. With the recent increased luminosities, this method become ineffective in completely stopping the positive ions. This causes a thin sheet of positive charge to leak around the edge of the grid between the inner and outer sectors ($\sim 119 \text{ cm}$ from the detector center). Most often distortions on the hit positions are found to be at the sector boundaries. Nowadays, RHIC is taking data with higher luminosities to achieve various physics goals.

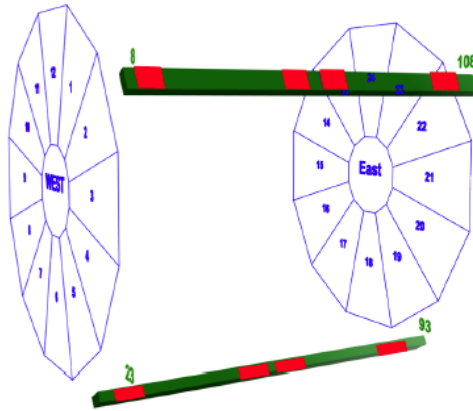


Figure 2.11: The schematic diagram of GMT positions (red box) in TOF trays placed outside TPC [34].

Therefore, it is necessary to properly account for the TPC track distortions and move them back to their original position. These distortion corrections are done through TPC calibrations. Earlier a model was used to correct the space charge distortion corrections at radii smaller than the inner radius of TPC and no points outside TPC were available to check the corrections. Therefore, to get reference point outside the TPC for these corrections, GEM based Monitor for TPC (GMT) tracking calibrations was proposed [34]. A total of eight GMT modules have been installed replacing few modules in four TOF trays 8, 23, 93, and 108 near $|\eta| \sim 0$ and $|\eta| \sim 1$ at $\phi \sim 30^\circ$ and $\phi \sim 300^\circ$ on the east and west sides at the same radius as the TOF in STAR in February 2013. The schematic diagram of GMT positions (red box) in TOF trays placed outside TPC is shown in Fig. 2.11. The details about GMT and its performance with cosmic ray will be discussed in the later part of this thesis in chapter 6.

2.3.3 Time-of-Flight and pseudo Vertex Position Detector

The TOF [23] system was mainly used to extend the particle identification (PID) capabilities of the experiment to the higher momentum region. It consists of two detectors, the pseudo Vertex Position Detector (pVPD) and the Time-of-Flight (TOF). The pVPD covers a pseudo-rapidity range $4.24 \leq \eta \leq 5.1$ and has 19 channels on the east side and 19 channels on the west side. It measures the start time of the event for TOF and can also provide the independent z -component of the vertex. It consists of two identical detector assemblies which are placed very close to the beam pipe. They are positioned outside of the STAR magnets, one on each side of STAR, at a $|Z|$ position around 5.7 m. The TOF is positioned inside the STAR magnet immediately outside of the TPC and measures the stop time. It consists of a total of 120 trays with 60 on east side and 60 on west side that cover the full azimuth and have a pseudo-rapidity range $|\eta| < 0.9$. STAR has performed the upgrade of full barrel TOF detector based on the MRPC technology [24] in the year 2010 and each tray

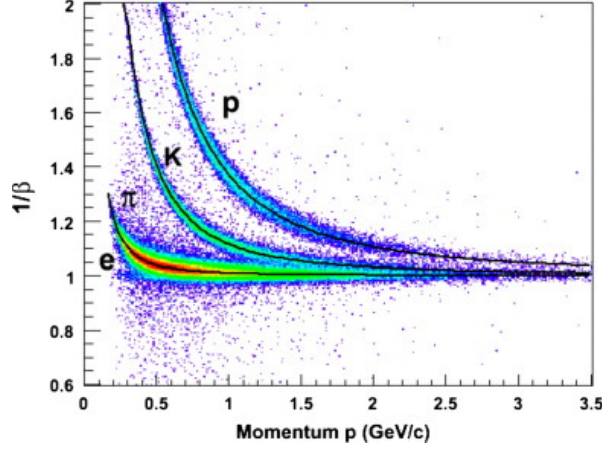


Figure 2.14: TOF $1/\beta$ as a function of momentum from p+p collisions at $\sqrt{s} = 200$ GeV [35].

of associated mass,

$$m^2 = p^2 \left(\frac{1}{\beta^2} - 1 \right) \quad (2.5)$$

Figure 2.14 shows $1/\beta$ from TOF measurement as a function of momentum (p) in p+p collisions at $\sqrt{s} = 200$ GeV for e, π , K, and p [35]. This shows the PID capability of TOF subsystem at higher momentum. Using TOF π^\pm , K^\pm , p, and \bar{p} can be separated up to $p_T = 3.0$ GeV/c.

2.3.4 Trigger Detectors

The STAR is designed to detect charged and neutral particles produced at RHIC. The trigger system looks at every RHIC crossing and decide whether or not to accept that event and initiate the recording of the data. The STAR data acquisition system (DAQ) [36] is fast, flexible, and receives data from multiple detectors which have a wide range of readout rates. The interaction rates at RHIC for the beams of highest luminosity can approach ~ 10 MHz. The major part of the STAR data is provided by the slow detectors such as TPC, FTPC, and EMC (Electro Magnetic Calorimeters), which can operate at rates of ~ 100 Hz

and not all events can be recorded by the DAQ. Therefore, the STAR trigger system [28] is based on input from fast detectors to control the selection of events for the much slower tracking detectors in order to record data. In addition, the trigger is used to select events with rare or specific signals of interest to increase the recorded statistics of these events. The ZDC, BBC, BEMC, and EMC are the main triggering detectors for STAR and these are described below. Figure 2.15 shows the schematic diagram of all the trigger detectors and the way they fit together in the STAR system [37].

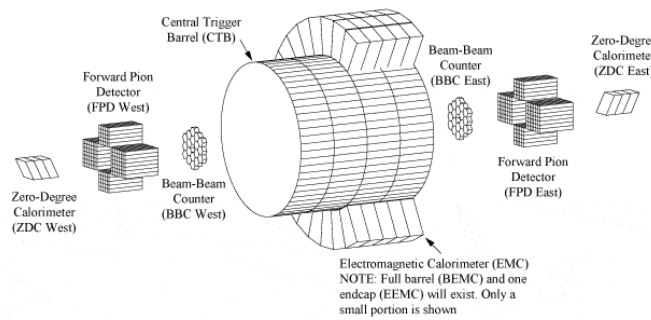


Figure 2.15: The schematic diagram of all the trigger detectors fit together in the STAR system [37]. Now Central Trigger Barrel (CTB) is replaced by the barrel TOF system and Forward Pion Detector (FPD) is preceded by Forward Meson Spectrometer (FMS) at STAR.

2.3.4.1 Zero Degree Calorimeter

To ensure comparability of the results all of the four heavy-ion experiments at RHIC, utilise one common detector subsystem, the Zero Degree Calorimeter (ZDC) [38]. A pair of ZDCs for each experiment is used to measure the energy of spectator neutrons [39] residing within a small solid angle from the beam to provide universal characterisation of the collision centrality across RHIC experiments. The ZDCs are hadronic calorimeters and are placed at ± 18 m from the center of the STAR detector and are at zero degrees ($\theta < 2$ mrad) with respect to the beam direction. Since the charged particles are deflected by the dipole magnets from the zero degree region, are not measured in the ZDCs, only the neutrons

can reach the ZDCs. The real collisions are distinguished from the background events by selecting events with ZDC coincidence from the two beam directions. This makes ZDC as a useful event trigger and a luminosity monitor in steering the beams to the collision point. In addition to the beam monitoring and triggering, ZDCs are also very useful locating interaction vertices by using the time delay between the coincidences. A shower maximum detector was installed between the first and second modules of each existing STAR ZDC to study the spatial distribution of the neutron hits on the transverse plane of the ZDCs. The addition of ZDC-SMD to the STAR experiment enhances its capability in different areas of physics such as anisotropic flow, ultra-peripheral collisions, and spin physics [40].

2.3.4.2 Beam-Beam Counter

The Beam Beam Counters (BBCs) are used as a measure of luminosity, triggering, and local polarimetry. It consists of hexagonal scintillating tiles mounted outside on the east and west pole tips of the STAR magnet at about 3.5 m from the center of nominal interaction region [41]. It covers full azimuth and pseudo-rapidity range of $2.2 < |\eta| < 5.0$. The inner ring consists of 18 small scintillating tiles and the outer ring consists of 18 large scintillating tiles. In p+p collisions, the BBC coincidence provides a baseline minimum bias trigger for the STAR detector. The timing difference between the two counters (east BBC and west BBC) is used to get information of the primary vertex position. The small tiles of BBC are also used to reconstruct the first-order event plane for flow analysis.

2.3.4.3 Electromagnetic Calorimeters

The main STAR calorimeters comprise a full Barrel Electromagnetic Calorimeter (BEMC), single Endcap Electromagnetic Calorimeter (EMC) plus a Forward Meson Spectrometer (FMS). The electromagnetic calorimeters allow STAR to trigger on and study rare and high p_T processes such as jets, leading hadrons, direct photons, and heavy quarks. They

provide large acceptance for photons, electrons along with neutral pions, and η mesons in all collision systems from polarised p+p to Au+Au collisions. These are also used for event characterisation in heavy-ion collisions including ultra-peripheral collisions. Electromagnetic calorimeters (BEMC and EEMC) are discussed below.

Barrel Electromagnetic Calorimeters: The BEMC designed largely for heavy-ion studies with full tracking coverage from the TPC and used for the detection of electromagnetically interacting particles, such as electrons and photons, from their energy deposition in the detector [25]. It completely surrounds the STAR TPC covering an area of nearly 60 m^2 and the pseudo-rapidity region, $|\eta| < 1$, with full azimuthal angle. It is basically a sampling calorimeter consisting of alternate layers of lead and scintillator planes. It has 20 layers of lead plates and 21 layers of scintillator. The full BEMC consists of 120 calorimeter modules, each covering 6° (~ 0.1 radian) in $\Delta\phi$ and 1.0 unit in $\Delta\eta$. The modules are positioned with 60 on the west end and 60 on the east end. Each module is further segmented into 40 towers, 2 in ϕ and 20 in η making each tower covering of 0.05×0.05 in $\eta - \phi$ space. Therefore, the full BEMC consists of a total of 4800 towers projecting back to the center of the interaction region. The deposition of energy in the individual towers, or a sum of towers, can be used to trigger on high p_T events [25]. Each tower consists of an alternating lead-scintillator stack and a SMD located about ~ 5 radiation lengths (X_0) from the front of the lead-scintillator stack. The SMD is used to provide fine spatial resolution in a calorimeter. Using BEMC, it is possible to reconstruct π^0 at relatively high p_T ($\approx 25\text{--}30 \text{ GeV}/c$) and also to identify single electron and pairs in dense hadron backgrounds from the heavy vector mesons like W and Z bosons decays.

Endcap Electromagnetic Calorimeters: The EEMC is primarily related to spin physics and have only partial TPC coverage. It is mounted on the inside of the west STAR magnet

pole tip. It covers the pseudo-rapidity region, $1 \leq \eta \leq 2$, with full azimuthal angle, supplementing the BEMC. There are 720 projective towers in the endcap and just like the BEMC they can be used for triggering purposes. Within its acceptance, it enhances STAR's capability to detect photons, π^0 , η , to identify electrons, positrons, and to trigger on high energy particles. The design of EEMC includes a SMD optimised to discriminate between photons and π^0 or η mesons over the energy region 10–40 GeV. It also consists of pre-shower and postshower layers used to discriminate between electrons and hadrons. In addition, the EEMC also enhances the acceptance and triggering capabilities for jets in STAR.

Bibliography

- [1] D. A. Bromley, in *Treatise on Heavy-Ion Science*, vol. 1, 3 (1984).
- [2] F. Karsch, *Nucl. Phys. A* 698, 199 (2002).
- [3] R. Lacasse (E877 Collaboration), *Nucl. Phys. A* 610, 153c (1996).
- [4] K. Redlich, CERN-TH/2001-342.
- [5] T. Matsui and H. Satz, *Phys. Lett. B* 178, 416 (1986).
- [6] G. Bunce, N. Saito, J. Soffer, and W. Vogelsang, *Ann. Rev. Nucl. Part. Sci.* 50, 525 (2000); W. Vogelsang, *Pramana* 63, 1251 (2004).
- [7] L. C. Bland, *AIP Conf. Proc.* 675, 98 (2003), M. Stratmann, arXiv:0211317.
- [8] M. Harrison, T. Ludlam, and S. Ozaki, *Nucl. Instr. Meth. A* 499, 235 (2003); H. Pernegger, *Nucl. Instr. Meth. A* 478, 68 (2001).
- [9] J. Benjamin *et al.*, IEEE Particle Accelerator Conference (PAC99).
- [10] L. Ahrens *et al.*, IEEE Particle Accelerator Conference (PAC2001).
- [11] M. Anerella *et al.*, *Nucl. Instr. Meth. A* 499, 280 (2003).
- [12] E. C. Aschenauer *et al.*, arXiv:1409.1633; R. G. Milner, *AIP Conf. Proc.* 698, 806 (2004).

- [13] R. Fernow, Introduction to Experimental Particle Physics (Cambridge University Press, Cambridge, 1986).
- [14] <http://www.agsrhichome.bnl.gov/RHIC/Runs/>.
- [15] K. H. Ackermann *et al.* (STAR Collaboration), Nucl. Instr. Meth. A 499, 624 (2003).
- [16] K. Adcox *et al.* (PHENIX Collaboration), Nucl. Instr. Meth. A 499, 469 (2003).
- [17] M. Adamczyk *et al.* (BRAHMS Collaboration), Nucl. Instr. Meth. A 499, 437 (2003).
- [18] B. B. Back *et al.* (PHOBOS Collaboration), Nucl. Instr. Meth. A 499, 603 (2003).
- [19] 3D picture of STAR detector by Alex Schmah and Maria.
- [20] <https://drupal.star.bnl.gov/STAR/starnotes/public/csn0121> (1996).
- [21] M. Anderson *et al.*, Nucl. Instr. Meth. A 499, 659 (2003); H. Wieman *et al.*, IEEE Trans. Nuc. Sci. 44, 671 (1997); J. Thomas *et al.*, Nucl. Instr. Meth. A 478, 166 (2002).
- [22] K. H. Ackermann *et al.*, Nucl. Instr. Meth. A 499, 713 (2003).
- [23] W. Llope *et al.*, Nucl. Instr. Meth. A, 522, 252 (2004); W. J. Llope (STAR TOF Group), Nucl. Instr. Meth. A, 241, 306 (2005).
- [24] B. Bonner *et al.*, Nucl. Instr. Meth. A, 508, 181 (2003); E. C. Zeballos *et al.*, Nucl. Instr. and Meth. A 374, 132 (1996).
- [25] M. Beddo *et al.*, Nucl. Instr. Meth. A 499, 725 (2003).
- [26] C. E. Allgower *et al.*, Nucl. Instr. Meth. A, 499, 740 (2003).
- [27] <https://drupal.star.bnl.gov/STAR/starnotes/public/sn0600>.

- [28] F. S. Beiser *et al.*, Nucl. Instr. and Meth. A, 499, 762 (2003).
- [29] M. Anderson *et al.*, Nucl. Instr. Meth. A 499, 679 (2003).
- [30] D. Liko, STAR Note 00087, 1 (1992).
- [31] H. Bichsel, Nucl. Instr. Meth. A 562, 154 (2006).
- [32] W. M. Yao *et al.*, J. Phys. G: Nucl. Part. Phys. 33, 1 (2006).
- [33] G. V. Buren *et al.*, Nucl. Instr. Meth. A 566, 22 (2006).
- [34] GMT proposal, “GEM Monitoring of TPC Tracking Calibration (GMT) in STAR”,
<http://drupal.star.bnl.gov/STAR/system/files/Proposal-to-Install-GEM-Chambers-GMT.pdf>.
- [35] W. J. Llope, Nucl. Instr. Meth. 661, S110 – S113 (2012).
- [36] A. Ljubicic *et al.*, IEEE Trans. Nucl. Sci., 99, NS-47 (2000); J. M. Landgraf *et al.*,
 Nucl. Instr. and Meth. A, 499, 758 (2003).
- [37] <http://www.star.bnl.gov/public/trg/trouble/operating-trigger/>.
- [38] C. Adler *et al.*, Nucl. Instr. Meth. A 470, 488 (2001).
- [39] H. Appelshauser *et al.*, Eur. Phys. J. A 2, 383 (1998).
- [40] B. I. Abelev *et al.* (STAR Collaboration), Phys. Rev. Lett. 101, 252301 (2008);
 STAR ZDC-SMD proposal, STAR Note SN-0448 (2003).
- [41] J. Kiryluk, Local polarimetry for proton beams with the STAR beam beam counters,
 718 (2005).

Chapter 3

Identified Particle Production in Au+Au Collisions at $\sqrt{s_{\text{NN}}} = 27 \text{ GeV}$

In this chapter, we discuss the mid-rapidity transverse momentum (p_T) spectra, yields, and particle ratios of identified particles like pion, kaon, proton, and their corresponding antiparticles in Au+Au collisions at $\sqrt{s_{\text{NN}}} = 27 \text{ GeV}$. This data set was taken in the year 2011. The main detectors used for the analysis are the TPC and TOF of the STAR experiment.

3.1 Introduction

Relativistic heavy-ion collisions provide an opportunity to study strongly interacting nuclear matter at different thermodynamic conditions. QCD, a fundamental theory to describe the interactions of quarks and gluons, predicts a transition from hadronic matter to a de-confined state of quarks and gluons called QGP phase at high temperature and/or high energy density [1]. The QCD phase diagram is characterised by the temperature (T) and the baryon chemical potential (μ_B) or the (net) baryon density (n_B), and it contains the

information about the separation between the QGP and hadronic phases [2]. Assuming a thermalized system is reached in heavy-ion collisions, both T and μ_B can be varied by changing the collision energy. Finite temperature lattice QCD calculations [3] predict a cross-over from hadronic to QGP phase at vanishing μ_B and large T , while several QCD-based calculations [4] show that at a lower T and larger μ_B a first-order phase transition may take place. The point in the QCD phase diagram, where the first-order phase transition ends would be the QCD critical point [5]. The QGP phase has been confirmed to exist by the experiments at both RHIC and LHC. The existence of a critical point and first-order phase transition needs to be confirmed experimentally at high μ_B . The BES-I program at RHIC has been carried out with the specific aim to explore several features of QCD phase diagram such as to search for the phase boundary and the location of QCD critical point. In the BES-I program, gold nuclei are collided at several center-of-mass energies in order to get different T and μ_B points in the phase diagram.

The STAR detector, due to its large uniform acceptance and excellent particle identification capabilities, has measured a variety of hadron species (π^\pm , K^\pm , p , \bar{p} , K_S^0 , Λ , $\bar{\Lambda}$, Ξ^- , $\bar{\Xi}^+$) produced in Au+Au collisions at $\sqrt{s_{NN}} = 7.7, 11.5, 19.6, 27$, and 39 GeV. These data are part of the BES-I program at RHIC and provide an opportunity to measure the p_T spectra, yields, and particle ratios of the particles produced in the collisions. The corresponding measurements allow to study the freeze-out properties and dynamics of heavy-ion collisions.

In this chapter, we discuss the identified p_T spectra, $\langle p_T \rangle$, dN/dy , and particle ratios as a function of energy and centrality in Au+Au collisions at $\sqrt{s_{NN}} = 27$ GeV. Similar measurements at other BES-I center-of-mass energies, $\sqrt{s_{NN}} = 7.7, 11.5, 19.6$, and 39 GeV are reported in Ref. [6].

3.2 Procedure for Data Analysis

Before going to the detailed discussion, an overview on the analysis framework is presented below. Following are the steps to obtain the final corrected p_T spectra;

1. Good events and tracks are selected on the basis of some specific quality cuts.
2. Measurements of the ionisation energy loss, dE/dx , of charged tracks in the TPC gas and TOF information from TOF, are used to identify pion, kaon, proton and their corresponding antiparticles.
3. A multi-Gaussian fit is performed to the normalised dE/dx distributions to extract the raw yields of different particle species from TPC. The raw yields from TOF are obtained using the predicted mass-square method.
4. In case of kaon and proton, each track is corrected for energy loss in the detector material.
5. The extracted raw yield is further corrected for track reconstruction efficiency and acceptance depending on particle type and centrality.
6. The pion yield is again corrected for weak decay and background contamination.
7. Systematic errors are estimated for particle spectra.

At the end, final corrected spectra are obtained and one can use this to extract the bulk properties of the medium formed in heavy-ion collisions which will be discussed in the results section.

3.3 Data Set, Trigger, and Analysis Cuts

Before using the selected dataset, at first the detector responses are stored in STAR raw data format for each run [7]. The STAR software reconstruction after applying proper alignment and calibration for each detector subsystem, using a subset of the data, carries out to complete the momentum reconstruction and track projection. Finally, all the re-

constructed tracks and their detector-associated quantities are written to files called μ -Data Summary Tapes (μ -DSTs). The dataset used for the results presented in this chapter were collected from Au+Au collisions at $\sqrt{s_{NN}} = 27$ GeV using STAR detector [8] in the year of 2011. Triggering [9] is a method of selecting specific events from the data according to the physics we are interested in. A trigger is used in combination with a prescaler, which scales down the raw rate presented to the detector electronics to the rates that those detectors are capable of reading out. The prescaler also keeps the data recording rate below the maximum rate and allows a rare event to be recorded if it occurs. Rare events can be selected by using more sophisticated trigger configurations. The data for this study were taken using a minimum-bias trigger which includes the whole range of collisions from peripheral to central. The minimum-bias trigger was based on a coincidence of the signals from the ZDCs, VPDs, and/or BBCs [10]. The VPD determines the vertex z position by measuring the time difference between the signals detected at its east and west positions which will be shown later in this chapter.

3.3.1 Event Selection

Collisions take place over a wide range of values along the z -axis. The primary vertex position has been limited to select events with approximately uniform detector acceptance in pseudo-rapidity (η). The primary vertex for each minimum-bias event is determined by finding the best point of common origin of tracks measured in TPC. As the STAR TPC is a symmetric detector we wanted to select those events whose primary vertex was near the center of the TPC ($z = 0$). This would ensure that the average particle would travel the largest distance inside the TPC and hence are better reconstructed. The x and y positions of the event vertex position come from the track and vertex reconstruction. The z -coordinate of event vertex comes from the drift length = drift time \times drift velocity. The drift velocity is obtained by doing a TPC laser calibration before each run [11]. The events having primary

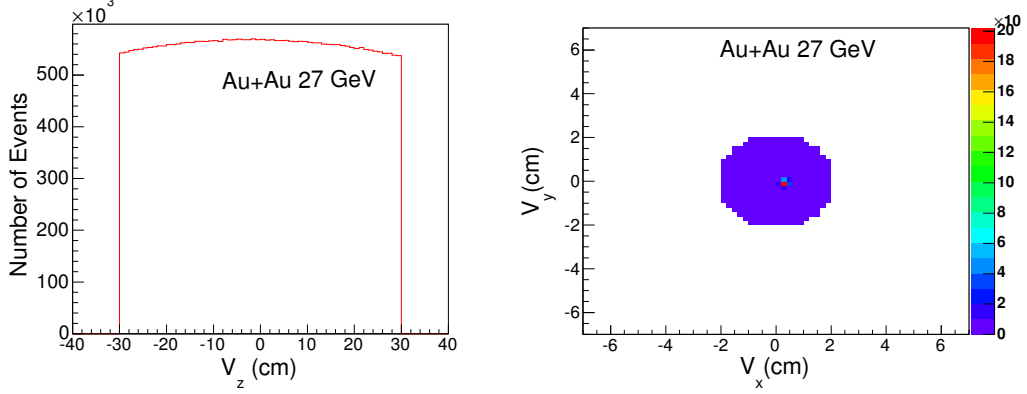


Figure 3.1: The vertex position distributions in Au+Au collisions at $\sqrt{s_{NN}} = 27$ GeV.

vertex z -position (V_z), within ± 30 cm from the center of the TPC along the beam line are selected for this analysis. In order to avoid getting events from beam-gas and beam-material interactions, we also required the events to be within the radius of 2 cm from the origin of the vertex distribution; a circular cut, defined as $V_r = \sqrt{V_x^2 + V_y^2}$, where V_x and V_y are the vertex positions along the x and y directions. The radius of the beam-pipe is 3.81 cm. With this vertex cut and minimum-bias trigger, 33 million good minimum-bias events are selected. The distributions of V_z and V_r are shown in Fig. 3.1 for Au+Au collisions at $\sqrt{s_{NN}} = 27$ GeV.

3.3.2 Track Selection

The optimal particle identification and momentum resolution depend upon the quality of the individual track measured in the TPC. Good tracks are selected by applying certain track quality cuts. To study identified particle spectra, we have chosen the particles that are produced only from the primary vertex. The distance of closest approach (DCA), between the track and the primary vertex, is required to be less than 3 cm. This ensures that the tracks come from the triggered event vertex and not from a secondary collision or interac-

Table 3.1: Event and track selection criteria for the analysis presented in this chapter.

Cut Variable	Value
$ V_z $	$< 30 \text{ cm}$
$ V_r $	$< 2 \text{ cm}$
$ y $	< 0.1
DCA	$< 3 \text{ cm}$
nHitsFit	≥ 25
nHitsFit/nHitsPoss	> 0.52
nHitsdEdx	≥ 15
p_T	$> 0.1 \text{ GeV}/c$

tion. Also the primary vertex is included as one of the fit point for track reconstruction. The tracks satisfying these criteria are generally called as primary tracks. A rapidity cut of $|y| < 0.1$ is used. Another criterion is the number of fit points cut defined as nHitsFit. Tracks traversing through the TPC volume can have a maximum of 45 hits. To avoid split tracks, we require at least 25 fit points associated with the track. The fraction of points used in the fit is required to be greater than 0.52 of the maximum fit points (nHitsPoss) to prevent over counting of split tracks (one track but counted as two). All tracks need to have $p_T > 0.1 \text{ GeV}/c$. The tracks having $p_T \leq 0.1 \text{ GeV}/c$ are avoided as these tracks can not traverse the entire TPC due to their large track curvature inside the solenoidal magnetic field of 0.5 T. In order to ensure that tracks have good $\langle dE/dx \rangle$ values, a condition is applied on the number of hits used to calculate $\langle dE/dx \rangle$ of the track, i.e. $\text{nHitsdEdx} \geq 15$.

These event and track cuts are varied in order to study the systematic errors. A summary of all these cuts used for the current spectra analysis is given in Table 3.1.

3.3.3 Centrality Selection

The collision centrality is related to the impact parameter (b) of the collision, which is the perpendicular distance between the centers of two colliding nuclei. A more central collision will have a smaller b (larger overlap area). In a nucleus-nucleus collision, b is of the order of fermi and cannot be measured experimentally. Therefore, some other experimental observables should be chosen that can correlate with b to define the centrality. That observable used in this thesis is the uncorrected reference multiplicity (N_{ch}), defined as the number of produced charged particles with at least 10 fit points, within $|\eta| < 0.5$ and having DCA within 3 cm. The $|\eta|$ requirement is necessary to ensure that the centrality estimate does not vary with the z -coordinate of the vertex. The DCA requirement eliminates most of the secondary interactions and decays. In STAR, a reference multiplicity correction is applied by identifying the bad runs, applying acceptance/efficiency correction of reference multiplicity for different z -vertex positions and performing low reference multiplicity correction for trigger inefficiencies for different z -vertices. The measured N_{ch} is compared with the simulated multiplicity density, which is calculated using the two-component model [12] and is defined as follows:

$$\frac{dN_{\text{ch}}}{d\eta} = n_{\text{pp}} \left[(1-x) \frac{N_{\text{part}}}{2} + x N_{\text{coll}} \right], \quad (3.1)$$

where n_{pp} is the average charged particle multiplicity in minimum-bias p+p collisions and x is the fraction of the hard component. N_{part} is defined as the total number of nucleons that undergo at least one collision. N_{coll} is the number of binary nucleon-nucleon collisions. The N_{part} , N_{coll} , and b can be calculated using a geometrical model of a nucleus-nucleus collision, which is named as Glauber model [13]. In a Monte Carlo Glauber calculation, the nuclei are independently generated and the nucleons are distributed inside the nucleus

according to the Wood-Saxon density profile:

$$\rho(r) = \frac{\rho_0}{1 + e^{\frac{r-r_0}{a}}}, \quad (3.2)$$

where ρ_0 is the normal nuclear density, r_0 is the nuclear radius, and a is the skin depth. Each nucleon in the nucleus is separated by a distance larger than minimum inter-nucleon separation. The nuclei generation and the nucleon-nucleon selection is repeated with a random selection of b . The extracted quantities can be studied as the fraction of the total geometrical cross-section (σ). The distributions of $d\sigma/db$, $d\sigma/dN_{\text{part}}$, and $d\sigma/dN_{\text{coll}}$ are determined. Each distribution is divided into bins corresponding to the fractions of the measured total cross-section of the used centrality bins and the average values of N_{part} and N_{coll} are extracted for each centrality bin. Systematic uncertainties on N_{part} and N_{coll} have been estimated by varying n_{pp} and x in the two-component model as well as varying the input parameters in the Glauber Monte Carlo simulation. The final errors are the quadrature sum of these individual systematic errors. In order to introduce event-by-event variation in multiplicity, the Negative Binomial Distributions (NBD) for multiplicities in p+p collisions have been convoluted with those of N_{part} and N_{coll} . The NBD distribution in multiplicity n has two parameters, n_{pp} and k , and is defined as,

$$P_{\text{NBD}}(n_{\text{pp}}, k; n) = \frac{\Gamma(n+k)}{\Gamma(n+1)\Gamma(k)} \frac{(n_{\text{pp}}/k)^n}{(n_{\text{pp}}/k+1)^{n+k}}, \quad (3.3)$$

where Γ is the Gamma function. The values $k = 1.65$ and $n_{\text{pp}} = 1.385$ are obtained by fitting the measured multiplicities with those from the simulation. The simulated multiplicity distribution is found not to be very sensitive to the k parameter. The x value is fixed at 0.12, obtained by extrapolating data at this energy from the PHOBOS collaboration [14]. The centrality is defined by calculating the fraction of the total cross-section obtained from the simulated multiplicity.

Table 3.2: Summary of centralities, average number of participating nucleons ($\langle N_{\text{part}} \rangle$), and average number of binary collisions ($\langle N_{\text{coll}} \rangle$) in Au+Au collisions at $\sqrt{s_{\text{NN}}} = 27$ GeV.

Centrality	$\langle N_{\text{part}} \rangle$	$\langle N_{\text{coll}} \rangle$
0–5%	343.3 ± 2.0	841.5 ± 28.4
5–10%	299.3 ± 6.2	693.9 ± 21.5
10–20%	233.6 ± 8.9	496.9 ± 26.2
20–30%	165.5 ± 10.7	311.6 ± 27.6
30–40%	114 ± 11.3	187.7 ± 25.4
40–50%	74.9 ± 10.3	106.4 ± 19.9
50–60%	46.7 ± 9.2	56.4 ± 14.7
60–70%	26.8 ± 7.8	27.5 ± 10.1
70–80%	13.8 ± 5.8	12.0 ± 6.3

In this analysis, the events are divided into nine centrality bins from central to peripheral, 0–5%, 5–10%, 10–20%, 20–30%, 30–40%, 40–50%, 50–60%, 60–70%, and 70–80%, which are defined by the percentage of the total multiplicity. N_{part} and N_{coll} are larger in central events than in peripheral events. The last centrality bin 80–100% is not used in this analysis because of its significant trigger bias and vertex inefficiency at low multiplicities, and the contamination from electromagnetic interactions. The average number of participating nucleons ($\langle N_{\text{part}} \rangle$), and average number of binary collisions ($\langle N_{\text{coll}} \rangle$) for different centralities in Au+Au collisions at $\sqrt{s_{\text{NN}}} = 27$ GeV are given in Table 3.2.

3.4 Particle Identification Using TPC and TOF

To identify a particle, it is necessary to know both of its charge and mass. Experimentally, mass can be calculated using at least two kinematic variables which depend on it. One of these is momentum, which is determined by TPC from the radius of curvature of the track in the magnetic field. The second variable can be the energy loss (dE/dx) measured in TPC or the velocity of the particle, defined as the ratio between the length of the trajectory and

its time-of-flight measured in TOF. TPC is basically used to identify particles at lower p_T while at higher p_T , both TPC and TOF are used. Here, we discuss an overview of particle identification (PID) using TPC and TOF, whereas the performance of different PID methods are explained in detail in Ref. [15].

In addition to tracking and momentum determination, TPC also provides particle identification for charged particles at low p_T by measuring their energy loss in the TPC gas. TPC is filled with P10 gas and regulated at 2 mbar above atmospheric pressure. Charged particles while traversing through the TPC gas volume, interact with the gas atoms and lose energy by ionising the electrons of the gas atoms. This specific ionisation energy loss, called dE/dx , is a function of the magnitude of the particle momentum and also of the mass and charge of the particle. Due to the random nature of the interactions, the energy loss distribution has a Landau shape [16] with a long tail towards the high ionisation region. The average dE/dx is sensitive to the fluctuations in the Landau tail. To reduce fluctuation, a truncated mean $\langle dE/dx \rangle$ is used to characterise the ionisation energy loss of charged particles. The truncated mean $\langle dE/dx \rangle$ is calculated by discarding highest 30% of the measured dE/dx values of the hits for each track and using the remaining 70%, defined as the average ionisation energy loss, which is used in this analysis. Theoretically, the ionisation energy loss by charged particles in material is given by the Bethe-Bloch formula [17]. For STAR detector material a modified Bethe-Bloch formula is used, which is defined as Bichsel formula [18]. With the measured particle momentum and $\langle dE/dx \rangle$, the particle type can be determined by comparing the measurements against the Bethe-Bloch (Bichsel) expectation. Figure 3.2 shows the $\langle dE/dx \rangle$ of e^\pm , π^\pm , K^\pm , p , and \bar{p} plotted as a function of rigidity, which is momentum/charge of the particle in Au+Au collisions at $\sqrt{s_{NN}} = 27$ GeV. Various bands corresponding to different mass of particles, are clearly separated at low p_T . From this figure, we can also see that as the particle momentum rises, the energy loss becomes

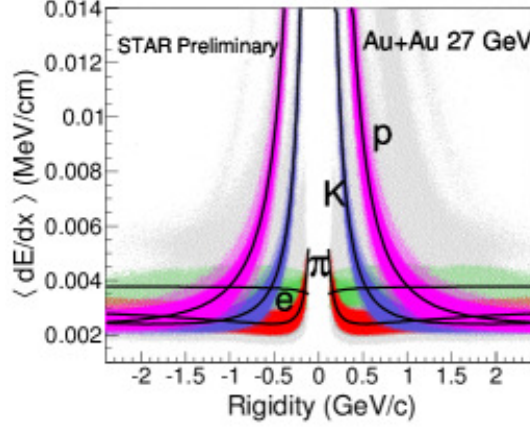


Figure 3.2: $\langle dE/dx \rangle$ of e^\pm , π^\pm , K^\pm , p , and \bar{p} as a function of rigidity in Au+Au collisions at $\sqrt{s_{NN}} = 27$ GeV.

less mass dependent. Using this method, π^\pm and K^\pm can be identified up to 0.75 GeV/ c whereas p and \bar{p} can be identified up to 1 GeV/ c . To obtain maximum separated dE/dx band, we have selected the mid-rapidity region of $|y| < 0.1$.

At intermediate p_T ($1 < p_T < 4$ GeV/ c) region, π , K , and p bands merge together, which makes it difficult to identify the particles with TPC alone. However, by using TOF, the PID capabilities can be extended to intermediate p_T . Mass of the particle can also be determined from the momentum and the velocity of the particle, which is defined as $\beta = l/t_{TOF}$, where l is the path length of the particle and t_{TOF} is the time-of-flight defined as the time taken by the particle to travel from the primary vertex to the TOF. So, the measured mass square (m^2) which is related to $1/\beta$ can be obtained experimentally obtained as follows:

$$m^2 = p^2 \left(\frac{1}{\beta^2} - 1 \right) = p^2 \left(\frac{t_{TOF}^2}{l^2} - 1 \right), \quad (3.4)$$

where p is the momentum. Figure 3.3 shows the dependence of $1/\beta$ as a function of rigidity

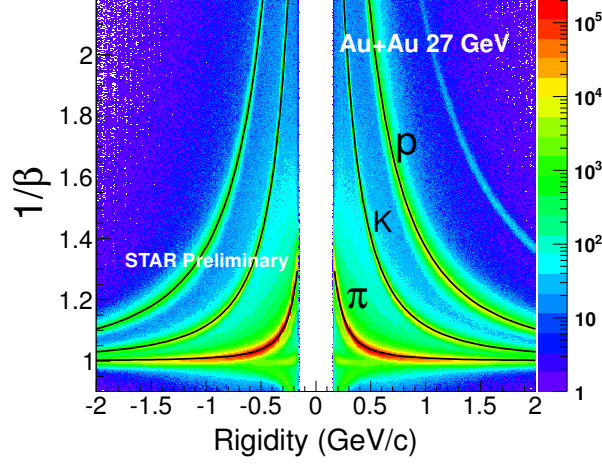


Figure 3.3: $1/\beta$ as a function of rigidity in Au+Au collisions at $\sqrt{s_{NN}} = 27$ GeV.

in Au+Au collisions at $\sqrt{s_{NN}} = 27$ GeV. Here, we can see π^\pm , K^\pm , p , and \bar{p} bands are well separated up to a higher p_T . By combining the dependence of $1/\beta$ on p_T from TOF and that of dE/dx on p_T , we are able to extend our PID capability up to 2 GeV/c for this study.

3.5 Raw Yields Extraction

3.5.1 Using TPC

To extract raw yields of positively and negatively charged hadrons (π^\pm , K^\pm , p , and \bar{p}) for a given p_T bin using TPC, we perform a multi-Gaussian fit to a new variable called z , which is defined as,

$$z_i = \ln \left(\frac{\langle dE/dx \rangle}{\langle dE/dx \rangle_i^{BB}} \right), \quad (3.5)$$

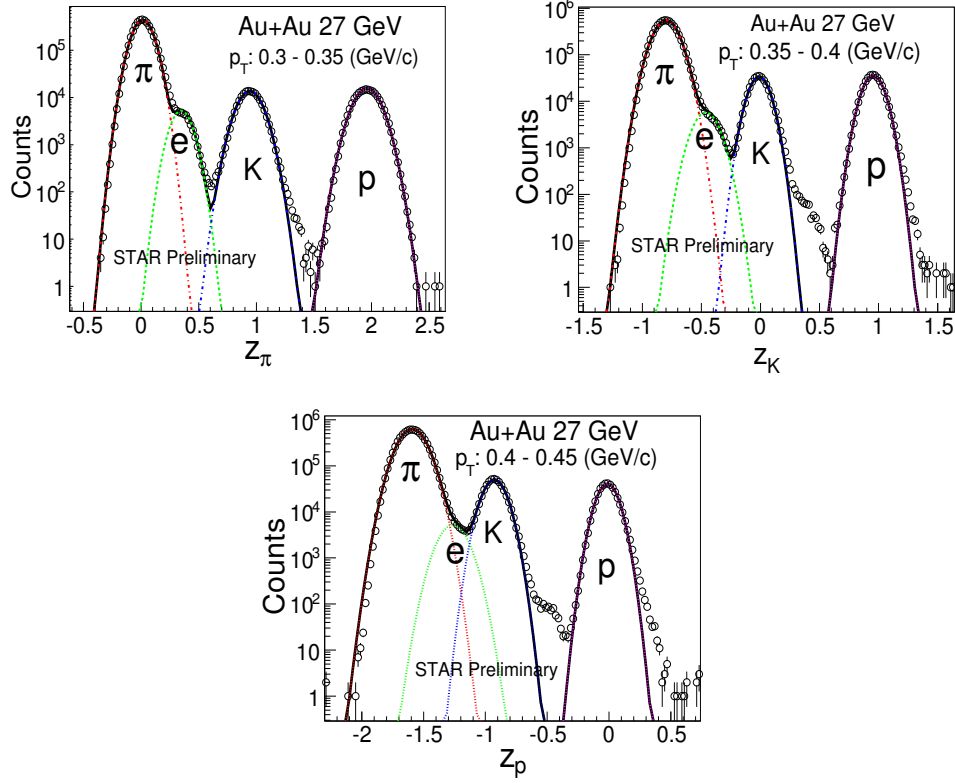


Figure 3.4: Distributions of z_π for π^+ , z_K for K^+ , and z_p for p in TPC for different p_T bins in mid-rapidity, $|y| < 0.1$ for 0–5% centrality in Au+Au collisions at $\sqrt{s_{NN}} = 27$ GeV. Errors are statistical only. The curves are Gaussian fits representing contributions from pions (dotted-red), electrons (dotted-green), kaons (dotted-blue), and protons (dotted-magenta).

where $\langle dE/dx \rangle_i^{BB}$ is the Bethe-Bloch (Bichsel [18]) expectation of $\langle dE/dx \rangle$ for the particle type i (e, π , K, p). $\langle dE/dx \rangle^{BB}$ is parametrised as,

$$\langle dE/dx \rangle_i^{BB} = A_i \left(1 + \frac{m_i^2}{p_{\text{mag}}^2} \right), \quad (3.6)$$

where m_i is the particle rest mass and p_{mag} is the magnitude of particle momentum. The z variable has the advantage that each particle has a Gaussian distribution around the expected Bethe-Bloch value, as $\langle dE/dx \rangle$ distributions for a fixed particle type is not Gaus-

sian [19]. This parametrisation is found to describe the data well, with the normalisation factor A_i is determined from data. The expected value of z_i for a particle under consideration is around 0. The z distributions of π^+ , K^+ , and p in Au+Au collisions at $\sqrt{s_{NN}} = 27$ GeV in different p_T bins are shown in Fig. 3.4. The peak of the particle of interest is centered around zero and the other peaks are well separated. A similar procedure is followed to obtain yields for other p_T ranges and for yields of π^\pm , K^\pm , and $p(\bar{p})$. During the multi-Gaussian fit to the z variable, the width of the electrons are set to be equal to the width of the pions because the widths of the peak depends on the detector resolution and in theory they should be equal. Further details of extracting raw yields of identified hadrons can be found in Ref. [20].

3.5.2 Using TOF

The m^2 distributions can be used to extract raw yields using TOF. But the real shape of m^2 distributions of identified particles are not purely Gaussian. Fitting those with Gaussian functions to extract raw yields introduces systematic uncertainties. To get better results, we use the predicted m^2 distributions to fit the total m^2 distribution instead of using Gaussian functions. The procedure is described below.

The TOF detector measures the time-of-flight, which is t_{TOF} (measured). The expected time-of-flight, t_{TOF} (expected), with a given momentum (p), path length (l) for a known particle type of mass (m_0) can be calculated by,

$$t_{\text{TOF}} (\text{expected}) = \frac{l}{c} \sqrt{\frac{m_0^2}{p^2} + 1} \quad (3.7)$$

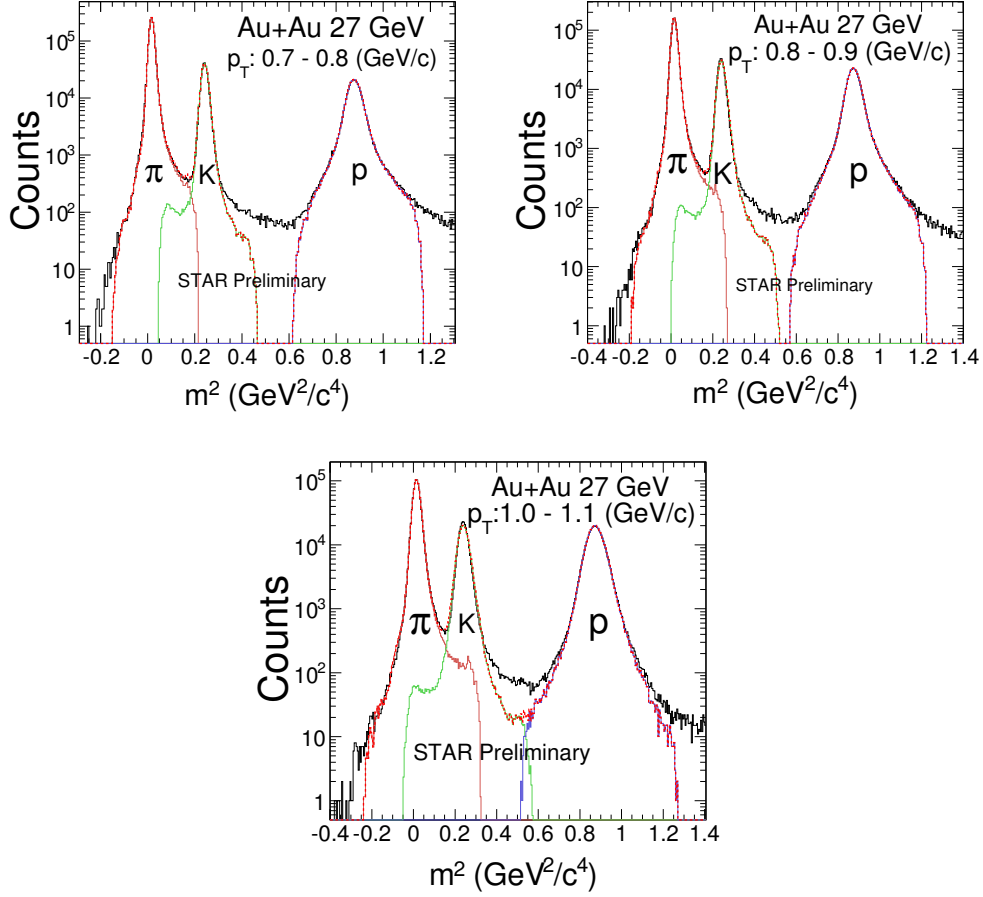


Figure 3.5: The m^2 distributions for positively charged particles in TOF for different p_T bins in mid-rapidity, $|y| < 0.1$, for 0–5% centrality in Au+Au collisions at $\sqrt{s_{NN}} = 27$ GeV. Errors are statistical only. The curves are predicted m^2 fits representing contributions from pions (solid-red), kaons (solid-green), protons (solid-blue), and the total fit (dot-dashed-red).

The difference between two times, $\Delta t = t_{\text{TOF}} (\text{measured}) - t_{\text{TOF}} (\text{expected})$, reflects the behaviour of TOF detector response to the matched tracks. The Δt distributions can be used to simulate TOF detectors behaviour. The simulated TOF, $t_{\text{TOF}} (\text{simu.})$, will be $t_{\text{TOF}} (\text{expected}) + t (\text{random})$, where $t (\text{random})$ is a random time shift, generated based on the Δt

distributions. Then the predicted m^2 distributions is determined by,

$$m_{\text{predicted}}^2 = p^2 \left(\frac{c^2 t_{\text{TOF}}^2(\text{simu.})}{l^2} - 1 \right) \quad (3.8)$$

We use χ^2 -minimisation method to fit m^2 distribution obtained from data with the predicted particle m^2 distributions to extract raw yields in TOF. Figure 3.5 shows the m^2 distributions for positive particles, π , K, and p in different p_T bins. A similar procedure is followed to obtain raw yields using TOF for other p_T ranges and for yields of π^\pm , K^\pm , and $p(\bar{p})$.

We have repeated the same analysis procedure as described above to extract raw yields from TPC and TOF for all the centrality bins studied in this thesis.

3.6 Raw Spectra and Corrections

The raw spectra is obtained by calculating $d^2N/2\pi p_T dp_T dy$ for each p_T bin. In STAR TPC, particles may not be detected due to geometry of the detector, some of the particles may hit in the dead region of the detector, or some of the tracks may not be well reconstructed if some hits are missing. Therefore, the obtained raw spectra need to be corrected for the detector acceptance, track reconstruction inefficiency, hadronic interactions, and resonance particle decays. They are determined by a procedure called embedding technique.

In this technique, the Monte-Carlo (MC) simulated π^\pm , K^\pm , p, and \bar{p} are generated using a flat p_T and a flat y distribution. The flat p_T distribution is used to have similar statistics in different p_T bins. Simulated tracks are embedded in each real event. These are then passed through GSTAR [21] (the software package to run the STAR detector simulation using GEANT [22, 23]) and TRS (the TPC Response Simulator [21]). The number of embedded MC tracks is kept low ($\sim 5\%$) relative to the number of real tracks to avoid

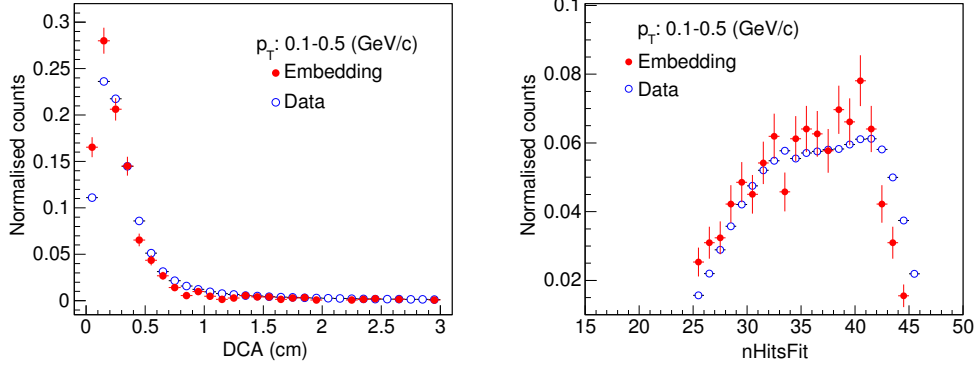


Figure 3.6: Comparison of the distributions of DCA and number of fit points (nHitsFit) for pions from embedding and from real data at mid-rapidity in Au+Au collisions at $\sqrt{s_{NN}} = 27$ GeV.

distorting the track density of the event. The simulated π^\pm , K^\pm , p , and \bar{p} combined with real raw events are referred as mixed events. These mixed events are then passed through the standard STAR reconstruction chain and those events after reconstruction are called as reconstructed event. The reconstructed information of those particles in the reconstructed event is then associated with the MC information in the mixed events. Then we get the total number of reconstructed simulated π^\pm , K^\pm , p , and \bar{p} from mixed events in a certain p_T bin. The reconstructed tracks also need to be identified which are matched to the input MC tracks, defined as matched tracks in the reconstructed events. A cut of 10 common hit points was applied on the number of common hit points in TPC between the reconstructed and the input MC simulated tracks. This procedure is called embedding, which provides nearly realistic simulation of the collision and detector environment. To ensure the correct embedding procedure, hit and track level properties have been checked between embedding and the real data. Figure 3.6 shows the comparison of the distributions of DCA and nHitsFit for pions obtained from embedding and real data at mid-rapidity in Au+Au collisions at $\sqrt{s_{NN}} = 27$ GeV. The overall agreement of the embedding and real data ensures that corrections extracted from embedding reflect realistic calculations. Since detector parameters

(gas pressure in TPC, temperature) can change over the run, a minimum uncertainty ($\sim 5\%$) is associated as the embedding procedure to the obtained corrected spectra.

In addition to the corrections related to embedding, there are some corrections which are done from data like energy loss and matching inefficiency. The following subsections discusses these corrections.

3.6.1 Energy loss Correction

When a particle moves through the detector material, it loses some energy due to several interactions. Low momentum particles lose a significant amount of energy in comparison to high momentum particles [24]. Due to this effect, the momentum recorded by the detector is less than the initial momentum when the particle freeze-out. The track reconstruction algorithm takes into account the Coulomb scattering and energy loss assuming the pion mass for each particle. Therefore, a correction for the energy loss by heavier particles (K^\pm , p , and \bar{p}) is needed. This correction is obtained from embedding Monte Carlo simulations as described above. So, the energy loss correction factor is obtained from the difference between the reconstructed momentum (p_T^{REC}) and the initial momentum (p_T^{MC}) as a function of p_T^{REC} which is shown in Fig. 3.7 for π^+ , K , and p in Au+Au collisions at $\sqrt{s_{\text{NN}}} = 27$ GeV for 0–5% centrality. The pion transverse momentum difference is flat at 0 through the measured p_T range, shown in Fig. 3.7, and the correction is very small at any p_T . This is because pion energy loss is corrected in reconstruction and the remaining small effect is negligible. However, K^\pm , p , and \bar{p} show larger discrepancy between p_T^{MC} and p_T^{REC} and the deviation from MC input is the same for particles and antiparticles (not shown in figure). The energy loss correction seems to have negligible dependence on centrality in Au+Au collisions. The energy loss correction for K^\pm , p , and \bar{p} can be parametrised as follows to

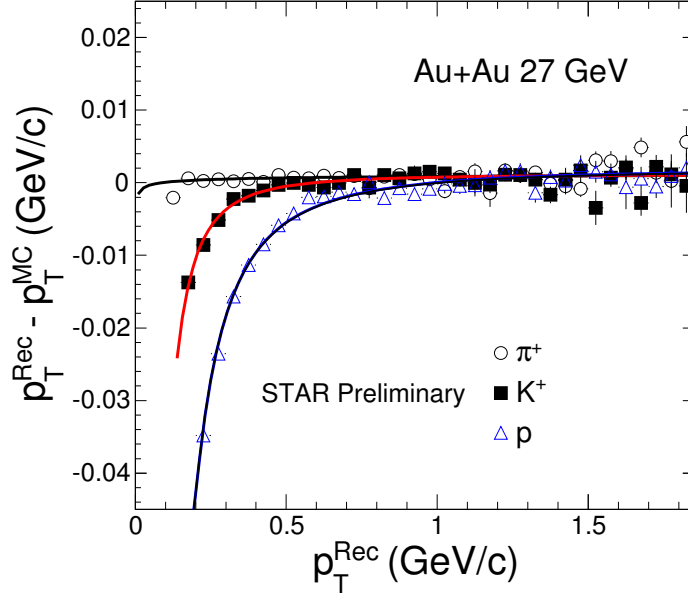


Figure 3.7: The energy loss correction for different particles as a function of p_T . Here p_T^{REC} is the reconstructed p_T before the energy loss correction, and p_T^{MC} is the input p_T of embedded track in Au+Au collisions at $\sqrt{s_{\text{NN}}} = 27$ GeV for 0–5% centrality. Errors are statistical only.

provide the correction function for the measured p_T ,

$$p_T^{\text{REC}} - p_T^{\text{MC}} = P_0 + P_1 \left(1 + \frac{P_2}{(p_T^{\text{REC}})^2} \right)^{P_3}, \quad (3.9)$$

where P_0 , P_1 , P_2 , and P_3 are the fit parameters. The values of these parameters are given in Table 3.3. The energy loss correction was applied to the raw data during selection of tracks from the dE/dx distribution. This correction shifts the position of p_T in the p_T spectra.

After energy loss correction, the efficiency corrections have to be applied to the obtained raw spectra. One of these include track reconstruction efficiency, as every primary track cannot be reconstructed and the other one is the TOF matching efficiency, as every reconstructed track in TPC can not be matched with a TOF hit.

Table 3.3: Summary of energy loss parametrisations for kaon and proton in Au+Au collisions at $\sqrt{s_{NN}} = 27$ GeV.

Parameters	Kaon	Proton
P_0 (GeV/c)	9.67085e-04	1.89952e-03
P_1 (GeV/c)	-2.78019e-06	-6.40699e-05
P_2 (GeV/c) ²	8.96313e+01	3.05697e+01
P_3	1.06881e+00	9.87498e-01

3.6.2 TPC–TOF Matching Efficiency Correction

As TPC and TOF are two separate detectors, the final combined spectra obtained using these two detectors need to be matched properly to combine. Only a fraction of the reconstructed primary tracks are matched with hits on the TOF detector. The matching efficiency depends on the fraction of tracks that are missing during the propagation from TPC to TOF. It could be due to the TOF detector's geometrical acceptance and inefficiency, some dead region on the TOF detector, the decays and the interactions with the material. So to verify the matching of the tracks between TPC and TOF, matching efficiency ($\epsilon_{\text{match-eff.}}$) correction is done in real data and it is calculated as;

$$\epsilon_{\text{match-eff.}} = \frac{\text{Number of TOF matched tracks}}{\text{Number of TPC tracks}} \quad (3.10)$$

Figure 3.8 shows the TOF matching efficiency of π^+ , K^+ , and p as a function of p_T for 0–5% centrality in Au+Au collisions at $\sqrt{s_{NN}} = 27$ GeV. This is fitted with a 9th order polynomial function to obtain the matching efficiency curve as a function of p_T . The raw spectra is corrected for matching efficiency as follows.

$$\text{Raw spectra}_{\text{match-effcorr.}}(p_T) = \frac{\text{Raw spectra}(p_T)}{\epsilon_{\text{match-eff.}}(p_T)} \quad (3.11)$$

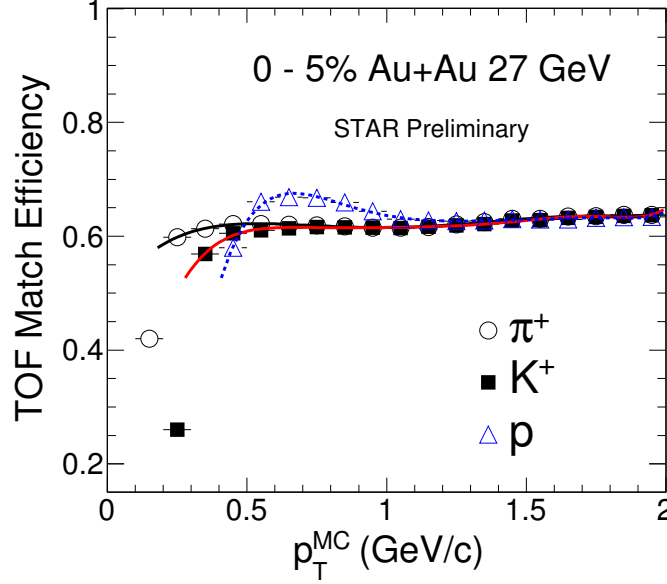


Figure 3.8: Matching efficiency of π^+ , K^+ , and p as a function of p_T and $|y| < 0.1$ for 0–5% centrality in Au+Au collisions at $\sqrt{s_{NN}} = 27$ GeV. Errors are statistical only. Lines represent parametrisations to the data and are used for corrections.

3.6.3 Track Reconstruction Efficiency and Acceptance Correction

Once the TOF matching efficiency correction is done, we need to correct the raw spectra for the track reconstruction efficiency ($\epsilon_{\text{track-eff.}}$), which is obtained using embedding method as described earlier. To calculate proper efficiencies, it is important to check the quality of the embedding process. So, the hit and track level quantities are compared between embedding and real data. The same analysis cuts have been applied on embedding as for the real data, to extract the efficiencies correction factors in this study.

The track reconstruction efficiency in the mid-rapidity range is obtained as follows:

$$\epsilon_{\text{track-eff.}} = \frac{\text{Number of matched MC tracks}}{\text{Number of input MC tracks}} \quad (3.12)$$

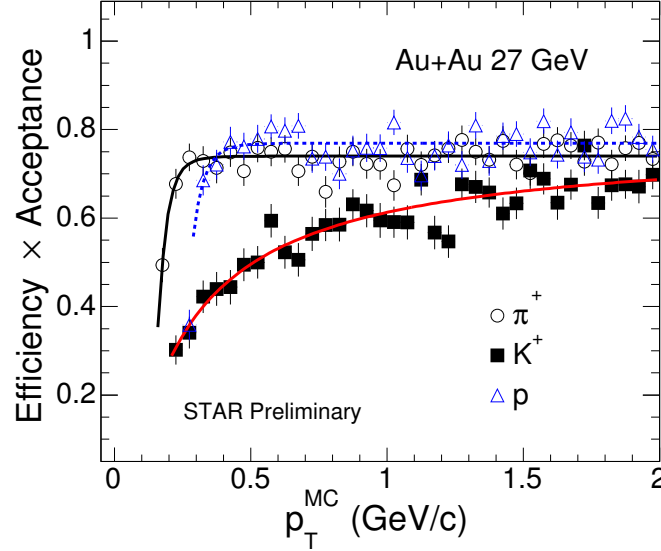


Figure 3.9: Tracking efficiency including detector acceptance for reconstructed π^+ , K^+ , and p in the TPC as a function of input MC p_T and $|y| < 0.1$ for 0–5% centrality in Au+Au collisions at $\sqrt{s_{NN}} = 27$ GeV. Errors are statistical only. Lines represent parametrisations to the data.

Figure 3.9 shows the TPC tracking efficiency of π^+ , K^+ , and p as a function of p_T for 0–5% centrality in Au+Au collisions at $\sqrt{s_{NN}} = 27$ GeV. Lines in the Fig. 3.9 represent parametrisations to the data and the fit parameters are listed in Table 3.4. The π^\pm efficiency is independent of p_T for $p_T > 0.3$ GeV/c, but falls steeply at lower p_T because particles below $p_T = 0.15$ GeV/c cannot traverse the entire TPC due to their large track curvature inside the solenoidal magnetic field. The efficiency for protons and antiprotons is flat above $p_T \sim 0.4$ GeV/c. At lower p_T , the efficiency drops steeply because of the large multiple scattering effect due to the large (anti)proton mass. The kaon efficiency increases smoothly with p_T . The significantly smaller kaon efficiency at small momentum than that of pions is caused by the large loss of kaons due to decays. The ratio obtained as above is fitted with a function given below to obtain the efficiency curve as a function of p_T ,

Table 3.4: Parametrisations to π^+ , K^+ and p efficiencies for 0–5% centrality in Au+Au collisions at $\sqrt{s_{NN}} = 27$ GeV.

Parameters	π^+	K^+	p
P_0	0.74	0.786	0.769
P_1	0.152	0.21	1.35e-05
P_2	6.36	0.889	8.11

$$f(p_T) = P_0 \exp(-P_1/p_T)^{P_2}, \quad (3.13)$$

where P_0 , P_1 , and P_2 are free parameters. These parametrisations are applied to the data in each p_T bin and to individual particle species for efficiency and acceptance corrections to get the corrected p_T spectra as given below,

$$\text{Raw spectra}_{\text{track-eff. corr.}}(p_T) = \frac{\text{Raw spectra}(p_T)}{\epsilon_{\text{track-eff.}}(p_T)} \quad (3.14)$$

The efficiencies discussed above depend on mass of the particle, centrality, and transverse momentum. Centrality-wise, more particles are produced as the collisions become more central, thus increasing the density of tracks inside the TPC. This lowers the tracking efficiency.

3.6.4 Pion Feed-down Correction

The obtained identified particle spectra can contain some product from the weakly decaying particles. As all the decays may not happen before the particle reach the detectors, and all the products may not fall in the detector acceptance, it is necessary to estimate the fraction of measured particles which are produced through weak decays. The corrections (e.g., $K_S^0 \rightarrow \pi^+\pi^-$) to the pion spectra are calculated using HIJING [25] and GEANT [22, 23] simulation. Therefore, after energy loss, efficiency and acceptance corrections, the charged

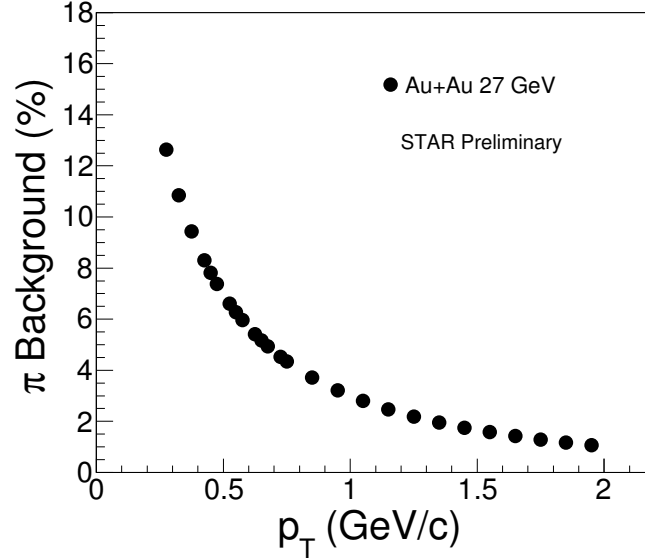


Figure 3.10: Percentage of pion background as a function of p_T in $|y| < 0.1$ in Au+Au collisions at $\sqrt{s_{NN}} = 27$ GeV.

pion spectra are further corrected for weak decays, muon contamination, and background pions produced in the detector materials.

To do this correction, the simulated events are reconstructed in the same way as the real data. For each simulated particle, the origin, the parent particle, and the decay particle type are known. From this information, we can select pions created in the simulated collision (primary particles) from the ones created in the detector material or produced from resonance decay. The weak-decay daughter pions are mainly from K_S^0 and are identified by the parent particle information accessible from the simulation. The muons from pion decay can be misidentified as primordial pions because of the similar masses of muon and pion. By selecting the parent particle information in the simulation, the muon contamination can be extracted. The total background rate for pion, which is dominated by weak decays and muon contamination, obtained from the MC simulations is shown in Fig. 3.10 as a func-

tion of p_T for Au+Au collisions at $\sqrt{s_{NN}} = 27$ GeV. Once these selections are applied, the amount of background contamination can be extracted for each p_T bin. The magnitude of the background pion contamination falls steeply. At low transverse momentum ($p_T = 0.3$ GeV/ c), it is in the order of 13% and decreases to $\sim 1\%$ at $p_T \geq 1$ GeV/ c . In this way, the fraction of the feed-down and background contribution is subtracted from the pion spectra for all centralities. In Au+Au collisions, the centrality dependence of the pion background is found to be very small. Therefore, a single correction is applied to all centralities [26].

3.6.5 Proton Background Correction

To detect the particles produced in a collision using TPC detector, they need to traverse through the beam pipe and different kinds of detector materials. Particles traversing through the detector materials create secondary particles (including secondary protons) due to interactions of energetic particles produced in collisions with detector materials. Due to the geometry of the detector, the secondary protons are produced far from the primary vertex (mainly in the beam pipe) and they appear as a long, nearly flat tail in the DCA distribution of primary protons. The effect is p_T dependent, which is highest at low p_T and significantly low at high p_T . Since antiprotons do not create secondaries, the long DCA tail is absent from their DCA distribution and their DCA distribution should be the same as that of primary protons. To correct the background contributions to protons, the DCA distributions of protons and antiprotons are extracted and compared from real data. We have used similar method as used in earlier STAR analysis [27, 28]. In this analysis, the DCA of primary tracks is used up to 3 cm, therefore to make the proper corrections, one needs to access the high DCA region (up to 10 cm or so). This can be done through the mapping of global tracks to primary tracks. By this mapping, proton and antiproton DCA distributions can be compared up to DCA ~ 10 cm, for each p_T bin.

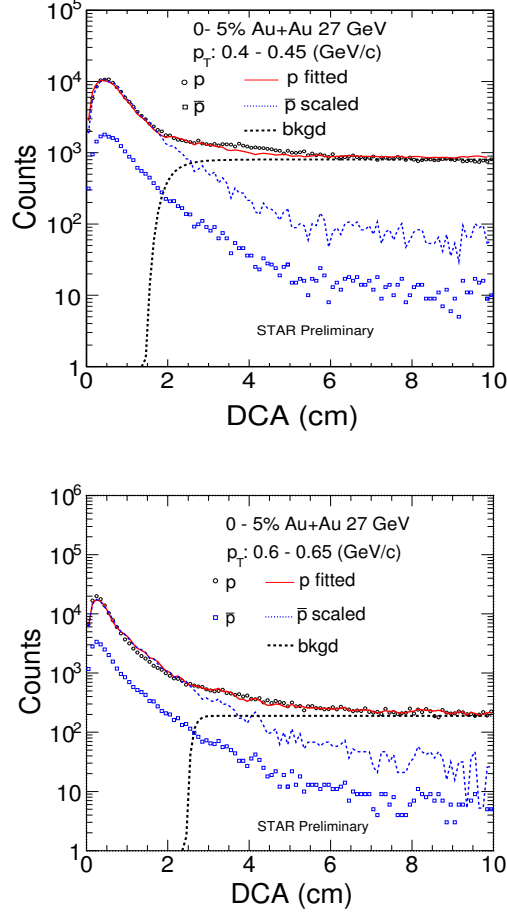


Figure 3.11: DCA distributions of p and \bar{p} for $0.4 < p_T < 0.45$ GeV/c and $0.6 < p_T < 0.65$ GeV/c for 0–5% centrality in Au+Au collisions at $\sqrt{s_{NN}} = 27$ GeV. Errors are statistical only. The solid red line represent the fitted p distribution, the dotted blue line represent the \bar{p} distribution scaled up by the \bar{p}/p ratio obtained from the fit, the dashed black line is the proton background obtained from the fit.

In order to correct for the background protons, the DCA dependence at $DCA < 3$ cm is needed for the knock-out protons. Since the background shape of the DCA distribution at small DCA is not known, a Monte Carlo simulation (GEANT) was used and can be

Table 3.5: Fraction of proton background as a function of p_T for 0–5% centrality in Au+Au collisions at $\sqrt{s_{NN}} = 27$ GeV.

p_T	Proton background (%)
0.4 - 0.45	6
0.45 - 0.5	4.2
0.5 - 0.55	1.8
0.55 - 0.6	1.0
0.6 - 0.65	0.5

described by an exponential function:

$$p_{\text{bkgd}}(\text{DCA}) = A [1 - \exp(-\text{DCA}/B)]^C \quad (3.15)$$

Assuming the identical shape of the DCA distribution of background subtracted proton to that of antiproton, Eq. 3.15 can be written as,

$$p(\text{DCA}) = \bar{p}(\text{DCA})/r_{\bar{p}/p} + p_{\text{bkgd}}(\text{DCA}), \quad (3.16)$$

where the magnitude of the background protons A , the parameter B , the exponent C , and the antiproton-to-proton ratio $r_{\bar{p}/p}$ are free parameters. The DCA distributions of protons and antiprotons in Au+Au collisions are fitted with Eq. 3.16 for each p_T bin and centrality bin. The fit results are shown in Fig. 3.11 for two different p_T bins in central collisions. The fraction of proton backgrounds for different p_T bins in central collisions are given in Table 3.5. Finally, the proton background fraction is subtracted from the proton raw yields for each centrality.

3.7 Results and Discussions

Here we present the transverse momentum spectra of identified particles π^\pm , K^\pm , p , and \bar{p} in Au+Au collisions at $\sqrt{s_{NN}} = 27$ GeV. The energy and centrality dependence of dN/dy , particle yield ratios, average transverse momentum, strangeness, and baryon production rates are investigated. The sources of systematic errors are also discussed.

3.7.1 Transverse Momentum Spectra

The shape of p_T spectra, measured particle dependence, and centrality dependence of the spectra are sensitive to the collision dynamics. In heavy-ion collisions, there are high density of particles produced. The particles collide frequently and act as a collective fluid, instead of as free particles. The pressure generated during the collision process boosts the produced particle away from the center of the collision. This leads to an expanding source, which might be thermalized. The scattering and collective expansion which is driven by internal pressure gradients introduce a blast velocity. This blast (hydro-like) velocity combined with the (thermal) freeze-out temperature, describes the shape of the p_T spectra, which depends on the mass of the measured identified particle [29]. So, a boosted thermal source, which describes the p_T spectra of different particles, also indicates the existence of strong radial flow.

The p_T spectra of identified particles are used simultaneously to extract the information about the combined effect of the kinetic (thermal) freeze-out temperature (T_{kin}) in the collision and the collective expansion of the fireball (radial flow) generated in the system through hydrodynamical model [30, 31]. The collective flow pushes the particles to higher p_T region. The low p_T spectra are dominated by late stage collision dynamics, which include soft collective effects (radial flow) and resonances, whereas the high p_T spectra are sensitive to the parton dynamics generated in the early stage of the collision (hard or semi-

hard processes). All the results presented here are based on the low p_T region. The final invariant spectra can be obtained as:

$$\frac{1}{N_{\text{events}}} \frac{d^2N}{2\pi p_T dp_T dy} = \frac{1}{2\pi p_T} \times \frac{1}{N_{\text{events}}} \times \frac{1}{\delta p_T \delta y} \times \frac{1}{C(p_T)} \times Y(p_T), \quad (3.17)$$

where $Y(p_T)$ and $C(p_T)$ are raw spectra and corrections to the raw spectra.

Systematic Uncertainties:

There are multiple sources of systematical errors such as tracking efficiency, PID efficiency, and fit to the spectra, which must be taken into account for the final results. For the spectra of π^\pm , K^\pm , p , and \bar{p} , the average systematic errors are estimated by varying the analysis event and track cuts, fitting methods, backgrounds, and matching efficiencies. The default cuts used in this analysis are listed in Table 3.1. Table 3.6 represents the variation of cuts for the systematic error study. The overall systematic errors are obtained by adding the separate errors in quadrature.

Table 3.6: Event and track cuts variation to study the systematic uncertainties.

Cuts	Changed Value
$ V_z $	$< 50 \text{ cm}$
$ y $	< 0.5
DCA	$< 1 \text{ cm}$
nHitsFit	≥ 20
nHitsdEdx	≥ 10
p_T	$> 0.15 \text{ GeV}/c$

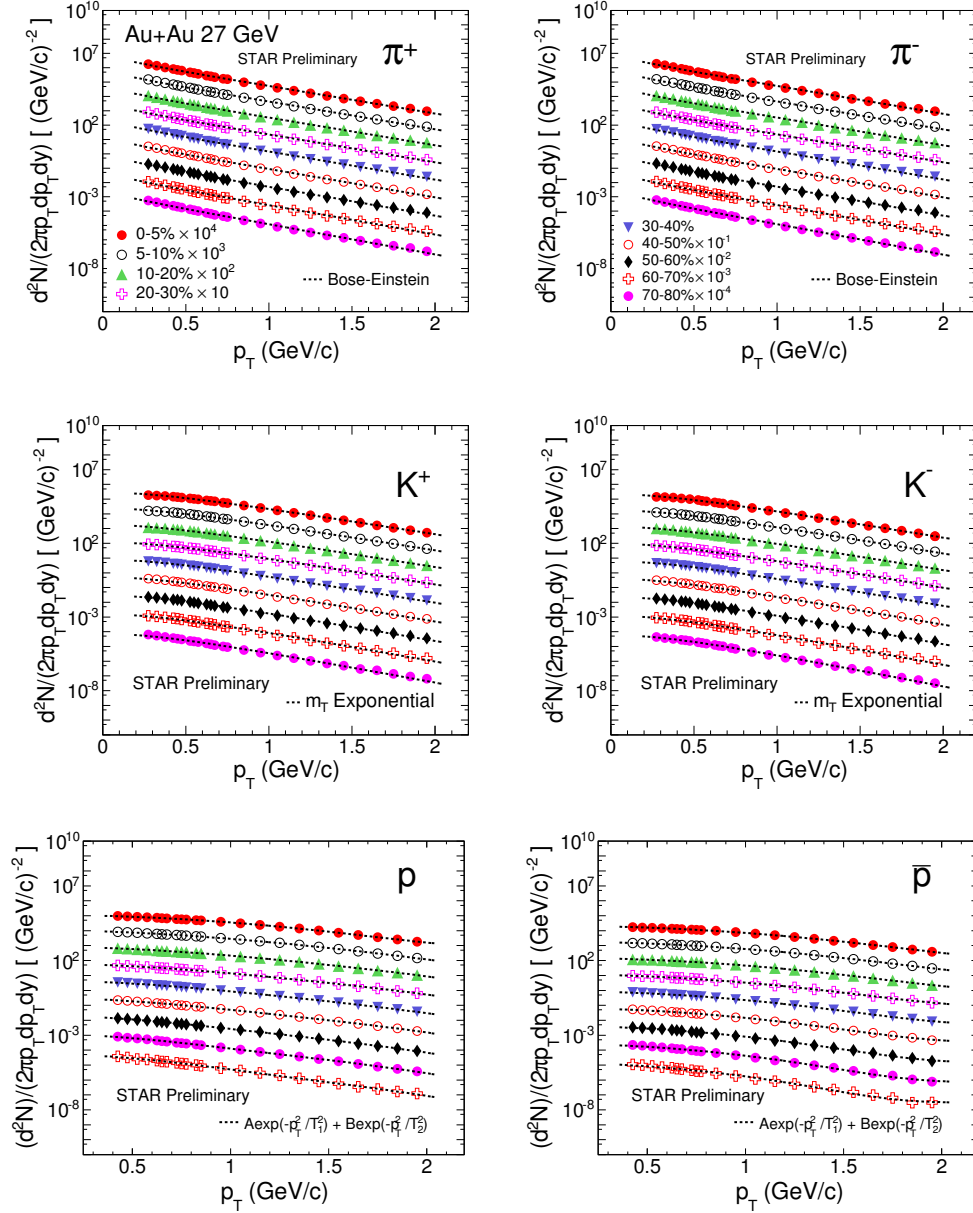


Figure 3.12: Centrality dependence of identified particle spectra measured in mid-rapidity ($|\eta| < 0.1$) in Au+Au collisions at $\sqrt{s_{NN}} = 27$ GeV. Spectra are plotted at nine centrality bins and are scaled for different collision centrality for clarity. Curves represent Bose-Einstein function for pions, m_T exponential for kaons, and double exponential for protons/antiprotons. Errors are statistical and systematic errors added in quadrature.

The Gaussian fit ranges are varied to estimate the systematic uncertainty on the extracted raw spectra. The estimated uncertainties are less than 5% for π^\pm , p, and \bar{p} , and those for K^\pm are less than 11% for p_T bins with significant overlap in dE/dx with e^\pm or π^\pm and less than 3% for other bins. The systematic uncertainties on the pion spectra due to background correction are negligible, and that of proton is found to be less than 6%. A correlated overall systematic uncertainty of 5% is estimated for all spectra and is dominated by uncertainties in the MC determination of reconstruction efficiencies. These errors are combined with the statistical errors on the spectra.

Figure 3.12 shows the π^\pm , K^\pm , p, and \bar{p} spectra in Au+Au collisions at $\sqrt{s_{NN}} = 27$ GeV for different centrality bins. Spectra are measured at mid-rapidity $|y| < 0.1$ and for nine centrality bins. The p and \bar{p} spectra are plotted without feed-down corrections, whereas the pion spectrum are feed-down corrected from K_S^0 . For each particle species, the spectra are scaled for different collision centrality for clarity. Curves shown on the spectra represent Bose-Einstein for pions, m_T exponential for kaons, and double exponential for (anti)protons. The used function shapes are given in the Eq. 3.20. These fit functions, which best describe the spectra are hence used to extract the integrated yield of the particles from p_T spectra which will be discussed later in this chapter.

The shapes of pion spectra look similar when compared between different centralities. The steepening (fall faster with increasing p_T) of the pion spectra at low p_T is due to the significant contributions of resonance decays. Kaons and (anti)protons spectra show a centrality dependence, a small gradual flattening with increasing centrality and this effect is more significant for (anti)protons. The shape of proton spectra is more concave from peripheral to central collisions which indicates a progressively stronger radial flow. As central collisions produce more particles, collective effects should be stronger, and heavier particles should be boosted to higher transverse momenta. As pions and kaons are lighter having higher

velocity than proton and antiprotons, they are not much affected by the collective flow in the p_T spectra. This collective flow results in the inverse slope rising with the mass of the particle, the effect is more at low p_T . From Fig. 3.12 we can observe the inverse slope variation with particle mass has the order $\pi < K < p$.

Spectra shapes at RHIC energies, $\sqrt{s_{NN}} = 7.7, 11.5, 19.6, 27, 39, 62.4, 130,$ and 200 GeV in Au + Au collisions are all similar [32]. At all energies, hardening of the spectra is more pronounced with increasing centrality and the particle mass. A dramatic change in spectral shapes from RHIC to LHC energies is observed, particularly with the protons [33]. For central collisions, about 10% stronger radial flow is observed at LHC than at RHIC [33]. As mentioned earlier, based on the idea of a hydro dynamically behaving boosted source, Blast-wave model is used to fit simultaneously all the particles and antiparticles spectra to determine the magnitude of the radial flow, as a function of collision centrality and energy [34]. The details of this study will be discussed in the later part of this thesis.

The spectra can be further studied by looking at $\langle p_T \rangle$ or $\langle m_T \rangle - m$ of the produced hadrons, where m is the rest mass of hadron and $m_T = \sqrt{m^2 + p_T^2}$ is the transverse mass. These are explained in the following subsections.

3.7.2 Average Transverse Momentum ($\langle p_T \rangle$)

The change in the measured spectral shapes can be quantitatively characterised by the $\langle p_T \rangle$ in terms of energy and centrality. In general, it provides information on the transverse dynamics of different types of particles. We calculate $\langle p_T \rangle$ as follows,

$$\langle p_T \rangle = \frac{\int p_T 2\pi p_T f(p_T) dp_T}{\int 2\pi p_T f(p_T) dp_T}, \quad (3.18)$$

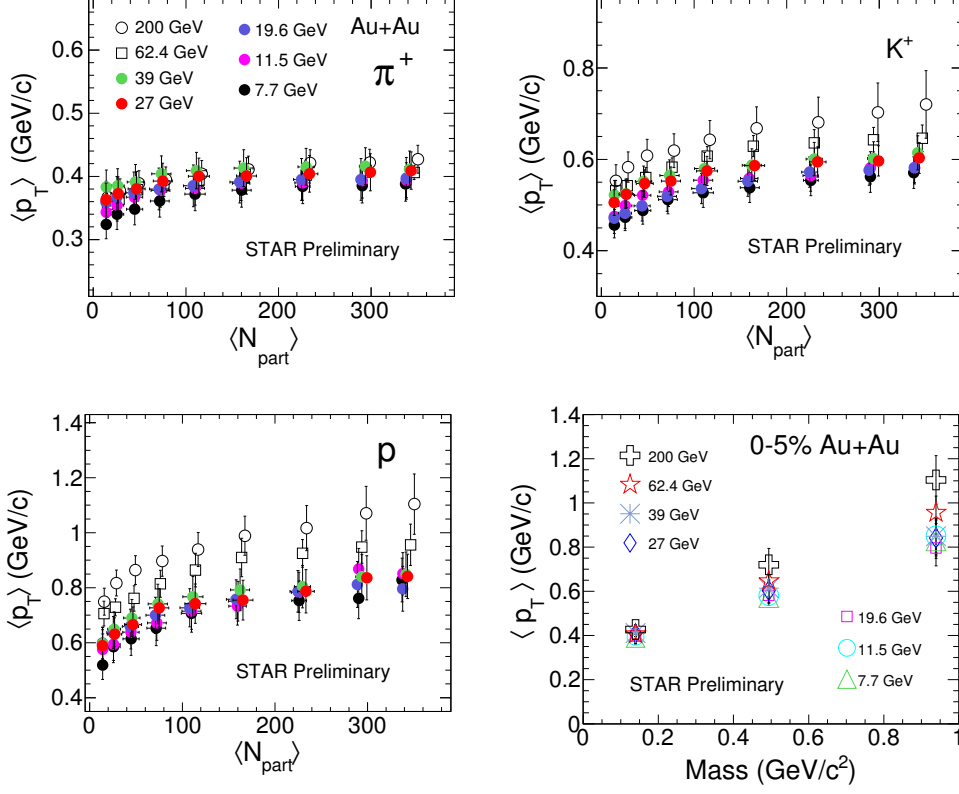


Figure 3.13: The variation of $\langle p_T \rangle$ of π^+ , K^+ , and p as a function of $\langle N_{part} \rangle$ measured in $|y| < 0.1$ in Au+Au collisions at $\sqrt{s_{NN}} = 27$ GeV and its comparison with other RHIC BES-I energies [35]. Errors are statistical and systematic errors added in quadrature. The 62.4 and 200 GeV results are from Ref. [32]. In the right bottom panel, the $\langle p_T \rangle$ as a function of mass is plotted for 0–5% centrality at RHIC energies.

where $f(p_T)$ are the fit functions used for different particles as mentioned earlier and the integration is over 0–10 GeV/ c .

Systematic Uncertainties:

Systematic uncertainties on $\langle p_T \rangle$ depend on the extrapolation of spectra. It is estimated by using the various functional forms used for extrapolation of the p_T spectra. For protons, an additional systematic uncertainty on $\langle p_T \rangle$ due to the p_T -dependent proton background

subtraction is estimated and included in quadrature to the total systematic uncertainties. The total uncertainties on $\langle p_T \rangle$ are 7%, 6% and 10% for pions, kaons, and (anti)protons, respectively.

Figure 3.13 shows the mid-rapidity $\langle p_T \rangle$ of positively charged pions, kaons, and protons as a function of $\langle N_{\text{part}} \rangle$ for Au + Au collisions at $\sqrt{s_{\text{NN}}} = 27$ GeV and its comparison with other RHIC energies [32, 35]. The trends are similar in all energies and for their corresponding antiparticles too. The values of $\langle p_T \rangle$ are same within errors at all energies for pions, show a little energy dependence for kaon from lower to higher energies, and for protons, the values of $\langle p_T \rangle$ agrees with each other within errors from lower 7.7 GeV up to 62.4 GeV energies. However, the $\langle p_T \rangle$ values of protons at 200 GeV is higher in comparison with the values at BES-I energies. This approximate similar values in all energies for each particle species implies similar system evolution despite the different initial conditions (energy density and baryon content of the collisions region). The increase of $\langle p_T \rangle$ with centrality implies large radial flow in central collisions. In Au+Au collisions, the increase is dominantly driven by the collective expansion of the system. These dependences are consistent with radial flow observations that it affects the heavier particles more than the lighter ones, and the strength of radial flow is larger in central collisions than in peripheral collisions. The hadron mass dependence of $\langle p_T \rangle$ is shown in the bottom right panel of Fig 3.13 for 0–5% centrality at RHIC energies. The $\langle p_T \rangle$ increases with the hadron mass.

3.7.3 Average Transverse Mass ($\langle m_T \rangle$)

Based on Van Hove’s argument [31] for better understanding of the spectral shape evolution, $\langle m_T \rangle$ has been investigated with the $\langle p_T \rangle$ [36]. Systematic uncertainties on $\langle m_T \rangle - m$ are calculated following the same procedure as that of $\langle p_T \rangle$ which is explained earlier.

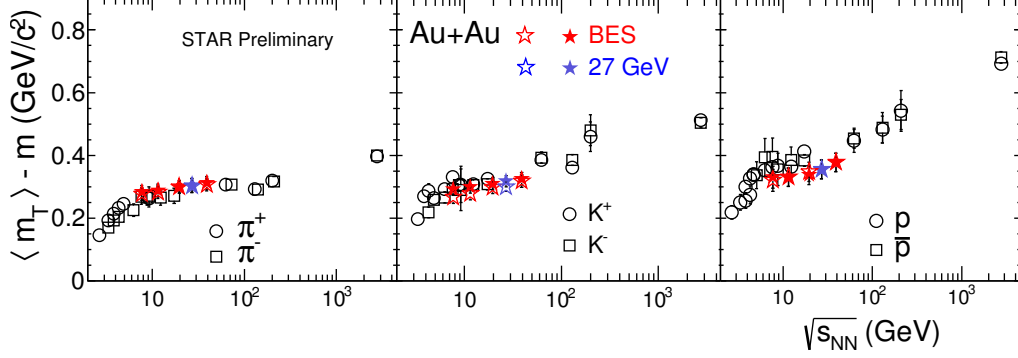


Figure 3.14: The variation of $\langle m_T \rangle - m$ of π^\pm , K^\pm , and p (\bar{p}) as a function of $\sqrt{s_{NN}}$ measured in $|y| < 0.1$ in Au+Au collisions at $\sqrt{s_{NN}} = 27$ GeV along with AGS [37], SPS [38], RHIC [32, 35], and LHC [33] energies. Errors are statistical and systematic errors added in quadrature.

Figure 3.14 shows the energy dependence of $\langle m_T \rangle - m$ for π^\pm , K^\pm , p , and \bar{p} in central (0–5%) Au+Au collisions at $\sqrt{s_{NN}} = 27$ GeV along with Pb+Pb/Au+Au collisions from AGS [37], SPS [38], RHIC [32, 35], and LHC [33] energies. The $\langle m_T \rangle - m$ increases with energy at lower energies, remains almost constant at SPS and lower RHIC BES-I energies, and then increases again towards higher energies up to LHC energy. The behaviour of $\langle m_T \rangle - m$ might indicate the onset of the phase transition [36]. If the system is assumed to be thermodynamic, $\langle m_T \rangle - m$ and $\sqrt{s_{NN}}$ can be related to temperature and entropy of the system ($dN/dy \propto \log \sqrt{s_{NN}}$), respectively. Based on this, the constant value of $\langle m_T \rangle - m$ can be interpreted as a signature of first-order phase transition. $\langle m_T \rangle - m$ could be sensitive to several other effects, which can be understood through proper interpretation of the data [39]. It is observed that with increasing centrality, the values of $\langle m_T \rangle$ increases indicating the development of stronger collective motion in more central collisions and the difference between particles of different mass also increases.

3.7.4 Particle Yields

The total particle multiplicity reflects the total entropy generated in the heavy-ion collision system. p_T spectra provides the information of transverse dynamics of collisions whereas dN/dy versus y provides the information on longitudinal dynamics of collisions. The invariant yield integrated over p_T gives the total integrated particle yield at mid-rapidity is as given below:

$$\frac{dN}{dy} = \int f(p_T) 2\pi p_T dp_T, \quad (3.19)$$

where $f(p_T) = \frac{1}{2\pi p_T} \frac{d^2N}{dp_T dy}$.

The dN/dy for π^\pm , K^\pm , p , and \bar{p} are extracted at mid-rapidity ($|y| < 0.1$) from the measured p_T spectra up to $p_T = 2$ GeV/c and extrapolated to the unmeasured region (up to $p_T = 10$ GeV/c). Extrapolation is done by fitting the p_T spectra through different functions. pions are fitted to the Bose-Einstein function, kaons are fitted with m_T exponential functions whereas for protons and antiprotons, double exponential function is used. The systematic uncertainties on the extrapolated yields are estimated by comparing the extrapolation with those using different fit functions. The functions are given as follows,

$$\begin{aligned} f_{\text{Bose-Einstein}} &= \frac{A}{\exp(m_T/T_{\text{BE}}) - 1} \\ f_{p_T\text{-exponential}} &= A \exp(-p_T/T_{p_T}) \\ f_{m_T\text{-exponential}} &= A \exp(-m_T/T_{m_T}) \\ f_{\text{Boltzmann}} &= A m_T \exp(-m_T/T_B) \\ f_{\text{double exponential}} &= A \exp(-p_T^2/T_1^2) + B \exp(-p_T^2/T_2^2) \end{aligned} \quad (3.20)$$

Table 3.7: Main sources of systematic uncertainties on yields of identified hadrons. The event and track cut variation to study the systematic uncertainties is given in Table 3.6.

Particles	V_z	y	track cuts	PID	extrapolation	correction
π	1%	2%	4%	6%	6%	5%
K	1%	2%	3%	8%	2%	5%
p	1%	4%	6%	7%	7%	5%

Table 3.8: Yields and $\langle p_T \rangle$ of π^\pm in Au+Au collisions at $\sqrt{s_{NN}} = 27$ GeV.

Centrality	dN/dy		$\langle p_T \rangle$ (GeV/c)	
	π^+	π^-	π^+	π^-
0–5 %	172.96 ± 19.02	177.1 ± 19.48	0.409 ± 0.025	0.407 ± 0.025
5–10 %	144.32 ± 15.87	147.5 ± 16.22	0.406 ± 0.025	0.403 ± 0.024
10–20 %	109.35 ± 12.03	111.6 ± 12.27	0.404 ± 0.024	0.399 ± 0.024
20–30 %	74.27 ± 8.17	75.9 ± 8.35	0.401 ± 0.024	0.396 ± 0.024
30–40 %	48.84 ± 5.37	49.95 ± 5.49	0.4 ± 0.024	0.393 ± 0.024
40–50 %	30.67 ± 3.37	31.5 ± 3.47	0.393 ± 0.024	0.385 ± 0.023
50–60 %	18.57 ± 2.04	18.96 ± 2.09	0.380 ± 0.023	0.378 ± 0.023
60–70 %	10.38 ± 1.14	10.63 ± 1.17	0.372 ± 0.023	0.368 ± 0.022
70–80 %	5.14 ± 0.56	5.31 ± 0.58	0.363 ± 0.022	0.362 ± 0.022

Table 3.9: Yields and $\langle p_T \rangle$ of K^\pm in Au+Au collisions at $\sqrt{s_{NN}} = 27$ GeV.

Centrality	dN/dy		$\langle p_T \rangle$ (GeV/c)	
	K^+	K^-	K^+	K^-
0–5 %	31.08 ± 3.11	22.62 ± 2.26	0.603 ± 0.037	0.581 ± 0.035
5–10 %	25.77 ± 2.58	18.7 ± 1.87	0.596 ± 0.036	0.575 ± 0.035
10–20 %	19.44 ± 1.94	14.45 ± 1.44	0.594 ± 0.036	0.567 ± 0.035
20–30 %	12.97 ± 1.29	9.83 ± 0.98	0.586 ± 0.036	0.556 ± 0.034
30–40 %	8.31 ± 0.83	6.23 ± 0.62	0.575 ± 0.035	0.553 ± 0.034
40–50 %	5.17 ± 0.52	3.86 ± 0.39	0.553 ± 0.034	0.535 ± 0.033
50–60 %	2.88 ± 0.29	2.17 ± 0.22	0.547 ± 0.033	0.524 ± 0.032
60–70 %	1.49 ± 0.15	1.1 ± 0.11	0.523 ± 0.032	0.505 ± 0.031
70–80 %	0.66 ± 0.07	0.51 ± 0.05	0.505 ± 0.03	0.488 ± 0.03

Table 3.10: Yields and $\langle p_T \rangle$ of p and \bar{p} in Au+Au collisions at $\sqrt{s_{NN}} = 27$ GeV.

Centrality	dN/dy		$\langle p_T \rangle$ (GeV/c)	
	p	\bar{p}	p	\bar{p}
0–5 %	31.73 ± 4.13	6.0 ± 0.78	0.841 ± 0.051	0.838 ± 0.076
5–10 %	26.51 ± 3.45	5.08 ± 0.66	0.836 ± 0.05	0.833 ± 0.075
10–20 %	19.38 ± 2.52	4.02 ± 0.52	0.787 ± 0.047	0.810 ± 0.073
20–30 %	12.85 ± 1.67	2.92 ± 0.38	0.755 ± 0.046	0.777 ± 0.07
30–40 %	8.99 ± 1.17	1.99 ± 0.26	0.742 ± 0.045	0.723 ± 0.065
40–50 %	5.58 ± 0.73	1.39 ± 0.18	0.726 ± 0.044	0.696 ± 0.063
50–60 %	3.21 ± 0.42	0.83 ± 0.11	0.666 ± 0.04	0.678 ± 0.061
60–70 %	1.72 ± 0.22	0.49 ± 0.06	0.631 ± 0.038	0.627 ± 0.057
70–80 %	0.76 ± 0.09	0.23 ± 0.03	0.589 ± 0.036	0.588 ± 0.053

Systematic Uncertainties:

The systematic uncertainties on the particle yields are obtained by using different fit functions and changing the fit ranges of p_T spectra for the obtained yields. The summary of the systematic uncertainties on particle yields is given in Table 3.7. The systematic uncertainties on total particle yields are dominated by the uncertainties in the extrapolation, which are estimated to be of the order of 6% for pions, 2% for kaons, and 8% for protons and antiprotons. The 5% overall MC uncertainty is added in quadrature. In addition to this, the uncertainty due to different corrections like background, TOF matching efficiency, and tracking efficiency are added in quadrature. Particle identification (PID) represents varying the dE/dx cuts and varying the Gaussian fit ranges to normalised dE/dx distributions. The total systematic errors are of the order of 11%, 10%, and 13% for pions, kaons, and (anti)protons yields respectively. The dN/dy and $\langle p_T \rangle$ of π^\pm , K^\pm , p , and \bar{p} in Au+Au collisions at $\sqrt{s_{NN}} = 27$ GeV at mid-rapidity are given in Table 3.8, 3.9, and 3.10.

Pions are the most abundantly produced charged particles and are produced by pair production, weak decays, resonances, and string fragmentation, etc. The production of (anti)proton yields at mid-rapidity involves two processes, first one is production of a pro-

ton and an antiproton through pair production during the hadronisation stage of the fireball and second is the transport of incident protons from beam rapidity towards mid-rapidity. Transport processes dominate proton production at SPS energies and lower RHIC BES-I energies, the production of antiprotons and protons at higher RHIC-LHC energies are dominated by particle pair production. So, the number of net protons ($p_{\text{net}} = p - \bar{p}$) is significantly smaller at higher RHIC energies which is referred as an almost net-baryon free region at mid-rapidity.

3.7.4.1 Centrality Dependence of dN/dy

The dN/dy is expected to be scaled with the $\langle N_{\text{part}} \rangle$, since the low p_T part of the spectra is dominant in particle abundance and it is produced by soft hadron production process. The $\langle N_{\text{part}} \rangle$ values are estimated using a Glauber Monte Carlo simulation calculation as described earlier.

Figure 3.15 shows the dN/dy normalised to the average number of participated nucleons, $(dN/dy)/\langle 0.5N_{\text{part}} \rangle$ vs. $\langle N_{\text{part}} \rangle$, for π^+ , K^+ , p , and \bar{p} in Au+Au collisions at $\sqrt{s_{\text{NN}}} = 27$ GeV. The errors on the points include both statistical and systematic errors. For the comparison, the $dN/dy/\langle 0.5N_{\text{part}} \rangle$ from the Au+Au system calculated at other BES-I energies [35] along with the published results from higher RHIC energies are also presented [32]. The behaviour of π^- and K^- (not shown) are similar to that of π^+ and K^+ . The yield per participant pair for pions at BES-I energies is almost independent of $\langle N_{\text{part}} \rangle$. The particle production of pions therefore scales with the number of participant pairs. Kaon and proton yields per participant pair increase with average participant number, which suggest that the yields could also depend on the number of nucleon-nucleon binary collisions. The increase in proton yields per participating nucleon with the increasing collision centrality is due to large baryon stopping in the lower energies. However, the N_{part} -scaled \bar{p} yields show weak

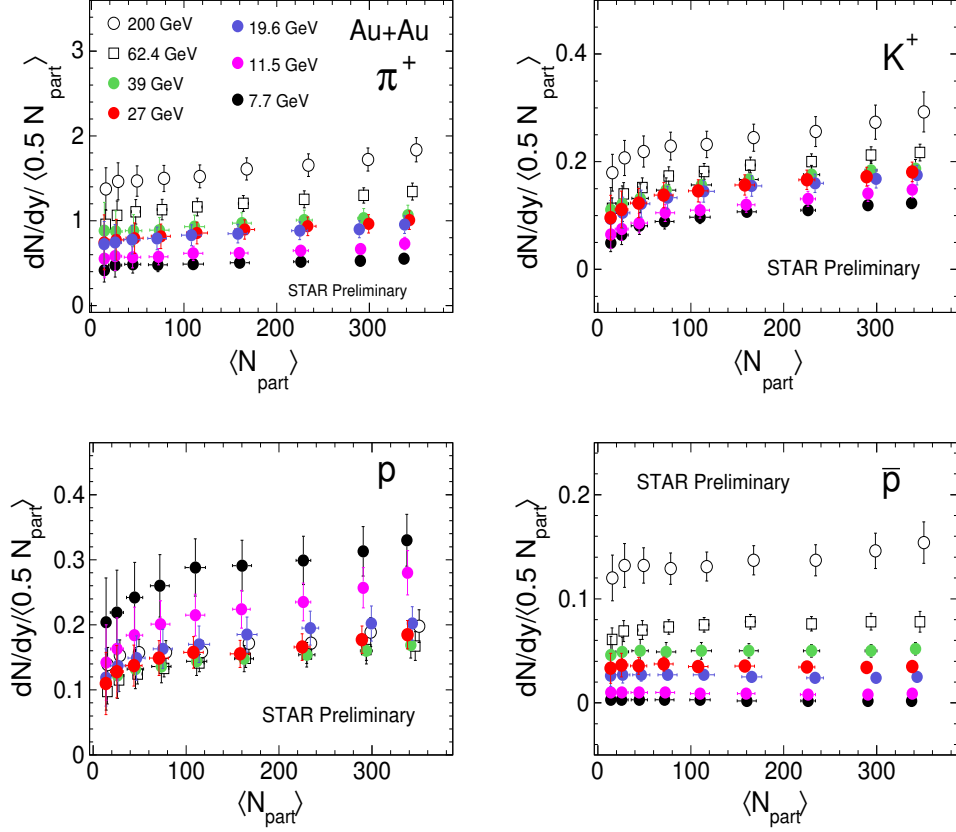


Figure 3.15: dN/dy of π^+ , K^+ , p , and \bar{p} scaled by $\langle 0.5N_{\text{part}} \rangle$ as a function of $\langle N_{\text{part}} \rangle$ in Au+Au collisions at $\sqrt{s_{\text{NN}}} = 27$ GeV are shown along with other RHIC BES-I [35] and top RHIC [32] energies. Errors are the quadratic sum of statistical and systematic errors.

centrality dependence. The particle yields determined at mid-rapidity are sensitive to the initial energy density.

3.7.4.2 Energy dependence of dN/dy

Figure 3.16 shows the dN/dy normalised to the average number of participated nucleons ($dN/dy/\langle 0.5N_{\text{part}} \rangle$) vs. $\sqrt{s_{\text{NN}}}$ for π^\pm , K^\pm , p , and \bar{p} for 0–5% centrality at $\sqrt{s_{\text{NN}}} = 27$ GeV along with other BES-I energies and published AGS [37], SPS [38], RHIC [32, 35], and

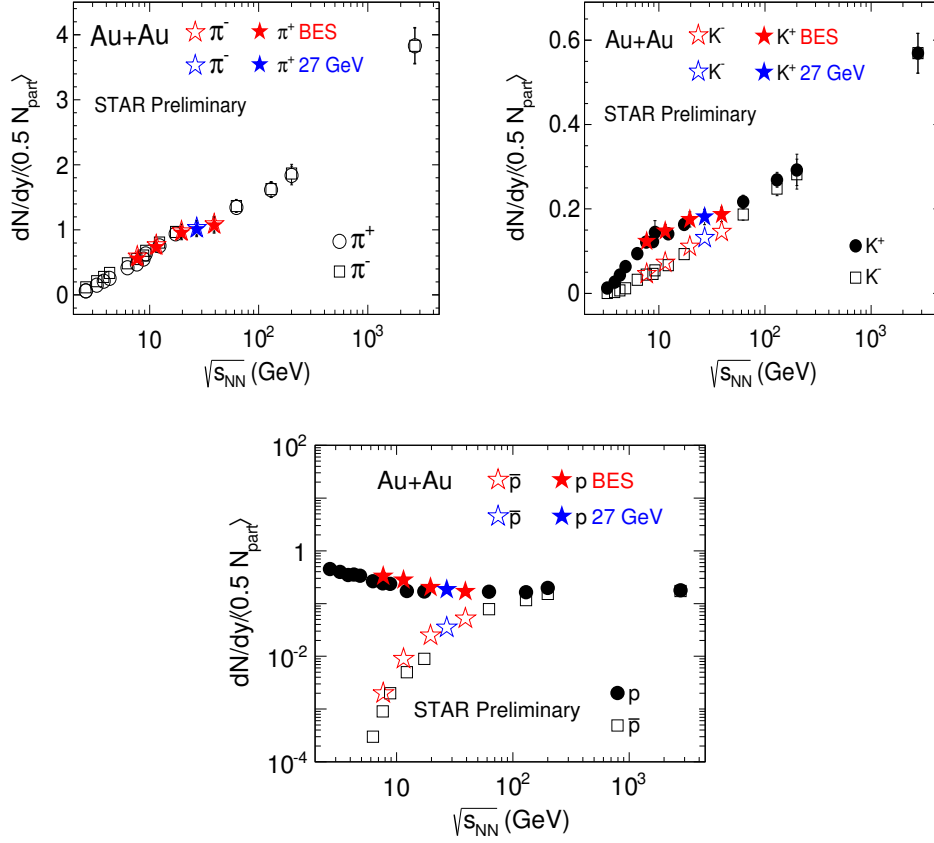


Figure 3.16: dN/dy of π^\pm , K^\pm , p , and \bar{p} scaled by $\langle 0.5N_{\text{part}} \rangle$ as a function of center-of-mass energy including Au+Au collisions at $\sqrt{s_{\text{NN}}} = 27$ GeV along with AGS [37], SPS [38], RHIC [32, 35], and LHC [33] energies. Errors are the quadratic sum of statistical and systematic errors.

LHC [33] energies. The errors on the points include both statistical and systematic errors. The yields of charged pions, kaons, and antiprotons increase with increasing collision energy whereas proton yields decrease with increase of collision energy. The result from $\sqrt{s_{\text{NN}}} = 27$ GeV is in agreement with the general energy dependence trend observed at AGS, SPS, RHIC, and LHC energies.

3.7.5 Particle Ratios

Particle ratios can be used to investigate the bulk properties of the system which include baryon content, strangeness production, and Coulomb potential of the charged source. These are calculated taking the ratios from the obtained different integrated yields. A set of different particle ratios can be collectively used to extract the information on the chemical freeze-out conditions. The ratios of π^-/π^+ , K^-/K^+ , \bar{p}/p , K^+/π^+ , K^-/π^- , and \bar{p}/π^- measured as a function of p_T , centrality, and energy at $\sqrt{s_{NN}} = 27$ GeV in Au+Au collisions are presented here. The error bars represent statistical and the systematic errors added in quadrature. The results are compared with other RHIC energies [32, 35]. The ratio between the charged kaons can tell us about the strangeness production. At mid-rapidity, the ratio between antiprotons and protons provides information on the net baryon content.

Systematic Uncertainties:

Most of the systematic errors cancel in the antiparticle to particle ratios. The common uncertainties due to efficiencies are canceled in the particle ratios. The extrapolation uncertainties are treated as uncorrelated in the unlike particle ratios (K^\pm/π^\pm , \bar{p}/π^- , etc.) and are cancelled for antiparticles to particle ratios (π^-/π^+ , K^-/K^+ , \bar{p}/p). So, all the correlated sources of uncertainty have been considered and cancelled in the ratios.

3.7.5.1 p_T Dependence of Particle Ratios

Antiparticle to particle ratios are flat in p_T as shown in Fig. 3.17 and having same values within errors in all centralities. Since we observe a flat kaon ratio versus p_T we can conclude that the K^+ , and K^- freeze-out at approximately the same time.

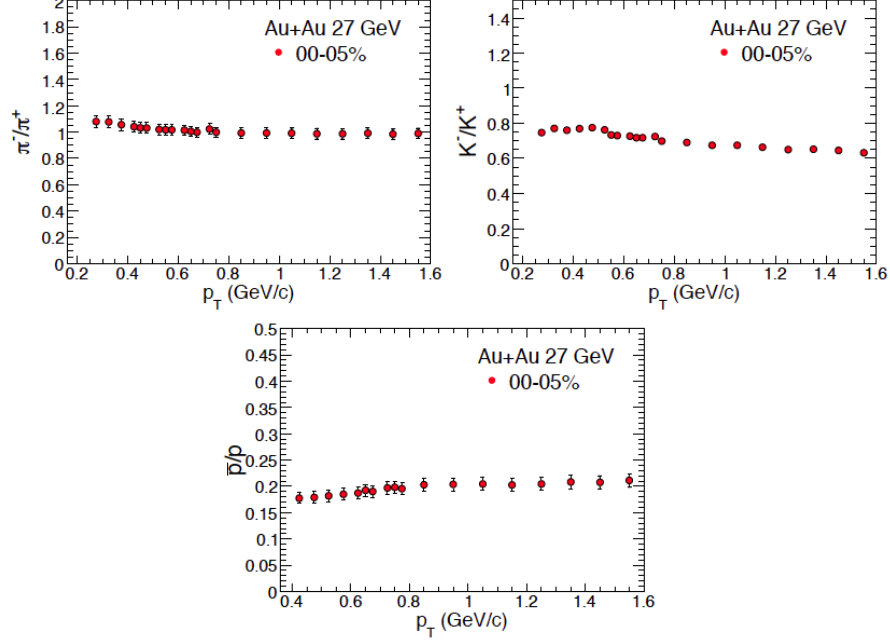


Figure 3.17: π^-/π^+ , K^-/K^+ , and \bar{p}/p as a function of p_T for 0–5% centrality in Au+Au collisions at $\sqrt{s_{NN}} = 27$ GeV.

3.7.5.2 Centrality Dependence of Particle Ratios

Figure 3.18 and 3.19 show the centrality dependence of different particle ratios in Au+Au collisions at $\sqrt{s_{NN}} = 27$ GeV and compared with other RHIC energies [32, 35]. Both statistical and systematic errors are added in quadrature for particle ratios.

The π^-/π^+ ratio shows no strong dependence on either centrality or colliding system, so there is no hard binary collision dependence in their production. The ratio is nearly equal to 1. The particles ratios do not depend on centrality tells us that the pion particle production mechanism is not significantly different from peripheral to central collisions.

The flat K^-/K^+ ratios indicate that the production mechanism do not change across centrality. It also suggests that the K^- and K^+ undergo similar collective flow. This result agrees with what we see at lower energies, where the kaon ratio is also flat as a function of

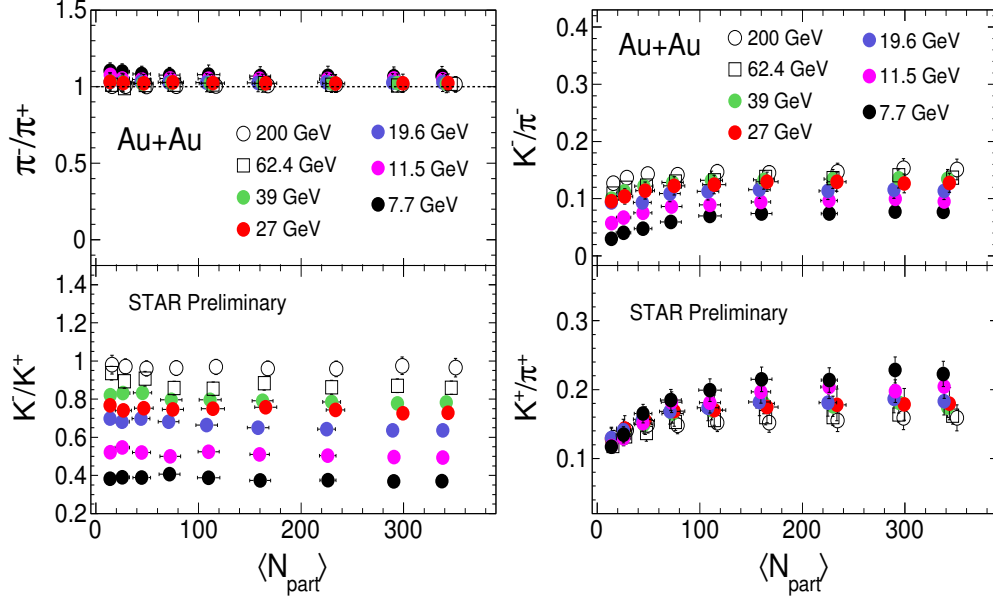


Figure 3.18: π^-/π^+ , K^-/K^+ , K^-/π^- , and K^+/π^+ as a function of $\langle N_{\text{part}} \rangle$ in Au+Au collisions at $\sqrt{s_{\text{NN}}} = 27$ GeV. The results are compared with other RHIC BES-I [35] and top RHIC [32] energies. Errors are the quadratic sum of statistical and systematic errors.

centrality.

The \bar{p}/p ratio is lower in central collisions than in peripheral collisions. This is consistent with that more annihilation of protons and antiprotons in central collisions relative to peripheral collisions. Since a central collision creates a large volume of hot and dense nuclear matter, the small centrality dependence of \bar{p}/p might be interpreted as the antiprotons being absorbed inside that large collision region. Larger baryon stopping in central region might also be the reason of this centrality dependence. The slight decrease in the \bar{p}/p ratio reflects the rich collision dynamics at RHIC; both initial baryon transfer and final stage hadronic rescatterings are important for the observation.

Then we look at the centrality dependence of the kaon to pion ratios as shown in the right panel of Fig. 3.18. The ratios in Au+Au collisions show a small increase with increasing centrality. The ratios K^+/π^+ and K^-/π^- gradually increase from peripheral to mid-central

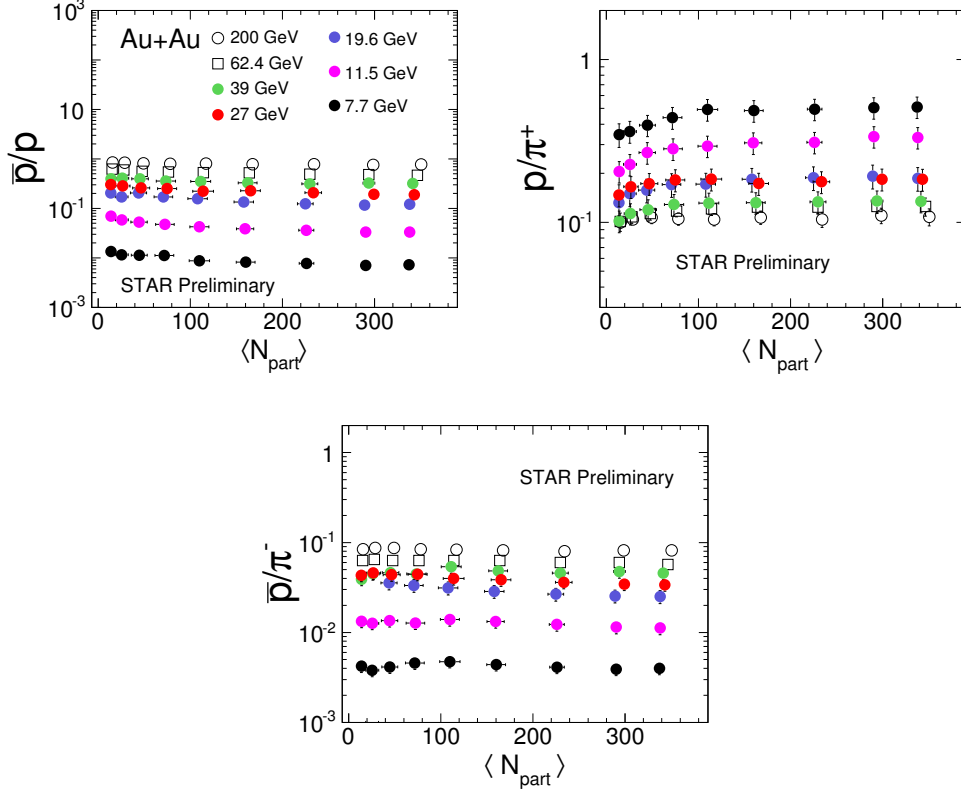


Figure 3.19: \bar{p}/p , p/π^+ , and \bar{p}/π^- in Au+Au collisions as a function of $\langle N_{\text{part}} \rangle$ at $\sqrt{s_{\text{NN}}} = 27$ GeV. The results are compared with other RHIC BES-I [35] and top RHIC [32] energies. Errors are the quadratic sum of statistical and systematic errors.

and saturate in mid-central to central collisions. The enhancement of the p_T integrated K/π ratio in more central collisions is related to strangeness equilibration in various thermal models [40, 41]. Thermodynamic models explain the increase of the K/π ratios with the system size from peripheral to central based on the transition from the canonical to grand-canonical ensemble [42, 43]. The antiproton is the lightest antibaryon. Most high-mass antibaryons decay into antiprotons. So, \bar{p}/π^- characterises well antibaryon production relative to total particle multiplicity. As mentioned earlier, the inclusive \bar{p} yield reported here, is the sum of the primordial \bar{p} yield and the weak-decay contributions. The \bar{p}/π^- is indepen-

dent on the number of participants while pair production may be the dominant mechanism for the \bar{p}/π^- . At higher RHIC energies, the \bar{p}/π^- ratio does not seem to be affected much by the net-baryon density, suggesting that antibaryon absorption is not a significant effect at these energies. However, at low energies, baryon stopping and the effect of net-baryon density are much stronger at low energies.

Unlike antibaryons, baryons come from two sources: pair production together with antibaryons and transport from the initial colliding nuclei at beam rapidities, which can be obtained from the difference between baryon and antibaryon yields. Baryon transport occurs very early in the collision and affects the subsequent evolution of the collision system. Further understanding of baryon transport can shed more light on the evolution of heavy-ion collisions. The p/π^+ ratios in the other centralities in Au+Au show a clear and consistent trend with slight increasing as the collisions become more central for lower RHIC energies (7.7, 11.5 GeV) however, for mid to higher RHIC energies (27–200 GeV), p/π^+ is constant over centrality as shown in Fig. 3.19.

3.7.5.3 Energy Dependence of Particle Ratios

Figure 3.20 shows the variation of different particle ratios as a function of center-of-mass energy in central Au+Au collisions at $\sqrt{s_{NN}} = 27$ GeV and its comparison with the results from AGS [37], SPS [38], RHIC [32, 35], and LHC [33] energies. The variation of K^-/K^+ as a function of \bar{p}/p for 0–5% centrality from SPS–LHC energies has also been shown. Errors are the quadratic sum of statistical and systematic errors.

As the collision energy increases, π^-/π^+ ratio decreases whereas K^-/K^+ ratio rise systematically. At higher energy, pair productions dominate resonance decays. Pair production results in the same number of positive and negative pions. Following this logic, the π^-/π^+ ratio is supposed to reach unity as the energy goes up. The energy dependence of

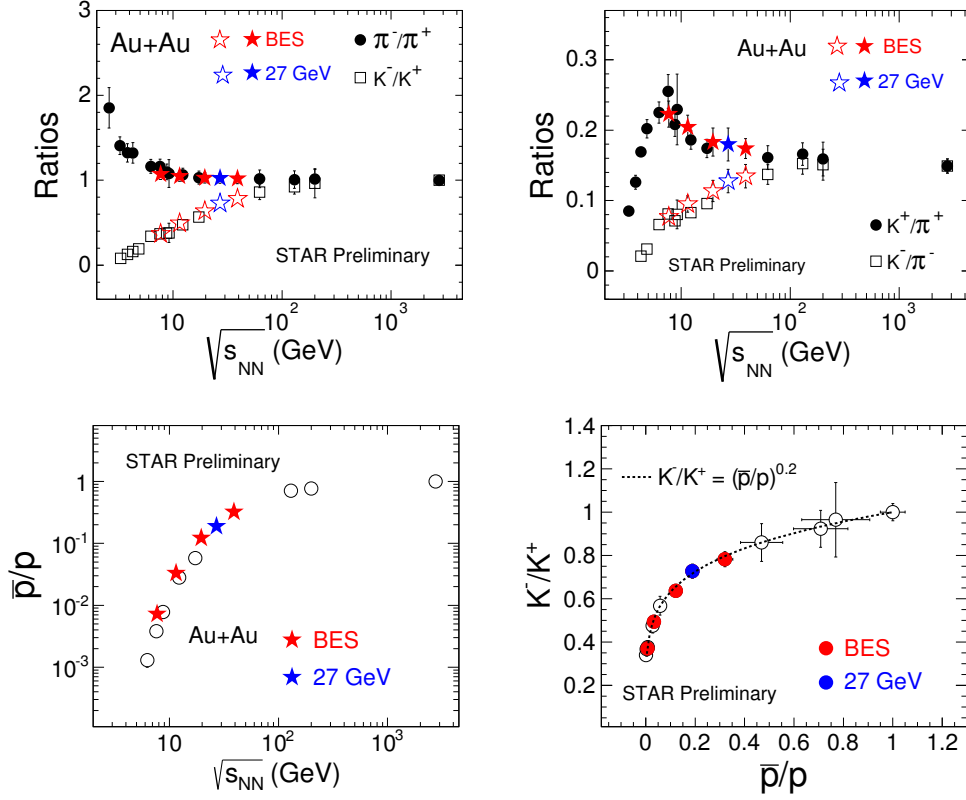


Figure 3.20: Particle ratios as a function of center-of-mass energy in Au+Au collisions at $\sqrt{s_{NN}} = 27$ GeV. The results are compared with AGS [37], SPS [38], RHIC [32, 35], and LHC [33] energies. Right bottom: the variation of K^-/K^+ as a function of \bar{p}/p for 0–5% centrality from SPS-LHC energies. Errors are the quadratic sum of statistical and systematic errors.

the pion ratio can be interpreted as a result of Coulomb interactions between the emitting source and the outgoing charged particles. The Coulomb force acts on all charged particles at any distance. Therefore, the produced charged kaons, protons, and antiprotons feel the effects as well. The effects on those heavy particles however, are small compared to the effects on the pions.

The K^-/K^+ ratio is indicative of the relative contribution of associated and pair production. The associated production mechanism can only produce K^+ via $N + N \rightarrow N + X + K^+$, π

$+ N \rightarrow X + K^+$, where N is nucleon and X is hyperon (Λ or Ξ), while the pair production mechanism produces K^+ and K^- via $N + N \rightarrow N + N + K^+ + K^-$. The rise of K^-/K^+ ratio as a function of energy can be attributed to the nature of kaon production channels. At lower energy, the associated production dominates due to a lower energy threshold. As the energy increases, the pair production, which produces the same number of K^+ and K^- , becomes more significant. With increasing energy, the net baryon density decreases and thus the associated production of K^+ also decreases, while pair production increases due to gluon-gluon fusion into strange quark-antiquark pairs [44, 45]. All these results combined, when compared with previous experiments, seem to be consistent with an enhancement in the strangeness production. At lower energies due to the non-zero net baryon density in the collisions zone, the associated production of kaons with hyperons will be different from those produced with antihyperons.

To further study the strangeness production, we look at the ratios of charged kaons, which carry the bulk of produced strangeness, to pions, the most abundantly produced hadron from the collisions, the K^+/π^+ and K^-/π^- ratios as functions of collision energy. The K^+/π^+ ratio increases monotonically with energy and reaches a maximum at around 7–8 GeV energy before dropping down at higher energy. In contrast, the negative ratio steadily increases with the energy. Different models also predict that the strange yields relative to non-strange yields reach a maximum near $\sqrt{s_{NN}} = 7.62$ GeV. However, the observed peak of the excitation function (“strangeness horn”) is sharper than expected [46, 47, 48]. The reason of such behaviour can be explained in the following way. K^+ is made of the $u\bar{s}$ quarks and the K^- is made of $\bar{u}s$ quarks. Since the colliding beams are made of protons (uud) and neutrons (udd), there is a net number of up quarks to start the process. Therefore, we know that all antiup, strange and antistrange quarks are formed in the initial fireball, while the up quarks can come from either the colliding nuclei or they could have been created in the fireball. The K^-/π^- increases with energy while K^+/π^+ increases then

decreases as a consequence of the net baryon density effect.

From the ratio \bar{p}/p as a function of energy as shown in the bottom left panel of Fig. 3.20, we can see that there is a dramatic increase of the \bar{p}/p ratio from SPS to RHIC and up to LHC energies. We can tell from \bar{p}/p ratio vs. $\sqrt{s_{NN}}$ that the baryon density changes as a function of energy. At RHIC–LHC energies, the net number of protons is close to zero, most of the baryons are produced as pairs. In heavy-ion collisions at AGS and CERN SPS energies, most of the protons are stopped at mid-rapidity.

We have also observed that the ratio of p/π decreases with the increasing collision energy. This could be due to higher pion production at low energies. Pions are produced primarily via resonance decays. Excited nucleons can turn into delta resonances, that in turn decay. The strong decay channel of the lightest delta resonance, $\Delta(1232) \rightarrow N + \pi$, results in a large number of pions. In addition, if we neglect rescatterings, the only three possible primary reactions in Au+Au collisions are $p+p$, $p+n$, and $n+n$. These three reactions create different numbers of pions.

The K^-/K^+ ratio vs. \bar{p}/p for 0–5% centrality in Au+Au at $\sqrt{s_{NN}} = 27$ GeV together with results from AGS [37], SPS [38], RHIC, other BES-I energies [32, 35] and ALICE [33] have been shown in bottom right panel of Fig. 3.20. Both ratios are affected by the net baryon content; they show a strong correlation. It is worth noting that at low energies, the absorption of antiprotons in the baryon-rich environment plays a vital role.

3.8 Summary

We have studied the identified particle production in Au+Au collisions at $\sqrt{s_{NN}} = 27$ GeV. The transverse momentum distributions of pion, kaon, proton, and antiproton are presented for 0–5%, 5–10%, 10–20%, 20–30%, 30–40%, 40–50%, 50–60%, 60–70%, and 70–80% centrality bins. The bulk properties are studied by measuring the identified hadron dN/dy ,

$\langle p_T \rangle$, and particle ratios. The results are compared with the other BES-I energies and the corresponding published results from other collision energies and experiments. The collision centrality dependence for the new results is similar to that at higher beam energies.

The yields of charged pions, kaons, and antiprotons decrease with decreasing collision energy. However, the centrality dependence of yields for antiprotons is weak. The dependencies of $\langle p_T \rangle$ on $\langle N_{\text{part}} \rangle$ is similar to other RHIC energies. An increase in $\langle p_T \rangle$ with increasing hadron mass is observed. The π^-/π^+ ratio is close to unity. The increase in K^-/K^+ ratio with energy shows the increasing contribution to kaon production due to pair production. The increase in \bar{p}/p ratio from central to peripheral collisions reflects the high baryon stopping at mid-rapidity at central collisions as compared to that in peripheral collisions. The K^-/π^- ratio increases with increasing energy and also from peripheral to central collisions. The centrality dependence K^+/π^+ is similar in all energies, i.e. the ratio increases from peripheral to central collisions. The p/π^+ ratio decreases with increasing energy.

The measured p_T distributions of identified particles can be used to extract the bulk properties of matter like kinetic freeze-out, where the elastic collisions among the hadrons have ceased. The measured integrated yields can be used to extract the parameters of chemical freeze-out, where the inelastic collisions among hadrons have stopped, which reflect the information about early stages. The detail study of centrality and energy dependence of chemical and kinetic freeze-out parameters at RHIC BES-I energies along with systematic study of freeze-out parameters from AGS, SPS, RHIC, and LHC will be discussed in the subsequent chapters.

Bibliography

- [1] J. C. Collins and M. J. Perry; Phys. Rev. Lett. 34, 1353 (1975); E. V. Shuryak, Phys. Rept. 61, 71 (1980), *ibid.* 115, 151 (1984; J. Adams *et al.* (STAR Collaboration), Nucl. Phys. A 757, 102 (2005).
- [2] P. Braun-Munzinger *et al.*, arXiv:1101.3167 (2011); B. Mohanty, Nucl. Phys. A 830, 899C (2009).
- [3] Y. Aoki *et al.*, Nature 443, 675 (2006); Phys. Lett. B 643, 46 (2006); A. Bazavov *et al.*, Phys. Rev. D 85, 054503 (2012).
- [4] S. Ejiri, Phys. Rev. D 78, 074507 (2008); E. S. Bowman and J. I. Kapusta, Phys. Rev. C 79, 015202 (2009).
- [5] S. Gupta *et al.*, Science 332, 1525 (2011).
- [6] L. Kumar (STAR collaboration), J. Phys. G, 38, 124145 (2011); S. Das (STAR Collaboration), arXiv:1412.0499.
- [7] “STAR Table Structures for TPC Data Distribution”,
<https://drupal.star.bnl.gov/STAR/starnotes/public/sn0325>.
- [8] K. H. Ackermann *et al.*, Nucl. Instr. Meth. A 499, 624 (2003).
- [9] H. J. Crawford *et al.*, Nucl. Instr. Meth. A 499, 766 (2003).

- [10] W. J. Llope *et al.*, Nucl. Instr. Meth. A 522, 252 (2004).
- [11] J. Abele *et al.*, Nucl. Instr. Meth. A 499, 692 (2003).
- [12] D. Kharzeev and M. Nardi, Phys. Lett. B 507, 121 (2001).
- [13] R. J. Glauber, in Lectures in Theoretical Phys, edited by W. E. Brittin and L. G. Dunham (Interscience, N.Y., 1959), Vol. 1, p. 315.
- [14] B. B. Back *et al.* (PHOBOS collaboration), Phys. Rev. C 70, 021902 (2004).
- [15] M. Shao, O. Barannikova, X. Dong, Y. Fisyak, L. Ruan, P. Sorensen, and Z. Xu, Nucl. Instr. Meth. A 558, 419 (2006).
- [16] S. Eidelman *et al.*, Phys. Lett. B 592, 1 (2004); H. Fanchiotti, C. A. G. Canal and M. D. Marucho, hep-ph/0305310.
- [17] W. M. Yao *et al.* (Particle Data Group), J. Phys. G 33, 1 (2006).
- [18] H. Bichsel, Nucl. Instr. Meth. A 562, 154 (2006).
- [19] M. Aguilar-Benitez *et al.*, Z. Phys. C 50, 405 (1991).
- [20] B. I. Abelev *et al.* (STAR Collaboration), Phys. Rev. C 79, 034909 (2009).
- [21] H. Long, Ph.D. thesis, UCLA, 2002.
- [22] <http://wwwinfo.cern.ch/asd/geant/geant4public/G4UsersDocuments/Welcome/IntroductionToGeant4/html/introductionToGeant4.html>.
- [23] P. Nevski, <http://www.star.bnl.gov/STARAFS/comp/simu/gstar/gstar.html>.
- [24] W. M. Yao *et al.* (Particle Data Group), J. Phys. G 33, 1 (2006).
- [25] M. Gyulassy and X. N. Wang, Comput. Phys. Commun. 83, 307 (1994).

- [26] J. Adams *et al.* (STAR Collaboration), Phys. Rev. Lett. 92, 112301 (2004).
- [27] J. Adams *et al.* (STAR Collaboration), Phys. Rev. C 70, 041901 (2004).
- [28] B. I. Abelev *et al.* (STAR Collaboration), Phys. Rev. C 79, 034909 (2009).
- [29] E. Schnedermann, J. Sollfrank, and U. Heinz, Phys. Rev. C 48, 2462 (1993).
- [30] E. Schnedermann and U. W. Heinz, Phys. Rev. C 50, 1675 (1994).
- [31] L. Van Hove, Phys. Lett. B 118, 138 (1982).
- [32] J. Adams *et al.* (STAR Collaboration), Phys. Rev. Lett. 91, 072304 (2003); Phys. Rev. Lett. 91, 172302 (2003); B. I. Abelev *et al.* (STAR Collaboration), Phys. Rev. Lett. 97, 152301 (2006); Phys. Lett. B 655, 104 (2007), J. Adams *et al.* (STAR Collaboration), Phys. Rev. Lett. 92, 112301 (2004); B. I. Abelev *et al.* (STAR Collaboration), Phys. Rev. C 79, 034909 (2009); *ibid.* Phys. Rev. C 81, 024911 (2010).
- [33] B. Abelev *et al.* (ALICE Collaboration), Phys. Rev. Lett. 109, 252301 (2012); B. Abelev *et al.* (ALICE Collaboration), Phys. Rev. C 88, 044910 (2013).
- [34] L. Kumar (for the STAR Collaboration), arXiv:1408.4209.
- [35] L. Kumar (STAR Collaboration), Nucl. Phys. A 904, 256c (2013); S. Das (STAR Collaboration), Nucl. Phys. A 904, 891c (2013); S. Das (STAR collaboration), J. Phys. Conf. Ser. 509, 012066 (2014).
- [36] M. I. Gorenstein, M. Gazdzicki, and K. A. Bugaev, Phys. Lett. B 567, 175 (2003).
- [37] L. Ahle *et al.* (E866 Collaboration and E917 Collaboration), Phys. Lett. B 490, 53 (2000); L. Ahle *et al.* (E866 Collaboration and E917 Collaboration), Phys. Lett. B 476, 1 (2000); J. L. Klay *et al.* (E895 Collaboration), Phys. Rev. Lett. 88, 102301 (2002); J. Barrette *et al.* (E877 Collaboration), Phys. Rev. C 62, 024901 (2000);

- Y. Akiba *et al.* (E802 Collaboration), Nucl. Phys. A 610, 139c (1996); L. Ahle *et al.* (E802 Collaboration), Phys. Rev. C 60, 064901 (1999); L. Ahle *et al.* (E802 Collaboration and E866 Collaboration), Phys. Rev. C 60, 044904 (1999); L. Ahle *et al.* (E802 Collaboration), Phys. Rev. C 57, 466 (1998).
- [38] S. V. Afanasiev *et al.* (NA49 Collaboration), Phys. Rev. C 66, 054902 (2002); C. Alt *et al.* (NA49 Collaboration), Phys. Rev. C 77, 024903 (2008); *ibid.* 73, 044910 (2006); T. Anticic *et al.* (NA49 Collaboration), Phys. Rev. C 69, 024902 (2004).
- [39] B. Mohanty *et al.*, Phys. Rev. C 68, 021901 (2003).
- [40] M. Kaneta and Nu Xu, arXiv:0405068 (2004).
- [41] J. Cleymans, B. Kampfer, M. Kaneta, S. Wheaton, and N. Xu, Phys. Rev. C 71, 054901 (2005).
- [42] J. Rafelski and M. Danos, Phys. Lett. B 97, 279 (1980).
- [43] R. Hagedorn and K. Redlich, Z. Phys. C 27, 541 (1985).
- [44] J. Rafelski and B. Muller, Phys. Rev. Lett. 48, 1066 (1982).
- [45] R. Koch *et al.*, Phys. Rep. 142, 167 (1986).
- [46] F. Wang *et al.*, Phys. Lett. B 489, 273 (2000).
- [47] F. Wang and N. Xu, Phys. Rev. C 61, 021904 (2000).
- [48] P. Braun-Munzinger *et al.*, Nucl. Phys. A697, 902 (2002).

Chapter 4

Study of Freeze-out Dynamics in STAR at RHIC BES Program

The p_T distributions and dN/dy of identified particles near mid-rapidity are discussed in the previous chapter. In this chapter, the p_T distributions, particle yields, and particle ratios are used to extract the kinetic and chemical freeze-out parameters in Au+Au collisions at RHIC energies. The main objective of this work is to study the production of particles in relativistic heavy-ion collisions in the light of a statistical-thermodynamic model.

4.1 Introduction

One of the major objective of the relativistic heavy-ions collision experiment is to create necessary conditions to investigate the phase diagram of hadronic matter, especially the expected phase transition to QGP state. In these experiments, hadrons are the major observable, whose yields and kinematic information can be used to characterise the formed system. As a result of ultra-relativistic collision between two heavy-ions, a fireball is formed which then rapidly thermalises. The enormous amount of energy deposited in the

fireball results in large pressure gradients that drives the expansion of the fireball. As the system expands, the average distance between hadrons becomes larger than the interaction length. At this point, the hadrons cease to interact and stream out freely to the detectors. The surface of last scattering is called as freeze-out surface. The dynamical informations, e.g., the number of particles, momentum and so on are frozen at that time [1]. Since the produced hadrons interact with each other via inelastic (where particles identities change) and elastic (where particles identities do not change) collisions, it is possible to have two distinct freeze-outs. One is chemical freeze-out (CFO), where inelastic collisions cease and particle yields get fixed. Other one is thermal/kinetic freeze-out (KFO), where elastic collisions cease and particle mean free path becomes higher than the system size, which forbids the elastic collision of the constituents in the system.

The CFO surface is determined by analysing the measured hadron yields or ratios, which are described by chemical potentials and temperature assuming the system to be in thermal and chemical equilibrium state [2, 3]. The KFO surface can be determined by studying the data of p_T distributions of the produced particles, which provide informations about dynamical evolution and collective flow [4, 5, 6]. In general, freeze-out could be a complicated process involving different types of particles and reactions which switch off at different times during the evolution of the system. The reactions with lower cross-sections are expected to be switch-off earlier in time at higher densities or temperature compared to reactions with higher cross-sections. Hence, the kinetic freeze-out, which corresponds to elastic reactions, occurs later in time compared to the chemical freeze-out, which corresponds to inelastic reactions.

4.2 QCD Phase Diagram and BES-I program

Quantum chromodynamics has three conserved charges, namely baryon number B , electric charge Q , and strangeness S . Thus, the equilibrium thermodynamic state of QCD matter is completely determined by temperature T and three chemical potentials μ_B , μ_Q , and μ_S corresponding to B , Q , and S , respectively. As it has been mentioned earlier, the BES-I program of STAR at RHIC primarily aimed at an experimental study of the QCD phase diagram in terms of T and μ_B . Several collision energies were used to create systems which corresponds to various initial coordinates in T and μ_B . As the systems evolve, adiabatic expansion is governed by the QGP equation of state. Therefore, as the system expands, T is reduced and μ_B , which is a measure of the excess of quarks relative to antiquarks, may also evolve. The excess of quarks is due to the valence quarks of the stopped participant baryons from two colliding nuclei.

4.3 Chemical Freeze-out

At chemical freeze-out, inelastic collisions stop and particle yields/ratios get fixed. The statistical models have been quite successful in describing the particle production in heavy-ion collision experiments across a wide range of beam energies with a few thermal parameters to be fitted from data [2, 3]. Apart from heavy-ion collisions, even in systems like $e^+ + e^-$ and $p+p$, statistical models have been found to be successful in describing the particle multiplicities [7, 8]. By comparing experimentally measured hadron yields to thermal model predictions, the thermodynamic state of the fireball can be deduced at the time of CFO. However, the locations of the phase boundary and the critical point basically depends on model assumptions [9].

Here we discuss a detailed study of chemical freeze-out dynamics from peripheral to central Au+Au collisions at various BES-I energies $\sqrt{s_{NN}} = 7.7, 11.5, 19.6, 27$, and 39 GeV

along with top RHIC energies $\sqrt{s_{\text{NN}}} = 62.4$ and 200 GeV. Experimental particle yields and ratios are used in a statistical thermal model in both grand canonical ensemble (GCE) and strangeness canonical ensemble (SCE) approach. The extracted chemical freeze-out parameters are chemical freeze-out temperature (T_{ch}), baryon chemical potential (μ_B), strangeness chemical potential (μ_S), and strangeness saturation factor (γ_S). The energy and centrality dependence of extracted chemical freeze-out parameters in Au+Au collisions at above mentioned RHIC energies are studied.

4.4 The Statistical-Thermodynamic Model

Thermal and/or statistical interpretation of the particle production is a common approach for ultra-relativistic heavy-ion collisions. The measured particle yields can be explained within the framework of a statistical model which assumes full thermal and chemical equilibrium of the hadronic matter at freeze-out. The system created in a relativistic heavy-ions collisions can be treated as an ideal gas of hadrons and resonances, which is described by local thermal distributions, by considering the freeze out parameters common to all species of particles [10]. The gas of hadrons, consist of light (u and d) quarks and/or strange (s) quarks. The hadrons containing heavy quarks (c, b, and t) are not included in the model because those heavy hadrons are not created by thermal production due to the suppression of the Boltzmann factor.

In statistical analysis, it is possible to enforce various conservations as exact (canonical ensemble) or partial (strangeness-canonical ensemble). In heavy-ion collisions, a large number of particles are produced, so that the grand-canonical treatment is quite reasonable. However, when dealing with peripheral or central collisions of low energy, the strangeness-canonical or canonical treatment is applicable [11].

4.5 The THERMUS Package

There are different formulations of statistical thermodynamic model which are publicly available to study the particle production in relativistic heavy-ion collisions such as THERMUS [10], SHARE (Statistical HAdronization with REsonances) [12], and THERMINATOR (Thermal heavy-ion generator) [13]. We have opted to use THERMUS formulation of statistical-thermodynamic model to study the particle production at RHIC BES-I energies. THERMUS consists of a set of classes and functions developed in C++ which is based on object-oriented programming ROOT [14]. Three distinct formalism are implemented in THERMUS, i.e. grand-canonical, strangeness-canonical, and canonical. A particle list has been provided by THERMUS which includes all mesons and baryons with u, d, and s quarks of mass less than $2.6 \text{ GeV}/c^2$. These particles are listed in the July 2002 Particle Physics Booklet [15]. For each unstable particle in the particle list, THERMUS includes a decay text file. Thermal model analysis of heavy-ion collision data require the calculation of both primordial particle densities and contributions from resonance decays. There are certain set of parameters for each ensemble. First, a set of thermalised particles with a set of parameters with relevant ensemble under consideration are required as input to model. Then it is possible to calculate all primordial quantities, i.e. number density as well as energy, entropy density, and pressure. With specific decay informations of the constituent hadrons, the final particle densities can be determined and compared with experiment. The output is the best fit to experimental data. In all ensembles, ROOT TMinuit class has been used in THERMUS to fit experimental data. The standard χ^2 -minimisation method yields the best-fit thermal parameters. Mass and widths of resonances can be included in the calculations. THERMUS provides the different decay chains for each experimental input in order to match the specific feed-down corrections in model with experimental data.

4.5.1 The Grand-Canonical Ensemble

Grand-canonical ensemble is mostly used in heavy-ion collisions due to large number of particle production within a small volume of the system. Within this ensemble, the quantum numbers of the system B, Q , and S are conserved on an average through the action of chemical potentials μ_B, μ_Q , and μ_S , respectively. Partition function is basically required to calculate the different thermodynamic observables of a system. Depending on the ensemble, the form of the partition function changes. It relates the microscopic properties of a system with the thermodynamic parameters of a macroscopic sample.

Considering an ideal gas composed of a single hadron species i with hadronic energy levels $\{\epsilon_i^1, \epsilon_i^2, \dots\}$ and corresponding occupation numbers $\{n_i^1, n_i^2, \dots\}$. The grand-canonical partition function can be written as [10, 11],

$$Z_i^{\text{GCE}}(T, V, \mu_i) = \text{Tr} \left[e^{-\beta (\hat{H} - \mu_i \hat{N})} \right], \quad (4.1)$$

where $\mu_i = B_i \mu_B + S_i \mu_S + Q_i \mu_Q$. B_i, S_i , and Q_i are the baryon number, strangeness, and charge, respectively, of species i and μ_B, μ_S , and μ_Q are the corresponding chemical potentials of hadron species i . $\beta \equiv \frac{1}{T}$, where T is the chemical freeze-out temperature, H is the hamiltonian operator, and N is the number operator. The above equation can be simplified as,

$$Z_i^{\text{GCE}}(T, V, \mu_i) = \prod_{\text{states } j} \left[1 \pm e^{-\beta (\epsilon_i^j - \mu_i)} \right]^{\pm 1} \quad (4.2)$$

In the large volume limit, the logarithm of the partition function is

$$\ln Z_i^{\text{GCE}}(T, V, \mu_i) = \frac{g_i V}{(2\pi)^3} \int d^3 p \ln (1 \pm e^{-\beta (E_i - \mu_i)})^{\pm 1}, \quad (4.3)$$

where V is the fireball volume, p is the momentum, g_i is the degeneracy, and $E_i = \sqrt{p^2 + m_i^2}$, where m_i is the particle mass.

Once the partition function is known, all thermodynamic quantities such as particle multiplicities (N_i^{GCE}), entropy (S^{GCE}), pressure (P^{GCE}), and energy (E^{GCE}) can be calculated by simple differentiation, From Eq. 4.3 the particle density is calculated as [10],

$$N_i^{\text{GCE}} = T \frac{\partial}{\partial \mu_i} \ln [Z] \quad (4.4)$$

From Eq. 4.4, the particle density is calculated as:

$$n_i = \frac{N_i^{\text{GCE}}}{V} = \frac{g_i}{2\pi^2} \sum_{k=1}^{\infty} (\pm 1)^{k+1} \frac{m_i^2 T}{k} K_2 \left(\frac{km_i}{T} \right) \exp(\beta k \mu_i), \quad (4.5)$$

where K_2 is second order Bessel function. The plus sign is for bosons and the minus sign is for fermions. The Maxwell–Boltzmann approximation (considering only first term in Eq. 4.5, $k = 1$) is generally sufficient for most particles. The use of quantum statistics (Fermi-Dirac or Bose-Einstein) requires the computation of infinite sums or integrals number, which considerably complicates the problem. Furthermore, Bose-Einstein distribution function is included in the integrands of all thermodynamic quantities for bosons, and diverges when,

$$e^{\beta(E_i - \mu_i)} \equiv e^{\beta(\sqrt{m_i^2 + p^2} - \mu_i)} = 1 \quad (4.6)$$

So, to avoid Bose-Einstein condensation, it is necessary that the chemical potentials of all bosons in hadron gas are smaller than their masses ($\mu_i \leq m_i$). An additional factor $\gamma_s^{|S_i|}$ is used to account for the lack of strangeness chemical equilibration observed in heavy-ion collisions, where γ_s is strangeness saturation factor and $|S_i|$ is the number of strange and antistrange quarks in species i . So, $\gamma_s^{|S_i|}$ is multiplied in the partition function of each ensemble. The particle density in GCE is modified as $n_i \rightarrow \gamma_s^{|S_i|} n_i$.

The grand-canonical ensemble contains the following parameters:

$$T, \mu_B, \mu_S, \mu_Q, \mu_C, \gamma_S, \gamma_C, R,$$

where R is the radius of the fireball, assuming a spherical fireball (i.e. $V = 4/3\pi R^3$). Each parameter can be set to fix or free whereas μ_Q and μ_S can be constrained to $B/2Q$ and 0, respectively.

4.5.2 The Canonical Ensemble

The quantum numbers B , S , and Q are exactly conserved in canonical ensemble. This approach is applicable in case of small systems, such as those created in collisions of $p+p$, $p+\bar{p}$, and $p+A$ [16, 17]. The canonical treatment can be used in peripheral collisions of $A+A$ [11].

The canonical partition function can be expressed in terms of the grand-canonical partition function both in case of Boltzmann statistics and quantum statistics [10],

$$Z_{B,S,Q}^{\text{CE}} = \frac{1}{2\pi} \int_{-\pi}^{\pi} d\phi_B e^{-iB\phi_B} \frac{1}{2\pi} \int_{-\pi}^{\pi} d\phi_S e^{-iS\phi_S} \frac{1}{2\pi} \int_{-\pi}^{\pi} d\phi_Q e^{-iQ\phi_Q} \times \exp\left(\sum_i \frac{g_i V}{(2\pi)^3} \int d^3 p e^{-\beta E_i} e^{i(B_i\phi_B + S_i\phi_S + Q_i\phi_Q)}\right), \quad (4.7)$$

where ϕ_B , ϕ_S , and ϕ_Q are introduced to impose the exact conservation of the quantities B , S , and Q . The more details can be found in Ref. [10]. In Maxwell-Boltzmann approximation, Eq. 4.7 can be written as,

$$N_i^{\text{CE}} = \left(\frac{Z_{B-B_i, S-S_i, Q-Q_i}}{Z_{B,S,Q}}\right) \frac{g_i V}{(2\pi)^3} \int d^3 p e^{-\beta E_i} = \left(\frac{Z_{B-B_i, S-S_i, Q-Q_i}}{Z_{B,S,Q}}\right) N_i^{\text{GCE}}|_{\mu_i=0}, \quad (4.8)$$

where $Z_{B-B_i, S-S_i, Q-Q_i}$ is the partition function with quantum numbers of the excluded particle i , $Z_{B,S,Q}$ is the total partition function. In the limit of very large volume, the result

of canonical ensemble tends to grand-canonical. In practice, canonical partition function calculation involves several numerical integrations and is only used for very small systems. The canonical ensemble contains the following parameters:

$$T, B, S, Q, \gamma_S, R$$

Due to exact conservation of B, S , and Q , there are no chemical potentials to satisfy constraints.

4.5.3 The Strangeness-Canonical Ensemble

Like grand-canonical ensemble, the conservation of quantum numbers B , Q , and S on an average becomes less acceptable as the number of particles in the fireball drops. The exact treatment of the quantum number S has been imposed since strangeness is typically less abundant compared to quantum numbers B and Q . This is enforced in the strangeness-canonical ensemble (SCE). In strangeness-canonical partition function, only the states within the volume, V , with exactly desired strangeness content, S , are allowed. So, strangeness is exactly conserved in this ensemble, whereas the baryon and charge content is fixed only on average by the chemical potentials μ_B and μ_Q , respectively like GCE. Thus, SCE is useful in intermediate cases, where the system is small enough to apply grand-canonical approach and the exact conservation of B and Q is not applicable, also it should not be big enough for that strangeness S to be conserved on average.

In Maxwell-Boltzmann approximation, the partition function for a hadron gas of strangeness S can be written as [10]

$$Z_S^{\text{SCE}} = \frac{1}{2\pi} \int_{-\pi}^{\pi} d\phi_S e^{-iS\phi_S} \exp\left(\sum_i \frac{g_i V}{(2\pi)^3} \int d^3p e^{-\beta(E_i - \mu_i)} e^{iS_i\phi_S}\right), \quad (4.9)$$

where $\mu_i = B_i \mu_B + Q_i \mu_Q$ and ϕ_S was introduced to conserve S exactly.

The particle multiplicities can be calculated as

$$\begin{aligned}
N_i^{\text{SCE}} &= \frac{\partial}{\partial(\frac{\mu_i}{T_i})} \log[Z] \\
&= \left(\frac{Z_S - S_i}{Z_S} \right) \frac{g_i V}{(2\pi)^3} \int d^3 p e^{-\beta(E_i - \mu_i)} \\
&= \left(\frac{Z_S - S_i}{Z_S} \right) N_i^{\text{GCE}}|_{\mu_S=0}
\end{aligned} \tag{4.10}$$

So, SCE differs from GCE with $\mu_S = 0$ by only multiplicative factors, which depend on the volume where the exact conservation of strangeness is imposed. The low production of strange particles such as in the experiments at the GSI-SIS requires a canonical treatment of strangeness [18]. The strangeness-canonical ensemble contains the following parameters:

$$T, \mu_B, \mu_Q, \gamma_S, R_C, R$$

where R_C is canonical or correlation radius; the radius inside which strangeness is exactly conserved. Each parameter can be set to fit or free whereas μ_Q and R_C can be set as constrain-type to $B/2Q$ and $R_C = R$, respectively.

4.6 Additional Considerations

4.6.1 Feed-down

At chemical freeze-out, the hadronic fireball consists of both stable hadrons, with respect to strong interactions and all hadronic resonances. In heavy-ion collision experiments, many of the detected particles are product of the decay of primarily created heavier particles. Thus, final observed multiplicities for a given particle is composed of primary particles (produced directly in the reaction) and secondary particles coming from the strong

decays of the resonances. For example, for a final multiplicity pions, it is given by [10],

$$N_\pi = N_\pi^{\text{prim}} + \sum_{\text{states } j} N_j^{\text{prim}} \text{B.R. } (j \rightarrow \pi), \quad (4.11)$$

where N_π is final multiplicity of π , N_π^{prim} is primordial multiplicity of π , N_j^{prim} is primary multiplicity of hadrons of species j , and $\text{B.R. } (j \rightarrow \pi)$ is the fraction of the decay of species j into π through all possible decay channels of j . The primordial hadrons are allowed to decay to the particles, which are considered as stable by the experiment, before comparing model predictions with experimental data. From feed-down study of π in statistical thermal model, it has been observed that at high energy, majority of feeding comes from mesons whereas at low energy, baryons dominate [10, 19]. In addition to this, strange particle yields can be obtained by reconstructing the electro-weak decays. Some of experimental data, which are the basic input to model, are feed-down corrected from their weak-decay contributions. So, the correct treatment of contributions from electro-weak decays is one of the important part of thermal analysis.

4.6.2 Deviations from Chemical Equilibrium in Strangeness Sector

In heavy-ion collision experiment at RHIC, it is believed that higher degree of thermalisation is attained even in the strangeness sector for central collisions. However, at peripheral collisions or low energy, possible deviations from equilibrium can occur in strangeness sector. For some elementary collisions e^+e^- , $p+p$, and $p+\bar{p}$ [16, 17], treatment of strangeness even in the canonical approach of statistical-thermal model fails to describe experimental data. To solve this problem, a purely phenomenological parameter γ_S [20, 21, 22], which is called strangeness saturation factor, is introduced to account for the observed deviation from chemical equilibrium in strange sector. The value of $\gamma_S = 1$ corresponds to complete strangeness equilibration.

There are some additional features like inclusion of resonance width, mass cut-off, and exclude volume correction which are described in detail in Ref. [10]. We have not included these features of THERMUS model in our study.

4.7 Analysis Details

Here we discuss the procedure followed to analyse heavy-ion data at BES-I energies along with top RHIC energies. We investigate the properties of thermodynamic parameters as a function of centrality and energy of the collision.

4.7.1 Data Set

We have studied particle yields as well as particle ratios at different energies of BES-I program at $\sqrt{s_{NN}} = 7.7$ to 39 GeV along with top RHIC energies 62.4 and 200 GeV. The dataset at $\sqrt{s_{NN}} = 14.5$ GeV which is a part of BES-I, taken recently in the year 2014, have not been used. An overview of BES-I dataset is given in Table 4.1

Table 4.1: Overview of data taken in the RHIC BES-I program.

Beam energy (GeV)	Year of data taking	Event statistics (millions)
39	2010	130
27	2011	70
19.6	2011	36
14.5	2014	20
11.5	2010	12
7.7	2010	4

4.7.2 Choice of Particle Yields and Ratios

The STAR detector at RHIC, due to its large uniform acceptance and excellent particle identification capabilities, has measured a variety of strange and non-strange hadron species (π^\pm , K^\pm , p , \bar{p} , K_S^0 , Λ , $\bar{\Lambda}$, Ξ^- , $\bar{\Xi}^+$, ϕ , Ω , $\bar{\Omega}$) produced in Au+Au collisions at $\sqrt{s_{NN}} = 7.7$, 11.5, 19.6, 27, and 39 GeV [23, 24, 25]. We have used particle yields of π^\pm , K^\pm , p , \bar{p} , Λ , $\bar{\Lambda}$, Ξ^- , and $\bar{\Xi}^+$ as default set for our study in BES-I energies along with top RHIC energies (62.4 and 200 GeV). Other yields are not included in these thermal fits because the yields are obtained for different event centrality bins due to limited statistics in data and we want to study the centrality dependence of freeze-out parameters. However, we have studied the effect on freeze-out parameters considering all particles in the fit in different centrality bins where all yields are available. The errors on particle yields are the quadratic sum of statistical and systematic uncertainties. The measurements of yields for π^\pm , K^\pm , p , and \bar{p} are for rapidity $|y| < 0.1$ [23, 24, 26] and those of Λ , $\bar{\Lambda}$, Ξ^- , $\bar{\Xi}^+$ are for rapidity $|y| < 0.5$ [25, 27].

The use of particle ratios has advantage that it ignores many dynamical effects such as it cancels the distortion due to flow effects and also cancels the fireball volume effect. As the thermodynamic model is quite sensitive to particle ratios used, the choice of set of ratios is important in the analysis. We have chosen the following set of antiparticle to particle and (anti)particle to pion ratios as default for our study;

$$\frac{\pi^-}{\pi^+}, \frac{K^-}{K^+}, \frac{\bar{p}}{p}, \frac{\bar{\Lambda}}{\Lambda}, \frac{\bar{\Xi}^+}{\Xi^-}, \frac{K^-}{\pi^-}, \frac{\bar{p}}{\pi^-}, \frac{\Lambda}{\pi^-}, \frac{\bar{\Xi}^+}{\pi^-}.$$

The systematic errors on yields are treated as independent. These uncertainties propagate to the systematic uncertainties on chemical freeze-out parameters. When particle ratios are used for fitting, we remove the correlated errors such as efficiency, and also the extrapolation error for antiparticle to particle ratios. We have also estimated the effect of

correlated errors in the particle yields on the extracted chemical freeze-out parameters. We have generated Gaussian random numbers with mean = 0 and sigma taken as error of the pion yields and checked the difference on freeze-out parameters. We found that the effect is within 1-3% for the extracted freeze-out parameters.

4.7.3 Choice of Ensemble

The large number of particle production in the final stages of heavy-ion collisions justifies the use of grand-canonical approach in the analysis of experimental data. Strangeness can be treated grand-canonically in central collisions of Pb+Pb and Au+Au at SPS, RHIC, and LHC energies. On the other hand, in peripheral collisions, treatment of strangeness-canonical ensemble may be required. In this study, we have used both grand-canonical and strangeness-canonical ensemble considering the quantum statistics (Fermi-Dirac and Bose-Einstein).

4.7.4 Choice of Freeze-out Parameters

For grand-canonical ensemble, it is possible to extract the freeze-out parameters T_{ch} , μ_B , μ_S , μ_Q , γ_S , and R from the yields. For particle ratios, the system volume gets cancelled and it doesn't affect the other freeze-out parameters. As a default parameter set, μ_Q is fixed to zero for all energies. We have also checked the results by constraining the value of $\mu_Q = B/2Q$ for Au+Au collisions which will be discussed in results section.

For strangeness-canonical ensemble, the parameters used are T_{ch} , μ_B , μ_Q , γ_S , R_C , and R . We have used the conditions $\mu_Q = 0$ and $R_C = R$ for yields and ratios.

Table 4.2: Fraction of feed-down contributions obtained from model and data in most central collisions.

Particles	Energy (GeV)	Experiment	THERMUS
$\Lambda \rightarrow p$	7.7	20%	16%
$\Lambda \rightarrow p$	39	25%	26%
$\Xi^- \rightarrow \Lambda$	7.7	14%	14%
$\Xi^- \rightarrow \Lambda$	39	22%	22%

4.7.5 Feed-down Correction

The contribution of weak decays, commonly called feed-down is very much sensitive to the extraction of freeze-out parameters. Experimentally, different particles are corrected in different ways and it is also difficult to obtain the feed-down contribution of all weak decays. At RHIC, proton yields have not been corrected for feed-down contributions and “inclusive” yields are presented. Pion yields have been corrected for feed-down from K_S^0 whereas Λ yields have been corrected for feed-down from Ξ , and Ξ^0 weak decays. However, we can estimate the contribution of feed-down to daughter particle from the parent particle decay, e.g., fraction of p from Λ decay. Since in case of experimental data, we apply different cuts such as $DCA < 3$ cm along with other kinematics cuts, it is worthwhile to check how much p from Λ decay contribute within our kinematics cuts. It is done using experimentally measured Λ spectra and Λ embedding sample. In embedding, we embed the Λ sample with the flat p_T distribution in real data. The sample is passed through the detector material in a similar way as would have done for real data. The track reconstruction is done in similar way as is done in real data. After all our kinematics cuts, we obtain the p coming from the Λ parent particles. In model, we can make the decay on and off from a particular parent particle to the required daughter particle. Then we can check the difference of particle density with decay on and with decay off for daughter particle which gives us the feed-down fraction from that particular parent particle. We have properly taken care of

feed-down correction in model with respect to the experimental correction. We have used individual particle set for each input particle to calculate the feed-down contributions. Table 4.2 represents the feed-down contributions from model and experimental data [24, 25] for most central collisions in Au+Au collisions at $\sqrt{s_{NN}} = 7.7$ and 39 GeV which are very close to each other.

Finally, with chosen ensemble and defined set of particle yields or ratios determines the freeze-out parameters that best describes the complete set of input experimental yields or ratios through χ^2 -minimisation method as given below;

$$\chi^2 = \sum \frac{(\text{Experimental value} - \text{Model value})^2}{(\text{Experimental error})^2} \quad (4.12)$$

4.8 Results and Discussions

Here we discuss results of energy and centrality dependence of the extracted freeze-out parameters for Au+Au collisions at BES-I and top RHIC energies in 7 centralities 0–5%, 5–10%, 10–20%, 20–30%, 30–40%, 40–60% and 60–80%.

4.8.1 Particle Yields

4.8.1.1 Grand-Canonical Ensemble (GCE)

Figure 4.1 shows a representative comparison plot of model with GCE and experimentally measured particle yields in most central (0–5%) and in most peripheral (60–80%) bins in Au+Au collision at $\sqrt{s_{NN}} = 7.7$ GeV. The standard deviations of data to thermal fit result are also shown at bottom panel of Fig. 4.1. Most of the results are within 2 standard deviation from the data. We found that model results are in good agreement with the experiment data for all centrality bins and for all energies (results shown in Appendix A). The χ^2/NDF

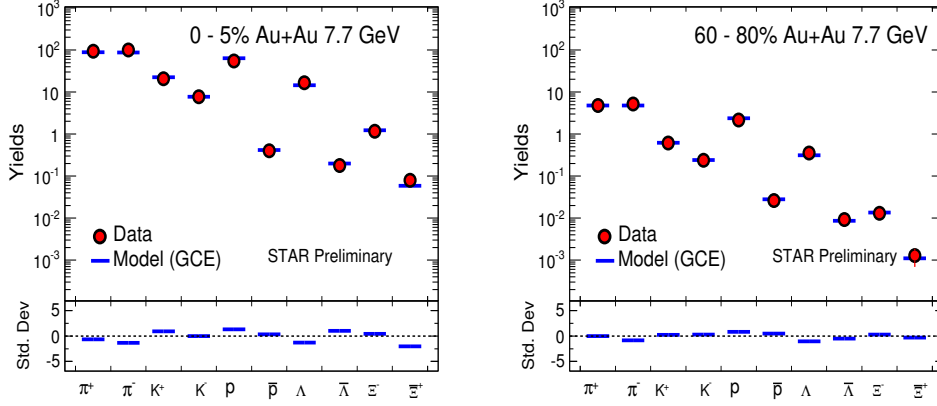


Figure 4.1: Comparison of statistical model prediction (lines) with experimental mid-rapidity particle yields using grand-canonical ensemble for 0–5% and 60–80% centrality in Au+Au at $\sqrt{s_{NN}} = 7.7$ GeV.

ranges from 0.5–4, where NDF is number of degrees of freedom and defined as the number of yields used for fit - number of free parameters.

Figure 4.2 shows the centrality and energy dependence of freeze-out parameters as a function of $\langle N_{part} \rangle$ from GCE in Au+Au collisions at $\sqrt{s_{NN}} = 7.7$ –200 GeV. The solid symbol represents the results for BES-I energies and the open symbol represents the results for top RHIC energies ($\sqrt{s_{NN}} = 62.4$ and 200 GeV). Here we always use $\mu_Q = 0$ with unconstrained fit parameters T_{ch} , μ_B , μ_S , γ_S , and R with particles π^+ , K^+ , p , Λ , Ξ^- and their corresponding antiparticles. The T_{ch} is found to be independent of centrality and with increase in energy its value increases from lower energy 7.7 GeV up to 19.6 GeV and afterwards its value remain consistent within errors for the top RHIC energy measurements. The values of T_{ch} is close to the lattice QCD calculation of the cross-over temperature at ($\mu_B = 0$ MeV) between the de-confined phase and the hadronic phase [27] suggesting that chemical freeze-out happens in the vicinity of the phase boundary shortly after hadronisation at

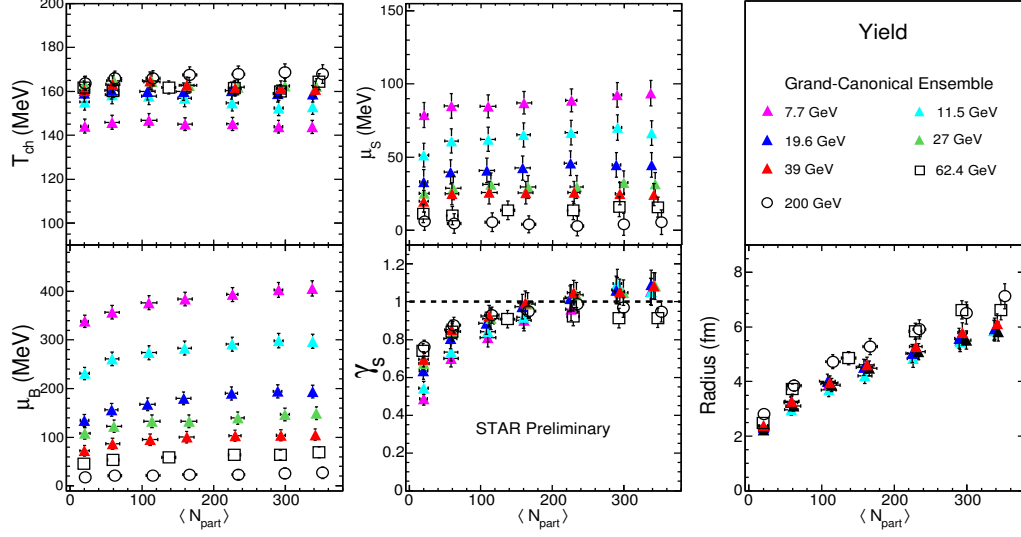


Figure 4.2: Chemical freeze-out parameters (T_{ch} , μ_B , μ_S , γ_S , and R) are shown as a function of $\langle N_{part} \rangle$ in Au+Au collisions at $\sqrt{s_{NN}} = 7.7, 11.5, 19.6, 27, 39, 62.4$, and 200 GeV obtained from THERMUS with GCE.

higher energies. The μ_B decreases with increasing collision energy and it increases from peripheral to central collisions at all energies. The μ_S seems to decrease with increase of collision energy following the same type of behaviour as μ_B . For central collisions, the γ_S is almost independent of energies, however, for peripheral collisions, there is a slight energy dependence showing increase with increasing energy. Centrality dependence has been observed for γ_S where it increases from peripheral to central for all the energies studied. In central collisions, γ_S is close to unity for top RHIC energies. Radius, R , also increases from peripheral to central region having range from 2–7 fm and it remain same for all BES-I energies whereas it has slightly higher values for top RHIC energies.

The chemical freeze-out parameters could be sensitive to combination of particle yields used. We have checked the effect on the freeze-out parameters using different possible sets of particle yields as given below:

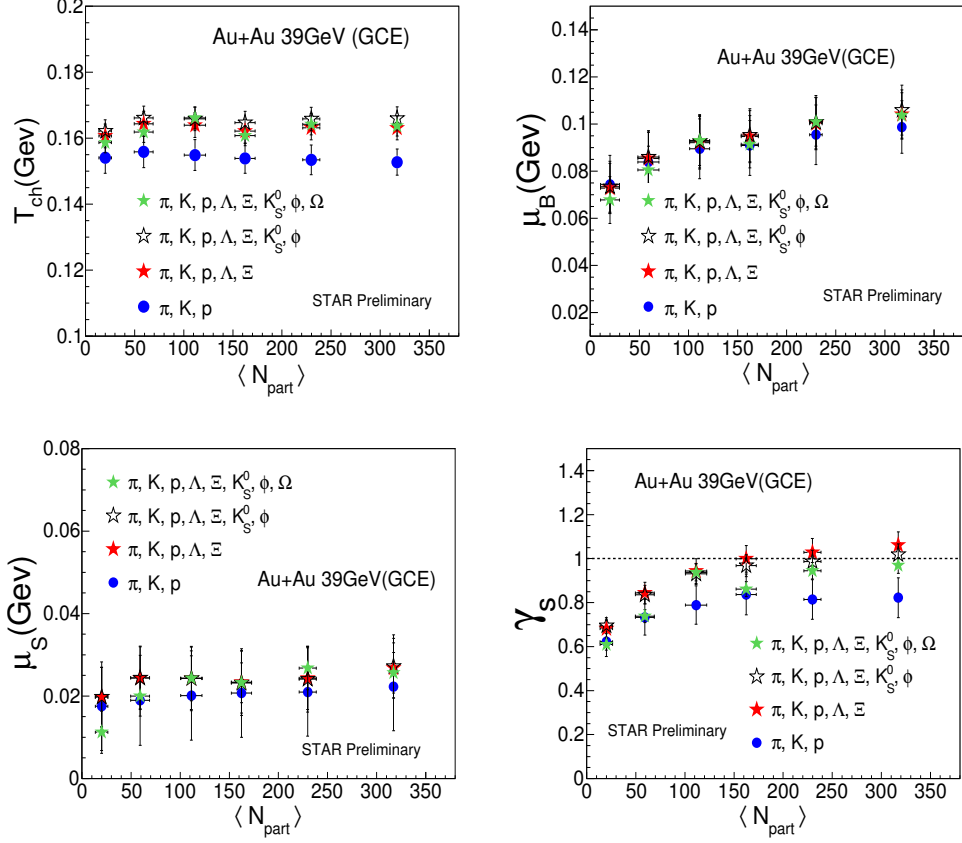


Figure 4.3: The variation of chemical freeze-out parameters as a function of $\langle N_{\text{part}} \rangle$ for different combinations of possible yields for Au+Au collisions at $\sqrt{s_{\text{NN}}} = 39$ GeV.

Set A: only yields of π , K, p and their corresponding antiparticles;

Set B: only yields of π , K, p, Λ , Ξ and their corresponding antiparticles;

Set C: only yields of π , K, p, Λ , Ξ , K_S^0 , ϕ and their corresponding antiparticles;

Set D: only yields of π , K, p, Λ , Ξ , K_S^0 , ϕ , Ω and their corresponding antiparticles.

As shown in Fig. 4.3, the chemical freeze-out parameters found to vary with the chosen data combination. The results of freeze-out parameters from set A deviates the most for T_{ch} and γ_S than that for other sets. For set B, C, and D, the deviation is small and con-

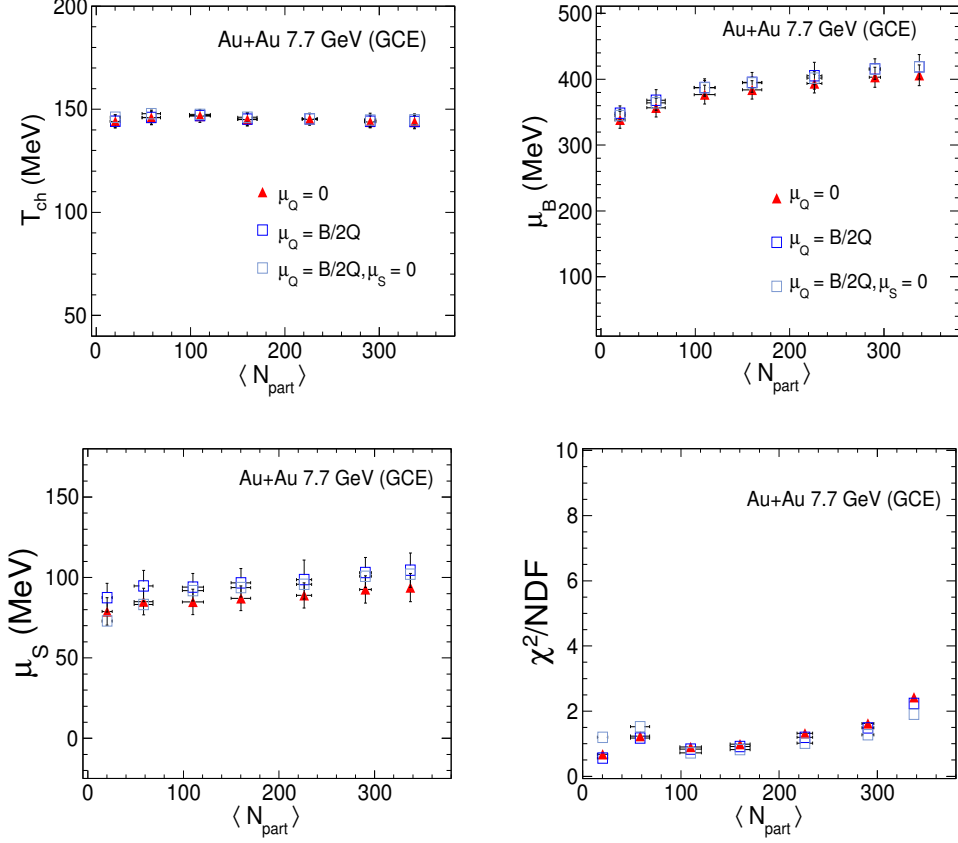


Figure 4.4: The variation of chemical freeze-out parameters as a function of $\langle N_{\text{part}} \rangle$ for different conditions on parameters (μ_Q and μ_S) for Au+Au collisions at $\sqrt{s_{\text{NN}}} = 7.7$ GeV.

sistent within errors for all of parameters. The energy and centrality dependence behaviour of freeze-out parameters as a function of $\langle N_{\text{part}} \rangle$ is independent of chosen sets. We have also checked the effect on the values of parameters by changing the constrains on some of the freeze-out parameters;

condition 1: $\mu_Q = 0$;

condition 2: $\mu_Q = B/2Q$;

condition 3: $\mu_Q = B/2Q$, $\mu_S = 0$;

The value of μ_Q , which is constrained to $B/2Q$, is 1.25 for Au+Au collisions. Using conditions 2 and 3, the values of the chemical potentials (μ_B and μ_S) increase in comparison with condition 1. All the variations are consistent within the errors. There is no such variation seen in rest of the freeze-out parameters along with χ^2/NDF as shown in Fig. 4.4. Same have been checked with all other energies and also in SCE and the conclusions remain same as for the GCE.

4.8.1.2 Strangeness-Canonical Ensemble (SCE)

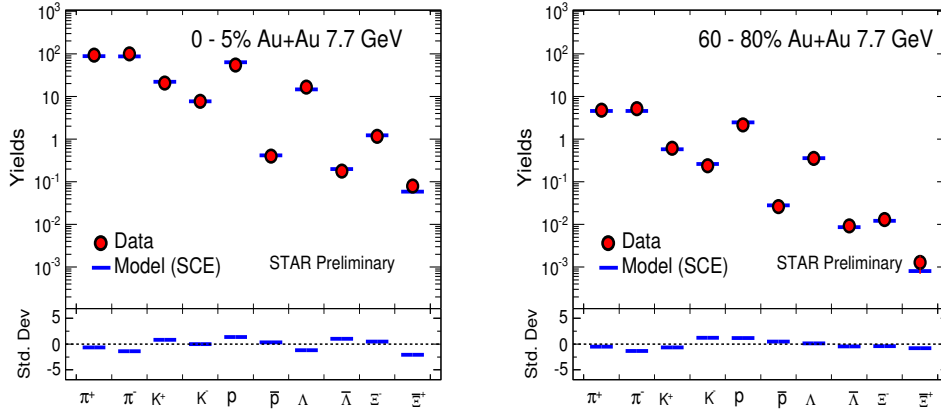


Figure 4.5: Comparison of fit results to experimental mid-rapidity particle yields using strangeness-canonical ensemble for 0–5% and 60–80% centrality in Au+Au at $\sqrt{s_{\text{NN}}} = 7.7$ GeV.

Figure 4.5 shows a representative comparison plot of model and experimentally measured particle yields in most central (0–5%) and in most peripheral (60–80%) bins in Au+Au collision at $\sqrt{s_{\text{NN}}} = 7.7$ GeV in strangeness-canonical ensemble. The results from model are found to be in good agreement with experimental measured data for all centrality bins and for all energies in SCE (results shown in Appendix A) with χ^2/NDF ranging from 0.5–4.

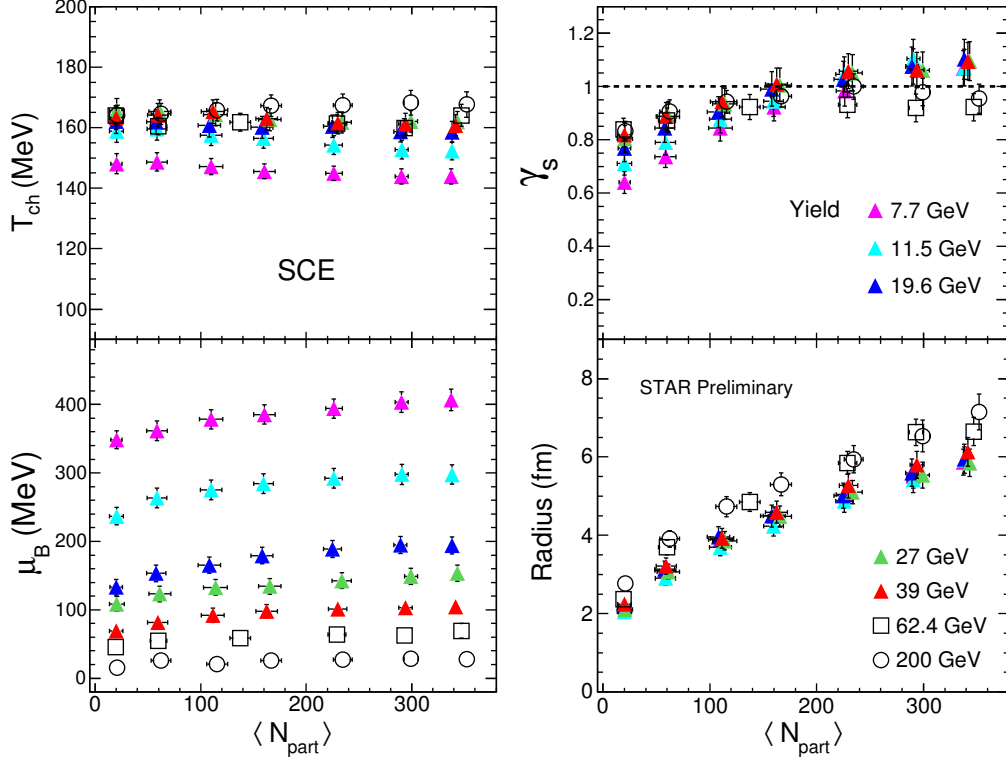


Figure 4.6: Chemical freeze-out parameters (T_{ch} , μ_B , γ_S , and R) are shown as a function of $\langle N_{\text{part}} \rangle$ in Au+Au collisions at $\sqrt{s_{\text{NN}}} = 7.7, 11.5, 19.6, 27, 39, 62.4$, and 200 GeV in SCE.

Figure 4.6 shows the centrality and energy dependence of freeze-out parameters as a function of $\langle N_{\text{part}} \rangle$ in SCE in Au+Au collisions at $\sqrt{s_{\text{NN}}} = 7.7\text{--}200$ GeV. Here we use $\mu_Q = 0$ and $R_C = R$ with unconstrained fit parameters T_{ch} , μ_B , γ_S , and R with particles π , K, p, Λ , Ξ and their corresponding antiparticles. The comparison of results on freeze-out parameters obtained from GCE and SCE are shown in Fig. 4.7. The energy and centrality dependence behaviour of freeze-out parameters μ_B , γ_S , and R in SCE remain same as in GCE. For central and mid-central collisions, T_{ch} and γ_S are same in both GCE and SCE. However, for peripheral collisions, T_{ch} and γ_S from SCE become higher than that of GCE (within errors) and are shown in Fig. 4.7.

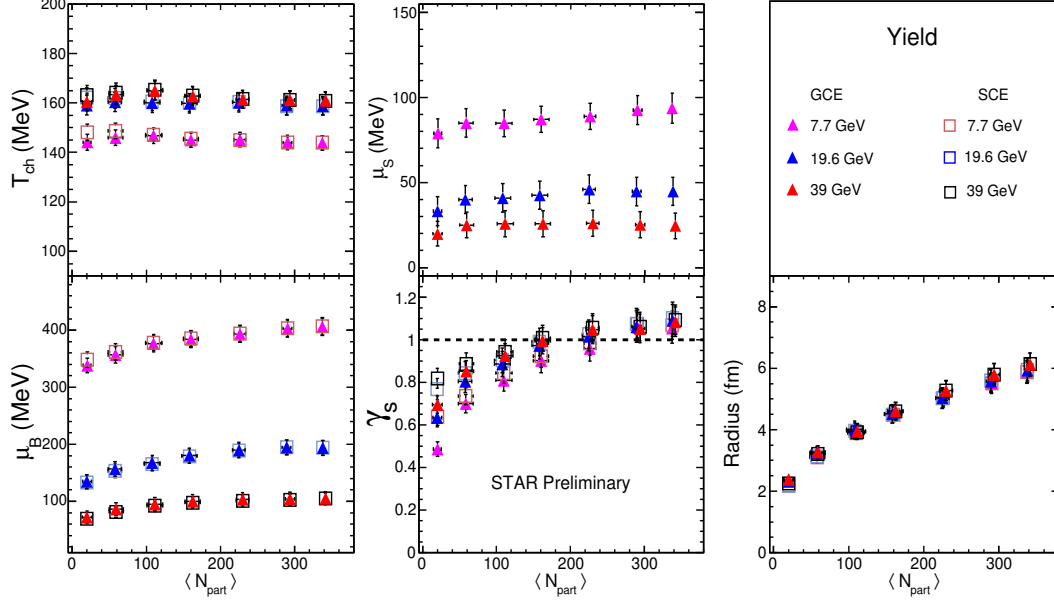


Figure 4.7: The comparison of chemical freeze-out parameters as a function of $\langle N_{\text{part}} \rangle$ between GCE and SCE obtained from the yields in Au+Au collisions at $\sqrt{s_{\text{NN}}} = 7.7, 11.5, 19.6, 27, 39, 62.4,$ and 200 GeV.

4.8.2 Particle Ratios

Particle ratios can also be used to obtain the freeze-out parameters along with the yields. We have carried out this study to see if there is any variation in freeze-out parameters. The comparison plot of model and experimentally measured particle ratios in most central (0–5%) and in most peripheral (60–80%) bins has been shown in Fig. 4.8 in Au+Au collision at $\sqrt{s_{\text{NN}}} = 7.7$ GeV for the GCE. The values obtained from model are in good agreement with experimentally measured ratios for all centrality bins and for all energies. Figure 4.9 shows similar studies with SCE in Au+Au collision at $\sqrt{s_{\text{NN}}} = 7.7$ GeV. The freeze-out parameters extracted from ratios are compared between GCE and SCE as shown in Fig. 4.10. The T_{ch} values remain same in central and mid-central collisions for all energies whereas in peripheral collisions, T_{ch} and μ_B in SCE are higher than that of GCE for lower energies such as $\sqrt{s_{\text{NN}}} = 7.7$ and 11.5 GeV. For higher BES-I energies and in top RHIC energies,

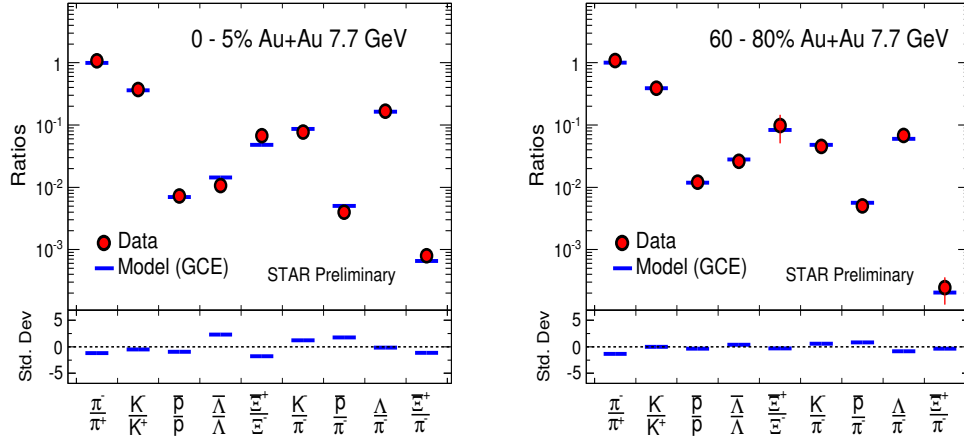


Figure 4.8: Comparison of fit results to experimental mid-rapidity particle ratios in GCE for 0–5% and 60–80% centrality in Au+Au at $\sqrt{s_{NN}} = 7.7$ GeV.

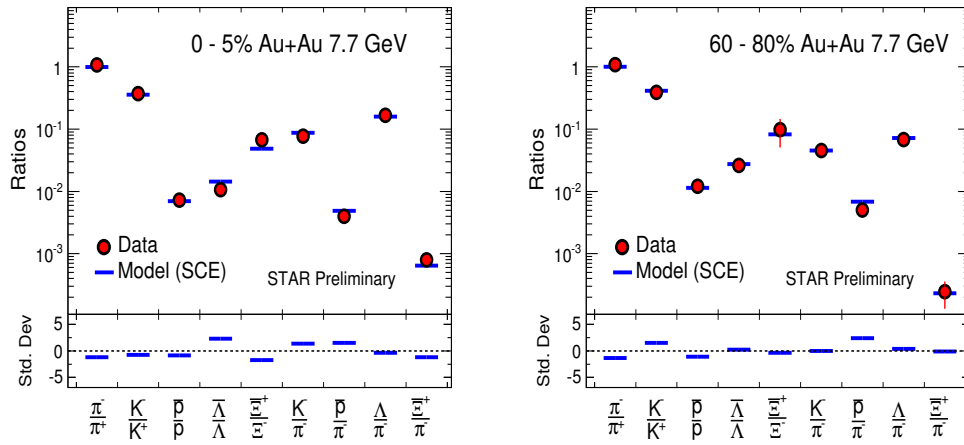


Figure 4.9: Comparison of fit results to experimental mid-rapidity particle ratios in SCE for 0–5% and 60–80% centrality in Au+Au at $\sqrt{s_{NN}} = 7.7$ GeV.

the values of the parameter are similar and consistent within errors for all of the freeze-out parameters.

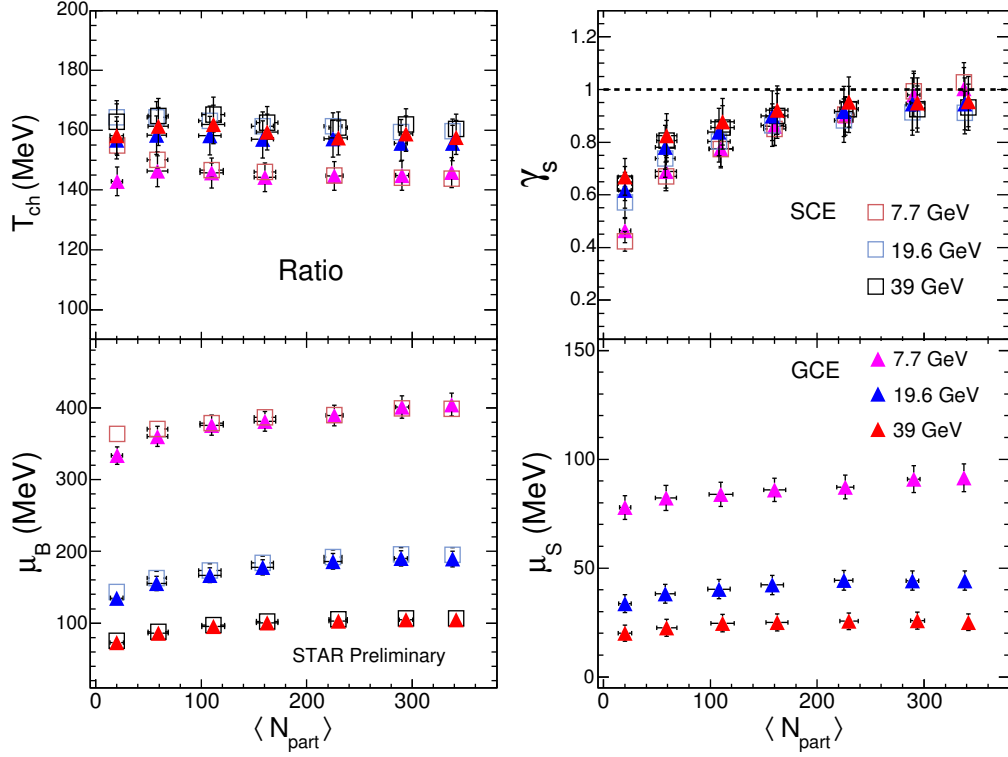


Figure 4.10: The comparison of chemical freeze-out parameters as a function of $\langle N_{\text{part}} \rangle$ between GCE and SCE obtained from the ratios in Au+Au collisions at $\sqrt{s_{\text{NN}}} = 7.7, 19.6$, and 39 GeV.

The results on freeze-out parameters obtained from ratios are also compared with that of yields both in GCE and SCE. The results on T_{ch} , μ_B , μ_S , and γ_S are slightly higher for yields (within errors) than that of ratios for all the energies studied in GCE as shown in Fig. 4.11 and in SCE as shown in Fig. 4.12.

4.8.3 Chemical Freeze-out Curve: T_{ch} vs. μ_B

Figure 4.13 shows chemical freeze-out curve which is here represented as temperature T_{ch} at different center-of-mass energies in Au+Au collisions as a function of μ_B . It shows that RHIC programs, the top energies and the BES-I energies, cover the μ_B region from ~ 20

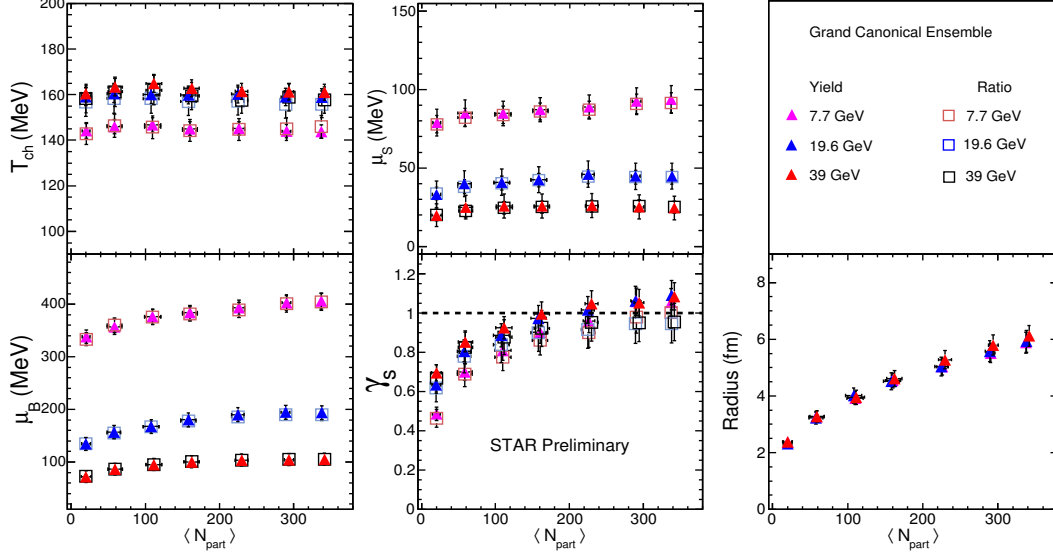


Figure 4.11: The comparison of chemical freeze-out parameters as a function of $\langle N_{\text{part}} \rangle$ obtained from the particle yields and ratios in Au+Au collisions at $\sqrt{s_{\text{NN}}} = 7.7, 19.6, \text{ and } 39$ GeV in GCE.

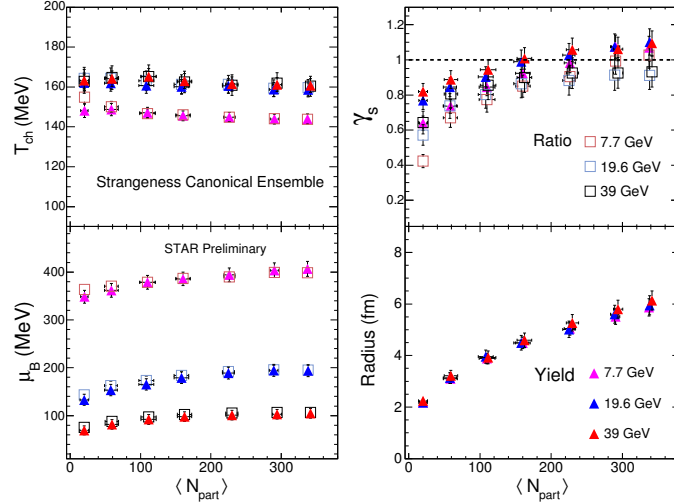


Figure 4.12: The comparison of chemical freeze-out parameters as a function of $\langle N_{\text{part}} \rangle$ obtained from the particle yields and ratios in Au+Au collisions at $\sqrt{s_{\text{NN}}} = 7.7, 19.6, \text{ and } 39$ GeV in SCE.

MeV ($\sqrt{s_{\text{NN}}} = 200$ GeV) to ~ 420 MeV ($\sqrt{s_{\text{NN}}} = 7.7$ GeV), which is the largest range covered compared to any other heavy-ion facility. The curves are the numerical parametrisations of T_{ch} vs. μ_B trends, based on the data obtained prior to the BES-I program using

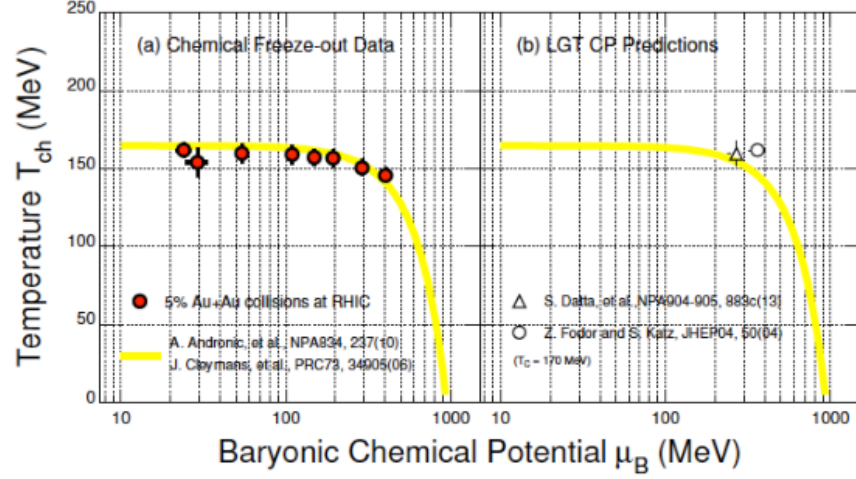


Figure 4.13: (a) Chemical freeze-out temperature (T_{ch}) vs. baryonic chemical potential (μ_B) obtained from a statistical model fit [10] to the yields of hadrons in 0–5% central Au+Au collisions at $\sqrt{s_{NN}} = 7.7, 11.5, 19.6, 27, 39, 62.4,$ and 200 GeV in GCE. (b) The positions of the QCD critical point from two different lattice gauge theory calculations in the T_{ch} vs. μ_B plane are shown.

statistical models [10, 28]. The values of T_{ch} and μ_B obtained in this analysis from the Au+Au collisions are in good agreement with the parametrizations. As the collision energy increases, the μ_B decreases continuously reaching very small values at $\sqrt{s_{NN}} = 200$ GeV. In contrast, the T_{ch} seems to increase up to 168 MeV. Figure 4.13 (a) represents as a single point at chemical freeze-out in the system's expansion trajectory in the T_{ch} vs. μ_B plane of phase diagram. The starting point is governed by the primordial conditions prevailing during the early equilibration phase. The equation-of-state influences the evolution of the system as the system expands and cools until it reaches chemical freeze-out. In addition to current analysis, the higher moments of multiplicity distributions of conserved numbers such as net-charge and net protons [29, 30] are suggested as good probes to extract freeze-out properties by comparing the results to QCD calculations of higher order susceptibilities on the lattice [31, 32]. This has been possible due to the construction of proper observables that allow for comparison between experiment and QCD calculations [33, 34].

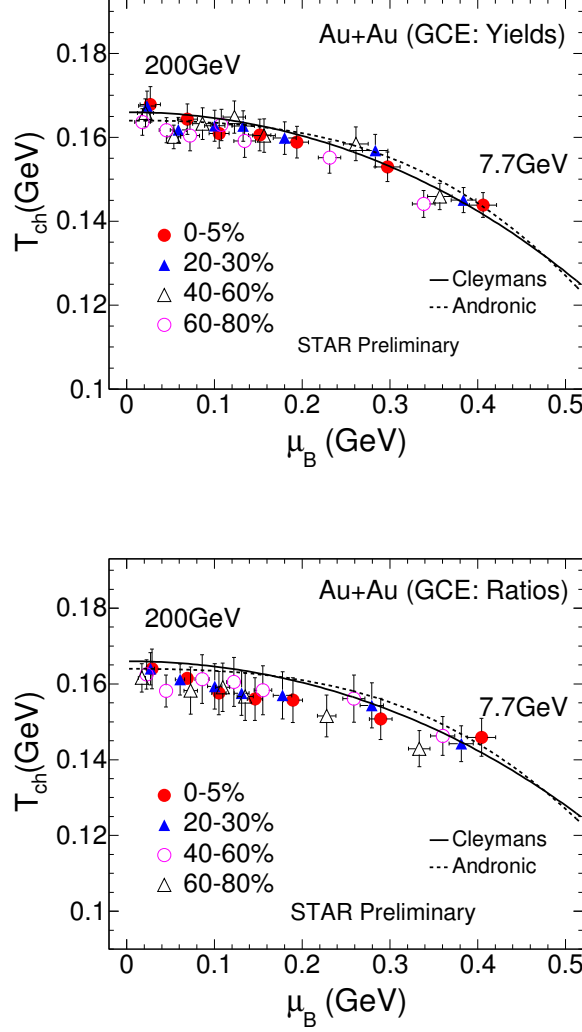


Figure 4.14: Chemical freeze-out temperature (T_{ch}) vs. baryonic chemical potential (μ_B) obtained from a statistical model fit [10] to the yields of hadrons and ratios in different centrality bins in Au+Au collisions at $\sqrt{s_{\text{NN}}} = 7.7, 11.5, 19.6, 27, 39, 62.4$ and 200 GeV in GCE.

Figure 4.13 (b) shows the estimations of the QCD critical point from lattice gauge theory calculations [35, 36] in the $T_{\text{ch}} - \mu_B$ plane considering $T_c = 170$ MeV. Based on these current estimations of the critical point from lattice QCD calculations, we observe that

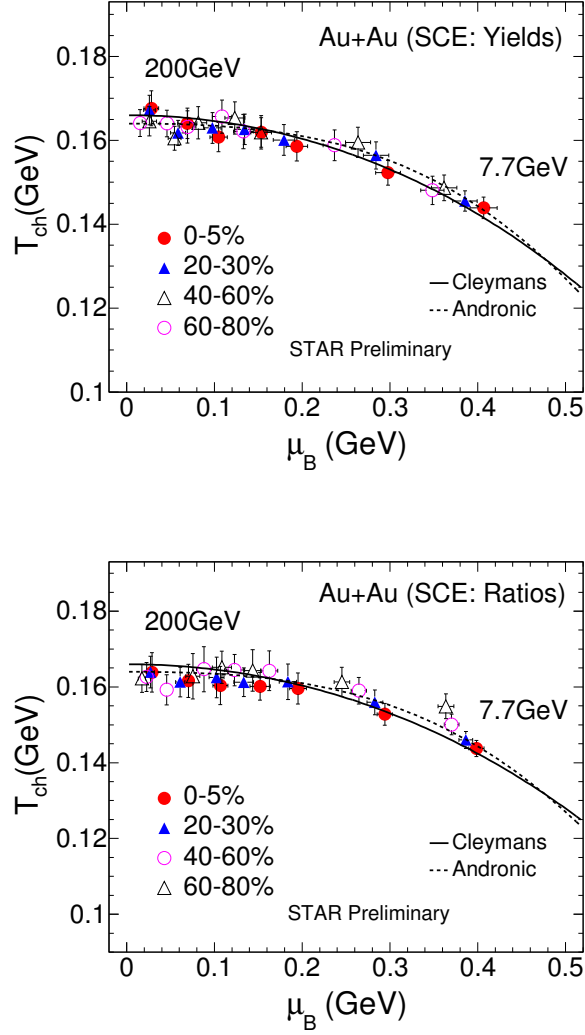


Figure 4.15: Chemical freeze-out temperature (T_{ch}) vs. baryonic chemical potential (μ_B) obtained from a statistical model fit [10] to the yields of hadrons and ratios in different centrality bins in Au+Au collisions at $\sqrt{s_{NN}} = 7.7, 11.5, 19.6, 27, 39, 62.4$ and 200 GeV in SCE.

the RHIC BES program scans energies for which the matter expands and cools through a crossover transition down to those which could contain key features of the phase diagram of QCD matter.

Figure 4.14 and 4.15 show the $T_{\text{ch}} - \mu_B$ variation obtained from the particle yields and ratios in grand-canonical and strangeness-canonical ensemble, respectively. We have observed the centrality dependence of freeze-out parameters T_{ch} vs. μ_B for BES-I energies [23, 24], which is not observed in top RHIC energies [27]. The $T_{\text{ch}} - \mu_B$ variation results from yields and ratios are consistent within error whereas it differs in SCE and GCE only for most peripheral bin.

The $\langle N_{\text{part}} \rangle$ values used for various collision energies are given in Table 4.3. The Tables 4.4 and 4.5 represent the summary of the values of all freeze-out parameters from the compilation of available STAR preliminary particle yields and ratios from BES-I energies and published data from top RHIC energies in both grand-canonical and strangeness-canonical ensemble.

4.9 Kinetic Freeze-out

At kinetic freeze-out, elastic collisions stop and the p_T distributions of produced particles get fixed. The kinetic freeze-out parameters have been extracted from the simultaneous fitting of π^\pm , K^\pm , p , and \bar{p} spectra with the hydrodynamics-motivated Blast-wave model [37, 38, 39, 40], assuming thermal equilibrium. The model assumes that the particles are locally thermalized at kinetic freeze-out temperature and are moving with a common transverse collective flow velocity. Assuming a radially boosted thermal source, with a kinetic freeze-out temperature, T_{kin} , and transverse radial flow velocity, β , the p_T distributions of the particles can be given by,

$$\frac{dN}{p_T dp_T} \propto \int_0^R r dr m_T I_0 \left(\frac{p_T \sinh \rho(r)}{T_{\text{kin}}} \right) \times K_1 \left(\frac{m_T \cosh \rho(r)}{T_{\text{kin}}} \right), \quad (4.13)$$

where $m_T = \sqrt{p_T^2 + m^2}$, $\rho(r) = \tanh^{-1}\beta$, and I_0, K_0 are the modified Bessel functions. We use the flow velocity profile of the form $\beta = \beta_S (r/R)^n$, where β_S is the surface velocity, r/R is the relative radial position in the thermal source, and n is the exponent of flow velocity profile. Average transverse radial flow velocity, $\langle\beta\rangle$, can then be obtained as: $\langle\beta\rangle = \frac{2}{2+n} \beta_S$. The extracted fit parameters are T_{kin} , $\langle\beta\rangle$, and n .

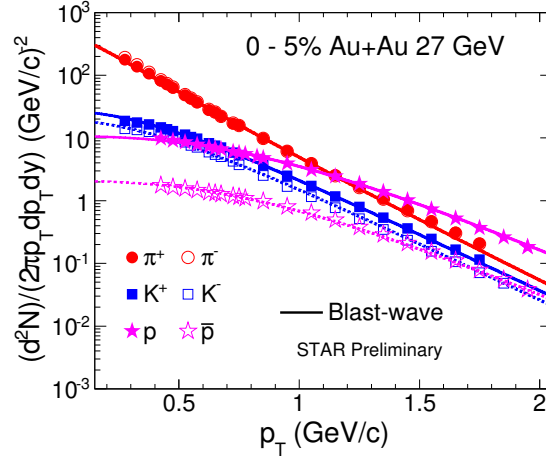


Figure 4.16: Invariant yields of π^\pm , K^\pm , p , and \bar{p} vs. p_T in 0–5% central Au+Au collisions at $\sqrt{s_{\text{NN}}} = 27$ GeV. Curves represent Blast-wave model fits [37].

Figure 4.16 shows the invariant yields of π^\pm , K^\pm , p , and \bar{p} vs. p_T for 0–5% centrality in Au+Au collisions at $\sqrt{s_{\text{NN}}} = 27$ GeV at mid-rapidity and the curves on the spectra represents the Blast-wave model fits. The point-to-point systematic errors on the spectra are included in the blast-wave fits. The measured pions contain large contributions from resonance decays, which vary as a function of p_T . The default blast-wave model does not include resonance decays. So to reduce the systematic error due to resonance decays, the low p_T part (< 0.5 GeV/c) for pion spectra are excluded from the blast-wave fit. The results from the blast-wave fits are very sensitive to the range of p_T used for fitting the spectra.

Here we have used the p_T ranges for pion $p_T : 0.5\text{--}1.3$ GeV/ c , for kaon $p_T : 0.25\text{--}1.4$ GeV/ c , and for (anti)proton $p_T : 0.4\text{--}1.3$ GeV/ c . The blast-wave model usually describe the spectra well for lower p_T . However, the effect on the extracted freeze-out parameters due to different p_T ranges used for fitting is also estimated. These variations are included as systematic error for kinetic freeze-out parameters [41]. The variation of T_{kin} with $\langle\beta\rangle$ is

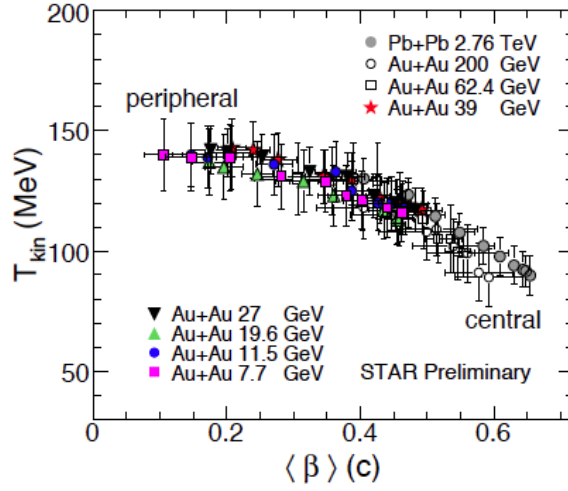


Figure 4.17: Variation of T_{kin} with $\langle\beta\rangle$ for different energies and centralities. The data points other than BES-I energies are taken from Refs. [26, 42].

shown in Fig. 4.17 for different energies and centralities. The $\langle\beta\rangle$ decreases from central to peripheral collisions suggesting more rapid expansion in central collisions, on the other hand, T_{kin} increases from central to peripheral collisions, consistent with the expectation of a shorter lived fireball at peripheral collisions with stronger radial gradients [1]. Furthermore, we observe that these parameters show a two dimensional anticorrelation band. Higher values of T_{kin} correspond to lower values of $\langle\beta\rangle$ and vice-versa.

4.10 Summary

The chemical freeze-out parameters have been extracted from a thermal model fit to the particle yields and ratios at mid-rapidity in GCE and SCE approaches. Chemical freeze-out temperature increases from 7.7 to 19.6 GeV after that it remains almost constant. For a given energy, the value of T_{ch} is almost similar for all centralities. In all the cases studied, the centrality dependence of μ_B is observed which is quite significant at lower energies. The BES-I energies along with the top RHIC energies have allowed to access the region of the QCD phase diagram covering a range of μ_B from 20 to 420 MeV corresponding to Au+Au collision energies from $\sqrt{s_{\text{NN}}} = 200$ to 7.7 GeV, respectively. A centrality dependence of $T_{\text{ch}} - \mu_B$ have been observed at BES-I energies. Current lattice QCD calculations suggest that key features of the phase diagram like the critical point and the first-order phase transition lie within the μ_B reach of the RHIC BES-I program. In RHIC BES-II program, a systematic measurement of the yields of a variety of produced hadrons versus rapidity, centrality, and beam energy will address various questions about the evolution of the hadron yields between the initial hadronisation and the final thermal equilibrium [43] and about the possibility of successive hadronisation [44]. This could lead to further understanding and refinement of the statistical models.

The kinetic freeze-out parameters have been extracted from the simultaneous Blast-wave model fit to the p_T distributions of π^\pm , K^\pm , p, and \bar{p} . The T_{kin} increases from central to peripheral collisions suggesting a longer lived fireball in central collisions, while $\langle\beta\rangle$ decreases from central to peripheral collisions suggesting more rapid expansion in central collisions. It is also observed that higher values of T_{kin} correspond to lower values of $\langle\beta\rangle$ and vice-versa.

Table 4.3: Summary of average number of participating nucleons ($\langle N_{\text{part}} \rangle$) in Au+Au collisions at RHIC energies.

$\sqrt{s_{\text{NN}}}$	Centrality	$\langle N_{\text{part}} \rangle$
Au+Au 7.7 GeV	0 - 5%	337.4 ± 2.1
	5 - 10%	290.4 ± 6
	10 - 20%	226.2 ± 7.9
	20 - 30%	160.2 ± 10.2
	30 - 40%	$109.9 \pm 11.$
	40 - 60%	58.4 ± 9.8
	60 - 80%	20.2 ± 5.3
Au+Au 11.5 GeV	0 - 5%	338.2 ± 1.9
	5 - 10%	290.6 ± 6.1
	10 - 20%	$226. \pm 8.17$
	20 - 30%	159.6 ± 9.4
	30 - 40%	109.9 ± 10.3
	40 - 60%	58.4 ± 9.4
	60 - 80%	20.1 ± 6.7
Au+Au 19.6 GeV	0 - 5%	338.1 ± 2.3
	5 - 10%	289.2 ± 6.0
	10 - 20%	224.9 ± 8.6
	20 - 30%	158.1 ± 10.6
	30 - 40%	108 ± 9.1
	40 - 60%	57.7 ± 9.4
	60 - 80%	19.9 ± 5.8
Au+Au 27 GeV	0 - 5%	343.3 ± 2.0
	5 - 10%	299.3 ± 6.1
	10 - 20%	233.6 ± 8.9
	20 - 30%	165.5 ± 10.7
	30 - 40%	114 ± 11.3
	40 - 60%	61.2 ± 10.4
	60 - 80%	20.5 ± 7.1
Au+Au 39 GeV	0 - 5%	341.6 ± 2.2
	5 - 10%	293.9 ± 6.4
	10 - 20%	229.8 ± 8.7
	20 - 30%	162.4 ± 10.2
	30 - 40%	111.4 ± 10.8
	40 - 60%	59.2 ± 9.6
	60 - 80%	20.03 ± 6.4
Au+Au 62.4 GeV	0 - 5%	347.0 ± 4
	5 - 10%	293.0 ± 6.4
	10 - 20%	229.0 ± 8.4
	20 - 40%	137.4 ± 9.8
	40 - 60%	59.9 ± 7.8
	60 - 80%	19.3 ± 4.6
Au+Au 200 GeV	0 - 5%	352.6 ± 3.7
	5 - 10%	299.3 ± 6.6
	10 - 20%	234.6 ± 8.8
	20 - 30%	166.7 ± 9.8
	30 - 40%	115.5 ± 9.9
	40 - 60%	62.4 ± 9.4
	60 - 80%	20.9 ± 5.8

Table 4.4: Freeze-out parameters obtained from yields in GCE and SCE ($\mu_Q = 0$).

$\sqrt{s_{NN}}$ (GeV)	Cent. (%)	T (MeV)		μ_B (MeV)		μ_S (MeV)		γ_S		R (fm)		χ^2/NDF	
		GCE	SCE	GCE	SCE	GCE	GCE	SCE	GCE	SCE	GCE	SCE	
7.7	0-5	143.9 (3.0)	143.9 (2.5)	406.1 (15.6)	406.8 (15.6)	93.7 (8.8)	1.05 (0.07)	1.06 (0.07)	5.9 (0.4)	5.9 (0.3)	2.4	2.0	
	5-10	143.9 (2.9)	143.9 (2.5)	403.0 (15.2)	403.7 (15.0)	92.5 (8.5)	1.05 (0.07)	1.07 (0.07)	5.5 (0.3)	5.5 (0.3)	1.6	1.3	
	10-20	145.2 (3.0)	144.9 (2.4)	393.6 (14.4)	394.1 (14.2)	88.9 (7.8)	0.96 (0.06)	0.98 (0.06)	5.0 (0.3)	5.0 (0.3)	1.3	1.1	
	20-30	145.0 (3.0)	145.5 (2.4)	383.9 (14.0)	385.5 (14.0)	87.1 (7.7)	0.90 (0.06)	0.92 (0.05)	4.5 (0.3)	4.5 (0.2)	1.0	0.8	
	30-40	146.8 (3.1)	147.1 (2.6)	376.6 (14.3)	378.4 (14.2)	84.8 (7.9)	0.81 (0.05)	0.84 (0.05)	3.9 (0.2)	3.9 (0.2)	0.9	0.7	
	40-60	145.9 (3.1)	148.7 (3.1)	356.8 (14.0)	361.8 (14.4)	85.0 (8.3)	0.69 (0.04)	0.74 (0.04)	3.3 (0.2)	3.1 (0.2)	1.2	1.2	
	60-80	144.1 (3.2)	148.0 (3.4)	338.4 (13.0)	348.4 (13.2)	78.9 (8.5)	0.49 (0.03)	0.64 (0.04)	2.4 (0.2)	2.2 (0.2)	0.7	1.1	
11.5	0-5	152.9 (3.5)	152.3 (3.0)	297.3 (14.2)	297.8 (14.1)	66.5 (8.4)	1.05 (0.07)	1.07 (0.07)	5.9 (0.4)	5.9 (0.3)	1.6	1.3	
	5-10	152.4 (3.5)	152.7 (3.1)	298.3 (14.8)	297.9 (14.7)	70.3 (8.7)	1.09 (0.08)	1.1 (0.07)	5.5 (0.4)	5.4 (0.3)	1.6	1.4	
	10-20	154.7 (3.7)	154.3 (3.1)	291.4 (14.5)	291.9 (14.4)	66.9 (8.4)	1.02 (0.07)	1.05 (0.07)	4.9 (0.3)	4.9 (0.3)	1.3	1.2	
	20-30	156.8 (3.9)	156.4 (3.2)	283.3 (14.5)	284.2 (14.4)	65.2 (8.3)	0.92 (0.06)	0.94 (0.06)	4.2 (0.3)	4.2 (0.3)	1.3	1.1	
	30-40	157.8 (3.9)	157.5 (3.3)	273.8 (14.3)	275.2 (14.2)	62.2 (8.3)	0.84 (0.05)	0.88 (0.05)	3.7 (0.3)	3.7 (0.2)	1.2	1.1	
	40-60	158.4 (4.0)	159.5 (3.6)	261.2 (14.2)	263.5 (14.3)	61.1 (8.3)	0.73 (0.05)	0.79 (0.05)	3.0 (0.2)	2.9 (0.2)	1.2	0.9	
	60-80	155.2 (3.7)	158.8 (3.7)	231.2 (12.7)	236.8 (12.9)	51.5 (8.1)	0.54 (0.04)	0.71 (0.04)	2.2 (0.1)	2.1 (0.1)	1.0	1.3	
19.6	0-5	162.5 (3.1)	161.5 (2.9)	202.9 (10.9)	203.7 (10.9)	46.4 (6.5)	1.07 (0.07)	1.08 (0.07)	5.6 (0.3)	5.7 (0.3)	4.1	3.4	
	5-10	160.7 (3.0)	160.3 (2.8)	195.6 (10.7)	195.9 (10.7)	45.5 (6.4)	1.08 (0.07)	1.09 (0.07)	5.4 (0.3)	5.4 (0.3)	4.0	3.3	
	10-20	162.9 (3.2)	162.7 (2.9)	195.9 (11.0)	196.3 (10.9)	47.2 (6.5)	1.01 (0.06)	1.03 (0.06)	4.8 (0.3)	4.8 (0.2)	3.3	2.7	
	20-30	162.3 (3.1)	162.4 (2.9)	184.3 (10.7)	184.5 (10.6)	44.2 (6.4)	0.97 (0.06)	0.99 (0.06)	4.3 (0.2)	4.3 (0.2)	2.4	2.0	
	30-40	162.1 (3.2)	162.6 (3.1)	170.3 (10.6)	169.9 (10.4)	41.7 (6.5)	0.89 (0.05)	0.91 (0.05)	3.9 (0.2)	3.8 (0.2)	2.1	1.8	
	40-60	162.7 (3.3)	163.4 (3.3)	153.2 (10.9)	154.8 (10.7)	34.3 (6.6)	0.75 (0.04)	0.79 (0.05)	3.1 (0.2)	3.1 (0.2)	1.8	1.5	
	60-80	159.1 (3.2)	162.3 (3.3)	136.9 (10.3)	138.1 (10.2)	33.3 (6.5)	0.63 (0.04)	0.75 (0.05)	2.3 (0.1)	2.2 (0.1)	0.7	1.1	
27	0-5	160.5 (3.8)	160.2 (3.7)	151.6 (12.8)	151.9 (11.5)	34.5 (8.3)	1.1 (0.07)	1.1 (0.07)	6.0 (0.4)	6.0 (0.4)	1.9	1.5	
	5-10	160.7 (3.8)	160.7 (3.7)	149.1 (12.8)	147.9 (11.5)	35.4 (8.3)	1.06 (0.07)	1.07 (0.07)	5.7 (0.4)	5.7 (0.4)	1.7	1.4	
	10-20	160.4 (3.8)	160.2 (3.7)	141.6 (12.7)	141.5 (11.2)	32.3 (8.2)	1.05 (0.07)	1.07 (0.07)	5.2 (0.3)	5.2 (0.3)	1.6	1.3	
	20-30	161.1 (3.9)	161.3 (3.8)	134.7 (12.7)	133.5 (11.2)	32.1 (8.2)	1.0 (0.06)	1.02 (0.06)	4.6 (0.3)	4.6 (0.3)	1.5	1.3	
	30-40	162.8 (4.1)	163.2 (4.0)	134.2 (12.9)	132.1 (11.5)	33.6 (8.4)	0.92 (0.06)	0.94 (0.06)	4.0 (0.3)	3.9 (0.3)	1.1	0.9	
	40-60	163.7 (4.2)	164.5 (4.1)	124.1 (12.8)	122.8 (11.4)	30.7 (8.4)	0.85 (0.06)	0.89 (0.06)	3.2 (0.2)	3.1 (0.2)	0.8	0.7	
	60-80	162.6 (4.2)	165.2 (4.2)	108.5 (12.3)	108.5 (10.9)	26.0 (8.5)	0.68 (0.04)	0.81 (0.05)	2.2 (0.2)	2.1 (0.2)	1.1	0.9	
39	0-5	160.9 (3.6)	160.8 (3.5)	105.3 (11.4)	104.7 (9.9)	24.5 (7.6)	1.09 (0.07)	1.09 (0.07)	6.1 (0.4)	6.1 (0.4)	1.9	1.5	
	5-10	161.2 (3.6)	161.2 (3.5)	104.3 (11.5)	102.9 (9.9)	25.1 (7.7)	1.05 (0.07)	1.06 (0.07)	5.8 (0.4)	5.8 (0.4)	1.5	1.2	
	10-20	161.3 (3.6)	161.5 (3.5)	103.4 (11.4)	100.9 (9.8)	25.9 (7.6)	1.05 (0.07)	1.06 (0.07)	5.3 (0.3)	5.3 (0.3)	1.8	1.5	
	20-30	162.7 (3.7)	162.9 (3.7)	100.3 (11.5)	97.7 (9.9)	25.7 (7.6)	0.99 (0.06)	1.0 (0.06)	4.6 (0.3)	4.6 (0.3)	1.6	1.4	
	30-40	164.8 (3.9)	165.3 (3.9)	95.2 (11.8)	91.9 (10.2)	25.8 (7.8)	0.92 (0.06)	0.94 (0.06)	4.0 (0.3)	3.9 (0.3)	1.1	0.9	
	40-60	163.2 (3.8)	164.2 (3.9)	86.4 (11.3)	81.5 (9.8)	25.0 (7.5)	0.85 (0.05)	0.89 (0.05)	3.3 (0.2)	3.2 (0.2)	1.3	1.2	
	60-80	160.4 (3.6)	163.2 (3.8)	72.3 (10.9)	69.3 (9.5)	19.9 (7.4)	0.69 (0.04)	0.82 (0.05)	2.4 (0.1)	2.3 (0.1)	1.1	0.9	
62.4	0-5	164.3 (3.6)	164.1 (3.6)	69.2 (11.4)	69.2 (10.8)	15.8 (6.8)	0.91 (0.05)	0.92 (0.05)	6.6 (0.4)	6.7 (0.4)	3.7	3.7	
	5-10	160.0 (3.2)	160.0 (3.2)	63.8 (9.9)	62.6 (9.5)	16.1 (6.8)	0.91 (0.05)	0.92 (0.05)	6.6 (0.3)	6.6 (0.3)	2.9	2.9	
	10-20	161.4 (3.1)	161.3 (3.0)	63.7 (9.3)	63.9 (8.8)	13.6 (6.3)	0.92 (0.05)	0.93 (0.05)	5.8 (0.3)	5.85 (0.3)	3.5	3.4	
	20-40	161.7 (2.9)	161.7 (2.9)	58.9 (9.1)	58.5 (8.5)	13.7 (6.3)	0.91 (0.05)	0.92 (0.05)	4.9 (0.2)	4.85 (0.2)	3.1	3.1	
	40-60	160.1 (2.8)	160.5 (2.9)	53.7 (7.9)	54.5 (7.4)	10.1 (6.3)	0.84 (0.04)	0.87 (0.05)	3.7 (0.2)	3.69 (0.2)	3.7	3.8	
	60-80	161.7 (2.9)	164.0 (3.1)	45.4 (8.3)	45.8 (7.9)	11.5 (6.2)	0.74 (0.04)	0.84 (0.04)	2.5 (0.1)	2.37 (0.1)	3.9	4.1	
	60-80	161.7 (2.9)	164.0 (3.1)	45.4 (8.3)	45.8 (7.9)	11.5 (6.2)	0.74 (0.04)	0.84 (0.04)	2.5 (0.1)	2.37 (0.1)	3.9	4.1	
200	0-5	167.8 (4.2)	167.6 (4.2)	26.9 (11.4)	28.1 (8.4)	5.6 (6.8)	0.95 (0.06)	0.95 (0.05)	7.1 (0.5)	7.2 (0.5)	2.7	2.2	
	5-10	168.5 (4.0)	168.2 (4.0)	25.7 (10.9)	28.5 (7.9)	4.2 (6.8)	0.97 (0.05)	0.98 (0.05)	6.5 (0.4)	6.5 (0.4)	2.9	2.5	
	10-20	167.8 (3.8)	167.4 (3.7)	23.2 (10.2)	26.9 (7.5)	3.0 (6.3)	0.99 (0.05)	0.99 (0.05)	5.9 (0.4)	5.9 (0.4)	3.9	3.2	
	20-30	167.5 (3.5)	167.2 (3.5)	23.3 (9.5)	25.9 (6.6)	4.1 (6.3)	0.95 (0.04)	0.96 (0.04)	5.3 (0.3)	5.3 (0.3)	3.4	2.8	
	20-30	165.9 (3.5)	165.8 (3.5)	21.5 (9.7)	20.7 (7.4)	5.6 (6.3)	0.93 (0.04)	0.94 (0.04)	4.7 (0.3)	4.7 (0.3)	3.2	2.6	
	40-60	165.8 (3.3)	164.5 (3.5)	21.3 (9.2)	25.9 (8.1)	4.8 (6.3)	0.88 (0.04)	0.91 (0.04)	3.9 (0.2)	3.9 (0.2)	2.0	1.4	
	60-80	163.6 (3.2)	164.1 (3.2)	17.9 (8.9)	15.3 (6.6)	6.3 (6.2)	0.76 (0.03)	0.83 (0.04)	2.8 (0.1)	2.8 (0.1)	1.1	0.9	

Table 4.5: Freeze-out parameters obtained from ratios in GCE and SCE ($\mu_Q = 0$).

$\sqrt{s_{NN}}$ (GeV)	Cent. (%)	T (MeV)		μ_B (MeV)		μ_S (MeV)	γ_s		χ^2/NDF	
		GCE	SCE	GCE	SCE	GCE	GCE	SCE	GCE	SCE
7.7	0-5	145.9 (5.0)	143.8 (2.5)	404.4 (16.1)	398.6 (8.6)	91.5 (6.4)	1.0 (0.08)	1.03 (0.08)	3.4	3.3
	5-10	144.9 (4.9)	144.1 (2.5)	400.1 (15.7)	398.9 (8.6)	90.8 (6.2)	0.98 (0.08)	0.99 (0.08)	2.0	1.2
	10-20	144.7 (4.7)	144.8 (2.4)	389.2 (14.3)	389.9 (7.8)	87.2 (5.5)	0.89 (0.07)	0.90 (0.07)	1.4	1.4
	20-30	144.2 (4.7)	146.0 (2.4)	381.3 (13.8)	386.5 (7.7)	86.0 (5.3)	0.86 (0.07)	0.85 (0.06)	0.8	0.8
	30-40	145.7 (5.0)	146.7 (2.6)	375.6 (14.1)	378.4 (8.0)	83.8 (5.6)	0.78 (0.07)	0.77 (0.07)	0.7	0.7
	40-60	146.3 (5.1)	150.1 (3.1)	360.1 (13.9)	370.2 (8.4)	82.2 (5.8)	0.69 (0.06)	0.67 (0.05)	1.1	1.2
	60-80	142.9 (4.8)	154.9 (3.4)	333.4 (12.3)	363.8 (9.1)	77.9 (5.5)	0.46 (0.05)	0.42 (0.03)	0.8	2.3
11.5	0-5	150.7 (5.4)	152.8 (2.9)	289.4 (12.8)	294.1 (8.7)	65.3 (4.9)	0.95 (0.09)	0.93 (0.08)	1.2	1.2
	5-10	151.4 (5.6)	153.4 (3.1)	291.1 (13.2)	295.8 (9.1)	66.8 (5.2)	0.99 (0.09)	0.98 (0.08)	1.6	1.6
	10-20	152.6 (5.7)	154.3 (3.1)	284.8 (13.1)	288.7 (8.9)	65.2 (5.0)	0.93 (0.09)	0.92 (0.08)	1.1	1.1
	20-30	154.3 (5.9)	155.9 (3.3)	279.4 (13.2)	282.9 (8.9)	64.4 (5.1)	0.86 (0.08)	0.85 (0.07)	0.8	1.8
	30-40	154.9 (5.9)	156.8 (3.3)	269.6 (12.8)	273.6 (8.8)	61.8 (5.0)	0.79 (0.08)	0.79 (0.06)	0.8	1.8
	40-60	156.1 (6.2)	159.0 (3.5)	258.9 (12.7)	264.6 (8.7)	60.0 (5.1)	0.70 (0.07)	0.69 (0.06)	0.7	0.7
	60-80	151.6 (5.5)	161.3 (3.9)	227.9 (10.5)	245.1 (8.8)	53.2 (4.3)	0.51 (0.05)	0.47 (0.04)	0.7	1.5
19.6	0-5	156.9 (4.9)	159.9 (3.1)	190.3 (8.0)	194.9 (5.9)	43.8 (3.1)	0.94 (0.08)	0.92 (0.07)	2.4	2.1
	5-10	155.7 (4.8)	160.5 (3.2)	184.2 (7.7)	191.5 (5.9)	43.1 (3.0)	0.96 (0.08)	0.93 (0.07)	2.5	2.3
	10-20	158.5 (5.2)	161.6 (3.3)	186.7 (8.0)	191.4 (5.9)	43.9 (3.2)	0.91 (0.08)	0.90 (0.07)	2.2	1.9
	20-30	158.0 (5.2)	162.3 (3.5)	177.5 (7.7)	183.5 (5.8)	41.9 (3.1)	0.90 (0.08)	0.87 (0.07)	1.4	1.3
	30-40	158.7 (5.3)	164.3 (3.8)	164.9 (7.4)	172.2 (5.9)	39.9 (3.1)	0.84 (0.07)	0.81 (0.07)	1.3	1.4
	40-60	158.9 (5.6)	164.9 (4.1)	155.2 (7.2)	162.4 (6.1)	37.2 (3.0)	0.76 (0.07)	0.73 (0.06)	0.8	1.0
	60-80	156.6 (5.4)	166.4 (4.5)	134.7 (6.4)	145.5 (5.8)	33.1 (2.8)	0.61 (0.06)	0.56 (0.05)	0.5	1.3
27	0-5	156.0 (5.6)	157.9 (4.5)	146.1 (8.6)	147.9 (8.3)	32.7 (3.9)	0.98 (0.10)	0.97 (0.09)	1.2	1.2
	5-10	156.2 (5.7)	158.9 (4.6)	143.9 (8.6)	146.7 (8.3)	33.1 (4.0)	0.96 (0.10)	0.94 (0.09)	1.1	1.2
	10-20	156.2 (5.7)	158.0 (4.6)	137.4 (8.4)	139.1 (8.2)	30.1 (3.9)	0.96 (0.09)	0.95 (0.09)	1.01	1.02
	20-30	157.6 (5.9)	159.1 (4.8)	130.9 (8.4)	132.3 (8.2)	29.3 (3.9)	0.94 (0.09)	0.93 (0.09)	1.05	1.04
	30-40	158.9 (6.1)	161.4 (5.1)	131.2 (8.5)	133.5 (8.3)	30.7 (4.0)	0.88 (0.09)	0.87 (0.08)	0.8	0.9
	40-60	160.5 (6.4)	163.7 (4.9)	122.3 (8.4)	124.9 (7.4)	29.7 (4.0)	0.81 (0.08)	0.78 (0.07)	0.5	0.7
	60-80	159.1 (6.4)	165.1 (5.7)	109.5 (8.1)	114.4 (8.4)	28.1 (3.8)	0.65 (0.07)	0.61 (0.06)	0.4	0.9
39	0-5	157.6 (5.7)	160.4 (5.0)	105.0 (8.2)	106.8 (8.4)	25.1 (3.8)	0.95 (0.09)	0.93 (0.09)	1.0	1.1
	5-10	158.8 (5.9)	161.9 (5.2)	104.8 (8.3)	106.8 (8.5)	25.8 (3.9)	0.95 (0.09)	0.93 (0.09)	0.9	1.0
	10-20	157.5 (5.7)	160.9 (5.1)	103.0 (8.1)	105.2 (8.3)	25.5 (3.9)	0.95 (0.09)	0.92 (0.09)	1.1	1.3
	20-30	159.4 (5.9)	162.5 (5.4)	100.4 (8.2)	102.5 (8.5)	25.1 (3.9)	0.92 (0.09)	0.90 (0.08)	0.9	1.1
	30-40	161.9 (6.4)	165.2 (5.8)	95.1 (8.2)	97.2 (8.5)	24.7 (3.9)	0.88 (0.09)	0.86 (0.08)	0.6	0.8
	40-60	161.3 (6.4)	164.7 (5.9)	86.0 (8.0)	88.1 (8.4)	22.6 (3.9)	0.83 (0.08)	0.81 (0.08)	0.6	0.9
	60-80	158.2 (6.2)	162.9 (5.9)	72.9 (7.5)	75.4 (8.1)	20.0 (3.7)	0.67 (0.07)	0.64 (0.06)	0.3	0.8
62.4	0-5	160.3 (4.9)	161.6 (4.4)	69.8 (5.6)	70.3 (5.7)	16.7 (3.3)	0.86 (0.06)	0.86 (0.06)	2.1	2.1
	5-10	158.4 (4.4)	159.5 (4.0)	66.1 (5.3)	66.4 (5.4)	15.7 (3.4)	0.87 (0.06)	0.87 (0.06)	1.7	1.8
	10-20	158.9 (4.3)	160.1 (3.9)	65.4 (5.2)	65.6 (5.3)	15.4 (3.3)	0.84 (0.06)	0.85 (0.05)	1.8	1.8
	20-40	159.8 (4.2)	161.3 (3.9)	60.7 (5.2)	60.9 (5.3)	15.3 (3.2)	0.84 (0.06)	0.84 (0.05)	2.1	2.2
	40-60	158.1 (4.3)	159.1 (4.0)	54.1 (5.2)	54.4 (5.2)	12.1 (3.2)	0.76 (0.06)	0.78 (0.06)	1.8	1.8
	60-80	157.4 (4.2)	159.3 (3.9)	44.6 (5.9)	45.6 (6.1)	10.3 (3.2)	0.69 (0.05)	0.73 (0.05)	1.6	1.9
	60-80	157.4 (4.2)	159.3 (3.9)	44.6 (5.9)	45.6 (6.1)	10.3 (3.2)	0.69 (0.05)	0.73 (0.05)	1.6	1.9
200	0-5	164.3 (5.3)	163.8 (5.2)	28.4 (5.8)	28.9 (5.5)	5.6 (3.9)	0.93 (0.08)	0.94 (0.08)	1.2	0.9
	5-10	163.5 (4.5)	162.9 (4.8)	28.4 (5.5)	29.2 (5.1)	5.0 (3.6)	0.95 (0.08)	0.97 (0.08)	1.4	1.1
	10-20	162.4 (4.4)	162.2 (4.3)	27.7 (5.1)	27.8 (4.8)	5.9 (3.2)	0.94 (0.07)	0.95 (0.07)	2.0	1.6
	20-30	163.9 (4.3)	163.9 (4.2)	27.4 (4.9)	27.2 (4.6)	6.4 (2.9)	0.90 (0.06)	0.91 (0.06)	1.8	1.5
	20-30	161.6 (3.9)	161.8 (3.9)	23.9 (4.8)	23.6 (4.7)	6.0 (3.1)	0.90 (0.06)	0.91 (0.06)	1.9	1.6
	40-60	162.3 (3.9)	162.6 (3.8)	22.9 (4.9)	22.7 (4.9)	5.8 (3.2)	0.84 (0.06)	0.86 (0.06)	1.2	1.0
	60-80	161.3 (3.8)	162.2 (3.7)	18.2 (4.5)	17.4 (4.2)	5.4 (3.3)	0.76 (0.05)	0.80 (0.05)	0.7	0.8

Bibliography

- [1] U. W. Heinz, arXiv:0407360.
- [2] P. Braun-Munzinger *et al.*, Phys. Lett. B 365, 1 (1996); G. D. Yen and M. I. Gorenstein, Phys. Rev. C 59, 2788 (1999).
- [3] F. Becattini *et al.*, Phys. Rev. C 64, 024901 (2001); A. Andronic *et al.*, Nucl. Phys. A 772, 167 (2006).
- [4] E. Schnedermann *et al.*, Phys. Rev. C 48, 2462 (1993); F. Retiere *et al.*, Phys. Rev. C 70, 044907 (2004).
- [5] D. Teaney *et al.*, Phys. Rev. Lett. 86, 4783, (2001); P. Huovinen *et al.*, Phys. Lett. B 503, 58 (2001).
- [6] P. Kolb *et al.*, Nucl. Phys. A 696, 197 (2001); U. W. Heinz *et al.*, Nucl. Phys. A 702, 269 (2002). Phys. Rev. C 81, 024911 (2010).
- [7] F. Becattini, *et al.*, Eur. Phys. Jour. C 66, 377 (2010).
- [8] P. Castorina *et al.*, <http://arxiv.org/abs/1409.3104>.
- [9] M. A. Stephanov, Prog. Theor. Phys. Suppl. 153, 139 (2004); Int. J. Mod. Phys. A 20, 4387 (2005).

- [10] S. Wheaton *et al.*, hep-ph/0407174; S. Wheaton and J. Cleymans, Comput. Phys. Commun. 180, 84 (2009).
- [11] P. Braun-Munzinger, K. Redlich, and J. Stachel, arXiv:0304013 (2003).
- [12] J. Rafelski. *et al.*, Comput. Phys. Commun. 167, 229 (2005).
- [13] A. Kisiel, T. Taluc, W. Broniowski, and W. Florkowski, Comput. Phys. Commun. 174, 669 (2006).
- [14] R. Brun and F. Rademakers, Nucl. Inst. Meth. Phys. 389, 81 (1997).
- [15] K. Hagiwara *et al.*, Phys. Rev. D 66, 010001 (2002).
- [16] F. Becattini, Z. Phys. C 69, 485 (1996).
- [17] F. Becattini and U. Heinz, Z. Phys. C 76, 269 (1997).
- [18] J. Cleymans, D. Elliott, A. Keranen, and E. Suhonen, Phys. Rev. C 57, 3319 (1998).
- [19] J. Cleymans and K. Redlich, Phys. Rev. Lett. 81, 5284 (1998) ; J. Cleymans and K. Redlich, Phys. Rev. C 60, 054908 (1999).
- [20] F. Becattini, M. Gazdzicki, A. Keranen, J. Mannien, and R. Stock, Phys. Rev. C 69, 024905 (2004); I. G. Bearden *et al.* (NA44 Collaboration), arXiv:0202019.
- [21] J. Rafelski, Phys. Lett. B 262, 333 (1991); P. Koch, B. Muueller, and J. Rafelski, Phys. Rep. 142, 167 (1986).
- [22] J. Letessier, J. Rafelski, and A. Tounsi, Phys. Rev. C 50, 405 (1994); C. Slotta, J. Sollfrank, and U. Heinz, AIP Conf. Proc. 340, 462 (1995).
- [23] S. Das (STAR Collaboration), Nucl. Phys. A 904, 891c, (2013); J. Phys. Conf. Ser. 509, 012066 (2014).

- [24] L. Kumar (STAR Collaboration), J. Phys. G Nucl. Part. Phys. 38, 124145 (2011).
- [25] X. Zhu (STAR Collaboration), Acta Phys. Polon. B, Proc. Supp. 5, 213 (2012).
- [26] B. Abelev *et al.* (STAR Collaboration), Phys. Rev. C 79, 034909 (2009).
- [27] M. Aggarwal *et al.* (STAR Collaboration), Phys. Rev. C 83, 024901 (2011); J. Adams *et al.* (STAR Collaboration), Phys. Rev. Lett. 98, 062301 (2007).
- [28] A. Andronic *et al.*, Nucl. Phys. A 772, 167 (2006).
- [29] L. Adamczyk *et al.* (STAR Collaboration), Phys. Rev. Lett. 113, 092301 (2014).
- [30] L. Adamczyk *et al.* (STAR Collaboration), Phys. Rev. Lett. 112, 32302 (2014).
- [31] S. Borsani *et al.*, Phys. Rev. Lett. 111, 062005 (2013).
- [32] A. Bazavov *et al.*, Phys. Rev. Lett. 109, 192302 (2012).
- [33] R. V. Gavai and S. Gupta, Phys. Lett. B 696, 459 (2011).
- [34] S. Gupta *et al.*, Science 332, 1525 (2011).
- [35] S. Dutta *et al.*, Nucl. Phys. A 904, 883c (2013).
- [36] Z. Fodor and S. D. Katz, JHEP 0404, 050 (2004).
- [37] E. Schnedermann *et al.*, Phys. Rev. C 48, 2462 (1993).
- [38] D. Teaney *et al.*, Phys. Rev. Lett. 86, 4783 (2001).
- [39] P. Kolb *et al.*, Nucl. Phys. A 696, 197 (2001).
- [40] U. W. Heinz and P. F. Kolb, Nucl. Phys. A 702, 269 (2002); F. Retiere and M. A. Lisa, Phys. Rev. C 70, 044907 (2004).

- [41] L. Kumar (for the STAR Collaboration), arXiv:1408.4209.
- [42] B. Abelev *et al.* (ALICE Collaboration), Phys. Rev. C 88, 044910 (2013).
- [43] F. Becattini *et al.*, Phys. Rev. Lett. 111, 082302 (2013).
- [44] S. Chatterjee *et al.*, Phys. Lett. B 727, 554 (2013).

Appendix A

Figure 4.1: Comparison of data and model for particle yields in GCE and SCE shown along with standard deviations for Au+Au collisions at $\sqrt{s_{NN}} = 7.7$ GeV.

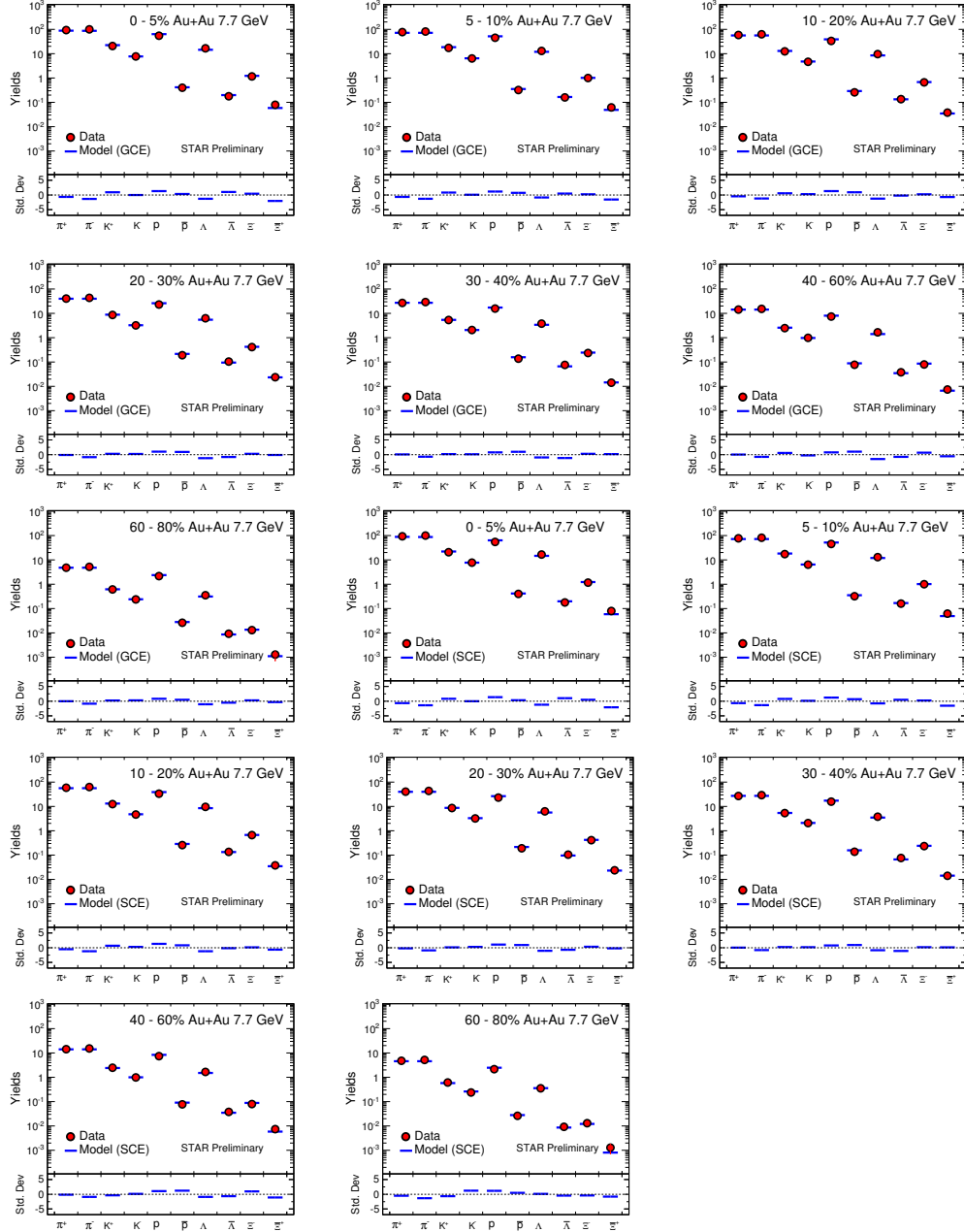


Figure 4.2: Comparison of data and model for particle yields in GCE and SCE shown along with standard deviations for Au+Au collisions at $\sqrt{s_{NN}} = 11.5$ GeV.

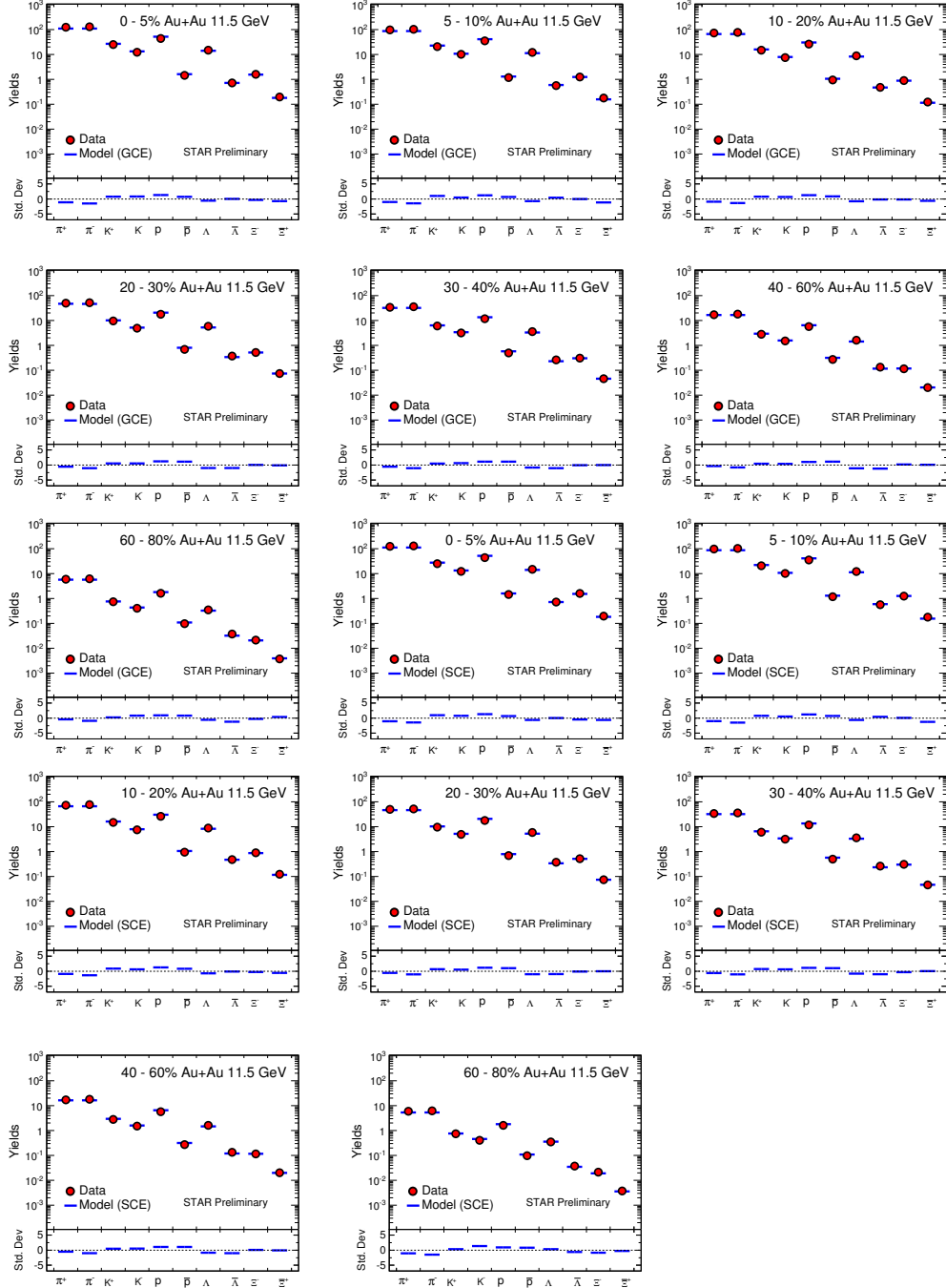


Figure 4.3: Comparison of data and model for particle yields in GCE and SCE shown along with standard deviations for Au+Au collisions at $\sqrt{s_{NN}} = 19.6$ GeV.

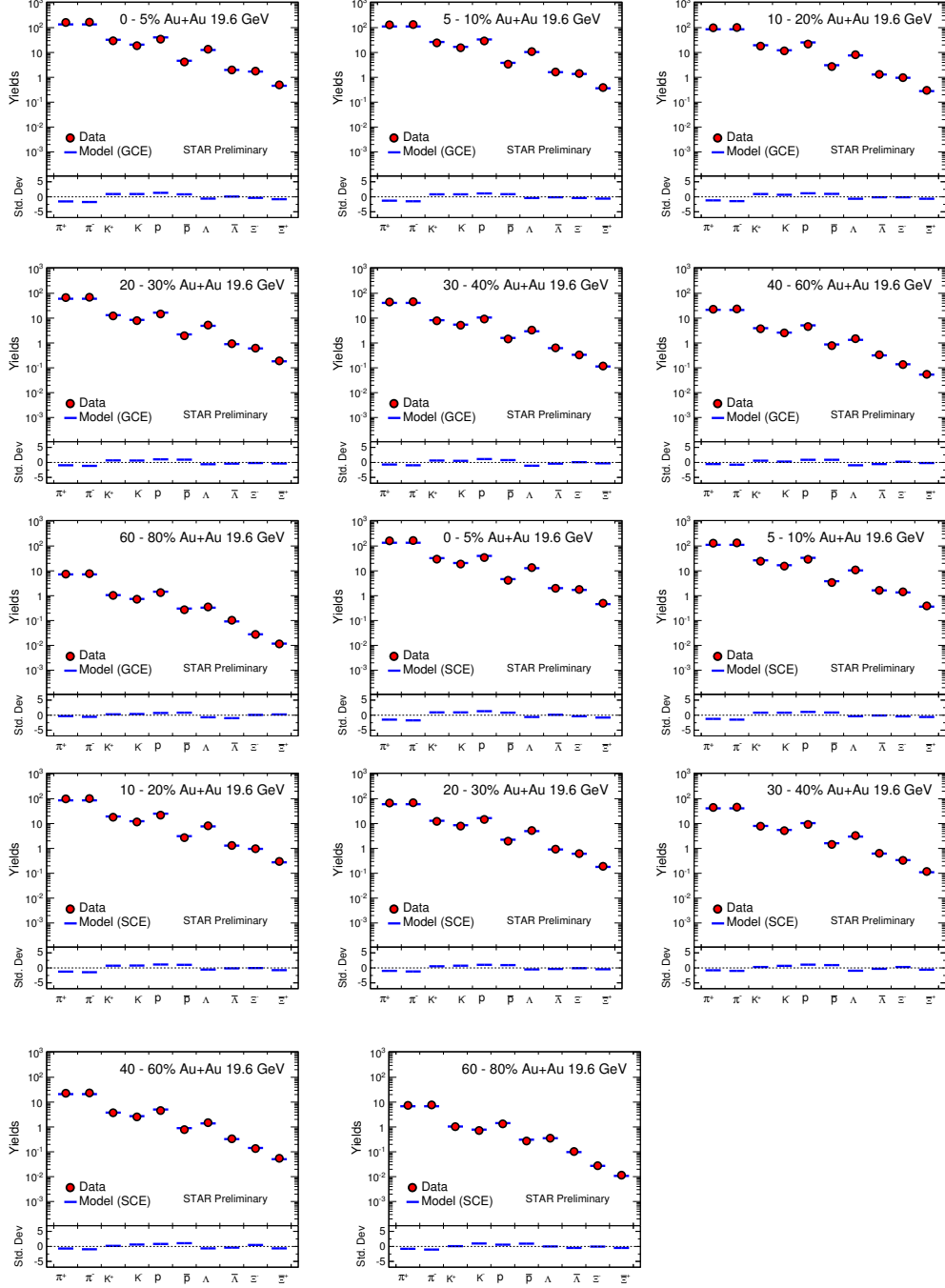


Figure 4.4: Comparison of data and model for particle yields in GCE and SCE shown along with standard deviations for Au+Au collisions at $\sqrt{s_{NN}} = 27$ GeV.

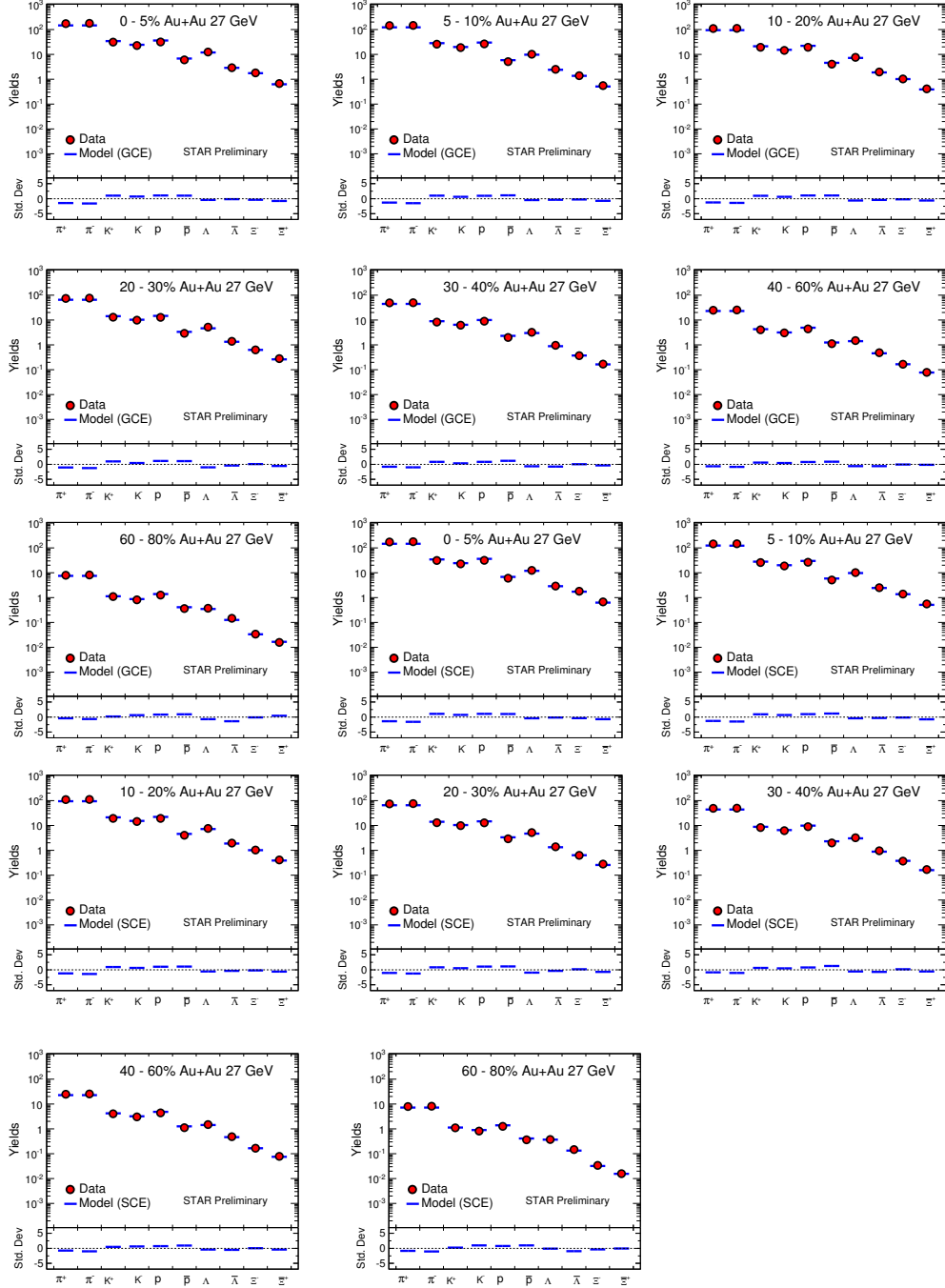


Figure 4.5: Comparison of data and model for particle yields in GCE and SCE shown along with standard deviations for Au+Au collisions at $\sqrt{s_{NN}} = 39$ GeV.

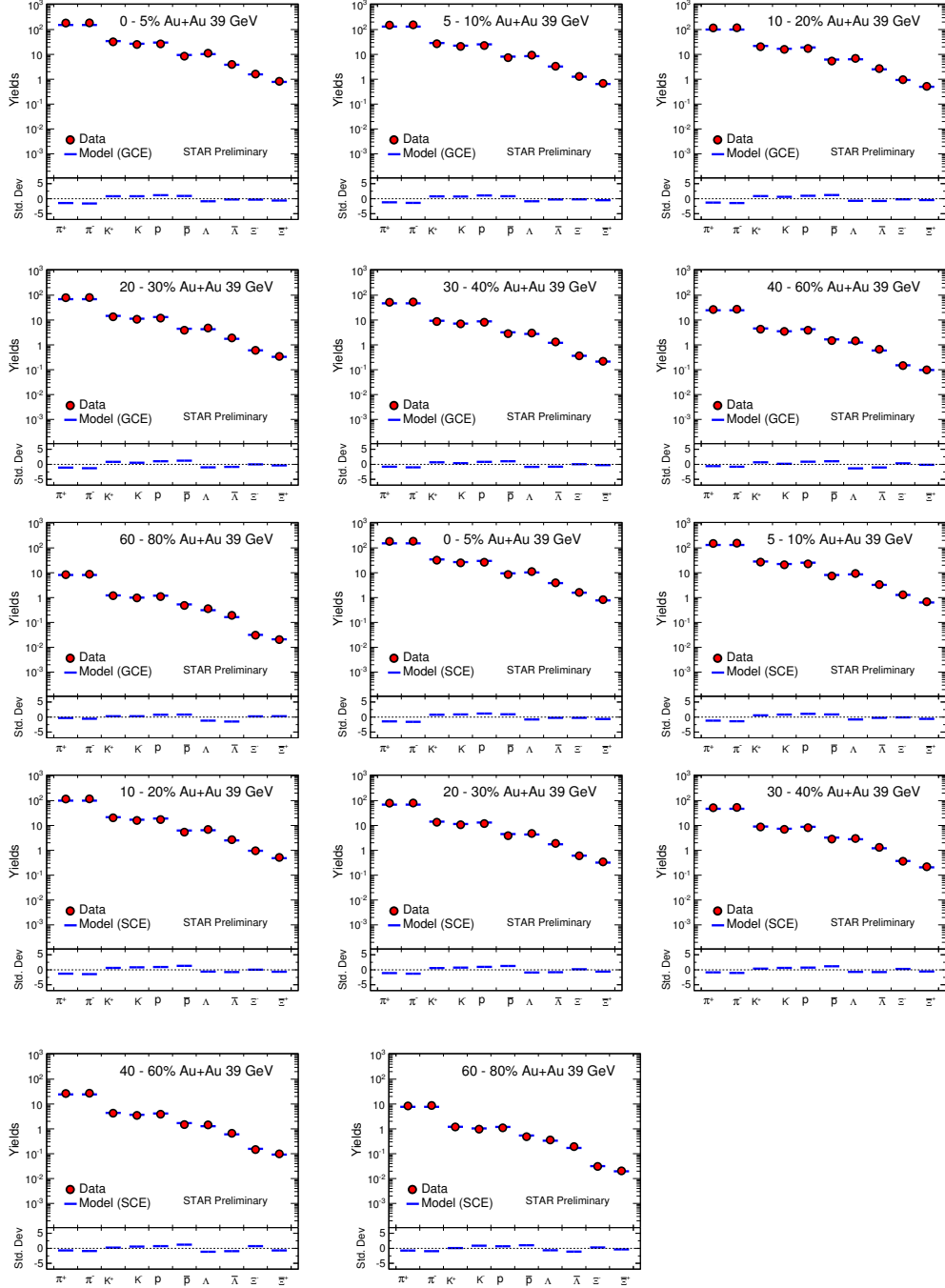


Figure 4.6: Comparison of data and model for particle yields in GCE and SCE shown along with standard deviations for Au+Au collisions at $\sqrt{s_{NN}} = 62.4$ GeV.

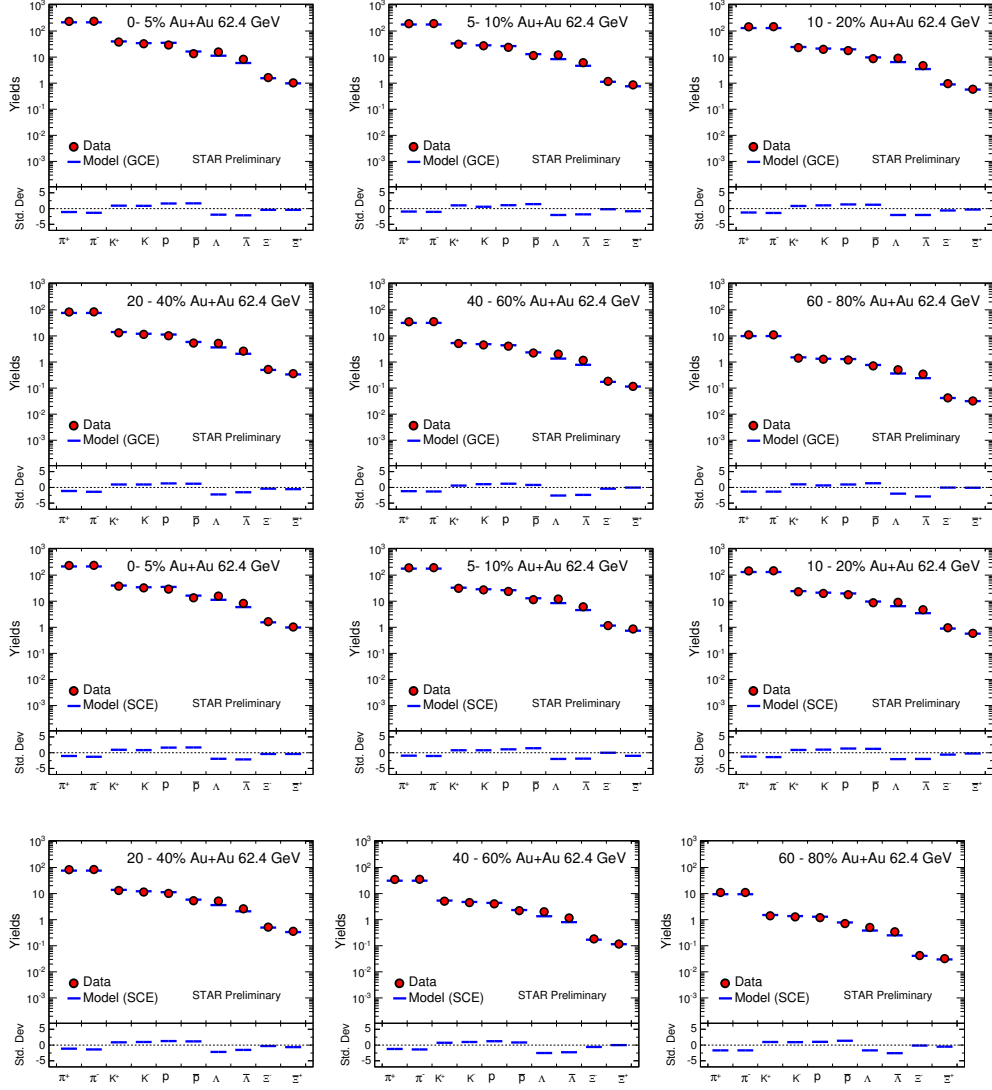
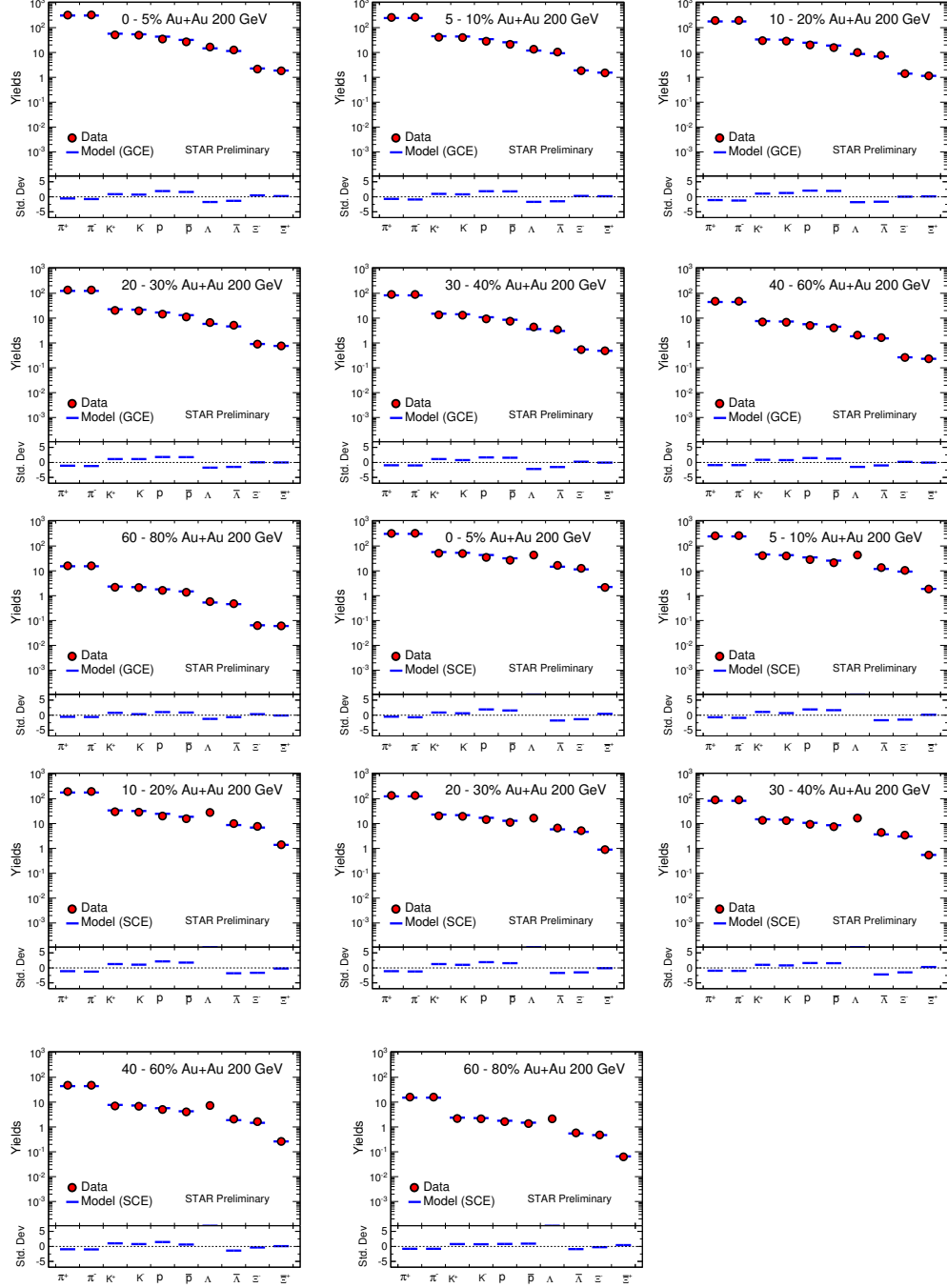


Figure 4.7: Comparison of data and model for particle yields in GCE and SCE shown along with standard deviations for Au+Au collisions at $\sqrt{s_{NN}} = 200$ GeV.



Chapter 5

Systematic Study of Freeze-out

Parameters in Central Heavy-ion

Collisions at AGS, SPS, RHIC, and LHC

Energies

In this chapter, a detailed systematic study on the chemical freeze-out in central heavy-ion collisions are discussed for AGS, SPS, RHIC, and LHC energies.

5.1 Introduction

At low temperatures and densities, hadrons determine the properties of nuclear matter. QCD predicts a transition, which separates the low temperature/density regime of hadronic matter from a high temperature/density region, where quarks and gluons – the basic constituents of QCD, become the most relevant degrees of freedom [1]. This de-confined state is known as QGP and believed to have existed just a few microseconds after the Big

Bang [2]. To understand the nature of the transition of nuclear matter from its initial state to a de-confined QGP and then to a hadronic phase has been a challenging effort for both theory and experiment [3, 4, 5]. In view of this, different experiments have been conducted to recreate the physical conditions experimentally, which can be thought of to have existed in the early universe. Such experimental program started in 1986 with fixed target collisions, accelerating silicon (Si) beams and later gold (Au) beams in the AGS at BNL [6]. At CERN, the SPS as a fixed target experiment, delivered sulphur (S) beams which were followed by lead (Pb) beams in 1995 [7]. Both of AGS and SPS as fixed target experiments had taken data from 2.7 GeV (AGS) up to 17.3 GeV (SPS) per nucleon in the terms of center-of-mass energy. In the fixed target experiments, the ion beams were accelerated to collide against the targets those are fixed in the laboratory frame. In these experiments, a part of the beam energy is locked up in the overall center-of-mass motion and the remaining energy going to physically interesting processes. However, in a collider, the two beams collide head-on and all of the beam energy is center-of-mass energy. In order to reach higher and higher energies, modern colliders have been developed. In 2000, RHIC at BNL started operation with Au+Au collisions which established the existence of QGP phase. Over the last 15 years, RHIC has collected data at different center-of-mass energies from $\sqrt{s_{NN}} = 7.7$ GeV up to 200 GeV in various systems such as Au+Au, d+Au, Cu+Cu, and U+U [8]. In late 2010, a novel opportunity was offered by the LHC at CERN, which started operating with Pb+Pb collisions at $\sqrt{s_{NN}} = 2.76$ TeV [9]. In addition to all these experiments, new experimental facilities have been designed, e.g., FAIR at GSI [10] and NICA at JINR [11] in order to study the freeze-out dynamics and to search for the QCD critical point.

The particle abundances provide information on the temperature and the baryon chemical potential of the system formed in heavy-ion collisions at chemical freeze-out. It may indicate the degree of chemical equilibration. This is of particular interest, because the appearance of a QGP, which is at (or close to) local thermal equilibrium, and its subsequent hadro-

nisation, should lead to chemical equilibrium in the resulting hadronic medium [12, 13, 14]. The level of equilibration of particles produced in different experiments can be studied by analysing the particle abundances using thermal models. Interpreting experimental particle abundances within statistical models have been quite successful for both heavy-ion and elementary collisions [15, 16, 17, 18], as mentioned in the previous chapter. The basic goal of the statistical analysis is to find a set of independent thermal parameters, which can reproduce all the particle yields (or the particle ratios) simultaneously, for a given system at a given energy.

The data collected in different experiments allow one to systematically study the properties of matter formed at freeze-out. We used the most recent preliminary integrated particle yields measured at RHIC BES-I energies at $\sqrt{s_{NN}} = 7.7, 11.5, 19.6, 27,$ and 39 GeV [19, 20, 21, 22] in addition to the data available from AGS ($2.7, 3.32, 3.84, 4.3,$ and 4.85 GeV), SPS ($6.27, 7.62, 8.76, 12.3,$ and 17.3 GeV), top RHIC ($62.4, 130,$ and 200 GeV), and LHC (2760 GeV) energies at mid-rapidity. The freeze-out study has been done for central Au+Au collisions at BNL AGS and RHIC and also for central Pb+Pb collisions at CERN SPS and LHC. This study covers the full range of energies from center-of-mass energy ranging from $\sqrt{s_{NN}} = 2.7$ GeV to 2760 GeV. We use THERMUS model [23] which assumes full thermal and chemical equilibrium of the hadronic matter at freeze-out and explains all the measured particle yields from AGS to LHC. The energy dependence of the chemical freeze-out parameters, $T_{ch}, \mu_B, \mu_S, \mu_Q,$ and γ_S for beam energies in the range $\sqrt{s_{NN}} = 2.7$ GeV to 2760 GeV have been studied. We also discuss the kinetic freeze-out properties obtained using hydrodynamic inspired Blast-wave model fit to the experimental data from AGS to LHC energies for central collisions.

5.2 Chemical Freeze-out

Chemical freeze-out (CFO) is the stage in the evolution of the system in heavy-ion collision when the inelastic processes stop and relative particle yields become fixed. To determine CFO, a set of parameters such as chemical freeze-out temperature T_{ch} , chemical potentials μ_B , μ_Q , μ_S corresponding to B , Q , S , and radius of the fireball, R , are extracted through fitting to the experimental data. An additional parameter γ_s , called the strangeness suppression factor is also used which accounts for out of equilibrium production of strangeness. A detailed study of the physics of CFO is necessary to determine the thermodynamic state of the fireball at the time of CFO. This also sets a baseline for all hadronic thermal physics to be pitted against data to isolate QGP signals as well as the QCD critical point.

The traditional picture of CFO is where all the hadrons chemically freeze-out together (single freeze-out – 1CFO). Such a picture provides a reasonably good description of the hadron multiplicities at all the beam energies with a few exceptions having significantly large χ^2/NDF . The latest LHC data has posed a serious challenge where the strange to non-strange particle ratios like Λ/p cannot be explained with this 1CFO model [24]. Following this, proposals for various alternate freeze-out schemes come out. In Ref. [25], hadronisation followed by hadronic afterburner within the hybrid UrQMD model was employed. PYTHIA generated initial condition was followed by hydrodynamic expansion. Using Cooper-Frye prescription around energy density of 700 MeV/fm^3 , hadrons were formed and the system entered a transport stage that mainly caused due to late stage baryon–antibaryon annihilation. This resulted in successful description of all the particle yields. With the same approach, the centrality dependence of the hadron yields at the LHC was successfully described [26]. For vanishing μ_B , these studies yield a hadronisation temperature of $164 \pm 3 \text{ MeV}$. In another approach, 1CFO with non-equilibrium quark phase

space factors for light and strange quarks were used [27]. This approach also gives a good description of the yields. Both the approaches mentioned above accounted for effects on particle yields due to departure from equilibrium physics. In yet another approach, a flavor dependent freeze-out surfaces was proposed to describe the particle yields [28, 29]. On the basis of hadro-chemistry, it was argued that strange and non-strange hadrons could freeze-out at different times (two freeze-out – 2CFO). In 2CFO, all strange hadrons and those with hidden strangeness freeze-out at the same surface while the rest of the non-strange hadrons freeze-out at a separate surface.

Here we will study the dependence of the extracted chemical freeze-out parameters on:

- (a) the choice of the thermodynamic ensemble,
- (b) choice of the free parameters,
- (c) choice of particles, whose yields are used as inputs to extract the values of the thermal parameters, and
- (d) choice of the CFO scheme.

We find that this program yields fairly robust values of the thermal parameters that show little sensitivity to the specific details of the fitting procedure. We have computed several particle ratios within a thermal-statistical model (THERMUS) in 1CFO and also in 2CFO. Those ratios have been compared with the available data. We find that ratios of particles of unlike flavor are particularly sensitive to the choice of the CFO scheme [30].

5.3 Model

In the last few years, thermal models have been used extensively by several groups [31, 32, 33] and the results of such studies show the successful reproduction of relative particle multiplicities. As different groups use different implementations of the model, the conclusions drawn from the vast applications of the thermal models may not be completely consistent. Both the model and the data set used differ in several important details such as the number of included resonances, the treatment of resonance widths, with or without inclusion of excluded volume corrections, etc. The different conditions may also introduce different results. In this study, to minimize such effects, both 1CFO [23] and 2CFO [28, 29] formulation of the model have been used in a consistent way to describe most of the available mid-rapidity data on central collisions from lower AGS to higher LHC energies. This allows us to observe similarities and differences between two CFO schemes and also the similarity of the various colliding systems to study the behaviour of parameters as a function of center-of-mass energy.

In 1CFO, the data analysis has been performed within an ideal hadron gas statistical model framework for Au+Au and Pb+Pb systems. In order to compute the hadron yields in 1CFO, the publicly available code THERMUS [23] has been used within GCE as well as other ensembles. The details about 1CFO have been described in chapter 4.

In 2CFO, different hadrons may chemically decouple from the fireball at different times at different freeze-out surfaces. As the freeze-out at two different surfaces are independent processes, so, the partition function Z of all the hadrons which are emitted at different times from the fireball can be written as a product of the partition function at each freeze-out surface. The relevant hadron resonance gas (HRG) partition function Z for a

given $\sqrt{s_{\text{NN}}}$ in the GCE is given by [28]

$$\log [Z(\sqrt{s_{\text{NN}}})] = \sum_i \log [Z_i], \quad (5.1)$$

$$Z_i = Z_i(T_i(\sqrt{s_{\text{NN}}}), \mu_i(\sqrt{s_{\text{NN}}}), V_i(\sqrt{s_{\text{NN}}})), \quad (5.2)$$

where Z_i is the partition function of the i^{th} hadron. T_i and V_i are the temperature and volume, respectively, of the fireball as well as the i^{th} hadron at the time of its CFO. There is a single freeze-out surface in 1CFO and hence $T_i(\sqrt{s_{\text{NN}}}) = T(\sqrt{s_{\text{NN}}})$ for all hadrons. Similarly, V_i , μ_{B_i} , μ_{Q_i} , and μ_{S_i} are same for all hadrons. In 2CFO, there are two freeze-out surfaces. $T_i = T_{\text{ns}}$ for all non-strange hadrons, while $T_i = T_{\text{s}}$ for all strange hadrons including the hidden strangeness content. Volume and chemical potentials are also treated similarly. The primordial yield of the i^{th} hadron, N_i^{p} , is given by,

$$\begin{aligned} N_i^{\text{p}} &= \frac{\partial}{\partial \left(\frac{\mu_i}{T_i}\right)} \log [Z] \\ &= \frac{V_i T_i}{\pi^2} g_i m_i^2 \sum_{l=1}^{\infty} (-a)^{l+1} l^{-1} K_2(l m_i / T_i) \\ &\quad \times \exp(l(B_i \mu_{B_i} + Q_i \mu_{Q_i} + S_i \mu_{S_i}) / T_i), \end{aligned} \quad (5.3)$$

where $a = -1$ for bosons and $+1$ for fermions. K_2 is the Bessel function of the second kind. m_i and g_i are the mass and degeneracy factor of the i^{th} hadron and its conserved charges are B_i , Q_i , and S_i .

The total multiplicity of hadrons obtained both in 1CFO and 2CFO, to be compared with experimental data, are determined by the sum of the primordial yield as well as feed-down from heavier resonances as explained in the previous chapter. This is a major part in the analysis procedure because experimental multiplicities used as input to the model may or may not include contributions from weak decays.

We have analysed all available hadronic yields and ratios at AGS, SPS, RHIC, and LHC experiments within GCE and SCE with 1CFO (THERMUS) and with 2CFO freeze-out scheme [28]. The thermal parameters obtained in 1CFO lie intermediate to the freeze-out parameters of the strange and non-strange CFO surfaces in case of 2CFO. We also report several particle ratios, particularly strange to non-strange particle ratios that are sensitive to the CFO mechanism chosen.

5.4 Results and Discussions

An exhaustive compilation of multiplicity data for the central collisions available at various beam energies are given in Tables 5.1, 5.2, 5.3, and 5.4. The 1CFO freeze-out parameters have already been well established for the AGS [34, 35, 36], SPS [37, 38, 39], top RHIC [40, 41], and LHC [42]. In addition to these data, here we have also analysed the preliminary data from RHIC BES-I program [43] at $\sqrt{s_{NN}} = 7.7, 11.5, 19.6, 27, \text{ and } 39$ GeV [19, 20, 21, 22]. The data for non-strange and strange hadrons are available for all the energies from SPS onwards. The multi-strange baryons are not available at the AGS energies (data for $\bar{\Lambda}$ and ϕ is only available at the top AGS energies $\sqrt{s_{NN}} = 4.85$ GeV). This has direct consequence on the extraction of the freeze-out parameters. The extracted value of μ_S observed to be significantly lower from the expected trend at the AGS energies due to the absence of the strange baryons from the fits. While T_{ch} and μ_B seem to be mildly sensitive to the presence of the strange baryons. This is expected since the fireball is baryon dominated at the lower energies (AGS) due to large baryon stopping. This results in higher values of μ_B at AGS energies as compared to SPS energies. Thus, to determine μ_S , strange baryons like Λ , Ξ^- , and Ω are expected to play a significant role as compared to K, which is dominant at higher energies where μ_B is small, and we have a meson dominated fireball.

For all the results reported in this chapter, we always obtain μ_Q from the Eq. 5.4 as given below.

$$\text{Net B/Net Q} = 2.5 \quad (5.4)$$

$$\text{Net S} = 0 \quad (5.5)$$

μ_S and γ_S are sometimes used as free parameters while at other times we obtain μ_S from Eq. 5.5 and fix γ_S to unity. T_{ch} , μ_B , and V are always treated as free parameters. For BES-I energies, particle yields of π^+ , π^- , K^+ , K^- , p , \bar{p} , Λ , $\bar{\Lambda}$, Ξ^- , and $\bar{\Xi}^+$ have been used. For a uniform treatment at all energies, we use the same particle yields for the SPS, top RHIC, and LHC energies. The extracted freeze-out parameters T_{ch} , μ (μ_B , μ_S , μ_Q), γ_s , and R , which is reflective of volume of the system, are shown in Fig. 5.1. The curves in the figures represent parametrisations from Refs. [44, 45]. Results for both SCE and GCE are shown for comparison. The results are found to be quite similar in both the ensembles studied. However, as shown in Fig. 5.6, the χ^2/NDF is consistently lower for SCE than GCE at all energies. This is mainly because there is one less parameter to fit in case of SCE. We have also repeated the fits using ratios instead of yields. We found that the extracted T_{ch} and μ_B parameters are consistent within errors for the two cases. The central values for T_{ch} (μ_B) are higher (lower) when particle yields are used for fitting compared to the case when particle ratios are used. The χ^2/NDF is reduced in case of ratio fits as the uncertainty over volume is irrelevant. However, the use of ratios for fitting is not advisable as the choice of independent ratios out of various possibilities could bias the results of the fits [46]. We have treated μ_S as a free parameter for the above cases and extracted it from fits to data. One could also impose strangeness neutrality condition as in Eq. 5.5 and extract μ_S from it. γ_s was also treated as a free parameter. However, as shown in Fig. 5.1, γ_s does not show any systematic dependence with $\sqrt{s_{\text{NN}}}$ and hovers around unity. We thus, repeated

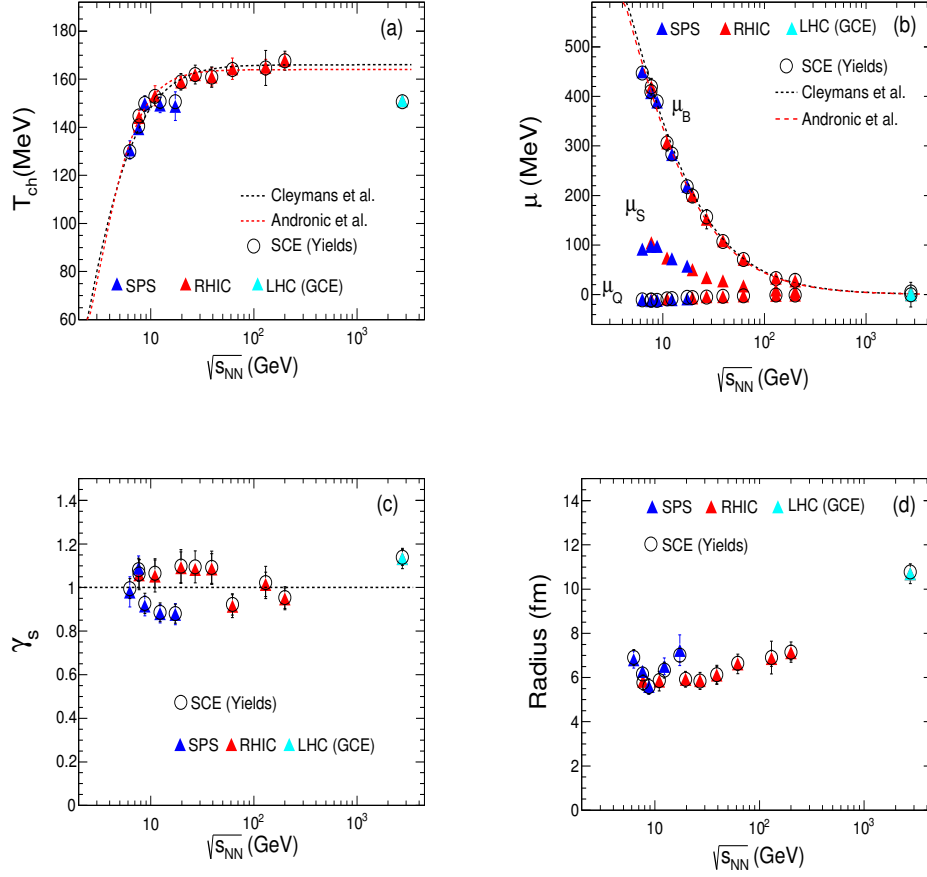


Figure 5.1: Dependence on the choice of ensemble: Thermal parameters (a) T_{ch} , (b) μ (μ_B , μ_S , and μ_Q), (c) γ_s , and (d) radius, plotted as a function of collision energy, extracted within the GCE and SCE ensembles with ICFO as the freeze-out scheme. The dotted curves in the figures represent parametrisations from Refs. [44, 45].

the fits for two further different conditions on parameters. We allowed γ_s to be free while fixed μ_S from Eq. 5.5 in one case, while in the other case we fixed $\gamma_s = 1$ in addition to fixing μ_S . We have compared these cases as shown in Fig. 5.2. The freeze-out parameters extracted seem to be very robust and hence, insensitive to the different fitting procedures. The χ^2/NDF is least for the case where $\gamma_s = 1$ and μ_S is solved from the constraint Eq. 5.5. This is mainly because of the least number of free parameters in this case and hence NDF

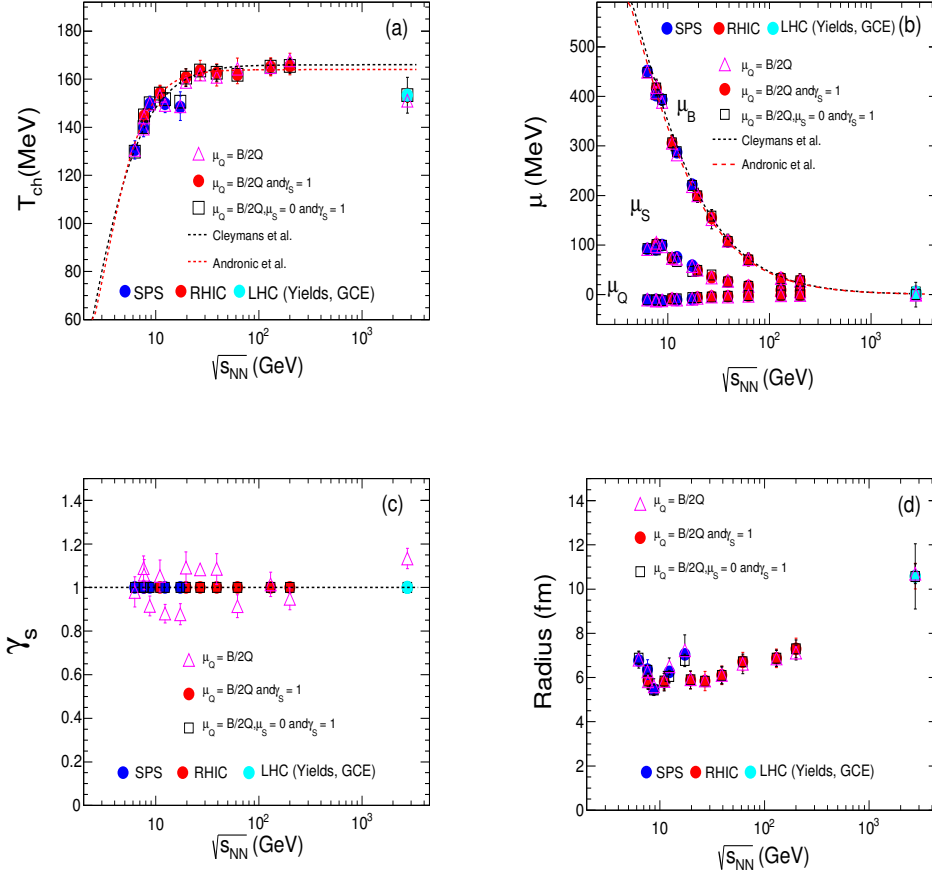


Figure 5.2: Dependence on the fitting procedure: Comparative study of the thermal parameters (a) T_{ch} , (b) μ (μ_B , μ_S , and μ_Q), (c) γ_s , and (d) radius, plotted as a function of collision energy, extracted within GCE with 1CFO as the freeze-out scheme in the three cases: both μ_S and γ_s free, $\gamma_s = 1$ and μ_S free, and in the third case $\gamma_s = 1$ and μ_S fixed from Eq. 5.5.

is the largest. So far, we have been working with only π^+ , π^- , K^+ , K^- , p , \bar{p} , Λ , $\bar{\Lambda}$, Ξ^- , and $\bar{\Xi}^+$ for uniform treatment. After the systematic study of dependence on the choice of ensembles and fitting procedures with the above mentioned uniform particle set at all available energies, we now extend our input particle yields to all available particles like ϕ and Ω at all energies. Figure 5.3 represents the above comparison within the GCE with $\gamma_s = 1$ and μ_S, μ_Q fixed from the constraints given by Eqs. 5.4 and 5.5. The inclusion of ϕ

and Ω yields shows mild dependence on the extracted freeze-out parameters. The extracted μ_Q and μ_S at AGS energies fall short of the expected trend from the SPS due to the absence of the strange baryons from the input data.

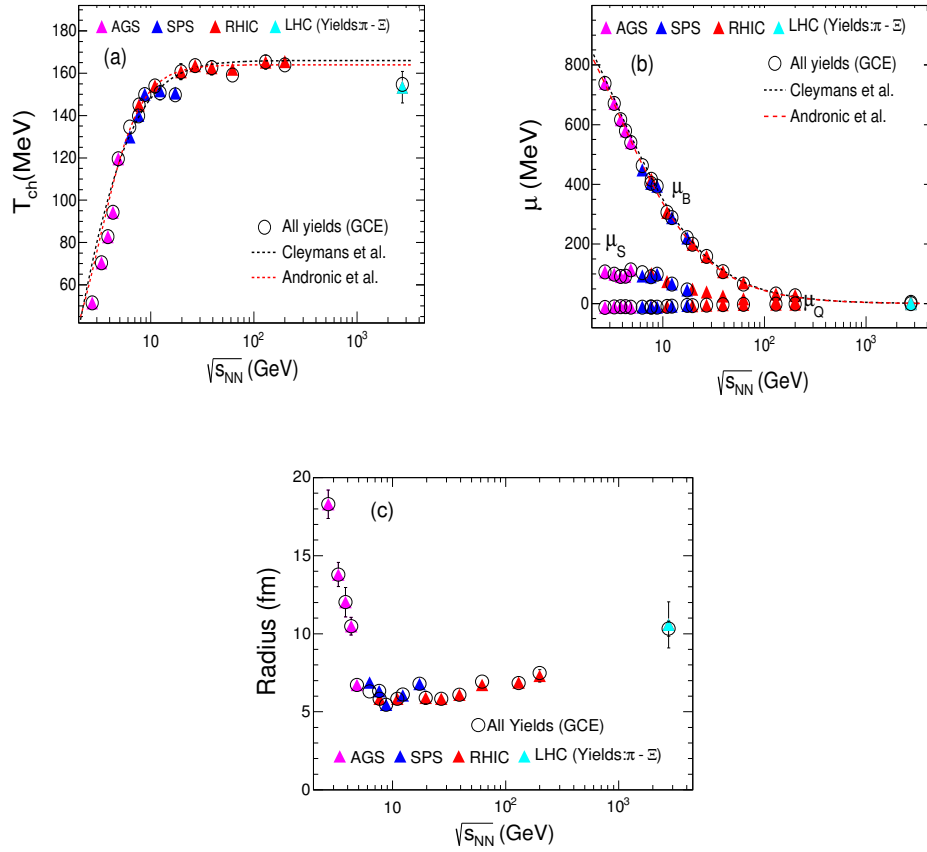


Figure 5.3: Dependence on the choice of particles whose yields are used as input to extract the thermal parameters: Comparative study of the thermal parameters (a) T_{ch} , (b) μ (μ_B , μ_S , and μ_Q), and (c) radius, plotted as a function of collision energy, extracted within GCE with 1CFO as the freeze-out scheme for the two cases: i) π^+ , π^- , K^+ , K^- , p , \bar{p} , Λ , $\bar{\Lambda}$, Ξ^- , and $\bar{\Xi}^+$ where available, and ii) all available particles at all energies as tabulated in Tables 5.1, 5.2, 5.3 and 5.4. Here $\gamma_s = 1$, μ_S fixed from Eq. 5.5, and μ_Q fixed from Eq. 5.4.

As the beam energy increases from lower to higher energies, the T_{ch} increases and chemical potentials decreases. The T_{ch} increases from lower AGS energies up to higher SPS and lower BES-I energies, then it seems to saturate up to top RHIC energies after that it shows a slightly lower value for LHC energy. While chemical potentials are decreasing with $\sqrt{s_{\text{NN}}}$. The trend of chemical potential shows less baryon stopping with increase in $\sqrt{s_{\text{NN}}}$. At lower AGS and SPS energies, the original baryons are stopped in the collision and the mid-rapidity region contains most of the net-baryons. Therefore, at lower energies, the chemical potential has a higher value than at higher energies, when the collisions are more transparent and the mid-rapidity region is almost a net-baryon free region. Net-baryon density decreases with increasing collision energies. From all of the above studies, the extracted freeze-out parameters are quite robust and insensitive to the choice of ensembles, fitting procedures and whether or not particles like ϕ and Ω are included in the fits. Till now, we have presented all the results within 1CFO. The 1CFO fits of all particle yields studied here in GCE and SCE are given in Appendix B. The χ^2/NDF , which is a measure of the goodness of fits, is found to be quite large at few energies. This has led to the development of new freeze-out schemes which can describe the yields better. One such development which we will discuss here is the 2CFO scheme of freeze-out. The freeze-out parameters extracted in the 1CFO scheme and compared with those of 2CFO [47] are shown in Fig. 5.4 in the SCE with $\gamma_s = 1$ and μ_Q solved from Eq. 5.4. We find that the non-strange freeze-out temperature, T_{ns} , is consistently lower than the strange freeze-out temperature, T_s , at all the energies. While at the LHC, T_s and T_{ns} differ by about 5% and at the top SPS energy they differ by about 15%. This can be interpreted as an early freeze-out for the strange hadrons [28, 48]. For all energies, the 1CFO freeze-out parameters lie intermediate to the corresponding 2CFO values for the non-strange and strange CFO surfaces. There is substantial improvement in χ^2/NDF for 2CFO as compared to 1CFO.

Now we will look into the different particle ratios within 1CFO and 2CFO freeze-out

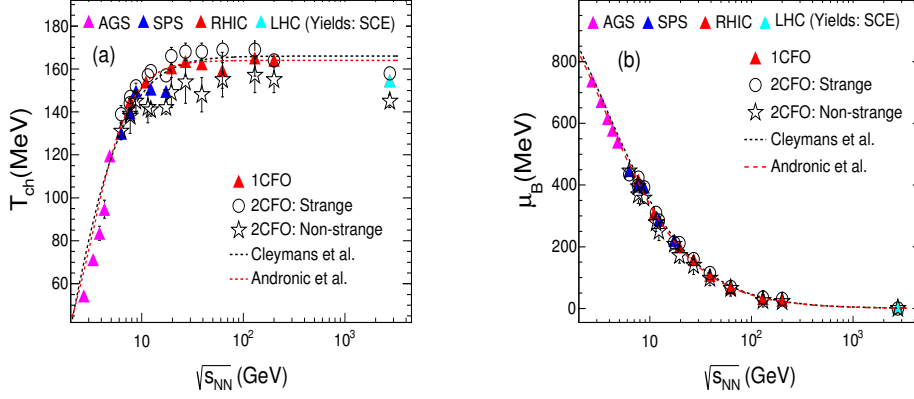


Figure 5.4: Dependence on the choice of CFO scheme: Comparative study of the thermal parameters (a) T_{ch} and (b) μ_B , plotted as a function of collision energy, extracted within SCE with 1CFO and 2CFO as the freeze-out schemes with $\gamma_s = 1$ and μ_Q obtained by solving Eq. 5.4.

schemes. Strange to non-strange particle ratios are particularly sensitive to the choice of CFO scheme as argued in [49]. This is easily understood from the following expression for the particle ratios in statistical model,

$$\begin{aligned}
 N_i/N_j = & \frac{g_i V_i}{g_j V_j} \left(\frac{T_i m_i}{T_j m_j} \right)^{3/2} \exp(m_j/T_j - m_i/T_i) \times \\
 & \exp(B_i \mu_{B_i}/T_i - B_j \mu_{B_j}/T_j) \times \\
 & \exp(Q_i \mu_{Q_i}/T_i - Q_j \mu_{Q_j}/T_j) \times \\
 & \exp(S_i \mu_{S_i}/T_i - S_j \mu_{S_j}/T_j)
 \end{aligned} \tag{5.6}$$

The above equation is obtained from Eq. 5.3 by taking the asymptotic limit $m/T \gg 1$. It is clearly evident from Eq. 5.6 that for ratios of particles of unlike flavors, the thermal factor coefficient $(V_i T_i^{3/2})/(V_j T_j^{3/2})$ do not cancel off. In 1CFO this additional factor does not arise at all. Thus ratios of particles of unlike flavor are good probes to distinguish different freeze-out schemes.

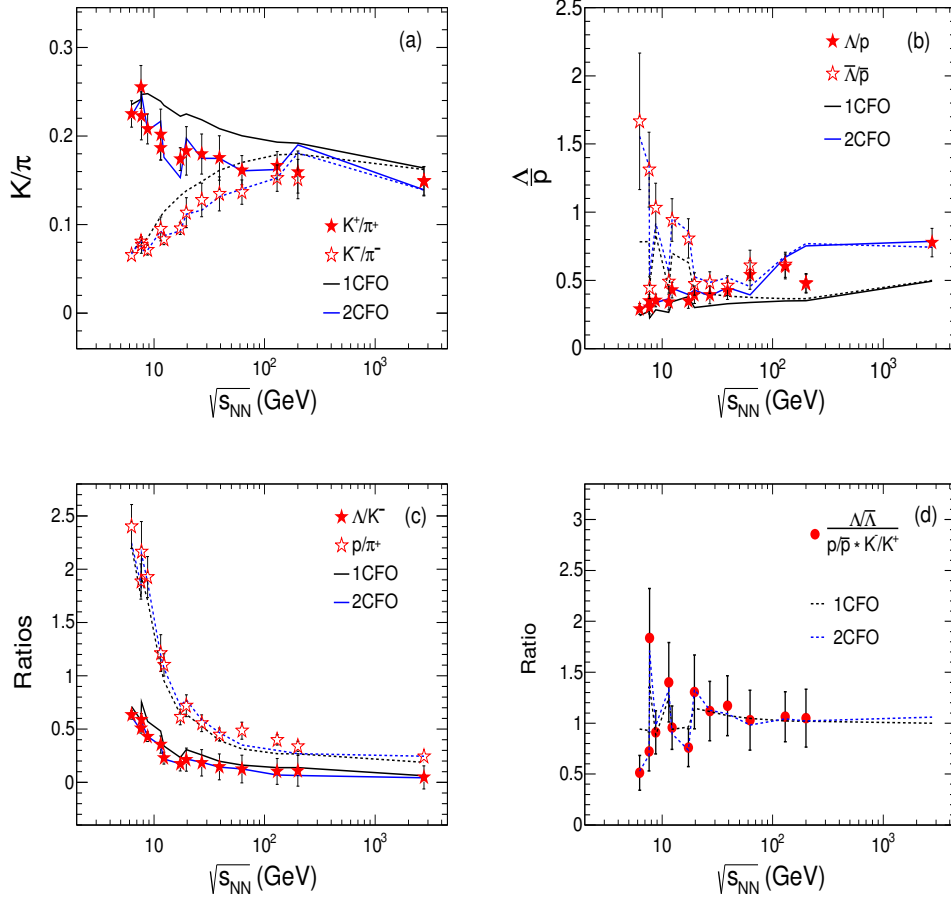


Figure 5.5: Dependence on the choice of CFO scheme on several particle ratios: Comparative study of different particle ratios (a) K^\pm/π^\pm , (b) Λ/p ($\bar{\Lambda}/\bar{p}$), (c) Λ/K^- and p/π^+ , and (d) triple ratio $\left(\frac{\Lambda/\bar{\Lambda}}{(p/\bar{p})(K^-/K^+)}\right)$, plotted as a function of collision energy, within SCE with 1CFO and 2CFO as the freeze-out schemes with $\gamma_s = 1$. The solid curves in the figures (a), (b), and (c) represent 1CFO (black curve) and 2CFO (blue curve) schemes corresponding to ratios shown with solid symbols. The corresponding dotted curves for 1CFO (black) and 2CFO (blue) are for the ratios shown with open symbols.

Figure 5.5 shows the comparison of particle ratios as obtained in 1CFO and 2CFO and compared them with data. The data for ratios are obtained from the ratios of the data of corresponding yields while the errors are propagated in quadratures. We see that particle ratios of same flavor like p/π and Λ/K^- appear similar in both the schemes while those of

unlike flavor like K/π and Λ/p discriminate between different CFO schemes. The 2CFO scheme is found to describe all the ratios better as compared to 1CFO. In bottom right panel of Fig. 5.5, a triple ratio $(\Lambda/\bar{\Lambda})/((p/\bar{p})(K^-/K^+))$ is shown. Since the total B , Q , and S charges carried by Λ is same as those carried by p and K together, the fugacity factors cancel off and this ratio is to a very good approximation unity in 1CFO [50]. However, in 2CFO there is no such constraint. We find in data appreciable deviation from unity below $\sqrt{s_{NN}} = 10$ GeV which can not be described in 1CFO. Currently the errors are very large and hence it is difficult to conclude anything definite. The main reason behind this is that

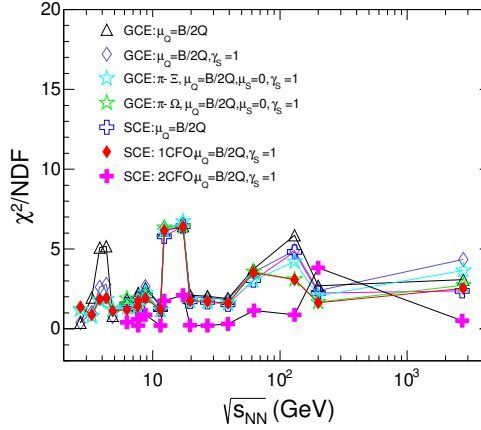


Figure 5.6: The χ^2/NDF as a function of collision energy for the different cases in GCE and SCE along with 1CFO and 2CFO schemes are shown together for comparison.

the errors have been computed in quadratures. This might have led to an overestimation of the errors. A proper estimate of the errors of these quantities by taking into account correlations among various sources of errors is highly desired from experimental side. For all the CFO results discussed above, the χ^2/NDF vs. $\sqrt{s_{NN}}$ is shown in Fig. 5.6.

With the availability of experimental data on light nuclei yields, the statistical model calculations for the light nuclei production in different CFO (2CFO and 1CFO/THERMUS)

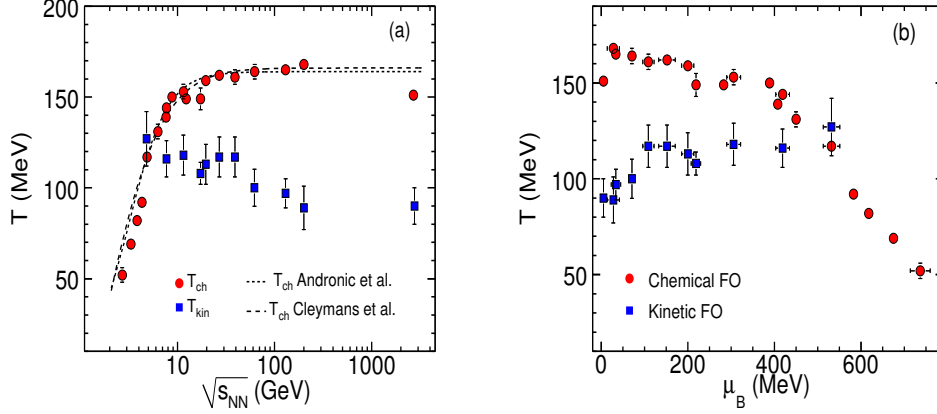


Figure 5.7: (Color online) (a): Energy dependence of T_{ch} and T_{kin} . Curves represent different theory predictions [44, 45]. (b): T_{ch} and T_{kin} plotted as a function of μ_B .

scheme have been reported in Refs. [51, 52, 49]. All the results discussed in this chapter are limited to mid-rapidity. In Refs. [53, 54], a study on rapidity dependence of the chemical freeze-out parameters were well described. The chemical potential is found to be increase from mid-rapidity to forward rapidities, reflecting the increase of the net-baryon density of protons over antiprotons.

After chemical freeze-out, elastic collisions keep the system together until the final thermal freeze-out. The p_T spectra helps to determine the kinetic (thermal) freeze-out (KFO). Figure 5.7(a) shows the energy dependence of chemical and kinetic freeze-out temperatures [47, 55]. The T_{kin} of the system have been obtained using the hydrodynamics-motivated Blast-wave model assuming thermal equilibrium [56, 57, 58, 59]. The simultaneous Blast-wave fits of π^\pm , K^\pm , p , and \bar{p} spectra in central collisions from AGS to LHC energies have been shown in Appendix B. For T_{ch} and/or μ_B , the values obtained from 1CFO GCE fit to the particle yields have been used. The values of kinetic and chemical freeze-out temperatures have been observed to be similar around $\sqrt{s_{\text{NN}}} = 4\text{--}5$ GeV. With the increase of collision energy, the T_{ch} increases and becomes constant after the

$\sqrt{s_{\text{NN}}} = 11.5$ GeV. However, the T_{kin} is almost constant around the 7.7–39 GeV and then decreases up to LHC energies. The separation between T_{ch} and T_{kin} increases with increasing energy (or decreasing μ_B as shown in Fig. 5.7(b)). This might suggest the effect of increasing hadronic interactions between chemical and kinetic freeze-out towards higher energies.

5.5 Summary

The systematic study of chemical freeze-out conditions is discussed at different energies from AGS, SPS, RHIC, and LHC. The very good agreement between the statistical model and the data suggests that a high degree of chemical equilibration is reached. The energy dependence of chemical freeze-out parameters on the choice of thermodynamic ensemble, choice of free parameters and fitting procedures, choice of particles sets in the fits, and choice of chemical freeze-out schemes have been studied in detail. While the weak dependence of the extracted thermodynamic parameters are found on most of the factors listed above, choice of chemical freeze-out scheme seems to influence the fitted freeze-out parameters significantly. In particular, strange to non-strange particle ratios are most sensitive to the chosen chemical freeze-out scheme. The extracted kinetic freeze-out temperature from the Blast-wave fits to the p_T spectra decreases from lower to higher energies. The separation between chemical and kinetic freeze-out temperatures increases while going towards lower μ_B (or higher energies) indicating increasing hadronic interactions between chemical and kinetic freeze-out at higher energies.

Table 5.1: Details of the AGS data sets used for fit with references.

$\sqrt{s_{NN}}$ (GeV)	Expt.	System	Cent.(%)	Particle yields (dN/dy)	Antiparticle yields (dN/dy)	Ref.
2.7	E866,E895 E866 E895 E895	Au+Au	0-5	$\pi^+ : 14.1 \pm 2.17$ $K^+ : 0.381 \pm 0.059$ $p : 82.2 \pm 8.2$ $\Lambda : 0.76 \pm 0.082$	$\pi^- : 21.3 \pm 1.3$	[34] [34] [35] [35]
3.32	E866,E895 E866 E895 E895	Au+Au	0-5	$\pi^+ : 26.4 \pm 3.97$ $K^+ : 2.34 \pm 0.35$ $p : 72.6 \pm 7.1$ $\Lambda : 3.6 \pm 0.37$	$\pi^- : 39 \pm 2.1$ $K^- : 0.19 \pm 0.03$	[34] [34] [35] [35]
3.84	E866,E895 E895 E895 E895	Au+Au	0-5	$\pi^+ : 38.9 \pm 5.85$ $K^+ : 4.84 \pm 0.74$ $p : 63 \pm 6.11$ $\Lambda : 6.8 \pm 0.71$	$\pi^- : 50.8 \pm 2.7$ $K^- : 0.61 \pm 0.09$	[34] [34] [35] [35]
4.3	E866,E895 E895 E895 E895	Au+Au	0-5	$\pi^+ : 49.7 \pm 7.5$ $K^+ : 7.85 \pm 1.2$ $p : 64.1 \pm 6.3$ $\Lambda : 10.25 \pm 1.1$	$\pi^- : 61.1 \pm 3.4$ $K^- : 1.26 \pm 0.2$	[34] [34] [35] [35]
4.85	E866,E895 E895 E895 E891 E891	Au+Au	0-5	$\pi^+ : 57.1 \pm 8.6$ $K^+ : 11.55 \pm 1.74$ $p : 61 \pm 6.2$ $\Lambda : 10 \pm 1$ $\phi : 0.362 \pm 0.085$	$\pi^- : 67 \pm 6.77$ $K^- : 2.21 \pm 0.33$ $\bar{p} : 0.02 \pm 0.002$ $\bar{\Lambda} : 0.02 \pm 0.005$	[34, 35] [34] [36] [35, 36] [36]

Table 5.2: Details of the SPS data sets used for fit with references.

$\sqrt{s_{NN}}$ (GeV)	Expt.	System	Cent.(%)	Particle yields (dN/dy)	Antiparticle yields (dN/dy)	Ref.
6.27	NA49	Pb+Pb	0-7	$\pi^+ : 72.9 \pm 3.6$ $K^+ : 16.4 \pm 0.7$ $p : 46.1 \pm 5.07$ $\Lambda : 13.4 \pm 1.1$ $\Xi^- : 0.93 \pm 0.16$ $\phi : 1.17 \pm 0.44$	$\pi^- : 84.8 \pm 4.2$ $K^- : 5.58 \pm 0.13$ $\bar{p} : 0.06 \pm 0.012$ $\bar{\Lambda} : 0.1 \pm 0.02$	[37] [37] [37] [38] [38] [38]
7.62	NA49	Pb+Pb	0-7	$\pi^+ : 83 \pm 4.2$ $K^+ : 21.2 \pm 1.7$ $p : 42.1 \pm 4.7$ $\Lambda : 14.7 \pm 1.2$ $\Xi^- : 1.17 \pm 0.18$ $\phi : 0.94 \pm 0.33$	$\pi^- : 96.5 \pm 4.83$ $K^- : 7.8 \pm 0.22$ $\bar{p} : 0.16 \pm 0.03$ $\bar{\Lambda} : 0.21 \pm 0.03$ $\Xi^+ : 0.05 \pm 0.014$	[37] [37] [37] [38] [38] [38]
8.76	NA49	Pb+Pb	0-7	$\pi^+ : 96.6 \pm 6.01$ $K^+ : 20.1 \pm 1.04$ $p : 41.3 \pm 4.28$ $\Lambda : 14.6 \pm 1.22$ $\Xi^- : 1.15 \pm 0.17$ $\phi : 1.16 \pm 0.21$ $\Omega : 0.1 \pm 0.03$	$\pi^- : 106.1 \pm 6.01$ $K^- : 7.58 \pm 0.42$ $\bar{p} : 0.32 \pm 0.04$ $\bar{\Lambda} : 0.33 \pm 0.04$ $\Xi^+ : 0.07 \pm 0.01$	[39] [39] [37] [38] [38] [38] [39]
12.3	NA49	Pb+Pb	0-7	$\pi^+ : 132 \pm 7.02$ $K^+ : 24.6 \pm 1.2$ $p : 30.1 \pm 3.2$ $\Lambda : 12.9 \pm 1.02$ $\Xi^- : 1.22 \pm 0.19$ $\phi : 1.52 \pm 0.25$	$\pi^- : 140.4 \pm 7.02$ $K^- : 11.7 \pm 0.6$ $\bar{p} : 0.87 \pm 0.11$ $\bar{\Lambda} : 0.82 \pm 0.09$ $\Xi^+ : 0.21 \pm 0.04$	[39] [39] [39] [39] [39] [39]
17.3	NA49 NA57	Pb+Pb	0-7	$\pi^+ : 170 \pm 9.03$ $K^+ : 29.6 \pm 1.53$ $p : 29.6 \pm 3.1$ $\Lambda : 10.3 \pm 1.1$ $\Xi^- : 1.56 \pm 0.19$ $\phi : 2.44 \pm 0.13$ $\Omega : 0.19 \pm 0.03$	$\pi^- : 175.4 \pm 9.03$ $K^- : 16.8 \pm 0.82$ $\bar{p} : 1.66 \pm 0.24$ $\bar{\Lambda} : 1.34 \pm 0.14$ $\Xi^+ : 0.35 \pm 0.04$ $\bar{\Omega} : 0.097 \pm 0.02$	[39] [39] [39] [39] [39] [39] [39]

Table 5.3: Details of the RHIC data sets used for fit with references.

$\sqrt{s_{NN}}$ (GeV)	Expt.	System	Cent.(%)	Particle yields (dN/dy)	Antiparticle yields (dN/dy)	Ref.
7.7	STAR	Au+Au	0-5	π^+ : 93.4 ± 8.4 K^+ : 20.8 ± 1.7 p : 54.96 ± 6.6 Λ : 16.7 ± 1.71 Ξ^- : 1.17 ± 0.12	π^- : 100 ± 9.03 K^- : 7.7 ± 0.62 \bar{p} : 0.39 ± 0.06 $\bar{\Lambda}$: 0.18 ± 0.02 Ξ^+ : 0.08 ± 0.01	[19] [19] [19] [21] [21]
11.5	STAR	Au+Au	0-5	π^+ : 123.9 ± 12.4 K^+ : 25 ± 2.5 p : 44 ± 5.7 Λ : 14.97 ± 1.52 Ξ^- : 1.59 ± 0.17	π^- : 129.8 ± 13.01 K^- : 12.3 ± 1.24 \bar{p} : 1.46 ± 0.2 $\bar{\Lambda}$: 0.72 ± 0.07 Ξ^+ : 0.19 ± 0.02	[19] [19] [19] [21] [21]
19.6	STAR	Au+Au	0-5	π^+ : 161.4 ± 17.8 K^+ : 29.56 ± 2.97 p : 34.2 ± 4.5 Λ : 13.5 ± 1.36 Ξ^- : 1.77 ± 0.18	π^- : 165.8 ± 18.3 K^- : 18.8 ± 1.89 \bar{p} : 4.16 ± 0.58 $\bar{\Lambda}$: 1.98 ± 0.19 Ξ^+ : 0.49 ± 0.05	[19, 20] [19, 20] [19, 20] [21, 22] [21, 22]
27	STAR	Au+Au	0-5	π^+ : 172.9 ± 19.02 K^+ : 31.1 ± 1.9 p : 31.7 ± 4.1 Λ : 12.5 ± 1.26 Ξ^- : 1.81 ± 0.18	π^- : 177.1 ± 19.5 K^- : 22.6 ± 2.3 \bar{p} : $6. \pm 0.78$ $\bar{\Lambda}$: 2.91 ± 0.29 Ξ^+ : 0.68 ± 0.07	[19, 20] [19, 20] [19, 20] [21, 22] [21, 22]
39	STAR	Au+Au	0-5	π^+ : 182.3 ± 20.1 K^+ : 31.9 ± 2.9 p : $26.5.7 \pm 2.92$ Λ : 11.2 ± 1.13 Ξ^- : 1.62 ± 0.17	π^- : 185.8 ± 20.5 K^- : $25. \pm 2.3$ \bar{p} : 8.49 ± 1.02 $\bar{\Lambda}$: 3.92 ± 0.39 Ξ^+ : 0.83 ± 0.08	[19] [19] [19] [21] [21]
62.4	STAR	Au+Au	0-5	π^+ : 233 ± 17 K^+ : 37.6 ± 2.7 p : 29 ± 3.8 Λ : 15.7 ± 2.3 Ξ^- : 1.63 ± 0.18	π^- : 237 ± 17 K^- : 32.4 ± 2.3 \bar{p} : 13.6 ± 1.7 $\bar{\Lambda}$: 8.3 ± 1.1 Ξ^+ : 1.03 ± 0.11	[40] [40] [40] [40] [40]
			0-20	ϕ : 3.52 ± 0.45		[40]
			0-20	Ω : 0.212 ± 0.033	$\bar{\Omega}$: 0.167 ± 0.031	[40]
130	STAR	Au+Au	0-5	π^+ : 278 ± 20 K^+ : 46.3 ± 3 p : 28.2 ± 3.1 Λ : 17 ± 1.75	π^- : 280 ± 20 K^- : 42.7 ± 2.8 \bar{p} : 20 ± 2.2 $\bar{\Lambda}$: 12.3 ± 1.24	[40] [40] [40] [40]
			0-10	Ξ^- : 2 ± 0.24	Ξ^+ : 1.7 ± 0.21	[41]
			0-10	ϕ : 5.73 ± 0.783		[41]
			0-20	Ω : 0.32 ± 0.1	$\bar{\Omega}$: $0.34 \pm$	[40]
200	STAR	Au+Au	0-5	π^+ : 322 ± 25 K^+ : 51.3 ± 6.5 p : 34.7 ± 4.4 Λ : 16.7 ± 1.1 Ξ^- : 2.17 ± 0.2	π^- : 327 ± 25 K^- : 49.5 ± 6.2 \bar{p} : 26.7 ± 3.4 $\bar{\Lambda}$: 12.7 ± 0.9 Ξ^+ : 1.83 ± 0.2	[40] [40] [40] [41] [41]
			0-10	ϕ : 7.42 ± 0.69		[41]
			0-5	Ω : 0.31 ± 0.06	$\bar{\Omega}$: 0.33 ± 0.07	[40]

Table 5.4: Details of the LHC data sets used for fit with references.

$\sqrt{s_{NN}}$ (GeV)	Expt.	System	Cent.(%)	Particle yields (dN/dy)	Antiparticle yields (dN/dy)	Ref.
2700	ALICE	Pb+Pb	0-10	π^+ : 669.5 ± 48 K^+ : 100 ± 8 <p>: 31 ± 2.5 Λ : 24.1 ± 2.6 Ξ^- : 3.34 ± 0.25 ϕ : 12.8 ± 1.5 Ω : 0.58 ± 0.10 </p>	π^- : 668 ± 47 K^- : 99.5 ± 8.51 \bar{p} : 30.5 ± 2.5 $\bar{\Xi}^+$: 3.28 ± 0.28 $\bar{\Omega}$: 0.60 ± 0.11	[42] [42] [42] [42] [42] [42] [42]

Bibliography

- [1] Y. Aoki *et al.*, Nature 443, 675 (2006).
- [2] B. B. Back *et al.*, Nucl. Phys. A 757, 28 (2005); J. Adams *et al.* (STAR Collaboration), Nucl. Phys. A 757, 102 (2005); M. Gyulassy and L. McLerran, Nucl. Phys. A 750, 30 (2005).
- [3] S. Ejiri, Phys. Rev. D 78, 074507 (2008).
- [4] X. Luo *et al.*, Science 332 (6037), 1525 (2011).
- [5] B. Mohanty (STAR Collaboration), New J. Phys. 13, 065031 (2011); B. Mohanty (STAR Collaboration), PoS CPOD2013, 001 (2013); B. Mohanty (STAR Collaboration) EPJ Web Conf. 66, 04022 (2014).
- [6] H. Foelsche, D. S. Barton and P. Thieberger, Proc. 13th International Conference on High Energy Accelerators, 1, 229 (1986); G. S. F. Stephans, Nucl. Phys. A 583, 653 (1995).
- [7] H. H. Gutbrod *et al.*, CERN/SPSLC 91-17, SPSLC/P260.
- [8] G. Baym, hep-ph/0104138; B. I. Abelev *et al.* (STAR Collaboration), STAR Internal Note, SN0493 (2009).

- [9] O. S. Bruning, P. Collier, P. Lebrun, S. Myers, R. Ostojic, J. Poole, and P. Proudlock (editors), CERN-2004-003-V1 (2004); L. Evans and P. Bryant (editors), JINST 3, S08001 (2008).
- [10] J. M. Heuser (for CBM Collaboration), Nucl. Phys. A 830, 563c (2009).
- [11] http://nica.jinr.ru/files/NICA_CDR.pdf (2008); Kh. A. Abraamyan *et al.*, Nucl. Instr. Meth. A 628, 99 (2011).
- [12] R. Stock, Phys. Lett. B 456, 277 (1999); Prog. Part. Nucl. Phys. 42, 295 (1999).
- [13] P. Braun-Munzinger and J. Stachel, Nucl. Phys. A 606, 320 (1996).
- [14] U. Heinz, Nucl. Phys. A 685, 414c (2001).
- [15] P. Braun-Munzinger *et al.*, Phys. Lett. B 365, 1 (1996).
- [16] G. D. Yen and M. I. Gorenstein, Phys. Rev. C 59, 2788 (1999).
- [17] F. Becattini *et al.*, Phys. Rev. C 64, 024901 (2001).
- [18] A. Andronic *et al.*, Nucl. Phys. A 772, 167 (2006).
- [19] L. Kumar (for the STAR collaboration), J. Phys. G: Nucl. Part. Phys. 38, 124145 (2011); Nucl. Phys. A 904, 256c, (2013).
- [20] S. Das (for the STAR collaboration), Nucl. Phys. A 904, 891c (2013); J. Phys. Conf. Ser. 509, 012066 (2014).
- [21] X. Zhu (STAR Collaboration), Acta Phys. Pol. B Proc. Supp. 5, 213 (2012).
- [22] F. Zhao (STAR Collaboration), J. Phys. Conf. Ser. 509, 012085 (2014).
- [23] S. Wheaton and J. Cleymans, Comput. Phys. Commun. 180, 84 (2009).

- [24] J. Stachel, A. Andronic, P. Braun-Munzinger, and K. Redlich, arXiv:1311.4662.
- [25] J. Steinheimer *et al.*, Phys. Rev. Lett. 110, 042501 (2013).
- [26] F. Becattini *et al.*, arXiv:1405.0710.
- [27] M. Petran *et al.*, Phys. Rev. C 88, 034907 (2013).
- [28] S. Chatterjee, R. Godbole, and S. Gupta, Phys. Lett. B 727, 554 (2013).
- [29] K. Bugaev *et al.*, Euro. phys. Lett. 104, 22002 (2013).
- [30] S. Chatterjee and B. Mohanty, arXiv:1405.2632.
- [31] J. Cleymans *et al.*, Phys. Rev. C 60, 054908 (1999).
- [32] F. Becattini *et al.*, Phys. Rev. C 64, 024901 (2001).
- [33] P. Braun-Munzinger, I. Heppe, and J. Stachel, Phys. Lett. B 465, 15 (1999).
- [34] L. Ahle *et al.*, Phys. Lett. B 476, 1 (2000); J. Klay *et al.*, Phys. Rev. C 68, 054905 (2003); L. Ahle *et al.*, Phys. Lett. B 490, 53 (2000).
- [35] J. Klay *et al.*, Phys. Rev. Lett. 88, 102301 (2002); C. Blume and C. Markert, Prog. in Part. and Nucl. Phys. 66, 834 (2011); B. B. Back *et al.*, Phys. Rev. Lett. 86 (1970); J. Barrette *et al.*, Phys. Rev. C 62, 024901 (2000).
- [36] L. Ahle *et al.*, Phys. Rev. C 60, 064901 (1999); B. B. Back *et al.*, Phys. Rev. Lett. 87, 242301 (2001); B. B. Back *et al.*, Phys. Rev. C 69, 054901 (2004).
- [37] C. Alt *et al.*, Phys. Rev. C 77, 024903 (2008); <http://arxiv.org/abs/nucl-ex/0512033>; Phys. Rev. C 78, 034918 (2008).
- [38] C. Alt *et al.*, Phys. Rev. C 78, 044907 (2008); S. Afanasiev *et al.*, Phys. Rev. C 66, 054902 (2002).

- [39] F. Antinori *et al.*, J. Phys. G: Nucl. Part. Phys. 32, 427 (2006); I. Bearden, H. Boggild, and J. Boissevain *et al.*, Phys. Rev. C 66, 044907 (2002); F. Antinori *et al.*, Phys. Lett. B 595, 68 (2004); S. Afanasev *et al.*, Phys. Lett. B 491, 59 (2000).
- [40] B. I. Abelev *et al.*, Phys. Rev. C 79, 034909, (2009); M. Aggarwal *et al.*, Phys. Rev. C 83, 024901, (2011); B. Abelev *et al.*, Phys. Rev. C 79, 064903, (2009); K. Adcox *et al.*, Phys. Rev. Lett. 89, 092302 (2002).
- [41] J. Adams, *et al.*, Phys. Rev. Lett. 92, 182301 (2004); C. Adler *et al.*, Phys. Rev. C 65, 041901 (2002); J. Adams *et al.*, Phys. Rev. Lett. 98, 062301 (2007); J. Adams *et al.*, Phys. Lett. B 612, 181 (2005).
- [42] L. Milano (ALICE Collaboration), Nucl. Phys. A 904, 531c (2013).
- [43] B. Mohanty, Nucl. Phys. A 830, 899 (2009).
- [44] J. Cleymans *et al.*, Phys. Rev. C 73, 034905, (2006); Phys. Lett. B 615, 50 (2005).
- [45] A. Andronic *et al.*; Nucl. Phys. A 834, 237 (2010).
- [46] F. Becattini, <http://arxiv.org/abs/0707.4154>.
- [47] S. Chatterjee, S. Das *et al.*, Adv. in High Eng. Phys., Article ID 349013, in press.
- [48] V. Begun *et al.*, <http://arxiv.org/abs/1405.7252>.
- [49] S. Chatterjee and B. Mohanty, Phys. Rev. C 90, 034908 (2014).
- [50] S. Chatterjee *et al.*, in preparation.
- [51] A. Andronic *et al.*, Phys. Lett. B 697, 203 (2011).
- [52] J. Cleymans, *et al.*, Phys. Rev. C 84, 054916 (2011).

- [53] J. Takahashi (for the STAR Collaboration), J. Phys. G: Nucl. Part. Phys. 36, 064074 (2009).
- [54] O. Ristea (for the BRAHMS Collaboration), Romanian Reports in Physics, 56, 659 (2004).
- [55] L. Kumar (for the STAR Collaboration), arXiv:1408.4209.
- [56] E. Schnedermann *et al.*, Phys. Rev. C 48, 2462 (1993).
- [57] D. Teaney *et al.*, Phys. Rev. Lett. 86, 4783 (2001).
- [58] P. Kolb *et al.*, Nucl. Phys. A 696, 197 (2001).
- [59] U. W. Heinz and P. F. Kolb, Nucl. Phys. A 702, 269 (2002); F. Retiere and M. A. Lisa, Phys. Rev. C 70, 044907 (2004).

Appendix B

Figure 5.1: Comparison of data and model (ICFO) for particle yields in GCE shown along with standard deviations for AGS and SPS energies ($\mu_Q = B/2Q$, $\mu_S = 0$, $\gamma_S = 1$).

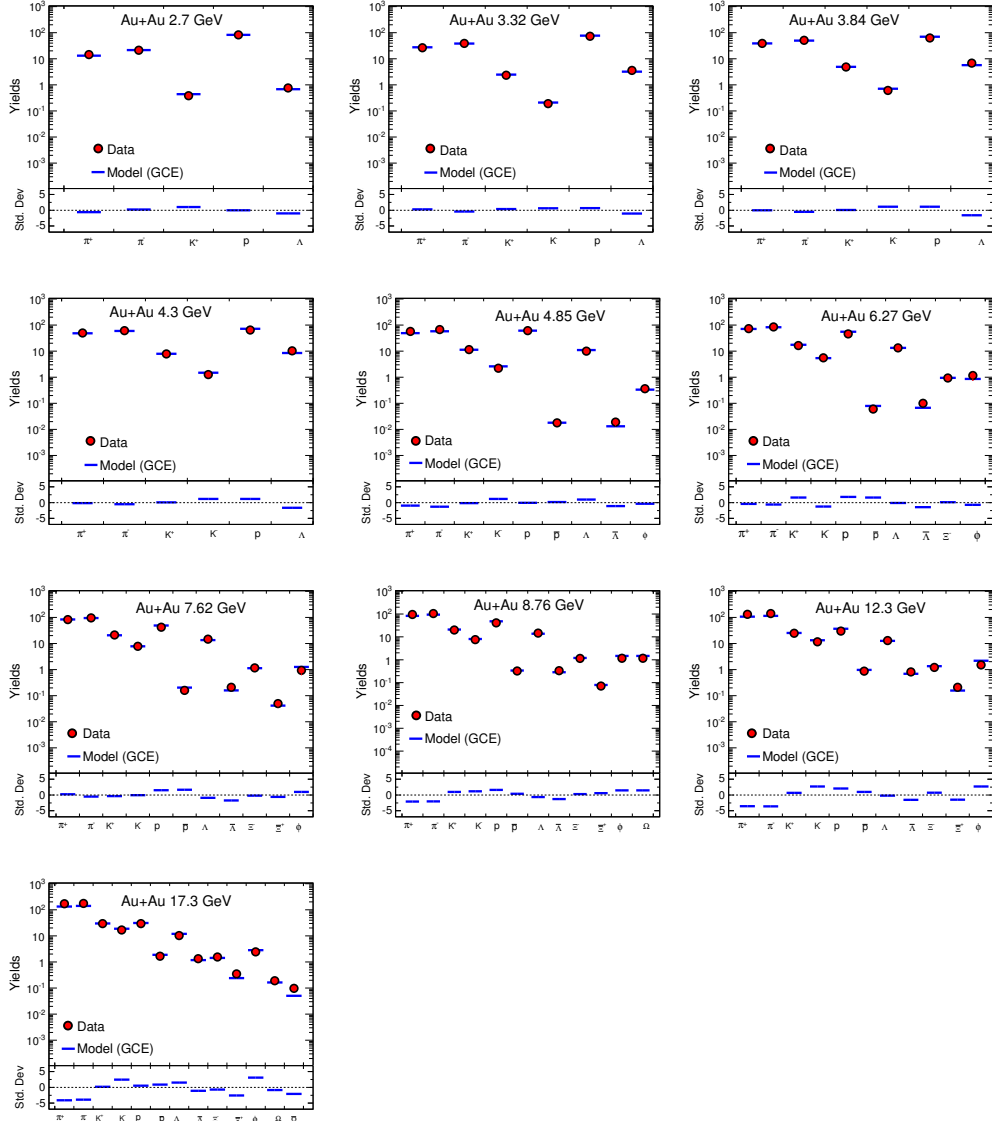


Figure 5.2: Comparison of data and model (ICFO) for particle yields in GCE shown along with standard deviations for RHIC and LHC energies ($\mu_Q = B/2Q$, $\mu_S = 0$, $\gamma_S = 1$).

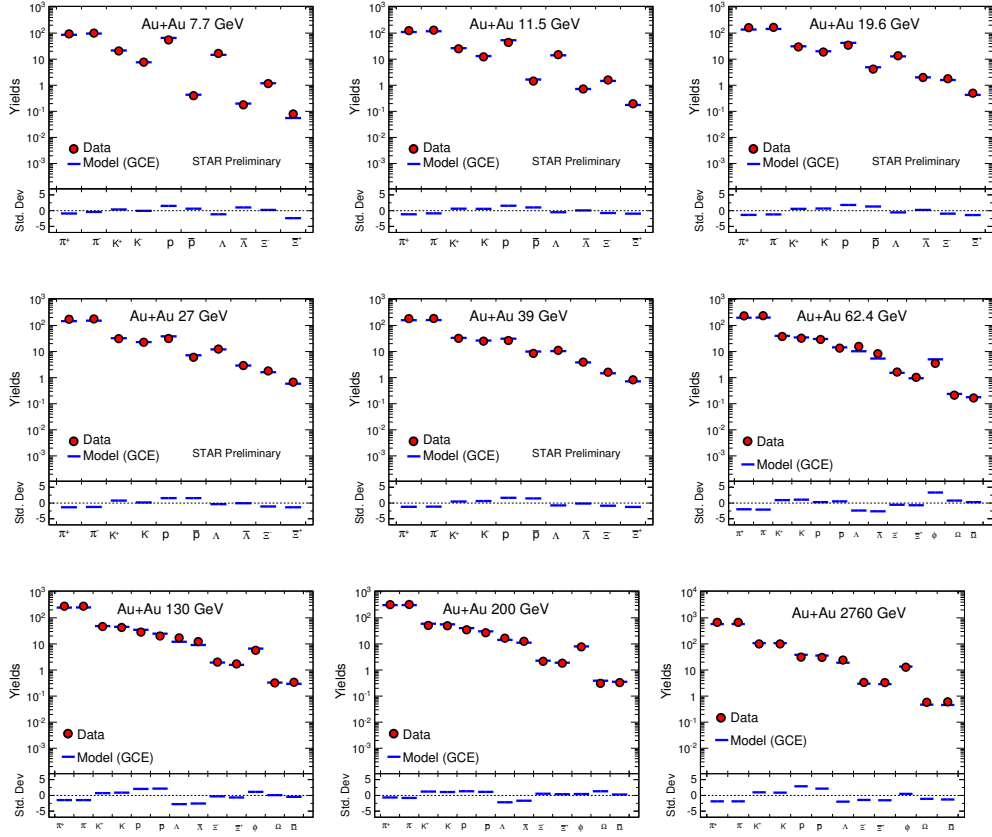


Figure 5.4: Comparison of data and model (1CFO) for particle yields in SCE shown along with standard deviations for RHIC and LHC energies ($\mu_Q = B/2Q, \gamma_S = 1$).

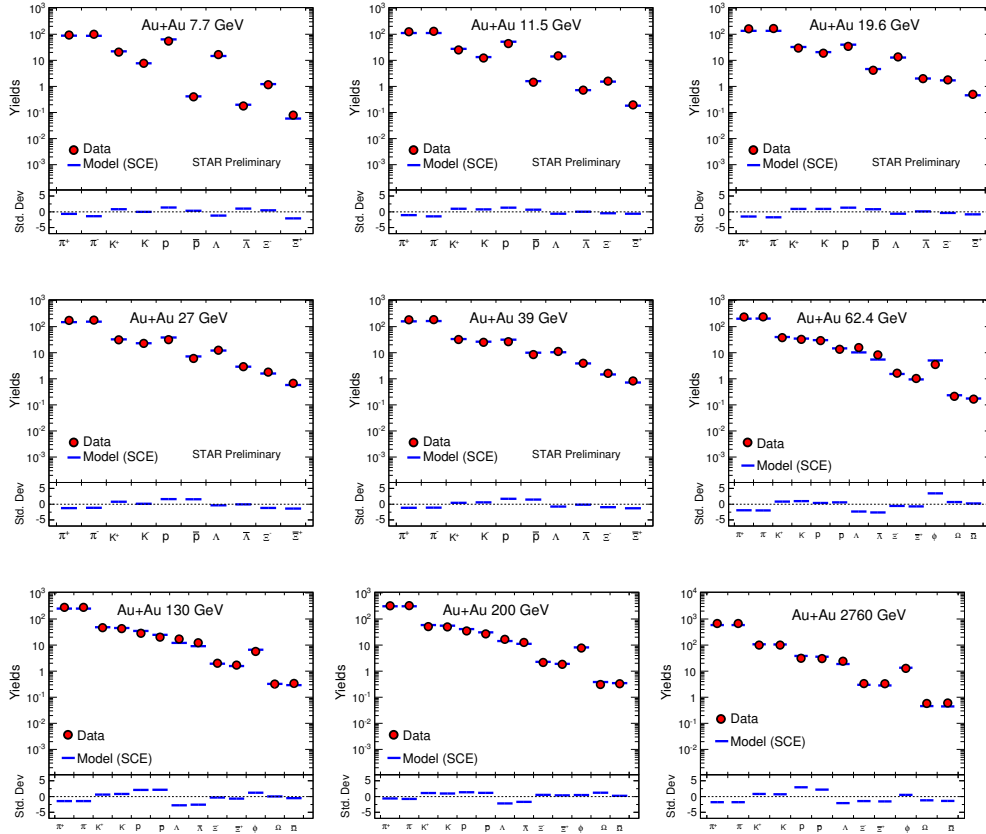
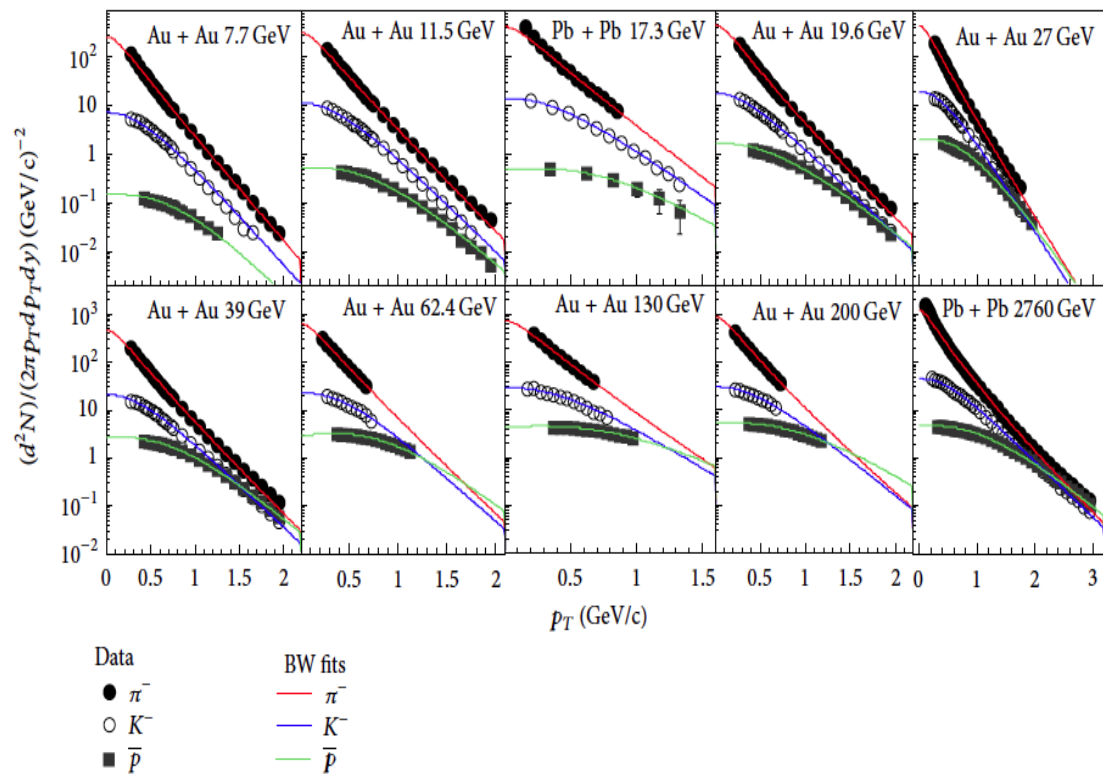


Figure 5.5: Invariant yields of pion, kaon and (anti)proton vs. p_T in central collisions at different energies. The curves represent the blast wave fits.



Chapter 6

Performance of the GEM Chambers to Monitor the TPC Tracking Calibrations in STAR

In this chapter, the performance of GEM chambers to monitor the TPC Tracking Calibrations (GMT) through its spatial resolution, gain, and efficiency study with cosmic rays are discussed. The installation and commissioning details of these GMT modules in STAR are also discussed.

6.1 Introduction

Relativistic heavy-ion collider have been taking data with increased luminosity to enable high statistics measurements, suppressing systematics that contribute to the measurements done using the TPC. The tracking resolution of TPC is important for various physics goals such as separation of upsilon states, high transverse momentum tracking for jet studies etc. Additionally, it will be necessary to maintain good pointing resolution to the silicon detec-

tors at the inner radii in STAR, to have efficient track matching for charm reconstruction. When particles move through TPC, they ionize the gas in it and create electrons and ions. As ions move much slower ($\sim 10^2$ cm/s) than the electrons ($\sim 5.5\text{--}5.58$ cm/ μ s), they create a positive charge density in drift space which is called space charge. One of the major corrections for tracking include the effect of space charge distortions. The magnitude of

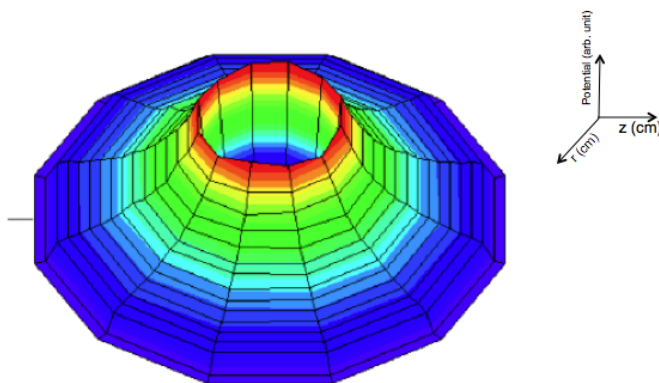


Figure 6.1: Space charge distributions in TPC.

the distortions can be studied using simulations. A simple model was proposed by Howard Weiman to study the space charge distributions in TPC. In this model, the space charge is assumed to be uniform in ϕ , and vary in r as $\sim 1/r^{1.71}$. It is also expected to be produced uniformly in z , but because of the drift to the central membrane, it builds up to a linearly growing density. Figure. 6.1 shows the space charge distributions in TPC. The overall magnitude of the space charge is assumed to vary linearly with luminosity. Earlier a model of the accumulated charge in the TPC was used to correct distortions, which can be checked at radii smaller than the inner radius of the TPC by using the interaction vertex and the silicon detectors [1]. However, no precision points outside the TPC were available to check the corrected tracks. Having such points will provide a strong constraint on the space charge distortion corrections. Also, for some of the RHIC runs, the observed charge distributions do not fit the model used for corrections. So to get reference points outside the TPC for

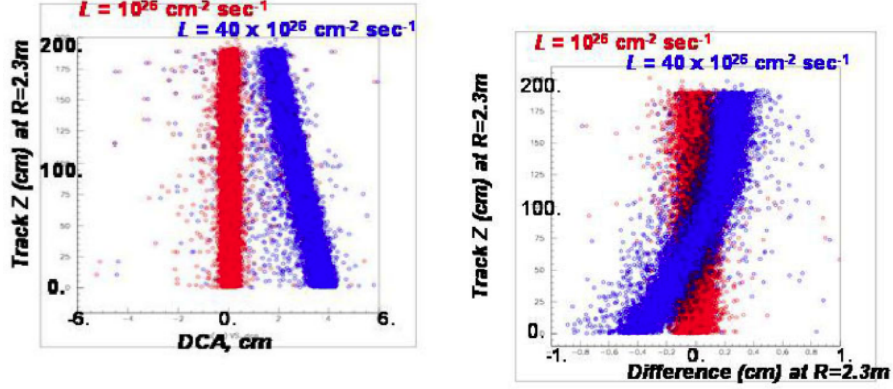


Figure 6.2: Left: the z -position of track at the TOF radius vs. DCA for pion tracks with uncorrected space charge distortions for luminosities of $10^{26} \text{ cm}^{-2} \text{ sec}^{-1}$ (red) and $40 \times 10^{26} \text{ cm}^{-2} \text{ sec}^{-1}$ (blue). Right: the z -position of track at the TOF radius vs. difference in actual track location and fitted TPC track projection at TOF radius for above mentioned luminosities [2].

space charge distortion corrections, eight GEM-based GMT chambers were proposed to be installed at TOF radius, (the same radius of $R = 2.3 \text{ m}$ at which the TOF detector is placed) in STAR by replacing some of the modules in TOF trays [2]. The left plot of Fig. 6.2 is the z -position of the track at TOF radius, $R = 2.3 \text{ m}$, as a function of the DCA distribution of pion tracks in the TPC from primary vertex with no correction for space charge distortion for low (red) and high (blue) luminosities [2]. The right plot of Fig. 6.2 is the z -position of the track at the TOF radius as a function of the difference between the position of the track at the TOF radius and the projection from the helix fit to the tracks with no space charge corrections at low (red) and high (blue) luminosities [2]. The largest differences are at $z = 0$ and $z = 200 \text{ cm}$. So, the GEM chambers located at those z -positions will have maximum sensitivity to the distortions.

This chapter includes the fabrication, study on various aspects of performance of GMT modules using Tech-Etch, Inc. produced GEM foils [3], such as tracking efficiency and spatial resolution using cosmic rays, and its installation in STAR at BNL. The detectors are found to provide high efficiency and a good spatial resolution.

6.2 The GEM Technology

Position sensitive detectors are widely used in different areas such as in nuclear and particle physics, astrophysics, medical diagnostics, and biology. Following this, Multi-Wire Proportional Chamber (MWPC) was introduced in 1968 at CERN [4, 5]. The limits in the granularity and rate capability of the MWPC led to the development of micro-pattern gas detectors, beginning with the introduction of the Micro-Strip Gas Chamber (MSGC) in 1988 [6]. The reduction of performance of MSGCs under sustained irradiation (aging) and damaging discharges, led to new developments in the area of micro-pattern gas detectors. The Gas Electron Multiplier (GEM) technology introduced by F. Sauli, is one of the most successful micro-pattern technologies and opened a new era in gas detector studies, which was first introduced in 1996 by CERN's Gas Detector Development Group [7]. For high resolution particle tracking, this type of micro-pattern gas detectors have proven to be quite successful devices. The GEM is a thin foil which is made up of kapton foil (a polyimide foil, which is a very good electric insulator), coated with a copper layer on both sides. It is chemically perforated with a pattern of holes. When high voltage is applied across the foil, it produces strong electric fields in the holes, which leads to an avalanche multiplication of electrons. So, to achieve higher gain and high operating stability for tracking applications, several GEM foils are cascaded [8]. Due to its reliability and ease of operation, GEM-based detectors have become an interesting alternative for radiation detection and imaging [9].

Although the GEM foil technology was originally developed at CERN [7], but for the proposed GMT modules, GEM foils manufactured by Tech-Etch, Inc. [3] are used. With the increased demand and use of GEM foils for several research applications, a SBIR (Small Business Innovation Research) proposal in collaboration with Tech-Etch, Inc. has been approved to provide the industrial production of GEM foils [3].

The Forward GEM Tracker (FGT) [8] of the STAR experiment is one of the successful ap-

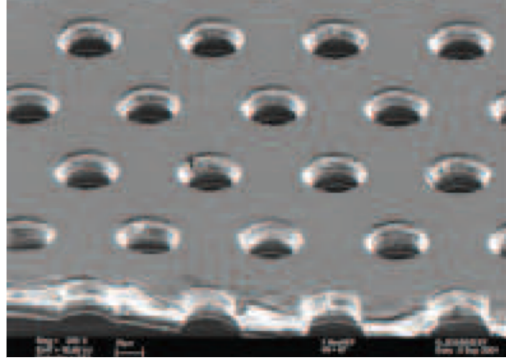


Figure 6.3: Electron microscope picture of a GEM foil [10].

plication of the GEM foils produced by Tech-Etch, Inc. [3]. Figure 6.3 shows an electron microscope picture of a GEM foil [10]. Here, the foils are made from a $5\text{ }\mu\text{m}$ copper coating on a $50\text{ }\mu\text{m}$ kapton insulator. The GEM foils are etched to produce holes throughout the surface. The double conical holes have an inner diameter of $\sim 50\text{ }\mu\text{m}$, an outer diameter of $\sim 70\text{ }\mu\text{m}$, and a pitch of $140\text{ }\mu\text{m}$ [11]. The GEM foils are powered from a single high voltage source through a high voltage divider with equal voltage sharing between the three foils. The drift gap of the detector between the cathode foil and the top GEM is 3.2 mm , the transfer gap between the other foils, and between the bottom GEM and the readout board, are 2.2 mm .

6.3 Read-out Electronics

In GEM based detectors, a GEM foil is basically used to amplify the charge deposited by the passage of an ionising particle. The signal is read out on a separate readout surface. The transfer of charge from the GEM foil to the readout plane is ensured by an electric field gradient. This method has the advantage of a fast (electron only) signal due to fast positive ion collection on the GEM foils and improved discharge tolerance due to a sepa-

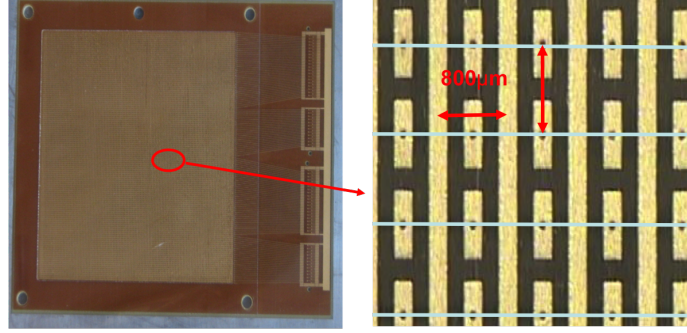


Figure 6.4: Two dimensional read-out board structure of GEM chamber with pitch width 800 μm in both x and y directions.

ration of the readout and amplification stage. The choice of readout geometries for these detectors are very flexible as the electron amplification occurs in the holes of the GEM foil and is separated from charge collection structures [11]. The readout electronics of GMT is very similar to those implemented in the STAR FGT system [12]. Both are based on commercially produced GEM foils, a laser-etched two dimensional readout board along with a APV25-S1 readout chip [13], which has been extensively tested for the CMS silicon tracker [14], and an earlier version of this chip (APV25-S0) was used for the COMPASS triple-GEM tracking detectors [10]. The APV25-S1 chip is also used in the recently installed Intermediate Silicon Tracker (IST) in STAR [15]. The design of the overall readout system for the STAR tracking upgrade has become simpler due to the advantage of using a common chip readout system for several sub-detectors.

The effective readout area given by the GEM foil for GMT is $10 \times 10 \text{ cm}^2$. The readout structure of the GEM chamber is shown in Fig. 6.4. The readout unit, with a pitch of 800 μm , is strip-style in x -direction while pad-style (inter-connected beneath) in y direction providing a total of 128 readout channels for each orthogonal direction (x/y).

6.4 Cosmic Ray Test System Setup

The cosmic ray test system setup is shown in Fig. 6.5 which consists of four regular GEM chambers. The thickness of the regular GEM chamber ionisation gap is 3.8 mm. The GEM chamber is placed in a gas-tight aluminium box with a gas mixture of argon and carbon dioxide (90% Ar + 10% CO₂) at atmospheric pressure. The advantage of using this gas is that it is non-flammable and chemically stable. In addition, fast electron drift velocity provides high gain. The gas flow is monitored by a bubbler to indicate flow.

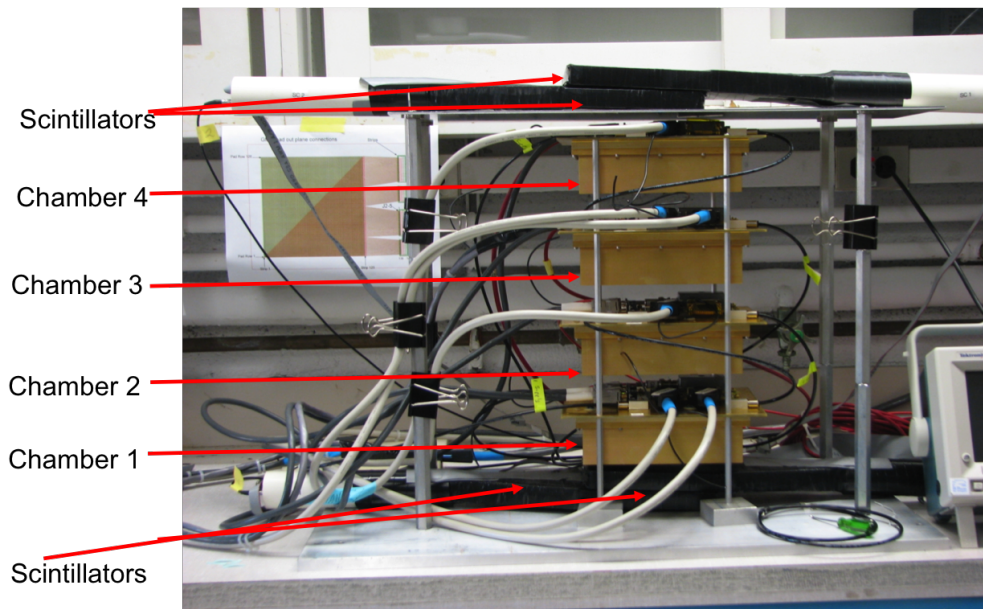


Figure 6.5: The cosmic ray test system setup with four regular GEM chambers.

Figure 6.6 shows the lower and upper part of a assembled chamber with the high voltage divider, the electronics read-out boards, and the gas inlets and outlets. The operating voltages for first, second and fourth chamber are 3100 V and that for third chamber is 3400 V. To characterise the performance of the GMT chambers we carried out measurements with cosmic rays on gain uniformity, tracking efficiency, and spatial resolution of the de-

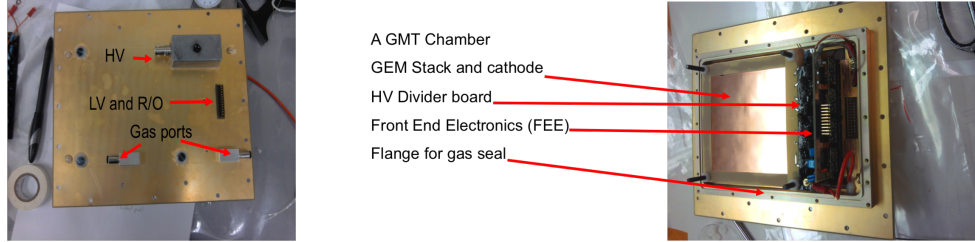


Figure 6.6: Lower and upper portion of an assembled chamber.



Figure 6.7: The FEE board assembled with two APV chips.

tector.

For generating a trigger for the system four scintillators pads, two at top and two at bottom were employed. The four-fold coincidence as obtained using photomultiplier readouts was used for a valid trigger. The effective trigger area was around $12 \times 12 \text{ cm}^2$. The vertical (z -direction) distance between these chambers was 10.5 cm. The readout boards of these GEM chambers were of 3.0 mm ionisation gap width. These chambers were placed parallel to each other in a field-free region. The front end electronics (FEE) of these GEM chambers were all based on the APV25-S1 chip [13]. The front end card assembled with two APV chips is shown in Fig. 6.7. Each APV chip has 128 channels and each read out unit is sampled in seven time bins (26.7 ns bin width) along the electron drift direction. An analog signal is created as the signal pulse from the electron multiplication is sent to a preamplifier, inverter, and shaper within the APV chip. One time bin holds the readout data for each strip/pad for a time period of approximately 26.7 ns. The seven time bins can be used to map out pulse shapes and adjust timing. The differential analog pulse is

driven from each APV chip to the APV Readout Module (ARM). In the ARM, the pulses are digitised by a 12-bit integrating analog digital converter (ADC). The data are collected from the ARMs by the APV readout controller (ARC) and then sent to the data acquisition system. The results from these raw data obtained with cosmic ray are explained below.

6.5 Performance of the GEM Chambers

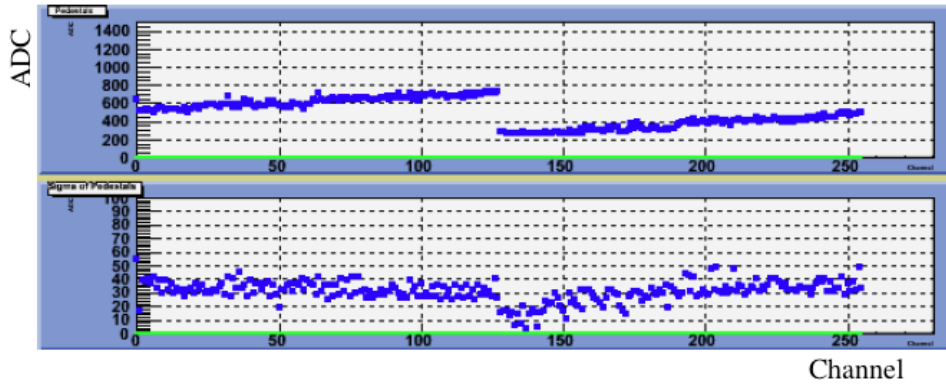


Figure 6.8: The display of mean and sigma of pedestals in ADC as a function of channel number for two APV chips obtained from cosmic ray test system setup.

The GMT modules operate through triple-GEM technology, where the charged particles ionize the gas as they traverse and the liberated electrons from this process are multiplied during collisions with gas-mixture atoms within a given electric field. The large number of electrons can induce a charge on many strips, and these strips can then be clustered to form a hit in the plane. So, the hit position is calculated from the weighted average on ADC.

$$\bar{x} = \frac{\sum_{ch} ADC_{ch} \times x_{ch}}{\sum_{ch} ADC_{ch}}, \quad (6.1)$$

$$ADC_{ch} = \sum_{timebin} \frac{ADC_{timebin}}{7}, \quad (6.2)$$

where \bar{x} is track average hit position in GMT weighted on ADC and ADC_{ch} is the average ADC of one channel. The hits of all GMT modules are fitted through a linear function to reconstruct a particle track. The data have a total of 8 APVs and each APV has 128 channels for four GMT modules as shown above. For each event, the pedestals were subtracted channel by channel.

The mean and sigma of pedestals in ADC as a function of channel number of a GMT module (two APV chips) obtained from cosmic ray test system are shown in top and bottom part of Fig. 6.8. The corrected channel amplitudes were then used to perform cluster finding for each of the GEM chambers separately. A minimum of $5\sigma_{\text{noise}}$ above pedestal was used

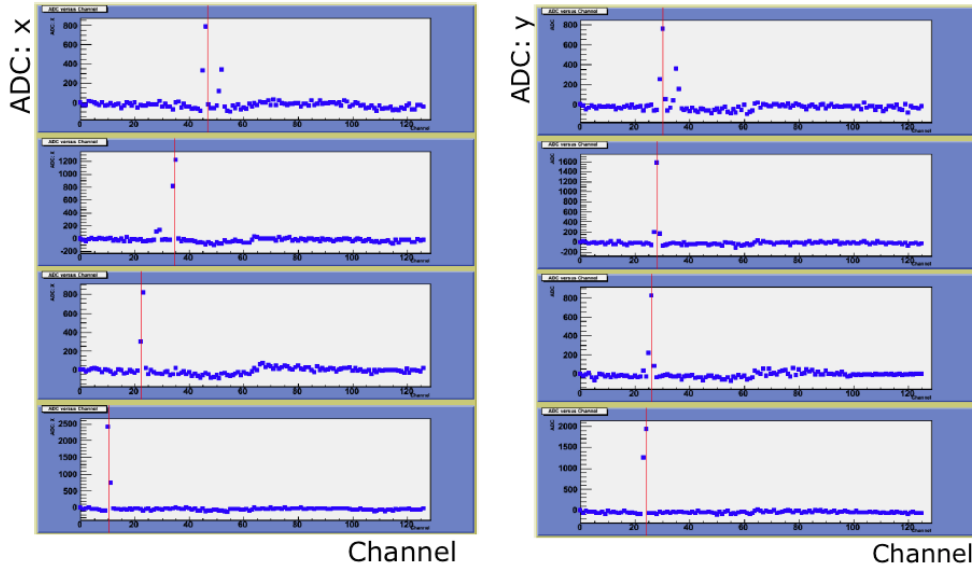


Figure 6.9: The event display of cosmic ray events for x and y co-ordinates. The red bar shows the linear track fit.

to find a cluster, where σ_{noise} was the standard deviation of the noise distribution of that particular channel. Adjacent strips were added into the cluster as long as their amplitude was more than $2\sigma_{\text{noise}}$ above pedestal. For all identified clusters, the x and y positions were calculated by the center of gravity method of the charge distribution within the cluster, and

the total charge was calculated by the integral of the signal over all strips in the cluster. The clusters found in the four GEM chambers were used to study the tracking efficiency, and spatial resolution. Since the detectors were placed in a field-free region, tracks were described as straight lines. Figure 6.9 shows the event display of reconstructed points and the fitted cosmic ray track for strip in x -direction and for pad in y -direction through all four GEM chambers. All GMT modules were aligned by finding x and y offsets.

Before installing the GMT modules in the STAR, the initial performance were studied in detail as described below.

6.5.1 Efficiency

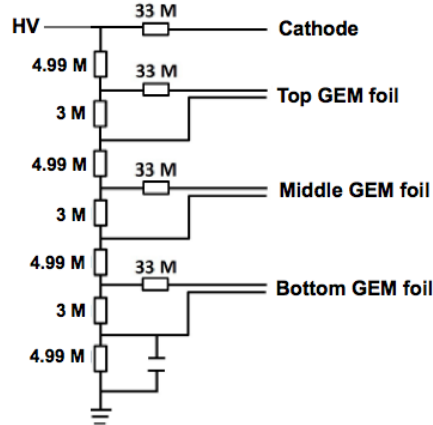


Figure 6.10: Schematic diagram of the GEM chamber high voltage divider.

To find the optimum operating voltage of the GEM chambers, the charged particle detection efficiency was scanned as a function of high voltage (HV) with the cosmic ray test system. The schematic diagram of HV divider used in the GEM chambers is shown

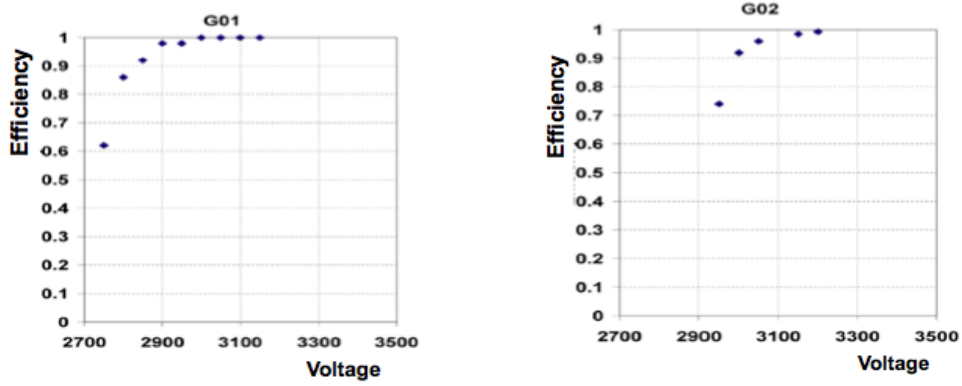


Figure 6.11: The efficiency plateau of first and second chamber.

in Fig. 6.10. Efficiency was calculated using the events with hits found in three chambers and the numbers of times hit found in the fourth chamber. Figure 6.11 shows the efficiency plateau of two regular GEM chambers. The detection efficiency went above 90% when the applied HV was higher than 3000 V. The operating voltages varied for the GEM chambers in the range 3100–3400 V, at which the efficiency was greater than 95% and reaches a plateau.

6.5.2 Gain

Each of the triple GEM detectors was evaluated with a ^{55}Fe source, dividing the active area in a 5×5 array of pads to study gain uniformity. Figure 6.12 shows the dependence of the absolute gain as a function of applied voltage. The gain was determined by using the Gaussian fitting of the 5.9 KeV peak of ^{55}Fe spectra at different voltages. The gain that was achieved with Tech-Etch Inc. triple-GEM detectors, demonstrates good performance of the GEM foils. All the GEM chambers ran at gain around 8000.

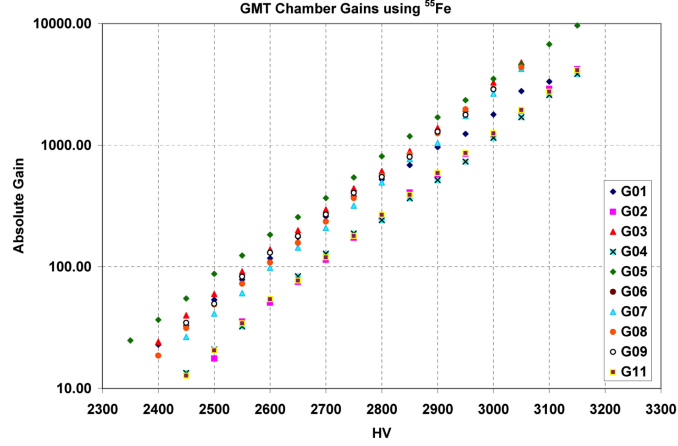


Figure 6.12: The absolute gain of different GEM chambers (G01, G02..etc.) as a function of voltage.

6.5.3 Spatial Resolution

For spatial resolution study, all four GEM chambers were required to have exactly one identified hit per projection. Spatial resolution was obtained from the width of the residual distribution, the mean distance of the reconstructed hits in one chamber to the real particle tracks formed by the other three chambers, assuming all four detectors have the same resolution. The residual distribution in the x -direction was given by $x_{\text{project}} - x_{\text{measure}}$, where

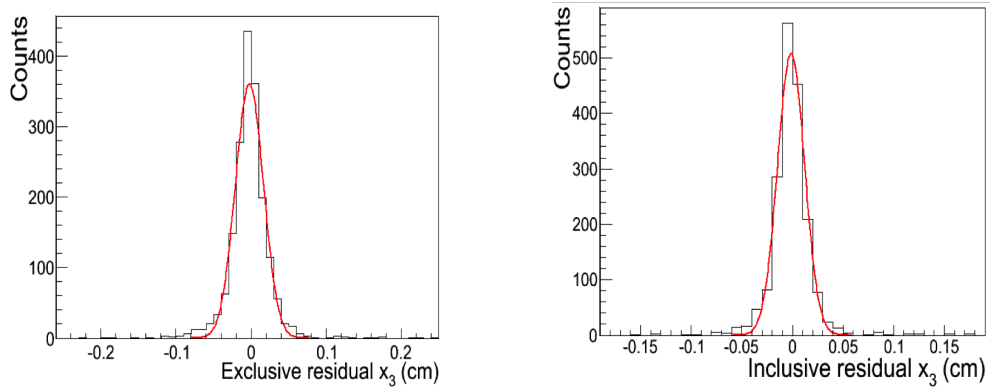


Figure 6.13: The exclusive and inclusive residual distributions in x -direction.

x_{project} was the cosmic ray trajectory position at the target GEM chamber projected from the three other GEM chambers and x_{measure} was the hit position measured by the GEM chamber. The residual distribution in the y -direction was obtained similarly. These residual distributions were fitted with the Gaussian function [16].

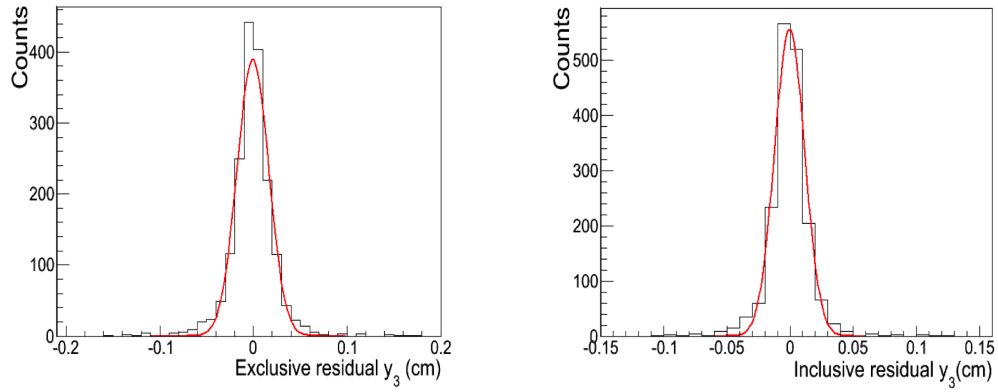


Figure 6.14: The exclusive and inclusive residual distributions in y -direction.

The intrinsic position resolution were calculated using the formula [17] given below,

$$\sigma_{\text{intr}} = \sqrt{\sigma_{\text{excl}}^2 - \sigma_{\text{intr}}'^2 [(\sigma_{\text{excl}}/\sigma_{\text{incl}}) - 1]},$$

where σ_{excl} and σ_{incl} are the resolution from the variance of residuals obtained with the exclusion and inclusion of a module for the track reconstruction, respectively. Figure 6.13 and 6.14 show the exclusive and inclusive residual distributions for x and y co-ordinates of third GMT module (x_3, y_3). The spatial resolution of x and y co-ordinate were found to be $150 \mu\text{m}$ and $134 \mu\text{m}$, respectively which was significantly better than the TPC pointing resolution ($\sim 1 \text{ mm}$).

6.6 Installation of GMT in STAR TOF trays

All eight GMT modules were tested individually and analysed using cosmic rays before installation. Figure 6.15 shows a schematic view of the detector configuration relevant to the GMT proposal. Eight GMT modules have been placed replacing some modules in four TOF trays as shown in Fig. 6.16 (schematic diagram) and installed in STAR at 2 and 5 o'clock near $|\eta| \sim 0$ and $|\eta| \sim 1$ at $\phi \sim 30^\circ$ and $\phi \sim 300^\circ$ on the east and west sides at the TOF radius in February 2013.

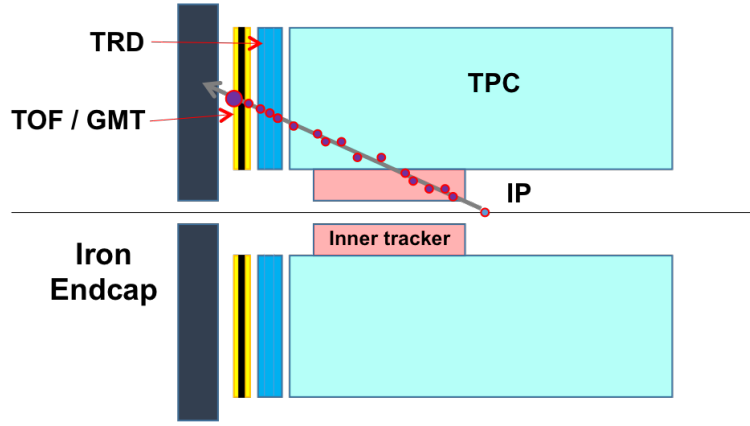


Figure 6.15: Schematic view of the GMT in STAR for space charge distortion correction to provide reference point outside TPC.

6.7 Commissioning in STAR

These GMT modules were tested again with cosmic rays in STAR experiment during RHIC runs, to be sure that the detector still operates in the same manner after its installation into STAR. One way to check this operation is to investigate the read out of the electronic pedestal. A pedestal is an ADC reading of a channel in the electronics, when no energy is deposited in the detector. Any signal from charged particles passing through the detector

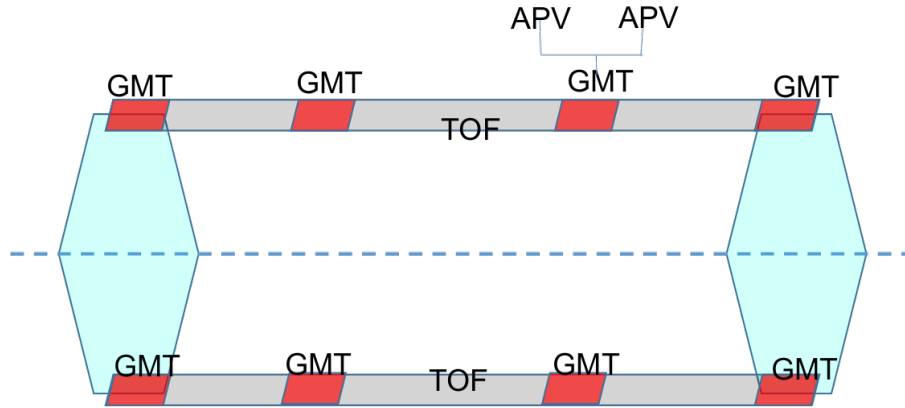


Figure 6.16: The schematic diagram of position of GMT chambers installed in STAR TOF trays.

should deposit energy above the pedestal value. When the high voltage on the GEM foils is turned off, there is no signal produced by charged particles, so the only data comes from the electronics. Figure 6.17 represents ADC as a function of channel number obtained from the STAR cosmic data. The pedestals ADC with the STAR cosmic data compared with the cosmic ray test stand results as shown in Fig. 6.8 were found to be similar. All the eight GMT modules were found to be working perfectly with the STAR data.

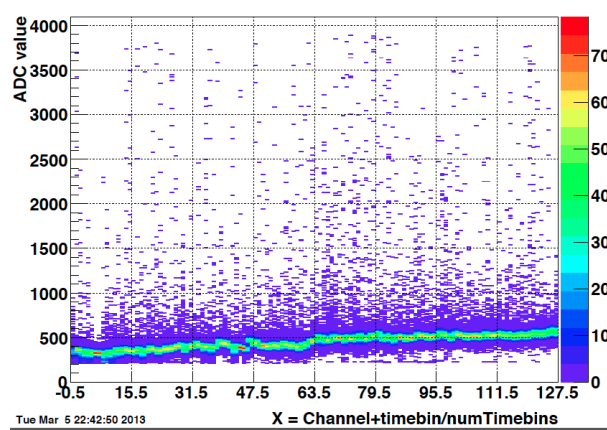


Figure 6.17: The display of ADC as a function of channel number obtained from STAR cosmic data.

6.8 Thick GEM for Transition Radiation Detector

A thick gas electron multiplier (THGEM) chamber with an effective read-out area of 10×10 cm² and a 11.3 mm ionisation gap also has been tested along with two regular gas electron multiplier (GEM) chambers in the cosmic ray test system [18]. The thick ionisation gap makes the THGEM chamber a mini-drift chamber. This kind of mini-drift THGEM chamber is proposed as part of a transition radiation detector (TRD) for identifying electrons at an Electron Ion Collider (EIC) experiment [19]. Through this cosmic ray test, a spatial resolution ~ 220 μ m was achieved for the thick GEM chamber as shown in Fig. 6.18.

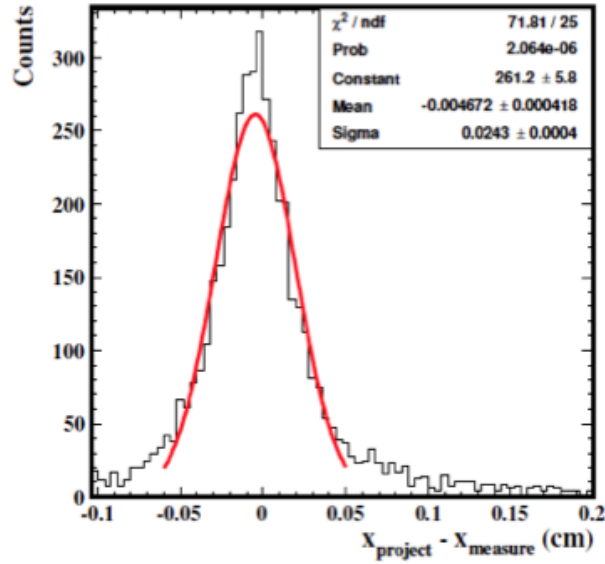


Figure 6.18: The residual distribution in x -direction, x_{project} is the x -position at the THGEM chamber projected from the two regular GEM chambers, x_{measure} is the x -position measured by the THGEM chamber.

6.9 Summary

The GMT modules with triple GEM chambers have been built and tested with cosmic rays. The results of the cosmic ray reveal the excellent performance of the regular GEM chambers along with the thick GEM chambers. The cosmic ray test results indicate a detection efficiency greater than 95% for GMT. A multiple-scattering dominated upper limit for the resolution has been measured using the cosmic ray test stand and meets the requirement of being significantly better than the TPC pointing resolution to the chambers. The spatial resolution of the GMT along the direction of the read-out strips (pad) was found to be $\sim 150\text{ }\mu\text{m}$. Eight GMT modules have been installed in STAR for TPC space charge distortion corrections. The Thick GEM chambers shows good spatial resolution $\sim 220\text{ }\mu\text{m}$, which offers an important reference for the proposed TRD design [\[20\]](#) at EIC.

Bibliography

- [1] G. Van Buren *et al.*, Nucl. Instr. Meth. A 566, 2225 (2006).
- [2] GMT Proposal, “GEM Monitoring of TPC Tracking Calibration (GMT) in STAR”,
<http://drupal.star.bnl.gov/STAR/system/files/Proposal-to-Install-GEM-Chambers-GMT.pdf>.
- [3] Tech-Etch Corp, 45 Aldrin Rd, Plymouth, MA 02360; F.Simon *et al.*, IEEE Trans. Nucl. Sci. NS-54, 2646 (2007).
- [4] G. Charpak *et al.*, Nucl. Instr. Meth. 62, 262 (1968).
- [5] F. Sauli and A. Sharma, Ann. Rev. Nucl. Part. Sci. 49, 341 (1999).
- [6] A. Oed, Nucl. Instr. Meth. A 263, 351 (1988).
- [7] F. Sauli, Nucl. Instr. Meth. A 386, 531 (1997).
- [8] F. Simon *et al.*, Nucl. Instr. Meth. A 598, 432 (2009); F. Sauli, Nucl. Instr. Meth. A 522, 93 (2004), and references therein.
- [9] T. Meinschad *et al.*, Nucl. Instr. Meth. A 535, 324 (2004).
- [10] M. C. Altunbas *et al.*, Nucl. Instr. Meth. A 490, 177 (2002).

- [11] FGT Proposal, “Forward GEM Tracker (FGT) - A Forward Tracking Upgrade Proposal for the STAR Experiment”,
https://drupal.star.bnl.gov/STAR/system/files/fgt_review_0.pdf.
- [12] F. Simon (for the STAR Collaboration), J. Phys. Conf. Ser. 110, 092029 (2008); F. Simon *et al.*, arXiv:0811.2432.
- [13] M. J. French *et al.*, Nucl. Instr. Meth. A466, 359 (2001).
- [14] CMS, CERN-LHCC-98-06.
- [15] HFT Proposal, “A Heavy Flavor Tracker for STAR experiment”,
http://drupal.star.bnl.gov/STAR/system/files/HFT_CDR_Final-1.pdf.
- [16] https://drupal.star.bnl.gov/STAR/files/gmt_poster_rhicags_21stJune_v2_0.pdf.
- [17] <http://drupal.star.bnl.gov/STAR/comp/calib/docs/intrinsic-resolution-a-tracking-element>.
- [18] S. Yang, S. Das, and Z. Xu *et al.*, arXiv:1412.4769.
- [19] A. Accardi *et al.*, arXiv:1212.1701.
- [20] TRD Proposal, “STAR Transition Radiation Detector Proposal”,
https://wiki.bnl.gov/conferences/images/3/3d/TRD_EIC_RDproposal_FY2012_v3.pdf.

Chapter 7

Conclusions

The first phase of BES program at STAR has the following goals: (1) to search the threshold energies for the QGP signatures which is already established at top RHIC energy ($\sqrt{s_{NN}} = 200$ GeV), (2) to search for the first-order phase transition and map the QCD phase diagram, where T_{ch} and μ_B form the axes of the QCD phase diagram and (3) to search the QCD critical point at high μ_B . To achieve these goals Au+Au data were collected by STAR experiment at $\sqrt{s_{NN}} = 7.7, 11.5, 19.6, 27,$ and 39 GeV in the year 2010 and 2011. An additional BES-I data were taken at $\sqrt{s_{NN}} = 14.5$ GeV in 2014. The statistical model analysis of the yields of several hadron species in STAR from BES-I program presented in this thesis, shows that the program covers a large part of μ_B ($20 - 420$ MeV) in QCD phase diagram. This thesis presents the identified particle production ($\pi^\pm, K^\pm, p (\bar{p})$) in Au+Au collisions at $\sqrt{s_{NN}} = 27$ GeV, which is a part of the data set taken in BES-I. An extensive study on extraction of chemical freeze-out parameters using the measured BES-I data, which includes T_{ch} and μ_B , have been done at all the BES-I energies. In addition to this, the systematic study of freeze-out dynamics have been performed by analysing the data taken at AGS, SPS, RHIC, and LHC energies. A summary of interesting results reported in this thesis are mentioned below.

The identified particles such as pion (π^\pm), kaon (K^\pm), protons (p), and antiprotons (\bar{p}) have been measured in Au+Au collisions at $\sqrt{s_{NN}} = 27$ GeV using the TPC and TOF detectors at mid-rapidity ($|y| < 0.1$). The raw yields have been extracted using the charged particle energy loss in TPC and the measured mass of the particle in TOF. The corrected p_T spectra for different hadron species have been obtained after doing various corrections such as energy loss of a charged track passing the TPC medium, efficiency of charged track reconstruction, acceptance, and weak-decay contributions for pions only. The p_T spectra are presented for nine centrality bins, 0–5%, 5–10%, 10–20%, 20–30%, 30–40%, 40–50%, 50–60%, 60–70%, and 70–80%, and are well described through Blast-wave model. Pion spectra are weak-decay corrected whereas proton spectra are inclusive. The bulk properties of matter have been studied through $\langle p_T \rangle$, $\langle m_T \rangle - m$, dN/dy , and particle ratios. The results for Au+Au collisions at $\sqrt{s_{NN}} = 27$ GeV have been compared with other RHIC energies and also with other experiments like AGS, SPS, and LHC to study the energy dependence. The $\langle p_T \rangle$ increases from peripheral to central for all species, which reflects the large radial flow in central collisions. It also increases with the increase of hadron mass, indicating some degree of collectivity in radial direction. The variation of $\langle m_T \rangle - m$ with energy shows an increase, then a plateau, and then further increase with energy. This could indicate the signature of first-order phase transition, at lower BES-I energies however, it requires a more careful study and also theoretical comparisons. The centrality and energy dependence of particle yields and particle ratios have also been studied. The pion yields per participating pair are found to be independent of centrality whereas kaon and (anti)proton yields per participating pair increase with centrality, which implies the yields could also depend on the number of nucleon-nucleon binary collisions. With the increase of energy, the yields of pions, kaons, antiprotons increase, whereas proton yield decreases. The ratios π^-/π^+ , K^-/K^+ remain independent of centrality. The \bar{p}/p ratio de-

creases from peripheral to central. The values of π^-/π^+ is higher at lower energies due to the dominant contributions from resonance decays and it becomes unity at higher energies. The K^+/π^+ ratio with $\sqrt{s_{NN}}$ shows peak around 7 GeV and then remains fairly constant towards higher energies. A strong correlation is found to be between the ratios K^-/K^+ and \bar{p}/p which follows a power-law behaviour.

The measured identified particle yields (π , K , p) in addition to strange hadron yields (Λ , Ξ , Ω , ϕ) and their corresponding antiparticles at mid-rapidity are observed to be well described by statistical thermal models at all RHIC energies. The freeze-out parameters T_{ch} , μ_B , μ_S , and γ_S have been extracted from both particle yields and particle ratios in GCE and SCE approaches of THERMUS model for all BES-I energies along with top RHIC energies ($\sqrt{s_{NN}} = 62.4$ and 200 GeV) except $\sqrt{s_{NN}} = 14.5$ GeV. The T_{ch} increases from 7.7 to 19.6 GeV after that it remains almost constant. For a given energy, the value of T_{ch} is almost similar for all centralities. The μ_B and μ_S follow the same trend, decreases with increase of energy and it also increases from peripheral to central collisions. γ_S increases from peripheral to central for all energies studied. The results from GCE and SCE found to be similar at all centrality bins except peripheral bins, where the value of T_{ch} from SCE is slightly higher (but within errors) than that of GCE. Also the freeze-out parameters obtained from yields are slighter higher (within errors) in comparison with that of values extracted from ratios. The extracted T_{ch} and μ_B values have been used to study the chemical freeze-out line in the QCD phase diagram, where RHIC covers a large range compared with other heavy-ion facility such as AGS, SPS, and LHC. From the results, it is seen that the RHIC BES-I program covers a μ_B range from 20 MeV (at $\sqrt{s_{NN}} = 200$ GeV) to about 420 MeV (at $\sqrt{s_{NN}} = 7.7$ GeV) in the QCD phase diagram. LQCD calculations and other QCD based calculations suggest that the μ_B range covered from BES-I energies could contain the key information on the QCD critical point and the region of the first-order phase transition.

The kinetic freeze-out parameters (T_{kin} , $\langle\beta\rangle$) are extracted from a simultaneous Blast-wave model fit to pion, kaon, and (anti)proton p_T spectra. Different p_T ranges in the p_T spectra are found to have little effect on the extracted kinetic freeze-out parameters. We have used p_T ranges 0.5–1.3 GeV/ c for pion, 0.25–1.4 GeV/ c for kaon, and 0.4–1.3 GeV/ c for proton to extract T_{kin} and $\langle\beta\rangle$. The T_{kin} decreases from lower to higher energies, whereas the extracted collective flow velocity increases significantly with increasing centrality and energy. The difference between the extracted chemical and kinetic freeze-out temperatures increases while going towards lower μ_B (or higher energies) indicating increasing hadronic interactions between chemical and kinetic freeze-out at higher energies.

In addition to a detailed study of chemical freeze-out dynamics at RHIC BES-I energies, systematic studies have been performed from lower AGS energy (2.7 GeV) up to higher LHC energy (2760 GeV) including SPS and RHIC energies for central Au+Au and Pb+Pb collisions. Systematic studies include the choice of freeze-out parameters, on the choice of ensembles, on the choice of particle yields included in the fit, and on the choice of freeze-out schemes. Thermal parameters are found to be very sensitive to the different freeze-out schemes like 1CFO (single freeze-out) and 2CFO (strange and non-strange hadrons having different freeze-out surfaces). However, we found a weak dependence of the extracted freeze-out parameters on other systematic variations. The T_{ch} from 1CFO found to be vary between the strange and non-strange T_{ch} obtained from 2CFO. Different particle ratios are used as good probe to distinguish between 1CFO and 2CFO schemes. We observed that 2CFO explains much better the unlike flavor ratios (strange to non-strange ratios: K/π , Λ/π). The like flavor ratios (strange to strange: Λ/K^- or non-strange to non-strange: p/π^+) are explained very well in both 1CFO and 2CFO schemes.

This thesis also reports on the fabrication of eight $10 \times 10 \text{ cm}^2$ GMT chambers, their testing with cosmic rays at BNL and installation in STAR in the year 2013. They provide reference points outside TPC for spatial distortion corrections. A 2D read-out foil with a pitch width $800 \text{ }\mu\text{m}$ in both x and y directions has been used. An efficiency greater than 95% has been observed for all the modules. A multiple-scattering dominated upper limit for the spatial resolution, $\sim 150 \text{ }\mu\text{m}$ has been measured with cosmic ray, which is much better than the TPC resolution ($\sim 1 \text{ mm}$). Thick GEM chamber with ionisation gap width 11.3 mm also have been tested with cosmic ray. The spatial resolution of thick GEM has been found to be $\sim 220 \text{ }\mu\text{m}$ and provides a reference for the design of proposed TRD detector for EIC.